Mechanical behavior of recycled polypropylene reinforced by coconut fibers using X-ray tomography and digital image correlation

Alexandre de Souza Rios

NNT : 2015SACLN023

DOCTORAL THESIS
of
UNIVERSIDADE FEDERAL DO CEARÁ
and
L'UNIVERSITÉ PARIS-SACLAY
prepared at École Normale Supérieure de Cachan

ÉCOLE DOCTORALE N° 579
Sciences mécaniques et énergétiques, matériaux et géosciences – SMEMAG

Doctoral speciality: Mechanical Engineering

by

Alexandre de Souza Rios

Mechanical behavior of recycled polypropylene reinforced by coconut fibers using X-ray tomography and digital image correlation

Thesis presented and defended in Fortaleza (Brazil) on 18 December 2015:

Panel members :

Sandro Campos Amico	Professor, Universidade Federal do Rio Grande do Sul	Rapporteur
José Ricardo Tarpani	Professor, Universidade de São Paulo	Rapporteur
Nikolaus Peter Schmitt	Professor, Université Paris-Est Créteil	Examiner (President)
Pierre Maurice Christophe Lamary	Professor, Universidade Federal do Ceará	Examiner
Enio Pontes de Deus	Professor, Universidade Federal do Ceará	Superviser
Ahmed Benallal	Research Director, CNRS	Superviser

université PARIS-SACLAY | ÉCOLE DOCTORALE Sciences mécaniques et énergétiques, matériaux et géosciences (SMEMAG)

Titre : Comportement mécanique de polypropylène recyclé renforcé par des fibres de coco en utilisant la tomographie par rayons-X et la corrélation d'image numérique

Mots clés : fibre de coco, recyclage, comportement morphologique, comportement mécanique, corrélation d'image numérique, mécanique de l'endommagement.

Les fibres naturelles ont gagnées récemment l'attention en raison du faible impact sur l'environnement, faible coût et bonne disponibilité. Dans cette étude, des caractérisations morphologiques et mécaniques ont été utilisées sur des fibres de coco brésiliens dans les conditions «brutes» et superficiellement traitées (NaOH, chauffé et de NaOH suivi par un chauffage), sur des tissus non-tissé de fibres de coco produit par compression, polypropylène (PP), polypropylène recyclé (RPP) et sur des composites impliquant ces matériaux. La microscopie électronique à balayage (MEB) et la tomographie à rayons X (XRT) ont été utilisées pour l'analyse morphologique et l'essai de traction uniaxiale suivi par corrélation d'image numérique (DIC) et thermographie infrarouge ont été utilisés pour l'analyse mécanique. Le MEB a montré que les fibres de coco traitées chimiquement ont des parois externes plus nettes et des particules circulaires avec des diamètres d'environ 10 µm. Les fibres ont des interfaces différentes à l'intérieur du composite: fibre-matrice, fibres-latex et fibres-fibres. La XRT a présenté les principaux constituants de la fibre de coco avec une superficie de vides internes d'environ 57 à 60% et un tissu non-tissé composé de fibres multidirectionnelles contournées par le latex. La distribuition de fibres de coco est liée à la direction d'injection lors de la fabrication de matériaux composites. La fraction volumique de fibres de coco dans les composites et les impuretés dans les PP et RPP ont été déterminés dans la direction 3D. Certaines fibres de coco non entièrement contournées par la matrice démontrent l'incompatibilité entre les fibres et la matrice. Le module initial (module d'élasticité) et la contrainte à la traction ont diminué avec l'augmentation de diamètre pour les quatre conditions de fibres de coco. L'analyse par DIC a montré des champs de déformations hétérogènes sur les fibres de coco et sur les tissus non-tissés; les champs de déplacement ont montrés le processus de rupture de la fibre de coco. Le coefficient de Poisson des matériaux manufacturés a été déterminée par des déformations transversales et longitudinales trouvées dans la région élastique. Les fibres de coco et le recyclage de polypropylène ont influencées les propriétés mécaniques des polymères. Le DIC a identifié les champs de déformation et les mécanismes de formation de striction sur PP et la thermographie infrarouge indique que le début de processus adiabatique pendant la déformation plastique a été formé pendant l'alignement des liaisons polymériques. Les zones de chauffage ont été régies par le régime post-striction et elles ont présentées des formes paraboliques avec la température de pic localisé. Un modèle numérique a prédit la courbe contrainte-déformation jusqu'à la contrainte maximale. À travers des paramètres numériques obtenus par ce modèle, il a été possible de déterminer chaque courbe d'endommagement. Des endommagements critiques et les composites fabriqués par RPP ont plus de temps à la propagation de la rupture. L'évolution de endommagement par des champs de déformation a démontré que les déformations longitudinales sont prédominants par rapport à la déformation transversale dans le processus de endommagement du matériel. L'évolution de endommagement par d'essais de traction de charge/décharge a présenté des changements dans le module d'élasticité et une hystérésis considérable. Une valeur de endommagent critique dans le composite conformément à la littérature a été trouvé. Des relations constitutives entre déformation longitudinale et endommagement ont été représentées par équations polynomiales. Les valeurs de déformation longitudinale relative à l'apparition de endommagement en utilisant champs de déformation et par charge/décharge sont similaires. Les micrographies de rupture du composite fabriqué par PP montrent une fracture ductile et la présence de saillies associées à des régions homogènes. Le RPP a présenté des fractures fragiles et ductiles et régions hétérogènes de rupture. Des micrographies montrent des microfissures autour de la rupture finale d'une fibre cassée à l'intérieur du composite similaire aux essais de traction sur les fibres individuelles.

Title : Mechanical behavior of recycled polypropylene reinforced by coconut fibers using X-ray tomography and digital image correlation

Keywords : coconut fiber, recycling, morphological behavior, mechanical behavior, digital image correlation, damage mechanics.

Natural fibers has recently gained attention due to low environmental impact, low cost and easy availability. In this study, morphological and mechanical characterizations were carried out on Brazilian coconut fibers in the 'as received' and superficially treated conditions (NaOH, heated and NaOH followed by heating), on coconut fiber mats manufactured by compressing, polypropylene (PP), recycled polypropylene (RPP) and composites involving these materials. Scanning Electron Microscopy (SEM) and X-ray tomography (XRT) were performed for morphological analysis and unidirectional tensile test following by Digital Image Correlation (DIC) and infrared thermography were used for mechanical analysis. SEM analysis showed that the chemically treated coconut fibers have sharper external cell walls and circular particles with diameters of approximately 10 µm. The fibers have different interfaces within the composite: fiber-matrix, fiber-latex and fiber-fiber. XRT presented the main constituents of natural coconut fiber with an area of about 57 to 60% of internal voids and a mat composed by multidirectional fibers involved by latex. Coconut fibers distribution is related to the injection direction during composites manufacturing. The volume fraction of coconut fibers in composites and impurities in PP and RPP were determined in 3D direction. Some coconut fibers not fully involved by matrix demonstrate the incompatibility between fiber and matrix. The initial modulus (modulus of elasticity) and tensile strength decreased with increasing diameters for the four conditions of coconut fibers. DIC analysis showed heterogeneous strains fields on coconut fibers and on mats; the displacement fields showed the rupture process of coconut fiber. Poisson's ratio on the manufactured materials was determined through the transverse and longitudinal strains found in the elastic region. The coconut fibers and the recycling of polypropylene influenced on the mechanical properties of the polymers. The DIC identified strain fields and yielding formation mechanisms on PP and the infrared thermography indicates that the adiabatic process onset during the plastic deformation was formed during the alignment of polymer chains. The heating zones were governed by post-yeld regime and presented parabolic shapes with localized peak temperature. A numerical model could predict the stress-strain curve until the maximum stress on the materials of this work. Through numerical parameters obtained by this model, it was possible to determine each damage curve. Critical damage was determined and the composites fabricated by RPP have more time for rupture propagation. Damage evolution using strain fields from DIC demonstrated that the longitudinal strains are predominant in relation to the transverse strain on the damage process. Damage evolution from load/unload tensile testing presented changes in modulus of elasticity and a representative hysteresis. A critical damage value of the composite in accordance with the literature was found. Constitutive relationships between the longitudinal deformation and damage were represented by polynomial equations. The values of longitudinal deformation related to the onset of damage using strain fields from DIC and from load/unload are similar. Rupture micrographs of the composite manufactured by PP show a ductile fracture and the presence of protrusions at homogeneous regions. RPP presented fragile and ductile fractures areas as well as heterogeneous regions of rupture. Rupture micrographs of a ruptured fiber inside the composite shows microcracks around the rupture, similar to tensile testing on individual fibers.

To my parents (Francisco and Ana), my brothers (Rafael and Larissa), my grandparents (Pedro and Terezinha, eternal living presence), and my nephew-godson Pedro Lucca

Acknowledgements

I first thank God for following me in every moment of my life.

I thank my family and friends, who gave me all the support to the realization and continuation of my career choice and presence during this work, especially during my period in France.

I thank Prof. Enio Pontes de Deus by his involuntary trust and for believing in his team. I thank him for the unique and indescribable international experience and integration to the project CAPES/COFECUB, project N° 773/13 (Brazil/France), in which the scientific-cultural learning will be forever in my memory and be part of me.

I thank all LAMEFF team (especially Abner, Luiz Flávio, Iasmyn, Rayanne and Santino) who spared no efforts to, even in unconventional schedules, collaborate with the preparation of samples and with this project in an intense way and making good exchange of knowledge.

I thank the Director of research at the *Centre National de la Recherche Scientifique* (CNRS), Ahmed Benallal, by parallel trust to the Prof. Enio in my work, by the dialogues involved in the thesis and for having included me in the *Laboratoire de Mécanique et Technologie* (LMT-Cachan), a mixed research unit between *École Normale Supérieure de Cachan* (ENS-Cachan), CNRS (UMR 8535) and *Université Paris Saclay*, internationally recognized and structured with equipment of last generation, and especially equipped with professors and researchers with great innovative ideas that serve to the interests of best current projects lines.

I thank all LMT-Cachan team (especially to François Hild, Patrick, Xavier Pinelli, Xavier Fayolle, Boubou, Remy) for instant readiness to adjust samples and equipment to carry out the experimental tests of this thesis.

I thank all the members of the Post-Graduate Program in Engineering and Materials Science of the Federal University of Ceará for their attention with the students and for exalting their potential.

I thank the CAPES/COFECUB project (project N° 773/13) for granting the scholarships and other financial aids in France.

Contents

List of Figures and Tables

Figures

Tables

Simbols and abbreviations

Simbols

$\vec{F}$: force

$\vec{n}$: versor

σ: nominal stress

$\tilde{\sigma}$: effective stress

σ_t, σ_{true}: true stress

σ_u: ultimate stress

σ_{sd}: standard deviation

σ_R: tensile strength

δ_u: systematic error

S: total area

So: area of defects

$\tilde{S}$: area without defects

A_o: area of the initial cross-section

l: lenght

w: width

t: thickness

D: damage variable

ϕ: diameter

D_n : damage associated with a plane normal $\vec{n}$

D_c: critical damage

ε: strain

ε_t: transverse strain

ε_l: longitudinal strain

ε_w: strain in width

ε_t: strain in thickness

ε_n: effective linear deformation

ε_{eq}: equivalent strain

ε_p: characteristic strain

ε_{eng}: engineering srain

u_{pre} : measured displacement

u_{est}: deformation truly occurred

u_l: longitudinal displacement

u_t: transverse displacement

Ux: displacement filed in *x* axis

Uy: displacement filed in *y* axis

C_p: amplitude identified in strain histograms

E: modulus of elasticity

$\widetilde{E}$: modulus of elasticity of a damaged material

λ, μ: Lame coefficients of the virgin material

ν: Poisson's ratio

ρ: error or fluctuation value in damage measurement by strain fields

χ: ratio of the standard deviation

a,b: characteristic parameters of the material

n: number of samples

λ: wavelength of the radiation

L_λ: power radiated

c_1, c_2: first and second radiations constants

T: temperarature

σ: Stefan–Boltzmann's constant

ε: emissivity

Abbreviations

ASTM: American Society for Testing and Materials

DIC: Digital Image Correlation

DIT: Digital Infrared Thermography

DSC: Differential Scanning Calorimetry

ENS-Cachan: École Normale Supérieure de Cachan

HDPE: high density polyethylene)

LDPE (low density polyethylene),

LMT-Cachan: Laboratoire de Mécanique et Technologie of ENS-Cachan

MFI: melt flow index

PC: polycarbonate

PEEK: poly (éteréter ketone)

PET (polyethylene terephthalate)

PP: polypropylene

PPS: poly (phenylene sulfide)

PS: polystyrene

PVC: polyvinyl chloride

RPP: recycled polypropylene

RVE: Representative Volume Element

SEM: Scanning Electronic Microscopy

XRT: X-ray tomography

1. Introduction

1.1. Overall considerations

The issues related to environmental impact and sustainable development has encouraged to interest in materials from natural sources, as well as they stimulate the development of new raw materials and products (George et al., 2001). The decreasing of global petroleum resources, along with an awareness of global environmental problems, such as a lack of landfills, has promoted the development of alternative materials, such as polymers and composites from natural sources. These newly developed materials are in agreement with the environmental concerns and its development is free of the non-renewable petroleum resources (Zulkifli et al., 2015).

In this sense, recycled, renewable and reusable materials have preference front of virgin materials, which require more energy and emit more CO_2 during its manufacturing. The recycling of plastic waste and the use of coconut husks, for example, as engineering materials corroborate with this environmental context.

Numerous vegetable fibers, such as green coconut fibers, are usually discarded. They are inside the coconut husks which are often discarded on Brazilian beaches after consumption of its water. This material disposal is significant in waste and landfills of the Brazilian great coastal cities. Its reutilization may provide the manufacturing of materials for industrial and civil sector in order to meet these current requirements. Moreover, Brazil has great potential to produce and market different vegetable fibers, due to their variety and abundance of its biomass (Razera, 2006).

In this context, these vegetable fibers have been investigated to be used as reinforcement in composite polymer matrices, because they combine important properties and are in agreement with sustainable project ideas. Furthermore, the coconut fibers present strong ecological appeal and characteristics such as low cost, low density, renewability, biodegradability, non-toxic and low abrasive, attractive thermal and acoustic properties (Bledzki & Gassan, 1999).

Due to these properties, coconut fibers can also be used as thermal and acoustic insulators. There are many studies in the literature looking for new applications with natural

fibers for the manufacture of materials in which the mechanical resistance is not the most important requirement (Defoirdt et al., 2010).

Compared to glass-fibers, the production of natural fibers causes less environmental impacts. This is because the cultivation of natural fibers depends primarily on solar energy and needs small amount of energy from fossil fuels in the production and extraction processes (Joshia et al., 2004).

However, there are some disadvantages in using natural fibers as reinforcement in composite materials, such as: quality and production efficiency, which depend on the natural conditions; heterogeneity of their properties which may be associated with the sazonality, production, extraction and processing conditions of the fibers, and the hydrophilic behavior which leads to water absorption in the composite systems, as well as poor compatibility with polymers (Tomczak, 2010).

A German company continually invests in the development of these materials, aiming, among other things, concern for ecological issues, the price and availability of these materials in nature (The National Non-Food Crops Centre, 2006). A vehicle of this German manufacturer, for example, uses 24 kg of renewable materials, of which more than 13 kg represent vegetable fibers (Figure 1.1). These materials are used in coatings doors and other internal parts of the vehicle.

Figure 1.1. Vehicle from a German company and vegetable fibers.

Source: The National Non-Food Crops Centre, 2006.

Associating the use of fibers from natural sources with the context of manufacturing of sustainable materials, the polypropylene (PP), a recyclable plastic may be highlighted. This thermoplastic polymer is a common and very popular material which has been used in many applications, for example: in electrical devices, automotive parts, food packaging, household

equipments and many others. PP possesses a number of preferable properties such as high thermal stability, low density and low cost. However, like other polymeric materials, the recycling of PP degrades its mechanical and thermal properties due to the high temperatures involved in the process. The inferior properties of recycled PP, compared to those of virgin PP, can be improved by incorporating synthetic or natural fibers (Zulkifli et al., 2015).

The use of coconut fiber with recycled polypropylene (RPP) to fabricate composites may be an advantageous alternative to reduce the cost of some products, combining the advantages of using vegetable fibers and reusing the polypropylene (PP).

The main problem encountered with cellulose reinforced polymer composites consists in the inherent incompatibility between the hydrophilic cellulose fibers and the hydrophobic PP matrix. Coupling agents, such as silanes, isocyanates, and graft copolymers of maleic anhydride, have been used in most natural fiber reinforced thermoplastics. Surface treatments on vegetable fiber also may be adopted. Their main roles is to improve the adhesion between the reinforcing fiber and the thermoplastic matrix.

Thus, the advantages and limitations technical of these composites fabricated by polypropylene matrix and coconut fibers need to be investigated in this work for identification of future commercial applications, aiming to increase its employability and commercial value.

Some theories and experimental techniques on mechanical performance are required to provide knowledge about applications, durability and dynamic response of engineering materials. Thereby, numerical simulation and structural computations, as well as formulation of damage models and damage identification procedures were developed. In this work, some of these damage models and numerical simulation will be explored.

Damage mechanics is a topic of applied mechanics that relies on the continuum mechanics. Most of the studies about damage mechanics uses state variables to represent the effects of damage on the stiffness and remaining life of the material that is damaging as a result of thermomechanical load and ageing. A damage activation criterion is needed to predict damage initiation (Struik, 1978).

Kachanov (1958) was the first researcher that introduced the concept of damage. Nowadays, this concept reached a stage which allows various practical engineering applications. In contrast to fracture mechanics which considers the process of initiation and growth of micro-cracks as a discontinuous phenomenon, continuum damage mechanics uses a continuous variable which is related to the defects density.

Furthermore, strain and displacement are critical parameters within engineering and construction projects. Measuring these parameters outside of the laboratory requires a difficult

choice between conventional techniques, as accuracy, simplicity and cost must be evaluated. Digital Image Correlation (DIC) is a technique which may prove to be ideally suited for the study of crack propagation and material deformation in real-world applications (McCormick & Lord, 2010).

Strain-field analysis via DIC also referred as photogrammetry is a powerful tool, which can be applied to map lateral strain distributions at different length scales. It allows a detailed investigation of complex micromechanical questions that are associated with the lateral distribution of the strain in heterogeneous materials (Godara et al., 2009). DIC technique is simple to use and cost effective compared to other techniques such as speckle interferometery, and more accurate and subjective than manual measurement methods, leading to a huge range of potential applications (McCormick & Lord, 2010).

Digital Infrared Thermography (DIT) is also strong tool for damage and failure identifications. DIT analysis one of the nondestructive inspection techniques to detect delaminations in composite and polymeric materials. These defects are identified by capturing the temperature gradient of material surfaces. In order for this technique to be effective in damage detection, DIT inspections should be conducted at certain time windows with favorable temperature conditions to get clear temperature gradients on inspected surfaces (Watase et al., 2015).

Apart from its use as non-destructive evaluation technique, infrared thermography is also employed to record a video during the impact event. The visualization of thermal signatures, caused by local dissipation of impact energy, allows gaining information which is useful for understanding the material response to mechanical loading. In particular, the two techniques allow for estimation, in a reliable way, of the overall delamination extension which is of utmost importance for material design purposes (Meola et al., 2015).

1.2. Objectives

This study aims to characterize and investigate the morphological and mechanical properties of manufactured materials of this study: coconut fiber mats, virgin and recycled polypropylene, and composites involving these materials. The morphological analysis consists to present and quantify the internal constituents (empty areas, impurities, interfaces, and distribution and content of fibers). The mechanical characterization includes the evaluating the of adding fibers effect on virgin and recycled polypropylene, evaluating of

strain fields in elastic and plastic regimes, as well as evaluating their temperature gradients during mechanical loading.

This study aims to investigate the effect of different treatment performed in green coconut fiber surfaces on morphological and mechanical properties.

This study also aims to formulate a numerical model describing the mechanical behavior of each material and formulate constitutive equations describing the materials degradation.

1.3. Thesis structure

Chapter 2 presents a literature review on the materials studied, with emphasis on polymer composites, polypropylene, polypropylene recycling, natural fibers, fiber-matrix interface and damage demonstrations in composite materials. This chapter concludes presenting the theory of continuum damage mechanics, with emphasis on the damage evolution by modification of stiffness in load/unload test and by damaged regions accompanied by images.

Chapter 3 presents the conditions for obtaining and manufacturing of these materials. Then, experimental procedures and equipment according to standards used will be described in order to obtain their morphological and mechanical behavior. Then, Chapter 3 will approach about a numerical model that aims to predict their stress-strain curves. Finally, this chapter describes three approaches used to describe the evolution of damage of these materials: from numerical model parameters, from images of deformed material and from stiffness modification during loading/unloading test. The fundamental concepts and calibration procedures of two monitoring techniques for mechanical tests used in this study will be described in Appendix: Digital Image Correlation (DIC) and Digital Infrared Thermography (DIT).

Chapter 4 presents the results of the morphological and mechanical behavior of coconut fiber and coconut fiber mat. Chapters 5 and 6 present these behaviors for polypropylene and composites, respectively. Some techniques, such as Scanning Electronic Microscopy (SEM) and X-ray tomography (XRT), will present the main constituents and morphological properties of the materials studied. Tensile tests monitored by DIC and DIT techniques will present their deformation and damage mechanisms, as well as provide important mechanical properties for their greater employability.

Chapter 7 describes the experimental results of the tensile test using a numerical model based on mathematical expressions of hyperbolic tangents governed by parameters that describe the elastic and plastic regions of the stress-strain curves.

In Chapter 8 will be presented the results of the three approaches employed to describe the evolution of damage in these materials: from numerical model parameters, from images of deformed material and from stiffness modification during loading/unloading test.

2. Literature review

This chapter presents a bibliographic review on the materials used in this study: fiber-reinforced composites manufactured by thermoplastic polymer, coconut fiber, virgin and recycled polypropylene. An emphasis will be given on the concepts of recycling effects in polypropylene, and deformation mechanisms during uniaxial loading, as well as the fiber-matrix interface.

This chapter presents also some theories on damage mechanics which will be applied on the materials of this work.

2.1. Polymeric composites

The addition of non-reinforcing fillers is an ancient practice in the plastics industry with the cost reduction as main objective (Rabello, 2000). The possibility of modifications in material properties with the addition of fillers in appropriate concentrations resulted in a new vision of techniques of manufacturing and consequently some classes of materials may be developed. The polymeric composites may belong to this category and are defined as systems composed by combining two or more components containing significant proportions of them, where the mechanical and performance properties are sometimes expected to be superior to the individual constituents.

Polymeric composites are constituted by polymer matrix and dispersed filler which generally works as reinforcement. The matrix is a continuous phase which supports and protects the reinforcement, transferring the mechanical loading to the fiber. The dispersed phase is distributed in the matrix and is typically more rigid and resistant than matrix. The reinforcements may be found in different shapes: particulate or lamellar or in the form of short or long fibers (continuous or discontinuous).

The final specific properties of polymer composites depend on several factors, such as the interaction between phases, geometry, size, distribution, orientation and the amount of the reinforcement. For example, long fibers and oriented in load direction provide a more effective transfer of stress than short fibers. The fiber extremities may act as stress concentrator, reducing the material resistance (Marsh, 2003). For the use of short fiber, there

is a minimum critical length for the reinforcement in polymer matrix that results in optimum mechanical performances.

The morphology variation of the natural fibers, when used as reinforcement, is responsible for influencing the tensile strength and toughness of composites. Other factors, such as fiber-matrix interface and fiber orientation, are crucial to predict and characterize their mechanical properties. For example, the tensile strength of composites reinforced by discontinuous fibers is lesser than composites reinforced by continuous fibers, when the same constituents and orientation are found in these materials (Zárate, 2000).

The most common arrangements of fibers in fiber-reinforced composite are: (a) continuous and aligned, (b) discontinuous and aligned, (c) discontinuous and randomly oriented, (d) two-directional and (e) three-dimensional fabrics, according to the scheme shown in Figure 2.1 (Matthews & Rawlings, 1994; Saeed et al., 2015).

Figure 2.1. Some fiber distributions in fiber-reinforced composites: (a) continuous and aligned, (b) discontinuous and aligned, (c) discontinuous and randomly oriented, (d) two-directional and (e) three-dimensional fabrics.

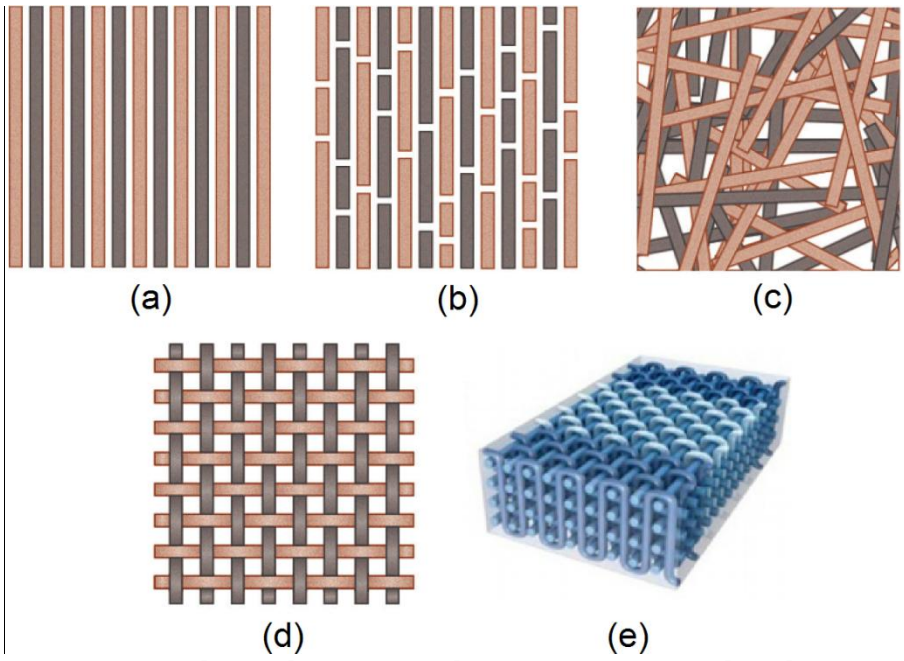

Source: (a-d) Matthews & Rawlings, 1994; (e) Saeed et al., 2015.

Problems related to thermoset processing in open molds and difficulties of recycling and recovery of these resins contributed significantly to the growing use of thermoplastics (polyvinyl chloride, polypropylene, polyethylene, among others) in the manufacture of composites, with main interest in the automotive industry (Karian, 2003; Marsh, 2003).

Currently, several studies of polymer composites are found in the literature in order to evaluate the mechanical, morphological and thermal properties through various processing possibilities, different types of matrices and reinforcements.

2.1.1. Polypropylene

Currently, the consumption of thermoplastic composites has increased in relation to thermoset composites due to the possibility of recycling of the thermoplastic polymers, thereby contributing to materials development in a sustainable manner. This utilization is also related to the development of thermoplastics with attractive physical and mechanical properties such as PP, poly (éteréter ketone) (PEEK), poly (phenylene sulfide) (PPS) and polycarbonate (PC). The polypropylene was first polymerized in 1955 by Natta and has been recognized as a polymeric material with a wide variety of uses due its design versatility at the molecular level with an attractive cost (Hamada et al., 2000).

Thermoplastic resins have long molecules with a length of about 20 to 30 nm and flow easily under mechanical loading at moderate temperatures, thus allowing be manufactured in desired shape while maintaining the same shape when cooled to room temperature (Davis et al., 1982). These polymers can be repeatedly heated, manufactured and cooled, thus, more easily recycled. The combination of low density, chemical resistance, low cost and a balance between stiffness and toughness allows thermoplastics materials to occupy the space of other materials in many important applications (Elmajdoubi & Vu-Khanh, 2003).

The polypropylene (PP) is a thermoplastic obtained by polymerization of propylene monomer (C_3H_6) through of polyaddition reaction process. This semicrystalline polymer has an approximate density of 0.90 to 0.91 g/cm^3. Its glass transition temperature and melting temperature are approximately -18°C and 165°C, respectively. Its mechanical strength and hardness are relatively attractive because its crystallinity is situated between 60 and 70%. The modulus of elasticity, tensile strength, yield strength and ultimate elongation of PP are approximately 1.14 to 1.55 GPa, 31.0 to 41.4 MPa, 31.0 to 37.2 MPa and 100 to 600%, respectively (Santos, 2006).

The properties of semicrystalline polymers, such as PP, are essentially determined by crystal morphology developed during the processing. The factors with higher influence over the polymer crystallinity are related to its synthesis. Thus, the molar mass, its distribution, chain regularity (stereoregularity) and morphology are determined by the Ziegler-Natter catalyst used during synthesis, although the property variation relative to changes in the

crystallization of the material may be attributed to post-crystallization phenomenon. The PP semicrystalline regions are bonded by amorphous regions and strongly influence the mechanical properties (Fiebig et al., 1999).

Semicrystalline polymers contain amorphous and ordered crystalline phases. When solidified from the pure melt, these polymers show a spherulitic structure in which crystalline lamellae composed of folded chain crystallites radiate from the center of the spherulite in such a way that a constant long period or crystallinity is approximately maintained. The amorphous regions reside in the interlamellar regions in the form of tie chains, whose ends are attached to adjacent lamellae; loop chains, whose ends are attached to the same lamella; cilia chains with only one end attached to a lamella (or dangling chain ends), and floating chains which are not attached to any lamellae. This hierarchical structure is illustrated in Figure 2.2 (a).

A sequence of deformation events leads to different forms of plastic deformation in polypropylene, which are not only of scientific interest, but also of engineering relevance (Galeski, 2003; Pawlak & Galeski, 2005, 2008; Friedrich, 1983; Narisawa, 1980). The initial stages of tensile deformation are governed by the straining of molecular chains of the interlamellar amorphous phase (Figure 2.2 (b)), twinning, twist, interlamellar shear, rotation of lamellae stacks and lamellae separation (Nitta & Yamana, 2012; Pawlak & Galeski, 2008).

Figure 2.2. Structure and deformation observations in polypropylene: (a) molecular structure in different dimensions. (b) modifications in polymeric bonds during mechanical loading, (c) stress-strain curve.

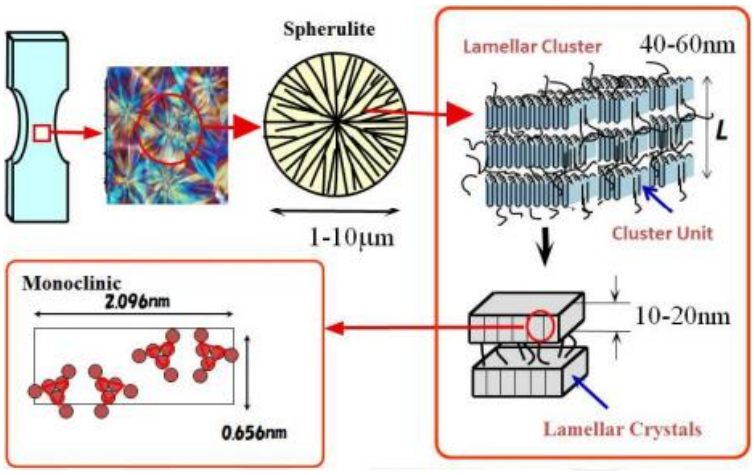

(a)

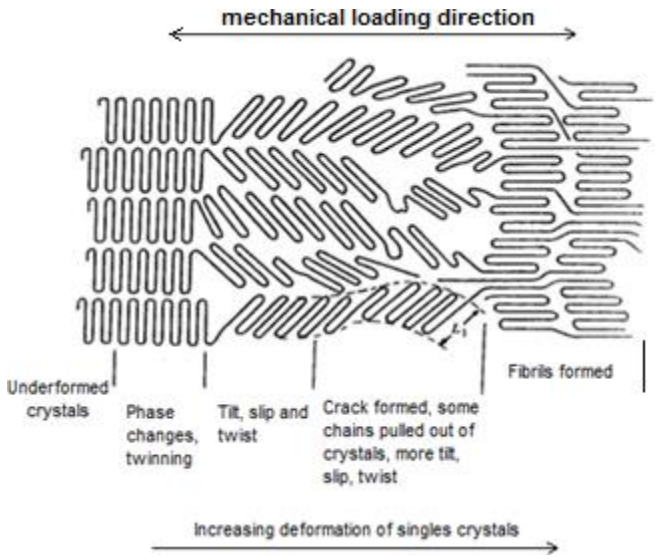

(b)

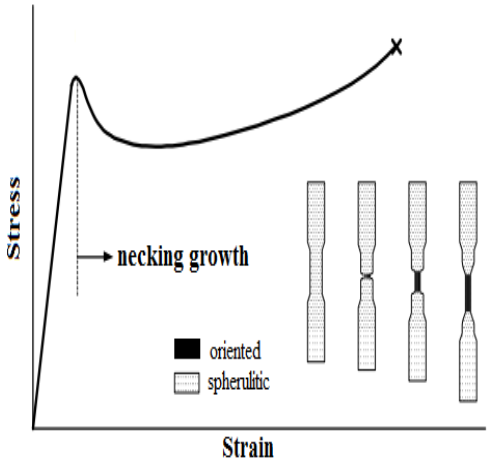

(c)

Source: Nitta & Yamana, 2012.

Above Tg, the initial deformation is located in the amorphous regions because of its low modulus. The tensile deformation of a spherulite is inhomogeneous because the amorphous regions and the radially oriented lamellae have different angles to the direction of the tensile force. The main mode of plastic deformation of the amorphous components is believed to be interlamellar sliding, or lamellae separation in the equatorial regions, where the lamellae are oriented perpendicularly to the loading direction (Figure 2.2 (c)). The mobility of amorphous chains may vary locally (Struik, 1987). The constraints imposed by the lamellae imply that only a limited amount of deformation can be accommodated by the interlamellar amorphous phase (Bartczak, 1996). When this limit is reached, further deformation can proceed either by cavitation of the amorphous phase or by plastic deformation of crystals. Polypropylene shows a transition in the temperature region around 80°C, which is associated with mobility in the crystalline phase. When drawing is performed at elevated temperatures approaching this transition region, a change of the dominating deformation from cavitation towards shear yielding can be expected.

These irreversible deformations begin at strains below the yield strain. Knowledge of the irreversible deformation modes and load limits for reversible behavior is therefore essential for proper modeling of mechanical behavior and for optimizing polymer component designs. However, appropriate techniques for determining mechanical strains in polymers are required (Tscharnuter, 2011).

2.1.2. Recycling of polypropylene

The nature and amount of different types of polymers in a given geographic area depend on the local consumer and industrial use. In addition, variations in these consumption indicators can have a high economic impact on the recycling industries and their investments (Strapasson, 2004).

Typically, the plastics present in higher quantities include HDPE (high density polyethylene), LDPE (low density polyethylene), PP, PS (polystyrene) and PET (polyethylene terephthalate), and therefore the recycling efforts typically focus on these polymers, in isolated form, added, combined in blends or reinforced by fibers (Strapasson, 2004).

Products made from recycled materials have attractive cost and present moderate quality, therefore a better understanding of these materials is needed in order to find appropriate and useful applications to replace, partially or fully, the virgin polymer. Some studies were performed to simulate the cycles of reprocessing (potential of recycling by multiple extrusions) or reprocessing/utilization (method of recycling simulation) using an accelerated thermal-oxidative aging stage (Strapasson, 2004).

Aurrekoetxea et al. (2001) used the reprocessing method by injection to study the mechanical properties of recycled PP. The melt viscosity was reduced and the crystallinity was increased due to reprocessing. Moreover, the modulus of elasticity and yield stress increased with the reprocessing, while elongation at break and fracture toughness decreased.

Incarnato et al. (1999, 2003) studied the effect of three processing cycles to evaluate the crystallinity and morphology of the PP by viscosity measurements, chromatography, Differential Scanning Calorimetry (DSC) and Scanning Electron Microscopy (SEM). During the recycling of post-consumer plastics, thermal and mechanical stresses (particularly shear) and macromolecule ruptures were reported. Furthermore, in the research of La Mantia and Dintcheva (2003) was noted that the presence of fillers, such as $CaCO_3$, increased the viscosity of PP in its molten state.

Jansson et al. (2003) reported an overall decrease in the elongation at break by using a sequence of simulated recycling cycles (aging cycles and extrusion) in PP added by antioxidant-amine. The virgin PP presented 700% for this mechanical property. It was also shown that the order of extrusions stages and aging methods also influenced the mechanical behavior of this polymer. It was also reported that the extrusion followed by aging test influenced more the thermal and mechanical properties than the inversion of sequences of recycling. The degree of crystallinity measured by DSC showed a slight increase (from 39 to

41%) after an extrusion cycle, remaining at this level for the last cycle. Multiple extrusions of this isolated material caused a reduction in elongation at break from 700 to 550% after 7 cycles. Another PP condition (added by phenolic antioxidant and HDPE) used by the same authors showed different results; the aging test showed no influence on the elongation even after 20 cycles; multiple extrusions of this material in isolation caused a slight reduction in elongation at break from 800 to 750% after 7 cycles. It was remarked that all results of elongation at break presented a large scattering, with more than 100% deviation.

2.1.3. Natural fibers

Natural resources play an important role in economic activities, contributing to economic and social development of rural areas and underdeveloped regions (Sanadi, 2004). Among these resources, the natural fibers stand out, mainly due to the wide variety of species and availability. These fibers can be mineral, animal and vegetable sources, the latter being the most widely used in the manufacture of composite materials (Frank, 2005). They may be used as reinforcements in the manufacture of polymer composites, mainly due to the properties that these materials present, with economic and environmental advantages (Sain & Panthapulakkal, 2004). Different fibers are able to act as reinforcement in plastics, such as jute, flax, sisal, hemp, wood, etc.

Since 1994, some cars from Mercedes-Benz in Brazil already have internal parts fabricated containing coconut fibers. Composites made with natural fibers and thermoplastic matrices are used by the automotive industry as coatings and internal parts in order to reduce consumption of oil reserves and facilitate the recycling of automobiles (Holbery & Houston, 2006).

The use of lignocellulosic fibers in polymer composites is due to several factors, including cost reduction and lower weight. The price of natural fibers is unstable, varying in accordance to the region and the methods to obtaining. In addition to the cost, the use of these fibers in the manufacture of composites presents advantages when they replace traditional fibers such as glass and carbon fibers (Bledski & Gassan, 1999; Satyanarayana et al., 2005). Its renewable nature, high availability and non-abrasive characteristic corroborates with the equipment maintenance and in the production of new materials with benefits to the environment, making natural fibers a great material to replace some traditional fibers.

The chemical composition of natural fibers, which is related to its mechanical properties, is influenced by several factors such as climatic conditions and cultivation, age and

part of the plant that are extracted (Bledski & Gassan, 1999). Table 2.1 presents the chemical composition of natural fibers from Brazil (B) and other countries (O) determined by different studies (Satyanarayana et al. 2007).

Table 2.1. Chemical composition of some natural fibers.

Fibers	Source	Cellulose (%)	Hemicellulose (%)	Lignin (%)	Grays (%)	Extractives (%)
Sugarcane bagasse	B	54.3 to 55.2	16.8 to 29.7	25.3 to 24.6	1.1	0.7 to 3.5
	O	32 to 44	27 to 32	19 to 24	4.3	-
Banana	O	60 to 65	6 to 8	5 to 10	1.2	-
Jute	B	60	22.1	15.9	1.0	-
	O	59 to 71	12 to 13	11.8 to 12.9	0.7	0.5 to 2
Ramie	O	80 to 85	3 to 4	0.5	-	6.4
Piaçava	B	31.6	-	48.4	-	-
Curaua	B	70.7 to 73.6	21.1	7.5 to 11.1	0.8 to 0.9	2.5 to 2.8
Sisal	B	74 to 75.2	10 to 13.9	7.6 to 8	-	-
	O	60 to 67	10 to 15	8 to 12	0.14 to 0.9	1.7 to 6
Coconut	B	43.4 to 53	14.7	38.3 to 40.7	-	3.5
	O	43.7	<1	45	-	4.5

Source: Satyanarayana et al. 2007.

As can be observed, the chemical composition of natural fibers is changeable. The main constituents of lignocellulosic fibers are cellulose, hemicellulose and lignin. Cellulose can be considered a linear polymer consisting of glucose beta 1,4-glycosidic bonds. The linear structure and organized cellulose allows the formation of crystalline regions, showing good properties, reflecting in the stiffness of natural fibers. Hemicellulose, other component present in significant quantities, has some repeating units composed of sugars, branched structure and inferior properties than cellulose. Lignin presents a complex structure, being an amorphous polymer constituted by aliphatic and aromatic groups and also has inferior mechanical properties than cellulose (Bledski & Gassan, 1999; John & Thomas, 2007).

In most natural fibers, the microfibrils are oriented in respect to the fiber axis, presenting a typical angle. The higher the amount of cellulose and the smaller the angle formed between the cellulose microfibrils in the fiber, the higher the values of the elasticity modulus for natural fibers (John & Thomas, 2007; Eichhorn & Baillie, 2001).

Physical and mechanical properties of composites based on natural fibers are generally lower than composites reinforced with glass-fibers; however, low density, low cost, high

availability and non-abrasive characteristic of natural fibers are attractive parameters for various applications. Table 2.2 shows the physical and mechanical properties of natural fibers in comparison to some conventional fibers used as reinforcement (Bledski & Gassan, 1999; Satyanarayana et al. 2007).

Table 2.2. Physical and mechanical properties of natural fibers compared with traditional fibers.

Fiber	Density (g/cm³)	Microfibrillar angle (°)	Elastic Modulus (GPa)	Tensile strenght (MPa)	Failure strain (%)
Sugarcane bagasse	0.45 to 0.49	-	27.1	222	1.1
Jute	1.45	7 to 17	27 to 32	400 to 800	1.5 to 1.8
Ramie	1.5	7.5 to 12	44	500 to 870	1.2
Piaçava	-	-	1.07 to 4.59	108 to 147	6.4 to 21.9
Curaua	0.92	18.8	30 to 80	1250 to 3000	4 to 5.6
Sisal	1.26 to 1.33	20	17 to 22	324 to 630	2 to 5.1
Coconut	1.25 to 1.50	30 to 51	2.5 to 6	95 to 220	13 to 51.4
Fiberglass	2.5	-	70	2000 to 3500	2.5
Aramide	1.4	-	63 to 67	3000 to 3150	1.4

Source: Bledski & Gassan, 1999; Satyanarayana et al. 2007.

Coconut fiber or coir is a versatile lignocellulosic fiber obtained from the coconut fruit (*Cocos nucifera*) which grows mainly in tropical countries (Frank, 2005). Brazil has a great potential in the production of these fibers, with an annual production of approximately 1.5 billion of fruit in a cultivation area superior than 270,000 hectares. The northern region of Brazil is an important area for this cultivation (Satyanarayana *et al*. 2007). These fibers can be used in various applications, generating environmentally correct products. Coconut fibers can be extracted from both the mature fruit, as a byproduct of its industrialization, as well as from the green fruit, which is widely consumed in the Brazilian coast. The structure of the coconut fruit can be seen in Figure 2.3 (Bledzki et al., 2010).

The fruit consists of three main parts: fibrous mesocarp, endosperm and exocarp. However, the coconut fibers or coir are extracted only from the fibrous mesocarp. The amount of fiber obtained from each fruit is very significant, because the mesocarp constitutes a representative volume of coconut fruit. Furthermore, the coconut fiber is one of the cheapest fibers among natural fibers and presents flexibility and non-toxicity (Frank, 2005).

Figure 2.3. Structure of the coconut fruit.

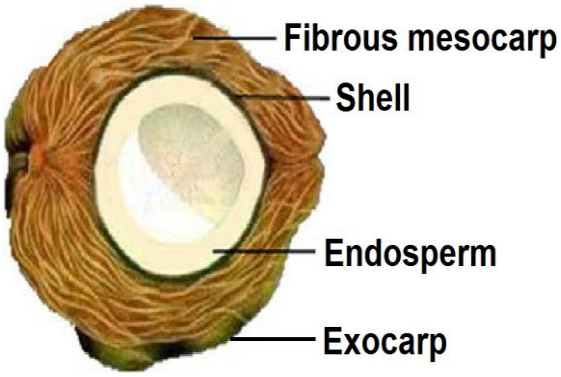

Source: Bledzki et al., 2010.

Tomczak et al. (2007) have characterized coconut fibers from northern of Brazil, and these fibers showed a lower density of defects in their cells and higher degree of crystallinity than fibers from other countries. In Brazil, companies such as Embrapa, Poematec and Amafibra manufacture artifacts made by coconut fibers (seating for car seats, mattresses, mats and pots for gardening utensils) (Embrapa, 2013; Poematec, 2007; Amafibra, 2007).

Thermal analysis in mats manufactured with coconut fibers and latex showed better stability and less emission of toxic gases than conventional polyurethane foams (Salazar, 2005). However, these fibers present limitations in terms of mechanical behavior. As for other natural lignocellulosic fibers, the use of coconut fibers in the preparation of polymeric composite materials is limited due the poor compatibility with polymeric matrices.

Results show that the mechanical performance of coconut fibers as reinforcement in plastics is poor and inferior to other natural fibers (Wambua et al., 2003). This lower performance can be related to the poor interface fiber-matrix, properties of the fibers (Tables 2.1 and 2.2), low content of cellulose and high lignin content in its composition, high angle formed between the microfibrils, large and variable diameter. On the other hand, the variable diameter and elliptical shape found in the cells of coconut fiber allows higher flexibility and resistance to contact with the water, improving the ability of molten polymer to maintain contact with the fiber (wettability) (Frank, 2005).

There are some key information related to the use of coconut fibers in thermoplastic composites in the literature. In general, these studies focus in fiber content and solutions to improve the fiber-matrix interface, evaluating the coconut fibers as reinforcements in the mechanical and physical performance on polymer composites with nonpolar matrices, in order to expand its use and explore new products obtained from coconut husk processing.

According to Kasliwal & Jones (2005), the use of natural fibers in thermoplastic resins is usually beneficial due to their availability, renewal capacity and favorable degree of efficiency in terms of strength/weight. As a result of these factors, plastic composites reinforced with natural fibers have received attention in the modification of thermoplastic resins such as PP, HDPE and PVC (polyvinyl chloride). These composites are potentially applicable on floors, furniture components, doors and building systems using light structures and pallets for storage structures. Another potential application is the manufacture of automotive interior panels, due to the increase of stiffness on the thermoplastic resin provided by these fibers and to the increase of softening temperature.

Brahmakumar et al. (2005) investigated the coconut fibers as reinforcement to LDPE. Some unique properties make it attractive for using it as reinforcement in LDPE composites. Coconut fibers possess high failure strain of 15–40% and contain a thin continuous surface layer of an aliphatic compound, hereinafter referred as waxy layer that difficults the compatibility between fiber and matrix (Prasad et al., 1983). On the other hand, long-chain aliphatic molecules and compounds have been used as adhesion promoters in wood fiber-reinforced non-polar thermoplastic composites (Bledzki & Gassan, 1999). Coconut fiber may, therefore, be used for reinforcing polyethylene without any surface treatment or modification. High failure strain of the fiber, which provides a better strain compatibility between the fiber and the matrix, could also be advantageous in short-fiber filled polyethylene composites (Brahmakumar et al., 2005).

2.1.4. Fiber-matrix interface and alkali treatment of natural fibers

One of the most important parameters in composite materials with one or more solid phases is the interface between the reinforcement and the matrix. The interface is the region where contact between the components of the composite occurs. The interfacial region is primarily responsible for the transfer of mechanical stress from the matrix to reinforcement. Inadequate adhesion between the phases involved in the interface may cause the onset of failures, affecting the composites performance (Santos, 2006).

Interaction between the components at the interfacial region in practice depends on two factors: the degree of contact surfaces at the interface (wettability), and cohesive forces in this region (adhesion). These factors are interdependent, because if there is not enough contact area between the components it will be difficult to ensure good adhesion between the phases.

The wettability of a surface by another depends on the surface energy and surface area of these contacts (Santos, 2006).

The components of natural fibers, mainly cellulose, provide a hydrophilic and polar character to natural fibers, resulting in a poor compatibility in the preparation of thermoplastic matrix composites with hydrophobic and nonpolar character. This incompatibility between natural fibers and polymeric matrices generates a poor fiber/matrix interface, as well as low resistance to moisture absorption (Bledski & Gassan, 1999). These characteristics reduce the potential of natural fibers as reinforcement in polymers. Some chemical and physical modifications in thermoplastics or surface treatments on natural fibers may improve this adhesion (Li et al. 2007).

Physical treatments act on the fiber surface, resulting in structural changes that influence the mechanical bond with the polymers. Physical and structural methods, such as treatment with electrical discharge (corona, plasma), heat treatment and production of woven fibers fabrics have been used (Bledski & Gassan, 1999). Composites containing 20% of wood fibers treated with plasma showed higher values of modulus of elasticity and tensile strength than composites made of untreated fibers. In this case, chemical changes occur on the surface of the fibers due to an increase in aldehyde groups (Yuan et al., 2004).

Chemical treatments act not only on the surface of the fibers as they can reach its internal layers. Several treatments are described, such as alkali treatment, treatment with isocyanates, acetylation, etc. (Li et al. 2007 and George et al., 2001).

The fiber treatment with NaOH is also called mercerizing and is widely used as a pretreatment or coating of natural fibers. In these systems, there is a rupture of the hydrogen bonds that unite cellulose chains, giving a rougher surface that helps the mechanical anchoring.

The increase in the percentage crystallinity index of alkali treated fibers occurs because of the removal on the cementing materials, which leads to a better packing of cellulose chains (Varma et al., 1984). Additionally, treatment with NaOH leads to a decrease in the spiral angle, i.e. closer to fiber axis, and increase in molecular orientation. A fair amount of randomness is introduced in the orientation of the crystallites due to the removal of non-cellulosic matter (Sreenivasan et al., 1996). The modulus of elasticity of fibers, for example, is expected to increase with increasing degree of molecular orientation.

Hemp fibers treated by a solution containing 10% NaOH, at 160°C for 45 min, showed higher tensile strength than untreated fibers due to the removal of some constituents such as lignin, which increases the degree of crystallinity of these fibers and facilitates the separation

of the cellulose microfibrils (Pickering, 2007). Well oriented cellulosic fibers such as flax have much higher Young's modulus than fibers with medium orientation, such as cotton. In addition to the modification of orientation and the consolidation of weak points, other important factors with regard to the mechanical properties after NaOH treatment could be the crystallite length and degree of crystallinity as well as the removal of fractions of cellulose at a very low degree of polymerization.

A widely used method to match composites prepared with natural fibers is the introduction of coupling agents. These systems differ in structure because it acts as a binder on the surfaces of the fibers and the matrix (Li et al. 2007; George et al., 2001). The use of coupling agents allows higher adherence at the interface of these systems, which results in changes on the final properties. Coupling agents have two functions, one able to react with the polar groups present in natural fibers, and one that promotes interaction with the polymer matrix. Several mechanisms describe the action of these agents in the fiber-matrix interface. The introduction of a coupling agent promotes the formation of resilient and flexible layers, forming an interfacial region that can present moderate values of modules among filler and matrix (Bledski & Gassan, 1999). The improvement in the wettability of the fiber-matrix is a result of the establishment of chemical bonds and acid-base effects between the fiber and the matrix (Sanadi et al., 1995).

2.2. Failure and damage mechanisms in polymeric and composite materials

The damage mechanisms start at plastic micro deformations. The plastic or damaged region in a polymeric material results from the breaking of bonds that composes the molecular chains, intrinsic discontinuities, residual stresses, the formation and propagation of "crazes" (Bueno, 2008).

Polymers do not contain crystallographic planes, dislocations, and grain boundaries; rather, they consist of long molecular chains. Fracture in these materials occurs in the atomic level and involves breaking bonds. A complicating feature for polymers, however, is that two types of bond govern the mechanical response: the covalent bonds between carbon atoms and the secondary van der Waals forces between molecule segments. Ultimate fracture normally requires breaking the latter, but the secondary bonds play a major role in the deformation mechanisms that lead to fracture (Anderson, 2005).

The factors that govern the toughness and ductility of polymers include the displacement rate, temperature, and molecular structure. At high displacement rates or low

temperatures (relative to Tg) polymers tend to be brittle, because there is insufficient time for the material to respond to stress with large-scale viscoelastic deformation or yielding. Highly cross-linked polymers are also incapable of large-scale viscoelastic deformation. The mechanism illustrated in Figure 2.4 (a), where molecular chains overcome van der Waals forces, does not apply to cross-linked polymers; primary bonds between chain segments must be broken for these materials to deform (Anderson, 2005).

Glassy polymers subject to tensile loading often yield by crazing, which is a highly localized deformation that leads to cavitation (void formation) and strains on the order of 100% (Bucknall, 1977). On the macroscopic level, crazing appears as a stress-whitened region, due to a low refractive index. The craze zone usually forms perpendicular to the maximum principal normal stress. Figure 2.4 (a) illustrates the mechanism for crazing in homogeneous glassy polymers. At sufficiently high strains, molecular chains form aligned packets called fibrils. Microvoids are formed between the fibrils. The aligned structure enables the fibrils to carry very high stresses relative to the undeformed amorphous state because covalent bonds are much stronger and stiffer than the secondary bonds. The fibrils elongate by incorporating additional material (Figure 2.4 (a)). Figure 2.4 (b) shows a fractograph of a craze zone (Anderson, 2005; Cayard, 1990).

Figure 2.4. (a) Craze formation in glassy polymers. Voids form between fibrils, which are bundles of aligned molecular chains. The craze zone grows by drawing additional material into the fibrils. (b) Craze zone in polypropylene.

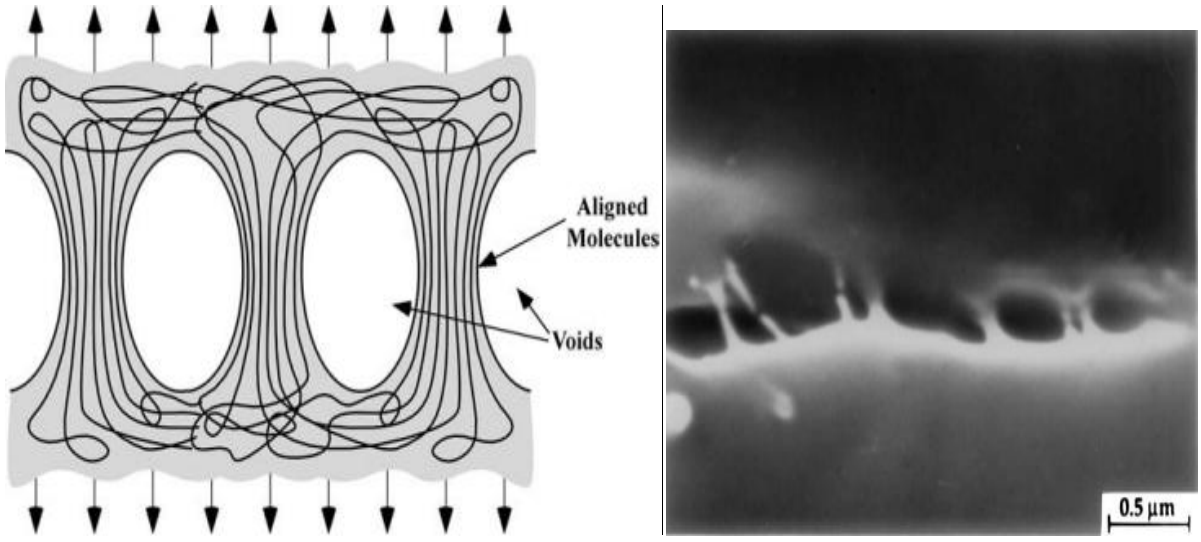

(a) (b)

Source: (a) Anderson, 2005; (b) Cayard, 1990.

Many have attempted to apply fracture mechanics to fiber-reinforced composites, and have met with mixed success. Conventional fracture mechanics methodology assumes a single dominant crack that grows in a self-similar aspect, i.e., the crack increases in size (either through stable or unstable growth), but its shape and orientation remain the same. Fracture of a fiber-reinforced composite, however, is often controlled by numerous microcracks distributed throughout the material, rather than a single macroscopic crack. There are situations where fracture mechanics is appropriate for composites, but it is important to recognize the limitations of theories that were intended for homogeneous materials (Anderson, 2005).

Figure 2.5 illustrates various failure mechanisms in fiber-reinforced composites. One advantage of composite materials is that fracture seldom occurs catastrophically without warning, but tends to be progressive, with subcritical damage widely dispersed through the material. Tensile loading (Figure 2.5 (a)) can produce matrix cracking, fiber bridging, fiber rupture, fiber pullout, and fiber/matrix debonding. Ultimate tensile failure of a fiber-reinforced composite often involves several of these mechanisms. Out-of-plane stresses can lead to delamination (Figure 2.5 (b)) because the fibers do not contribute significantly to the strength in this direction. Compressive loading can produce the microbuckling of fibers (Figure 2.5 (c)); since the polymer matrix is soft compared to the fibers; the fibers are unstable in compression. Compressive loading can also lead to macroscopic delamination buckling (Figure 2.5 (d)), particularly if the material contains a preexisting delaminated region (Anderson, 2005).

Figure 2.5. Examples of damage and fracture mechanisms in fiber-reinforced composites.

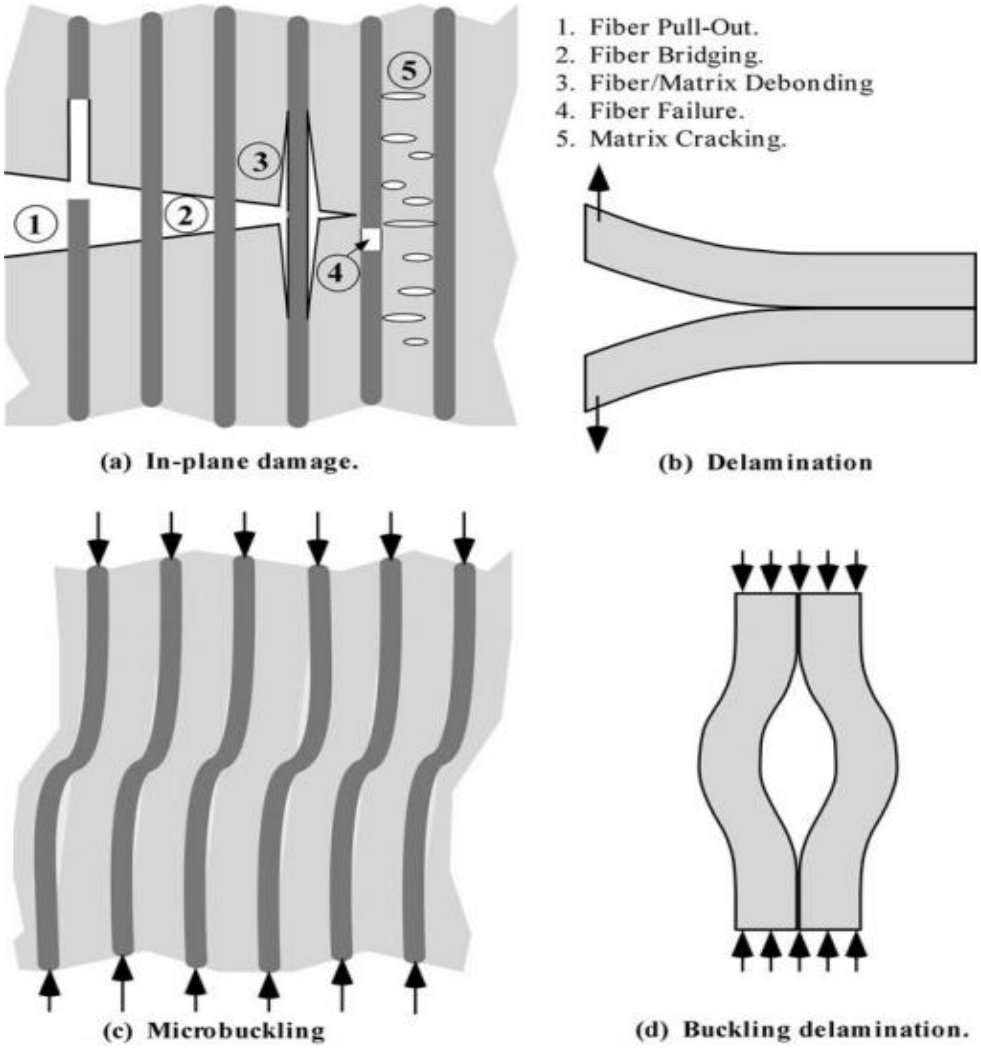

Source: Anderson, 2005.

2.3. Damage mechanics

The failure by damage is a result of the progressive development of at least one defect under the influence of mechanical loading. When a field defect nucleates a crack, a macroscopic damage is initiated within the material. This damage was originated by accumulation of defects in a certain area or due to stress concentrations, such as porosity, abrupt change of geometry, dislocations concentration, precipitations, inclusions, etc. In the case of natural fiber composites, the failure by damage is mainly related to the fiber-matrix interface.

Elements of damage mechanics

A defect within the microstructure of a solid is presented in the Figure 2.6. A Representative Volume Element (RVE) must be large enough to be considered that the distribution of defects in its interior is homogeneous. Furthermore, it is assumed that this element has no local high gradients quantities of discontinuity, such as deformation. Thus, a continuum material will be assumed for the representative functions of the occurring phenomena in an element and their properties will be considered in terms of average values associated to any material point.

Figure 2.6. Representative volume element of a damaged material.

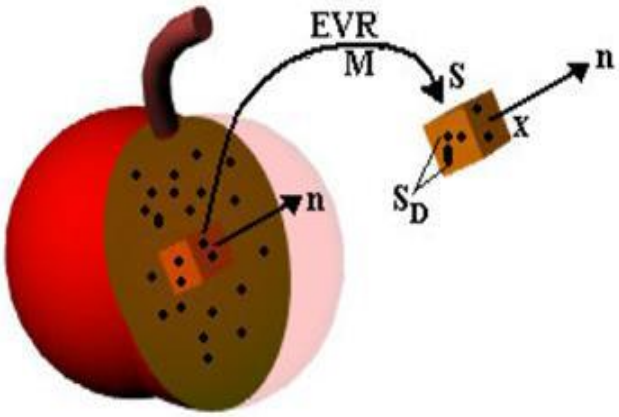

Source: Lemaitre, 1984.

Definition of effective stress

A situation where a mechanical loading on the Representative Volume section is considered according to previous section, where a force $\vec{F}$ is applied to the opposite faces and oriented by $\vec{n}$ versor (Figure 4.8); a total area S of section normal $\vec{n}$ inside of the element is also adopted. Under these conditions, $\sigma = F/S$ is the nominal stress at any point on generic section. Assuming that the number of defects is totally unable to transfer stress, it is possible to define an effective stress by taking in consideration only an intact part of the section. Considering $\tilde{S}$ as the area with no defects (area which effectively resists to mechanical loading) of the S section. Then the area of defects (S_o) is:

$$S_o = S - \tilde{S} \tag{2.1}$$

By definition, the damage D_n, in case associated with a plane normal $\vec{n}$, is defined by the relation (Lemaitre, 1984):

$$D_n = \frac{S_o}{S} \tag{2.2}$$

Note that the damage variable takes values in the range $0 < D_n < 1$, and $D_n = 0$ corresponds to the situation where the material has no damage (intact material) and $D_n = 1$ indicates a total state of deterioration. Thus, portion of the effectively resistant section can be expressed in terms of damage variable as:

$$\tilde{S} = S - S_o = S\,(1 - D_n) \tag{2.3}$$

Thus, the nominal stress σ and effective $\tilde{\sigma}$ are defined by:

$$\sigma = \frac{F}{S} \quad \text{and} \quad \tilde{\sigma} = \frac{F}{\tilde{S}} \tag{2.4}$$

Therefore, we have:

$$\tilde{\sigma} = \frac{\sigma}{(1 - D_n)} \tag{2.5}$$

As the entire area is smaller than the nominal area, the effective stress in damage means results comparatively larger than nominal stress for the same force applied. In particular, note that:

- $\tilde{\sigma} = \sigma$, for intact material;
- $\tilde{\sigma} \rightarrow \infty$, for completely damaged material.

Note that, for the same point, the variable D_n can assume different values according to the orientation of normal $\vec{n}$. This characteristic indicates a tensor nature for the variable representing the damage on the volume element.

The damage scale corresponds to a situation in which the micro defects presented in the volume element are approximately distributed in an uniform manner, so that the measurement of damage is the same in any point or surface, ie, independent of the orientation of normal $\vec{n}$. In other words, a single value of the damage variable is sufficient to characterize completely the local state of deterioration, as follows:

$$D = D_n \, , \forall \vec{n} \tag{2.6}$$

Definition of effective strain

The effective stress concept is analogous to the effective strain and also is determined from the analysis of a uniaxial strain situation imposed on the volume element oriented at a certain direction defined by $\vec{n}$ versor. Assuming Δl as a variation of the initial length l_o due the effect of deformation imposed, the strain measurement is defined by the relation:

$$\varepsilon = \frac{\Delta l}{l_o} \tag{2.7}$$

However, the length of a material will be increased during mechanical stress if the volume element presents initial defects or internal discontinuities (Figure 2.7). This increment or failure propagation may be represented by Δd. Thus, in the deformation process only the portion Δl - Δd can effectively be considered a deformation measurement of this material.

Figure 2.7. Increase in length due to the opening of defects.

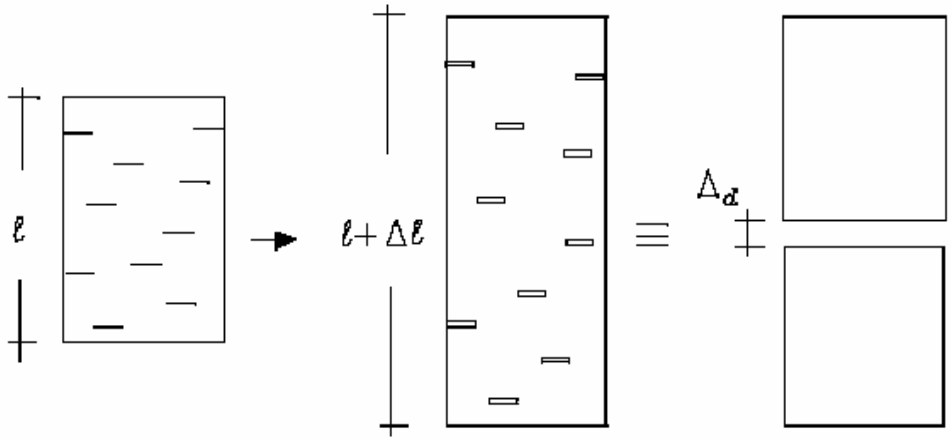

Source: Lemaitre, 1984.

Therefore, the measure of effective linear deformation can be defined as:

$$\varepsilon_n = \frac{\Delta l - \Delta d}{l_0} \tag{2.8}$$

Other definition for a damage variable can then be proposed:

$$D_n^* = \frac{\Delta d}{\Delta l} \tag{2.9}$$

Note that this definition is also associated with a certain direction $\vec{n}$. Taking in consideration the new variable of the damage, it follows that the measures of nominal and effective linear deformation are related by:

$$\varepsilon_n = (1 - D_n^*)\varepsilon \tag{2.10}$$

The two scalar damage variables introduced before (So and Δd) can be unified if one considers that the volume corresponding to the damaged part is the same in both cases. This consideration can be coherent, because the equilibrium of stress or the deformations compatibility is analyzed in a situation of uniaxial mechanical loading on the same volume. Thus, the damaged volume can be represented by:

$$V_d = S_o \Delta l = S \Delta d \tag{2.11}$$

Taking in consideration the previous relations it is easy to see that $D_n = D_n^*$.

Constitutive relationship involving equivalence of deformation

The principle of equivalence of deformation proposed by Lemaitre (1984) describes that the deformation of the intact materials where the effective stress acts is the same of damaged materials. In other words: "The deformation state of a damaged material is obtained by the law of behavior of the intact material, where the stress tensor is replaced by the effective stress tensor".

In context of a damage response in composite materials, this principle is based on the proposition that the material has continuous fibers arrangement with slightly different strengths from one another, which are submitted to the same deformation. Due to the different resistance of fibers, they start to break, initiating the damage process. Rearranging the previous equations, it is obtained:

$$\frac{\sigma}{1-D} = E\varepsilon \quad \text{or} \quad \sigma = (1-D)\,E\varepsilon \tag{2.12}$$

In this way, the secant modulus of elastic stiffness $\tilde{E}$ for a continuous materials of equivalent response to the damaged material is:

$$\tilde{E} = (1-D)E \tag{2.13}$$

and damage variable can be identified by:

$$D = 1 - \left(\frac{\tilde{E}}{E}\right) \tag{2.14}$$

This method requires accurate measurements of deformation and strain gauges are usually used for higher accuracy in the values obtained during the loading/unloading cycles. An example is given in Figure 2.8 for a ductile damage on copper by large deformations, where σ_t is the true stress:

$$\sigma_t = \sigma\,(1+\varepsilon) \tag{2.15}$$

Figure 2.8. Measurement of ductile damage on copper (99.9 %) at room temperature.

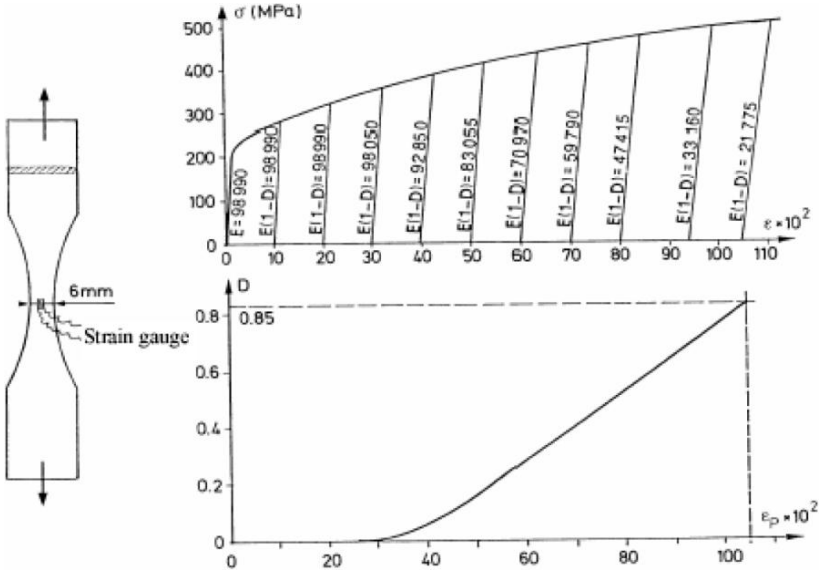

Source: Lemaitre, 1996.

Criterion failure: critical damage (D_c)

The definition of meso-scale rupture is given during the crack initiation or when the degradation process of the fiber-matrix interface represents all the surface of Representative Volume Element. In this case, therefore, D = 1. In many cases, this process is caused by an instability which leads to the rupture of atomic bonds. It corresponds to a critical value of damage, D_c, which depends on the material and loading conditions.

The final separation of atoms is characterized by a critical value of the effective stress acting on an area resistance. This stress is called σ_∞ because it is the maximum stress that could be applied in the material:

$$\tilde{\sigma} = \frac{\sigma}{1 - D_c} = \sigma_\infty \tag{2.16}$$

In practice, σ_∞ must be approximated by a ultimate stress σ_u, thus we have:

$$D_c = 1 - \frac{\sigma}{\sigma_u} \tag{2.17}$$

These equations provide the critical value of damage during the initiation of a mesocrack occurring in a tensile testing σ_R. The ultimate strength σ_u may be identified for each material. D_c should range between $D_c \approx 0$ (for pure brittle fractures) and $D_c \approx 1$ (for pure ductile fractures), however D_c is usually about 0.2 to 0.5.

This relation is applied to a pure monotonic tensile test and is taken as a reference. Therefore, it is possible to define the critical damage D_{1c} for each material as follows:

$$D_{1c} = 1 - \frac{\sigma_R}{\sigma_u} \tag{2.18}$$

where σ_R is the tensile strength.

Measurement of damage fields

The measurement methods of displacement fields by digital image correlation can be used to directly obtain damage maps, in addition to the imprecise or indirect measurements (Lemaitre *et al.*, 2009).

Damage maps from displacements fields: given an equilibrium condition $\sigma_{ij,j} = 0$ and considering the three-dimensional law of elasticity associated to the isotropic and scalar damage, is obtained $\sigma_{ij} = 2\mu\ (1 - D)\ \varepsilon^e_{ij} + \lambda\ (1 - D)\ \varepsilon^e_{kk}\ \delta_{ij}$, where λ and μ are Lame coefficients of the virgin material and ν is Poisson's ratio,

$$\lambda = \frac{E\nu}{(1-2\nu)(1+\nu)} \quad \text{and} \quad \mu = \frac{E}{2(1+\nu)} \tag{2.19}$$

One approach by indexes is used in this study. The field equation is obtained as follows:

$$(2\mu\varepsilon^e_{ij} + \lambda\varepsilon^e_{kk}\delta_{ij})\ [ln(1 - D)]_{,j} + (2\mu\varepsilon^e_{ij} + \lambda\varepsilon^e_{kk}\delta_{ij})_{,j} = 0 \tag{2.20}$$

where the field $ln\ (1 - D)$ (values relating to the nodes $ln\,(1 - D^{(p)})$) is unknown (the unknown nodal discretize) if the elastic deformation fields ε^e_{ij} and are known by Digital Image Correlation (DIC). The discretization of this problem leads to an overdetermined linear system that can be described as follows:

$$[A]\ \{d\} = \{q\} \tag{2.21}$$

where the 'unknown' vectors {d} have as components the values of the logarithm of (1 - D) to the different nodes 1, ..., p ... N,

$$\{\boldsymbol{d}\} = \begin{bmatrix} ln\left(1 - D^{(1)}\right) \\ \vdots \\ ln(1 - D^{(p)}) \\ \vdots \\ ln(1 - D^{(N)}) \end{bmatrix} \tag{2.22}$$

where the matrix [A] has only values of 0, 1 and -1. The second member, {q}, is a function of the measured nodal displacements and of interpolation finite element chosen. The system is solved with the aid of the minimum squares method:

$$([A]\ \{d\} - \{q\})^T\ [W_{cor}]([A]\ \{d\} - \{q\}) \quad \text{minimum} \quad \text{given } \{d\} \tag{2.23}$$

the matrix [W_{cor}] was introduced as a matrix "weight " diagonal. The previous problem does not lead to relative stiffness measurements and, therefore, is not able to determine the damage. It is necessary to specify one of the components {d} and define as new vector "unknown", the vector {δ},

$$\{\delta\} = \{d\} - \{d\}_0 \quad , \quad \{d\}_0 = \begin{bmatrix} 0 \\ \vdots \\ 0 \\ \ln(1-D)_{i_0} \\ 0 \\ \vdots \\ 0 \end{bmatrix} \tag{2.24}$$

such that the damage field is finally defined,

$$([A]^T [W_{cor}][A])\{\delta\} = ([A]^T[W_{cor}])\{q\} - ([A]^T[W_{cor}][A])\{d\}_0 \tag{2.25}$$

Marigo's damage theory (1981)

There are several stages of transverse and longitudinal deformations during the mechanical testing. There are some theories that relate the deformations with damage to the material (Marigo, 1981; Bonnet & Constantinescu, 2005; Claire *et al.*, 2002, 2004, 2007; Chalal *et al.*, 2004, 2006). According to the Marigo's damage theory (1981), these strains can be associated with the Poisson's ratio of the material through equivalent deformations, which can be defined as:

$$\varepsilon_{eq} = \frac{\langle\varepsilon_1\rangle^2 + 2\nu\langle\varepsilon_1\rangle\langle\varepsilon_2\rangle + \langle\varepsilon_2\rangle^2}{2(1-\nu^2)} \tag{2.26}$$

where:
ε_1 is strain in direction 1 (longitudinal); ε_2 is strain in direction 2 (transverse); ν is Poisson's ratio.

The damage variable, therefore, associated to the summation of the strains in each instant along the test is defined as:

$$D = \sum C_p \left[1 - \exp\left(\frac{\varepsilon_{eq}}{\varepsilon_p}\right)\right] \quad (2.27)$$

where:

C_p is the amplitude identified in strain histograms and provided during the execution of the algorithm of DIC technique; ε_p is the characteristic strain inserted as input data in the algorithm and that should be between the lower and higher value of equivalent strains along the mechanical loading stages captured by DIC.

The algorithm created by Hild & Roux (2008), based on Marigo's damage theory and operating in the MATLAB software requires the characteristic strain (ε_p) and Poisson's ratio (ν) as input. The value of the ε_p can be determined from the histogram of the equivalent strain, also generated by this algorithm, respecting the following inequality $\varepsilon_{eq\ mín} \leq \varepsilon_p \leq \varepsilon_{eq\ máx}$. The Poisson's ratio (ν) may be determined by DIC through the rate measurements between the transverse (ε_t) and longitudinal (ε_l) strains during the elastic regime and may be defined as follows:

$$\nu = -\frac{\varepsilon_2}{\varepsilon_1} = -\frac{\varepsilon_t}{\varepsilon_l} \quad (2.28)$$

According to this theory, it is important to initiate the ε_p with low values and gradually increase it up to an optimal quality identification of the damage and low fluctuation or error values, ρ. In the validation of this algorithm, Hild & Roux (2008) evaluated the displacement field, $u_{computed}$, which was calculated using the present law, in comparison with the measured and strained field by DIC, $u_{mesured}$, along the region of interest and it was found lower values to 7% and with a good identification of the damage fields along this region. The error or fluctuation shown at the end of the algorithm and after the damage determination is defined by:

$$\rho = \frac{\chi\,(u_{computed} - u_{mesured})}{\chi\,(u_{mesured})} \quad (2.29)$$

where:

χ = ratio of the standard deviation

By definition, this way takes into consideration both the material strains, and an elastic property (Poisson's ratio), and adds to the mechanical damage theory developed by Lemaitre (1984), which in turn contemplates the damage of a material through the decrease in mechanical properties as a function only of its longitudinal strain measured during a cyclic uniaxial tensile test.

As an example of this technique, the Figure 2.9 (a) presents a specimen for a biaxial test in Astree equipment (2D-traction) at LMT-Cachan (Périe et al., 2009). The material was a composite of 2.5 mm thick and manufactured with vinyl ester matrix and glass-fibers, considered as isotropic material due its random distribution of fibers. The area of the region of interest is 36.5 x 36.5 mm².

Figure 2.9. (a) Vinyl ester/glass-fiber composite under biaxial loading, (b) total rupture and (c) damage field close to onset of its rupture.

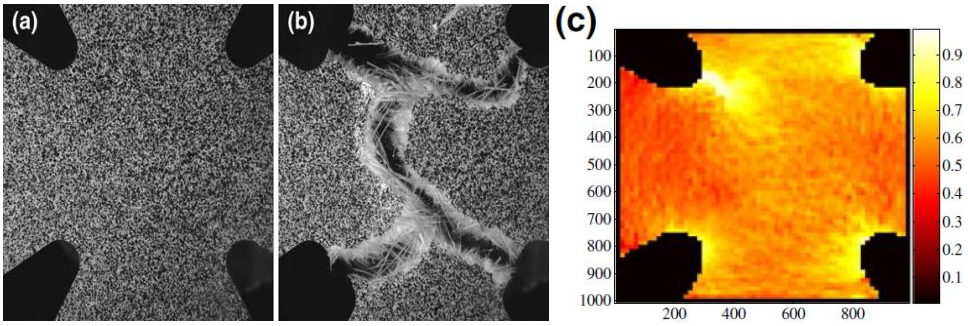

Source: Périe et al. (2009).

The material ruptured shows fracture in various directions (Figure 2.9 (b)). However, only the damage fields shown in Figure 2.9 (c) were able to demonstrate and predict the failure onset. After its initiation, the cracks were propagated throughout specimen. The more damaged elements (D close to 1, in blank color and located in top left) corresponds to the onset of mesoscopic rupture, leading to specimen breaking.

This example only illustrates a determination of damage fields applied in composite material. Vinyl ester/glass-fiber is a brittle material and its deformation mechanisms are different than thermoplastic composites used in this research.

3. Materials and experimental procedures

This chapter aims to present the materials and experimental procedures used in this study. In general, the obtaining and processing of materials focused on activities carried out at the laboratories of the Federal University of Ceará (Brazil). The morphological and mechanical characterizations on these materials were performed at the *Laboratoire de Mécanique et Technologie* (LMT-Cachan) from *École Normale Supérieure de Cachan* (France).

Manufacturing and testing procedures followed international standards, such as EN ISO and ASTM, or successful literature references, such that its methods may provide repeatability and reproducibility.

3.1. Coconut fibers and coconut fibers mats

The coconut fibers from green coconut fruits used in this work were provided by EMBRAPA Tropical Agroindustries in Fortaleza (Brazil). Figure 3.1 shows these fibers in the received condition. Green coconut fruits were collected after 6 or 7 months of their appearances in the coconut tree (maturation condition).

Figure 3.1. Coconut fibers in the received condition.

Source: author.

For extracting coconut fibers, EMBRAPA inserts the coconut husks in water tanks for six months or in salted tanks that require from 10 to 12 months of anaerobic fermentation. The fibers are then cut, washed and dried prior to separation and cleaning. The remaining residue may be used as horticulture product. The next procedure uses a defibrillator to process the husks after other five days of water immersion, followed by slashing the shell, softening and opening the fibers. Cylinders are used to separate long and short fibers. The strongest fibers are washed, cleaned, dried and softened. The quality of the fiber is extremely affected by this process. It is possible to extract approximately 80 to 90 g of fiber for each coconut husk. The husk is composed of 70% of powder and 30 % of fibers (Pannirselvam, 2005).

Other significant application of coconut fiber is the confection of mats or non-woven fabric (discontinuous and randomly oriented, Figure 2.1 (c)), which can be used as reinforcement when the composite is mechanically loaded in various directions.

Nonwoven fabrics or mats were manufactured by Embrapa through the random distribution of untreated coconut fibers and 250 g/m² surface density (grammage) (Figure 3.2 (a)). An aqueous solution of latex was used as binder and a roller was used for fibers compression (approximately 100 g of fiber per 100 mL of aqueous solution of latex). The fiber orientation showed an isotropic and random distribution for this mat (Figure 3.2 (b)).

Figure 3.2. Coconut fiber mat: (a) after processing and (b) specimen.

(a) (b)

Source: author.

After fabrication, the weight of coconut fiber in a given mat area was measured in order to obtain its experimental grammage. For this, three specimens with different square areas of

the mat were used: with 5, 15 and 100 cm of side. The weighing scale Bel Engineering (model Mark 210 A) with an accuracy of 0.0001 g was used for samples of 5 and 15 cm side. For specimen 100 cm side, it was used a weighing scale from same manufacturer (model S-Mark 5201), with an accuracy of 0.1 g. Both measuring systems belong to the Corrosion Laboratory of Federal University of Ceará (Brazil). Table 3.1 shows these weight measurements.

Table 3.1. Experimental measurements of grammage of coconut fiber mat.

Sample size	Weight (g)	Grammare (g/m²)
5 cm x 5 cm	0.502	200.8
5 cm x 5 cm	0.4855	194.2
5 cm x 5 cm	1.224	489.6
15 cm x 15 cm	3.299	146.62
15 cm x 15 cm	4.623	205.47
15 cm x 15 cm	6.131	272.47
1 m x 1 m	235.8	235.8
Average grammare		249.26

Source: author.

According to Table 3.1, the average grammage of the mat is 249.26 g/m². This value is close to the expected value. However, due to the manual distribution of fibers before the binder application, dispersed values for this measurement were found. Values such as 146.62 and 489.6 g/m² demonstrate the wide scattering in the distribution and concentration of coconut fibers along the mat.

3.1.1. Surface treatments on coconut fibers

In this work, techniques that aim to remove impurities and wastes from processing and handling around the coconut fibers were performed. A chemical treatment by NaOH aqueous solution was used to remove external impurities and improve chemical affinity with polymer, as presented previously.

The moisture or water vapor may be considered as an impurity during the composite processing, because the thermoplastic polymers reach temperatures sufficient to evaporate the water during its melting, forming bubbles or empty areas. Therefore, coconut fibers will also be studied after heating.

Even not being manufactured composites reinforced by dried and chemically treated coconut fibers in this study, these fiber conditions will be evaluated in order to understand their individual properties, in terms of morphological and mechanical behavior, and in further studies they will be evaluate as reinforcement in composites. Finally, these natural fibers were evaluated in four different conditions:

- Untreated coconut fibers or in 'as received' condition or *in natura*;
- Coconut fibers that received chemical treatment by immersion of NaOH in a 5% solution of NaOH (100g of coconut fiber per liter of NaOH solution). These fibers were soaked in the alkaline solution for an hour at the room temperature (25 ± 5°C) under mechanical agitation in the mixer. After this period, coconut fibers were washed with deionized water to remove the residues from the chemical treatment. Then, they were dried at room temperature and humidity for 48 hours;
- Coconut fibers in the 'as received' condition followed by drying in an oven at 60 ± 10 °C for 24 hours;
- Coconut fibers that received the same chemical treatment by NaOH as described above and also were dried in an oven at 60 ± 10 °C for 24 hours.

These procedures were carried out at Corrosion Laboratory from Federal University of Ceará (Brazil).

3.2. Virgin and recycled polypropylene

The thermoplastic resin used in this study was the polypropylene in pellet form in virgin (copolymer; Braskem® CP 201) and recycled conditions (Figure 3.3). The recycled condition was obtained after 9 cycles of injection of this virgin polypropylene. As previously presented, this polymer has wide application and can be manufactured in various methods and, according to the literature, has already been used to manufacture composite materials with coconut fibers.

Figure 3.3. Polypropylene from Braskem® in pellet form in (a) virgin and (b) recycled conditions.

(a) (b)

Source: author.

According to the manufacturer and melt flow index (MFI) measurements performed in the LMS-Plastometer P101, the MFI of virgin and recycled polypropylene are 20.33 and 20.11 g/10 minutes. The melt flow index range of a polymer for injection processing is from 6 to 42 g/10 minutes (PlasticsTechnology, 2014). Therefore, the polymers and natural fiber composites fabrication in this study were carried out by the injection process.

3.3. Manufacture of polymers and composites

The injection machine (manufacturer Furnax; capacity 140 tons) from SENAI (Maracanaú, Brazil) was used for the manufacturing of polymer and composite specimens. This equipment has six heating zones: zone 6 is related to hopper, zones 2 to 5 possess the cylinder injection and zone 1 contains the nozzle. The polymers and composites were injected at 3 bar pressure, using the following temperature profile: 30 °C in zone 6, 35 °C in zones 5 and 4, 180 °C in zone 3, 175 °C in zone 2 and 170 °C in zone 1. The samples used in this study were obtained through the mold specimens for mechanical testing from SENAI in Maracanaú. This mold fabricates specimens in the dimensions in accordance to ASTM D638-10 (standard test method for tensile properties of plastics). Figure 3.4 (a) shows the injection schematic and the manufacturing steps of the materials used in this study.

Figure 3.4. Manufacture of polymers and composites: (a) injection schematic, (b) polypropylene in hopper, (c) molten polypropylene output in nozzle, (d) mold with coconut fiber mats and (e) manufactured materials.

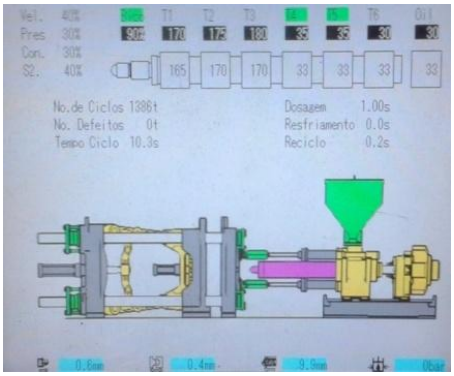

(a)

(b)

(c)

(d)

(e)

Source: author.

Polymeric samples of virgin and recycled polypropylene and composite samples reinforced by coconut fibers mats were manufactured. Prior to injection and manufacturing of composites, pieces of mat were cut manually and inserted into the internal cavity of the mold

(Figure 3.4 (d)). The cuts were carried out in order to occupy the whole area of the specimen. Then, the mold was closed and the molten polypropylene was injected into this cavity, remaining closed until its complete solidification (Figures 3.4 (b-c)). Thereby, composites were produced with one or two layers of coconut fibers mat (Figure 3.4 (e)). The volume fraction of fiber will be measured by the morphology studies, which will be presented in next section. Finally, the manufacturing of injected specimens was as follows:

- Virgin polypropylene (PP);
- Recycled polypropylene (RPP);
- PP reinforced by one layer of untreated coconut fiber mat (PP-1L);
- PP reinforced by two layers of untreated coconut fiber mat (PP-2L);
- RPP reinforced by one layer of untreated coconut fiber mat (RPP-1L);
- RPP reinforced by two layers of untreated coconut fiber mat (RPP-2L).

3.4. Morphological analysis

The internal and external morphology of a material may influence its application and present its geometric details. In this context, sophisticated techniques, such as Scanning Electronic Microscopy and X-rays tomography, have been important to present the micro-constituents of a material. Morphological observations on the materials of this study, using both techniques, allowed to understand and quantify some of its components and evidence the fiber-matrix interface, as well as determine its impurities, effective areas and volume fraction of fiber within of the composites.

3.4.1 Scanning Electronic Microscopy (SEM)

Morphological characterization of PP, PP-1L, PP-2L, RPP, RPP-1L, RPP-2L, untreated and treated coconut fibers was performed by Scanning Electron Microscopy (SEM), Hitachi, model S-3400N (Figure 3.5 (a)). Acceleration voltages of 2 to 5 kV and magnifications 200, 300 and 500x were used to observe the main constituents of coconut fibers. Acceleration voltage of 20 kV and magnification of 11 to 3000x were used to present the rupture micrographs of polymers and composites. For all materials and conditions, the distance between the SEM camera and these materials was between 8-10 mm.

All samples were gold metalized surface by vacuum (minimum pressure of 0.05 mbar) for 20 seconds and 20 mA with the equipment Balzers SCD004 Sputter Coater (Figure 3.5 (b)) before being observed in the SEM. Both equipments belong to the LMT-Cachan.

SEM micrographs were carried out to measure the diameters of coconut fibers. Due to the large variation on this measure, a set of 22 randomly selected fibers were evaluated. This measurement procedure was necessary to determine the cross-sectional area on the coconut fibers. A large variation of diameter along its length may influence the mechanical behavior.

Figure 3.5. SEM preparation: (a) SEM used and (b) metallization equipment.

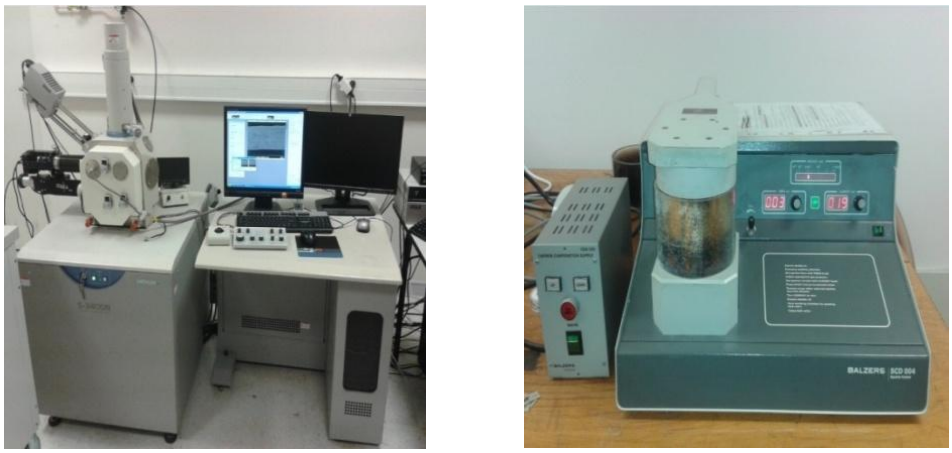

(a) (b)

Source: author.

3.4.2. X-ray tomography

Morphological characterization of PP, PP-1L, PP-2L, RPP, RPP-1L, RPP-2L and coconut fibers was also performed by X-ray tomography. This technique allows visualization of internal objects without the need to physically open them.

The X-ray tomography equipment used in this study was the North Star Imaging Company. Inc. (NSI), model X 50 (Figure 3.6 (a)), from LMT-Cachan. It consists of a protected radiation cabin up to 250 kV, a 5 axis manipulator, a dual X-ray tube of 225 kV of energy with dual source (reflection and transmission) and a detector with scintillator plane cesium 3072 × 3888 pixels, 14-bit and 26 frames/second (fps) at full resolution. A software suite manages the manufacturer's own data acquisition, image processing and 3D reconstruction. Figure 3.6 (b) shows a sample of coconut to be viewed in the X-ray

tomography equipment. In this work, 175 kV of energy, 50 µA of emission current and 7 fps are used.

Figure 3.6. (a) X-ray tomography equipment and (b) coconut fiber sample.

(a) (b)

Source: author.

It was created a script in MATLAB software able to represent the pixels related to the fiber constituents, through of tomography images. This script was able to differentiate the white pixels or pixels with low gray levels of other pixels. Thereby, it was possible to determine the pixels relative to the fiber and separate the pixels related to empty areas. This script represented numerically the gray levels found in a given image and presented the pixels related with the coconut fiber constituents. The script created also informs the surface fraction that each gray level corresponds.

3.4. Mechanical behavior

In-situ testing is especially attractive for micro/nanoscale samples because one can monitor the overall macroscopic response while simultaneously observing the deformation mechanisms and thus establish the structure-property relationship.

Deformation and failure mechanisms in coconut fibers, coconut fibers mats, virgin and recycled polypropylene and composites involving these were evaluated by Digital Image Correlation (DIC) technique and, in some cases, by Digital Infrared Thermography (DIT) technique during tensile testing. The principles and calibration of both techniques are

available in Appendix A and B, respectively. The experimental procedures to carry out these methods will be presented.

3.4.1. In-situ tensile testing of coconut fibers

In-situ tensile tests under four conditions of coconut fiber was performed in accordance with ASTM C1557–03 (2013) within the same Scanning Electron Microscope (SEM) used to evaluate their morphological behavior with the aid of an electromechanical testing machine inserted inside the SEM to perform tensile tests in small samples.

The magnifications of 200, 300 and 500x and an accelerating voltage of 5 kV were used. Each pixel size of the coconut fibers images are 496, 331 and 99 nm for the magnifications of 200, 300 and 500x, respectively. This resolution was sufficient to measure the mechanical deformation by DIC technique.

The data output provided during the mechanical response of coconut fibers, such as displacement and load, were processed by Kammrath & Weiss GmbH DDS software, version 3.007, in communication with a load cell of accuracy of 0.1 N and measuring range from 0 to 500 N, and connected to the electromechanical testing machine.

The coconut fibers were evaluated by DIC technique after the application of gold metallization as described previously. The gold plating is a procedure widely used by the literature to obtain good images with textures on the surface of coconut fibers into the SEM. Therefore, the external texture of coconut fiber covered by metallization was responsible to monitor the deformation mechanisms of this fiber (Tomczak, 2010; Cassales et al., 2011; Monteiro et al., 2006).

It was possible to capture the reference (not deformed) images prior the test. During the test, the two grips moved in opposite directions, imposing a displacement rate of 1 μm/s for tensile test, allowing the capture of stable images to each 0.5 N of increase of loading. Then, these images were stored and inserted in MATLAB software for the use of DIC technique. Kammrath & Weiss GmbH DDS software allows interruptions during the execution of tensile test. The time of each interruption for capture an image was approximately 30 s. These measuring systems are available at LMT-Cachan.

For each test, a fiber was fixed with an instant glue type (composed of cyanoacrylate ester) on rectangular paper, grammage 180 g/m², 40 mm of length and 10 mm of width, with a rectangular cut of 15 mm of length and 8 mm of width at its center, where the fiber was fixed at its ends. The specimen preparation for the tensile test is shown in Figure 3.7.

Figure 3.7. Preparation of coconut fibers prior to the in-situ tensile test: (a) fibers fixed on the paper, (b) fiber glued on paper, (c) cuts of the paper sides and (d) fibers inserted in the SEM.

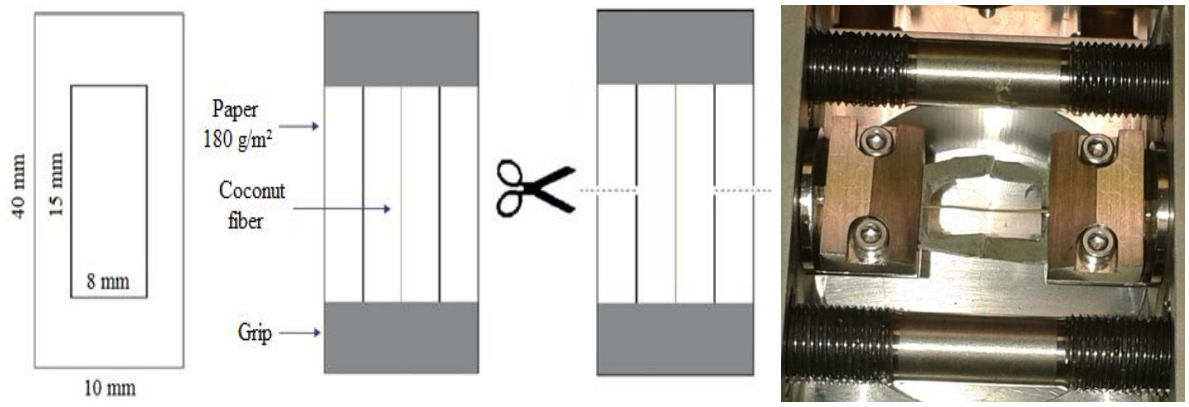

(a) (b) (c) (d)

Source: author.

The distance between grips was 15 mm, the same as the length of the cut in the center of the paper. During the test, the two grips moved in opposite directions, imposing a displacement rate of 1 μm/s for tensile test.

The applied nominal stress on the coconut fiber was calculated by the expression $\sigma = \vec{F}/A_o$, where $\vec{F}$ is the applied force and A_o is the area of the initial cross-section. Prior the mechanical tests, each cross-sectional area of coconut fiber was calculated using the average diameter along the length and by the expression $A_o = (\pi\phi^2/4)$. At least five diameter measurements were carried out along its length. However, natural fibers present non-circular and irregular section and discrepancies among mechanical properties may be found (Fidelis et al., 2013; Mota & Agopyan, 2007).

Motta & Agopyan (2007) studied about the diameter dispersion of coconut fibers. Here, the actual areas (measured by micrometer) and the elliptical areas (calculated through the largest and smallest cross-sectional dimension of the fiber observed by optical microscope) were compared and the correlation coefficient of 1.0062 was found. Therefore, by this research, the non-circular effects of coconut fiber were neglected.

This proximity allowed the present work to determine the cross-sectional area of the fiber as a circle of area $A_o = (\pi\phi^2/4)$, where ϕ is the average diameter of each fiber, after minimum five measurements performed by SEM along the length between the grips of tensile machine. Through this procedure, it was possible to determine the tensile strength, failure strain, modulus of elasticity, and modifications on the four conditions of coconut fibers and with different diameters.

The diametric deformations identified after tensile testings were captured by SEM and were calculated by the following equation:

$$Diametric\ deformation = \left(\frac{\emptyset_{initial} - \emptyset_{final}}{\emptyset_{initial}}\right).100 \quad (3.1)$$

3.4.2. Tensile testing of coconut fibers mat

In accordance with the EN ISO 10319:2008 and studies of Ridruejo et al. (2010) the uniaxial tensile tests on coconut fiber mat were performed on an Instron 5882 machine. The displacement rate used was 0.2 mm/s (12 mm/min) with a load cell of 0.5 N of accuracy and measuring range from 0 to 500 N. The Edmund Optics® camera spaced frontally at 100 mm from the specimens captured one image per second during the execution of the test. For better stability and quality of the images a black background was placed behind the specimens and a front light was directed to them (Figure 3.8).

For this test, ten rectangular specimens 20 mm wide were tested with a distance of 10 mm between the grips (20 x 10 mm²). Ten other rectangular specimens 40 mm wide were tested with a distance of 20 mm between the grips (40 x 20 mm²). In both cases, the length of each grip inside was 10 mm, respectively, and the pixel size in the captured images was 12 µm.

It was reported previously that coconut fibers were randomly distributed and presented dispersions in their grammage values. Therefore, their weights were measured and were related to their mechanical properties prior to the tensile test in the coconut fiber mat. For this, a weighing scale, Mettler Toledo (model AT261), with an accuracy of 0.01 mg was used.

Due to the manual overlapping and dispersion of coconut fibers during the mat manufacturing process it was not possible to determine its thickness and, consequently, its cross-sectional area and stress also were not determined. Therefore, the force per width (N/m) and elongation at break (%) of specimens will be provided by this test.

Figure 3.8. Tensile test on coconut fiber mats: (a) specimen dimensions and (b-c) apparatus coupled in tensile machine.

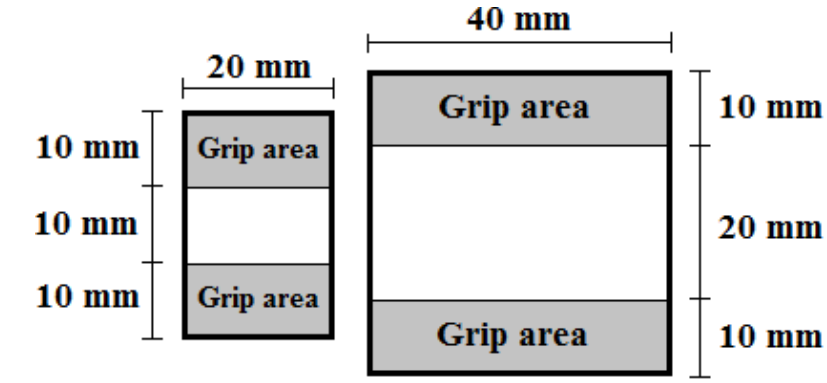

(a)

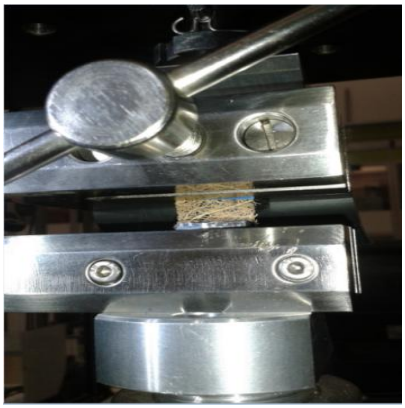

(b)

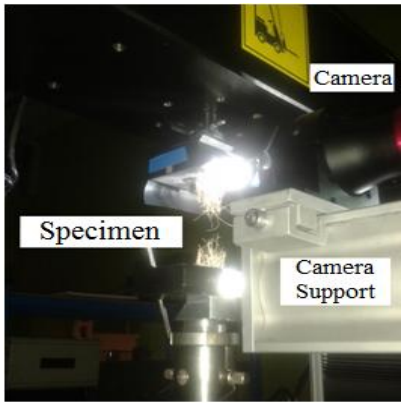

(c)

Source: author.

3.4.3. Tensile testing of polymers and composites

Tensile tests on PP at displacement rates of 10, 15, 20, 25, 30 and 35 mm/min and tensile testing at displacement rate of 10 mm/min on PP-1L, PP-2L, RPP, RPP-1L and RPP-2L were performed according to ASTM D638-10 and followed by an infrared camera (Cedip Infared Systems; Camera Jade 570M) for Digital Infrared Thermography (DIT) and a digital camera (model manta IT CCD Sony ICX 285 ExViewHAD and 0.125x of lens objective) for Digital Image Correlation (DIC). The displacement rates adopted in this work were slightly different to ASTM standard, because these mechanical tests aimed to monitor the deformation mechanisms of polymers and composites.

The tests were performed at LMT-Cachan through of MTS servo-hydraulic machine (model 810 with 10 kN load cell) at room temperature (25 ± 5°C). Each camera was distanced frontally from the opposite side at 25 cm (Figure 3.9 (a)) and captured 500 and 2 images per

second by infrared and digital cameras, respectively. The two surfaces of the specimen were sprayed by JELT Jeltouch RAL 9005 and RAL 9010, one side sprayed with black color for DIT and the other side sprayed with white along non-uniform black points for DIC (Figure 3.9 (b)), according to procedures that requires images with good texture and appropriate gray level for DIC analysis in the Correli[Q4] software. The criteria for appropriate and calibration of DIC technique are presented in Appendix A (Tscharnuter et al., 2011; Jerabek et al., 2010; Grédiac & Hild, 2011).

Figure 3.9. (a) Apparatus for tensile test in virgin polypropylene and (b) surface prepared for DIC analysis. 1 pixel represents 52 µm.

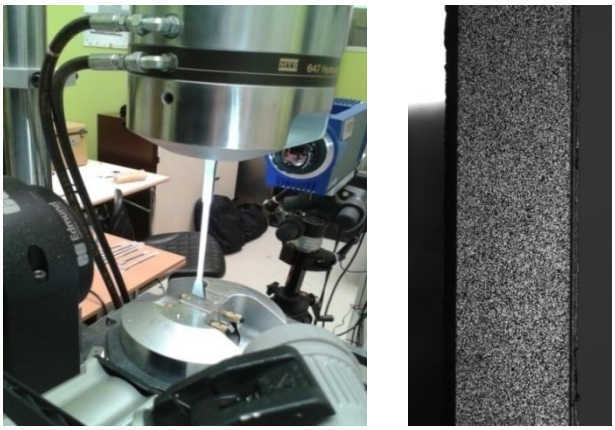

(a) (b)

Source: author.

3.4.4. Stress and strain measurements: true strain-stress curves

The engineering strains in the longitudinal direction, $\varepsilon_{eng} = \Delta L/L_0$, with the same relationship in the width and thickness directions. This had to be converted into true (or logarithmic) strain and the following formula was used:

$$\varepsilon_{true} = \ln (1 + \varepsilon_{eng}) \quad (3.2)$$

During testing, the force, cross-head displacement and time were measured by the testing machine and logged together with the images captured with the DIC technique. The true stress can be found by dividing the force F by the cross-sectional area A at any time during the test:

$$\sigma_{true} = \frac{\mathrm{F}}{\mathrm{A}} \tag{3.3}$$

The change in area during the test is difficult to measure, therefore the initial cross-sectional area A_0 is used to get the engineering stress.

$$\sigma_{eng} = \frac{F}{A_0} \tag{3.4}$$

Since the DIC was applied on both the front and the side of the specimen, it is possible to extract the strains in the width and thickness directions, as well as the longitudinal direction. The true strains in each direction is shown in Equation 3.5.

$$\varepsilon_l = ln\frac{l}{l_0} \quad , \quad \varepsilon_w = ln\frac{w}{w_0} \quad \text{and} \quad \varepsilon_t = ln\frac{t}{t_0} \tag{3.5}$$

where *l*, *w* and *t* is the gauge length, width and thickness respectively at any time during the test, and l_0, w_0, and t_0 is the initial length width and thickness of the specimen, respectively.

The cross-sectional area of the specimen is $A = wt$. Putting the exponent in front of ε_w and ε_t and rearranging gives:

$$w = w_0 e^{e_w} \qquad \text{and} \qquad t = t_0 e^{e_t} \tag{3.6}$$

which inserted in the area gives:

$$A = w_0 t_0 e^{e_w} e^{e_t} = A_0 e^{e_w} e^{e_t} \tag{3.7}$$

Inserting Equation 3.7 into Equation 3.4 gives the true stress expressed as a function of the engineering stress and the true strains in the width and thickness.

$$\sigma_{true} = \frac{F}{A_0} e^{-e_w} e^{-e_t} = \sigma_{eng} e^{-e_w} e^{-e_t} \tag{3.8}$$

If the strains in the width and thickness directions are equal, or close to equal, $\varepsilon_w \approx \varepsilon_t$, this is often simplified using only the transverse strain ε_w, since it is easier to only measure ε_w.

Amundsen (2014) reported that ε_w and ε_t on PP were similar during monotonic loading. Therefore, the Equation 3.8 may be replaced by:

$$\sigma_{true} = \sigma_{eng} e^{-2e_w} \tag{3.9}$$

3.5. Numerical simulation

Mathematical models can both help delineate the relationship between various parameters and aid in the design of products. Through of hyperbolic tangent functions is possible to predict a linear curve, representing the elastic regime of a stress-strain curve; with these functions is also possible to model a curve, representing a plastic regime of a stress-strain response. According to Cofer (1999), Marcelo (2004), Duncan & Chang (1970) and Gerscovich (2009), the mechanical behavior in tensile testing on polymeric composite materials reinforced by fibers can be represented by the following numerical-hyperbolic tangent function:

$$\sigma = a.tanh(b.\varepsilon) \tag{3.10}$$

or,

$$\frac{\partial \sigma}{\partial \varepsilon} = \frac{a.b}{cosh(b.\varepsilon)} \tag{3.11}$$

where,

a,b: characteristic parameters of the material;

σ,ε: stress and strain obtained in the tensile test, respectively.

By definition we have:

$$\left.\frac{\partial \sigma}{\partial \varepsilon}\right|_{\varepsilon=0} = a.b = E\ (modulus\ of\ elasticity) \tag{3.12}$$

Therefore, it was possible to evaluate the mechanical behaviour numerically and compare with the experimental results.

3.6. Damage measurements

3.6.1. Damage mechanics using strain fields from DIC

Through the determination of the strain field by DIC, was also determined damage variable according to the Marigo's theory (1981), which through an algorithm, the longitudinal and transverse deformation of the elastic and plastic regions are inserted and associated with a damage law. A camera of 0.125x objective (manta CCD Sony ICX 285 ExViewHAD) captured two images per second during the uniaxial tensile testing previously presented. For this damage evaluation, the size of each pixel was 144 μm (Figure 3.10) and the analyzed area (region of interest) on specimen was about 1078 mm² (measurements performed with ImageJ software).

Figure 3.10. Specimen texture used to determine damaged fields during uniaxial tensile testing.

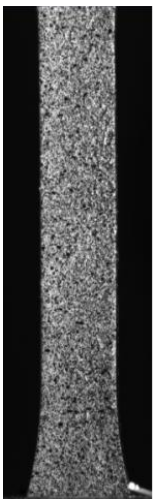

Source: author.

3.6.2. Damage mechanics from load/unload tensile testing

Loading/unload tensile testing were performed for determination of the damage variable of the studied materials through the evaluation of the decrease in the modulus of elasticity during this test, according to the procedure used by Lemaitre et al. (2009) described above. The modulus of elasticity of a virgin material, E, and a damaged material, $\tilde{E}$, were measured by eliminating areas of greater instability at stress-strain curve, known as regions out of range

$0.15\sigma_R$ to $0.85\sigma_R$, where σ_R is the tensile strength found in traditional tensile test (Lemaitre et al., 2009).

The longitudinal strain contained in an area of 12 x 12 mm² in the center of the specimens was precisely measured by an extensometer (Figure 3.11). The displacement rates adopted for loading and unloading were 10 mm/min. The tests were performed at room temperature (25 ± 5°C) in MTS servo-hydraulic machine, model 810, equipped with a 10 kN load cell.

Figure 3.11. Use of extensometer to measure the stiffness modification during load/unload tensile testing.

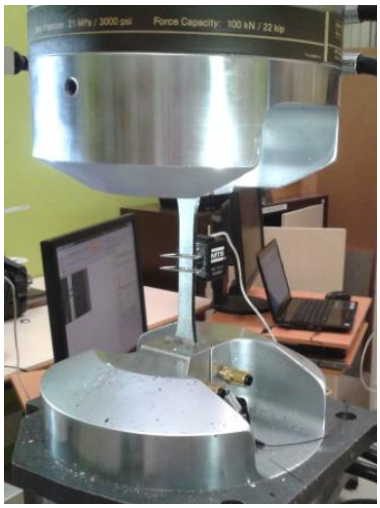

Source: author.

3.6.3. Numerical simulation of damage

The modulus of elasticity of a damaged material or measured in the plastic regime ($\tilde{E}$) and virgin or measured in the elastic regime of the stress-strain curve (E) are related as follows:

$$D = 1 - \left(\frac{\tilde{E}}{E}\right) \tag{3.13}$$

According to the numerical simulation model used in the mechanical behavior of fiber-reinforced polymer composite, it was possible to describe a function to its degradation process by mechanical damage theory. Rearranging some terms of the Equations 3.13 and 3.11, we have:

$$D = 1 - sech^2(b.\varepsilon) \tag{3.14}$$

Thus, it was possible to represent the process of degradation by damage-strain curves.

3.7. Summary of procedures

This study proposes to evaluate the individual morphological and mechanical properties of coconut fibers in four different conditions. Virgin and recycled polypropylene were evaluated in terms of the same analysis. Then, composites made with coconut fibers untreated and these polypropylenes were studied. Studies with treated coconut fibers are suggestions for future work. Table 3.2 summarizes the techniques used to characterize all materials of this study. The techniques used in each material are marked with the letter X.

Table 3.2. Summary of characterizations employed in this work.

Material	SEM	XRT	Tensile testing	DIC	DIT	Numerical modeling	Damage from numerical parameters	Damage from DIC	Damage from load/unload tensile testing
Untreated coconut fiber	X	X	X	X		X	X	X	
Dried coconut fiber	X		X						
Chemically treated coconut fiber	X		X						
Chemically treated and dried coconut fiber	X		X						
Untreated coconut fiber mat (UCFM)	X	X	X	X					
PP	X	X	X	X	X	X	X	X	X
PP-1L (manufactured with UCFM)	X	X	X	X	X	X	X	X	X
PP-2L (manufactured with UCFM)	X	X	X	X	X	X	X	X	X
RPP	X	X	X	X	X	X	X	X	X
RPP-1L (manufactured with UCFM)	X	X	X	X	X	X	X	X	X
RPP-2L (manufactured with UCFM)	X	X	X	X	X	X	X	X	X

Source: author.

4. Morphological and mechanical behavior of the coconut fibers and fibers mats

In the first part of this chapter, morphological observations by means of Scanning Electronic Microcopy (SEM) and X-rays tomography on four conditions of coconut fibers will be presented. Statistical measurements about the diameter variations and effective areas of microconstituents of these natural fibers will be provided in this chapter. The fibers distribution and thickness of coconut fibers mat will be also determined.

In the second part of this chapter, mechanical characterizations trough of uniaxial tensile testing on four conditions of coconut fibers and mats will be presented. Deformation and failure mechanisms on coconut fibers and mats were determined by DIC technique.

4.1. Morphological observations

4.1.1. Scanning Electronic Microscopy (SEM)

Figure 4.1 shows SEM micrographs from the external surface of four different coconut fibers in as received condition.

Figure 4.1. External surface of coconut fibers in ‘as received’ condition.

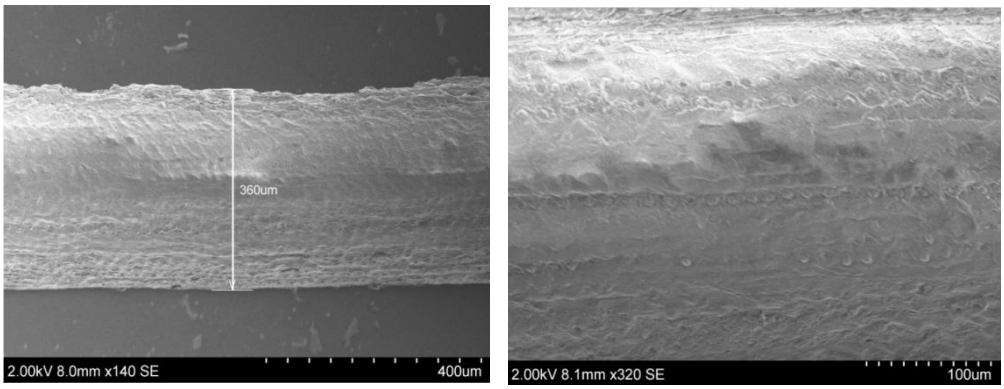

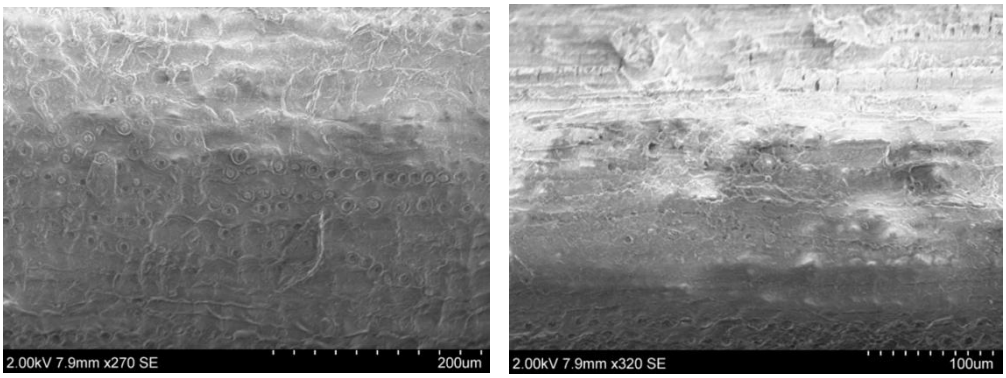

Source: author.

It was possible to observe that the fiber surface in the ‘as received’ condition is slightly roughened due to presence of impurities, fats and waste organic materials that were adhered on its surface due its vegetable origin associated to the extraction methods. This impurity layer prevents the observation of the constituents of its external layer. Figure 4.2 shows micrographs from the external surface of four different dried coconut fibers.

Figure 4.2. External surface of dried coconut fibers.

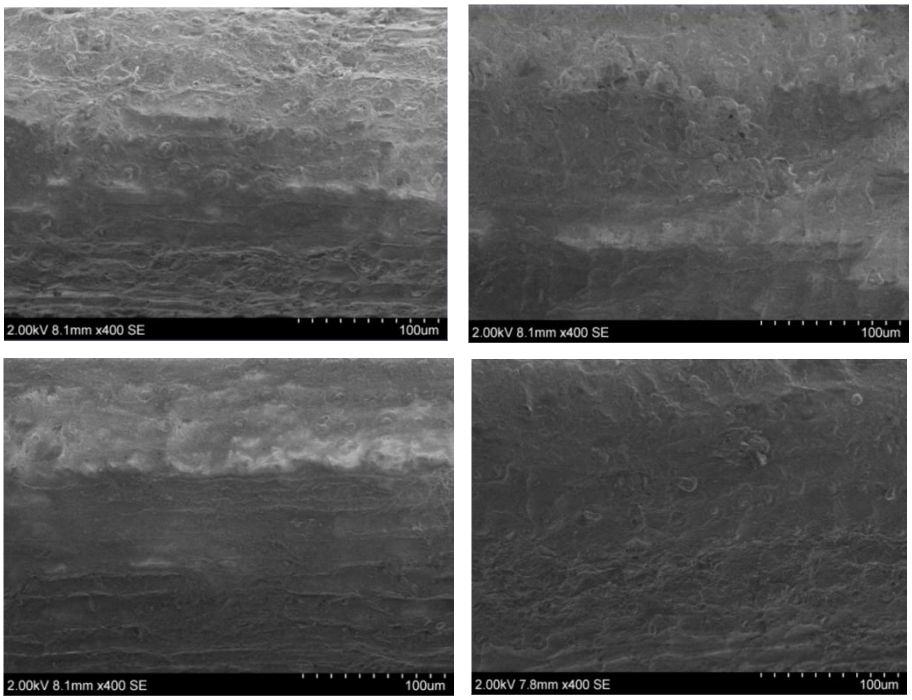

Source: author.

The external morphology of dried coconut fibers are similar to the conditions presented by untreated fibers, since there was no removal of impurities. However, the heating at 60°C for 24 hours may eliminate moisture or residual water arising from its extraction or improper

storage. This elimination allows the manufacture of polymeric composites without pores arising from evaporation of water. Figure 4.3 shows the SEM micrographs of the external surface of four chemically treated coconut fibers.

Figure 4.3. External surface of coconut fibers chemically treated.

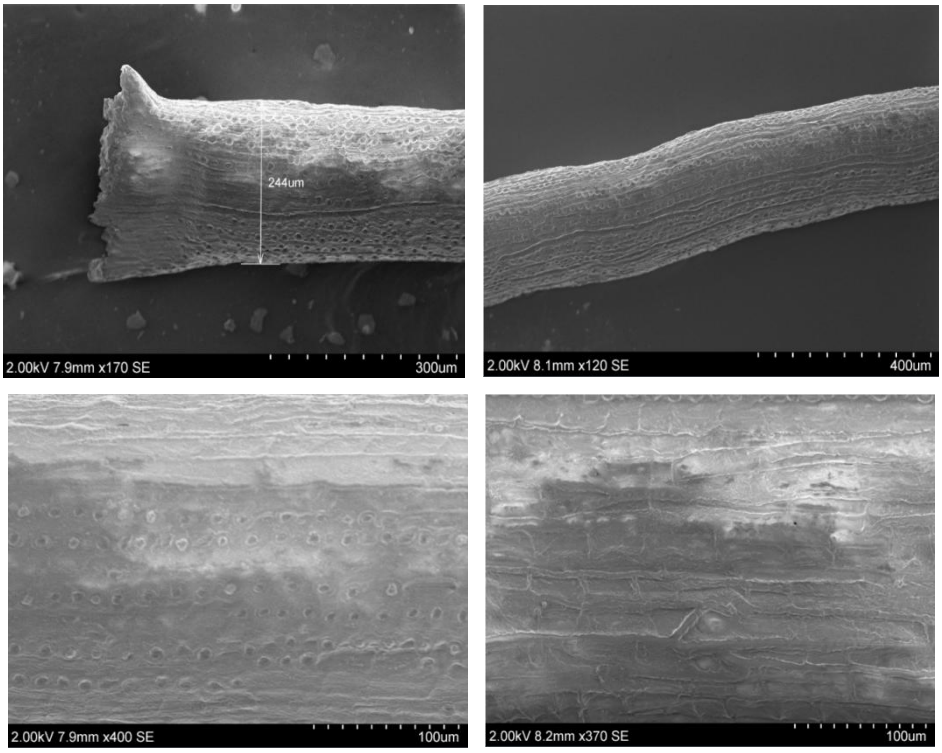

Source: author.

According to Figure 4.3, it is possible to see more clearly the external cell walls after chemical treatment in the four fibers. Furthermore, some circular and globular particles with diameters of approximately 10 μm can be observed at regular intervals and incorporated under its surface, after the removal of external impurities. These observations are in accordance with the results reported in the literature (Fernandes et al., 2013; Brahmakumar et al., 2005; Bismarck et al., 2001).

The removal of the surface impurities revealed a rough surface around the coconut fiber and exposes the oriented cells and pores (Brahmakumar et al., 2005). In the case of a composite material, the presence of roughness and protrusions hinders the detachment of the fiber with the resin, improving the interface fiber/matrix.

In addition to the removal of waste after treatment of coconut fibers, the partial removal of lignin, cellulose and hemicellulose in the fiber surfaces was observed. This modification around the surface layer is also verified in parenchymas cells, favoring the gain of contact

area through more exposure of the fibrils (indentations) and globular traits (protrusion) with polymers (Mulinari et al., 2011). Figure 4.4 shows SEM micrographs of the external section of four different coconut fibers chemically treated and dried.

Figure 4.4. External surface of coconut fibers chemically treated and dried.

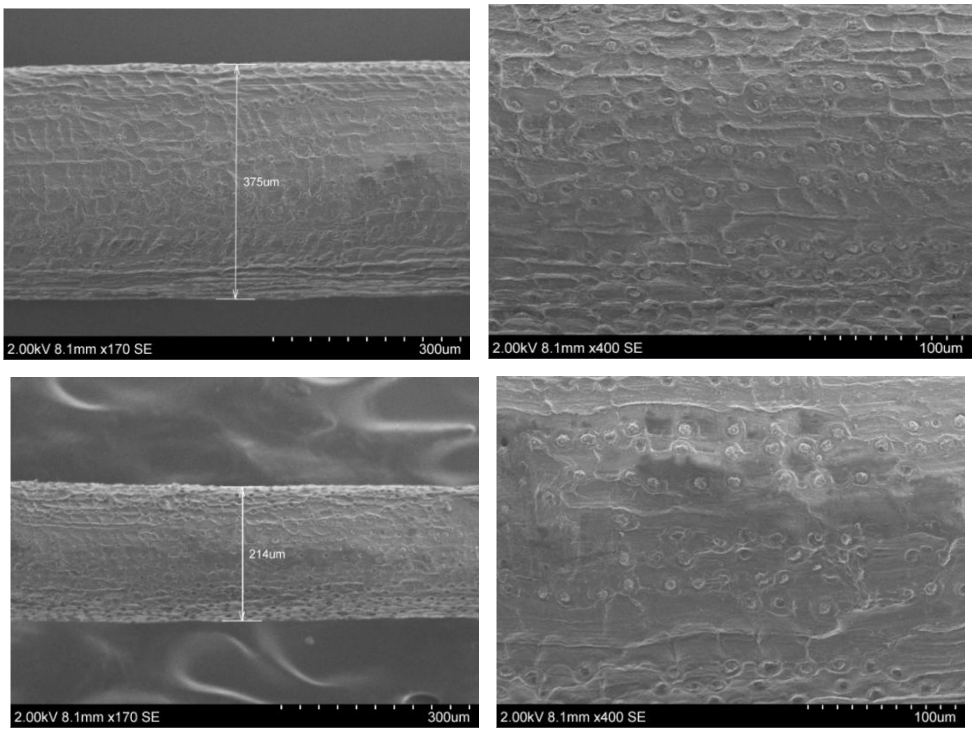

Source: author.

The chemically treated and dried fibers show similar morphological observations than chemically treated fibers. However, heating may remove the residual humidity or water after the chemical treatment in which water was used in addition to the sodium hydroxide. The moisture presence could form pores during the polymeric composite materials manufacturing.

Furthermore, it was observed in literature, through SEM micrographs and shear strength tests, that protrusions and indentations found after the external chemical treatment facilitated the impregnation with a polymeric matrix (Monteiro et al., 2006).

However, microcracks were found in a sample of chemically treated and dried fibers. Microcracks in the range 7 to 60 μm at the transverse direction were observed (Figure 4.5), as well as partial removal of external fiber constituents (lignin, hemicellulose and cellulose). These discontinuities may have been originated by the heating associated with stiffness modification imposed by chemical treatment. These discontinuities compromise the mechanical properties of the fibers.

Figure 4.5. Microcracks on a sample of a fiber chemically treated and dried.

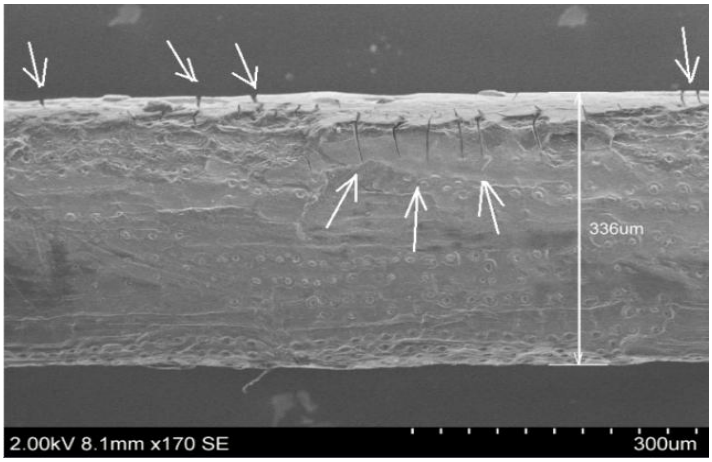

Source: author.

The diameters of 22 fibers selected randomly were measured in six regions along the length of 15 mm by SEM (total 132 measurements). Figure 4.6 displays the measurements points for fiber samples in the four conditions evaluated. Table 4.1 shows the averages and standard deviations of the values found for this fibers group.

According to the Figure 4.6 and Table 4.1, it can be reported that there was no significant change along the length of the as received and dry conditions, while fibers 4 and 5 of the chemically treated fibers and fibers 1, 3 and 6 of the chemically treated and dried have standard deviations greater than 30%. This can be explained by the unequal removal of constituent fibers after chemical treatment by NaOH, as shown in the previous micrographs.

Figure 4.6. Diameter measurements along the fibers length in the conditions: (a) 'as received', (b) dried, (c) chemically treated and (d) chemically treated and dried.

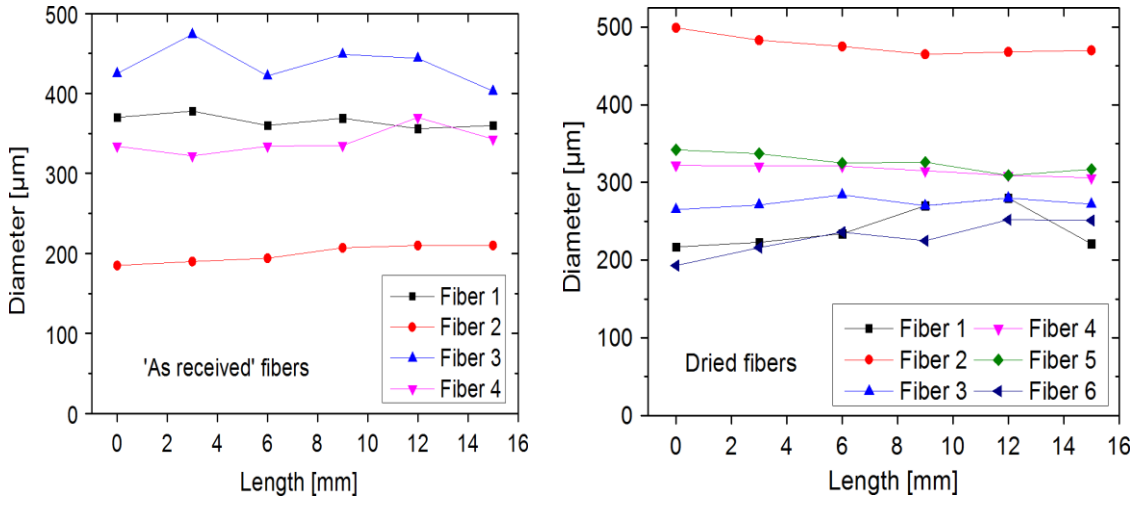

(a) (b)

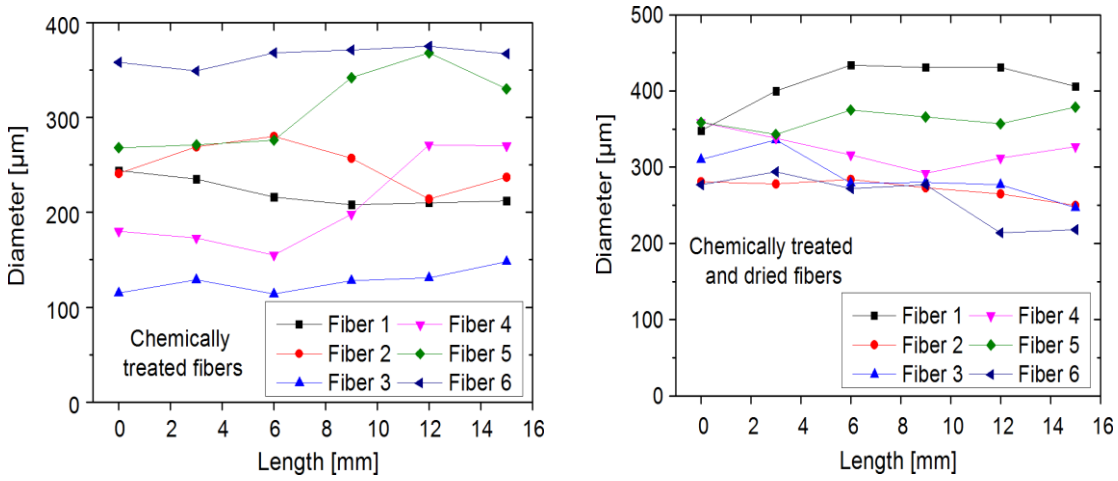

(c) (d)

Source: author.

Brígida et al. (2010) used a chemical treatment by immersing 5g of fibers in 4 to 6% NaOCl solution to 100 mL for 2 hours at 30°C and then washing the fibers with water and 10% of 100 mL of NaOH solution for 1 hour at 30°C. The treatment used by Brígida et al. (2010) was severe and removed external constituents, causing a significant reduction in approximately one third of the average diameter of coconut fiber, comparing to the natural fiber measurements.

According to Table 4.1 and Figure 4.6, the measured diameters ranged from 114 to 499 µm, minimum and maximum values measured, respectively. Figure 4.7 (a) shows the standard deviation diameters variation in which it is shown that chemically treated fibers have a greater diameter dispersion, contributing to report that treatment with NaOH aqueous solution removed constituents or impurities of the coconut fiber external layer. Figure 4.7 (b) shows the histogram of the measured coconut fibers diameters through the relative frequency histograms for 132 measurements, obtaining a mean of 299.83 µm and a standard deviation of 84.63 and a Gaussian distribution fit.

Large variations of the diameter values were also observed by Silva et al. (2000) with minimum and maximum values of 269 and 419 µm respectively, and a mean diameter of 337 ± 55 µm. Different studies reported mean diameters ranging from 40 to 400 µm for Brazilian coconut fibers (Satyanarayana et al., 2007). The climate variation, maturation, species, location and method of extracting coconut influence in different morphological behavior for coconut fiber (Tomczak, 2010).

Table 4.1. Average and standard deviations of the coconut fiber diameters measurements.

Condition	Sample	Diameter (µm)			
		Minimum	Maximum	Mean	Standard Deviation
As received	Fiber 1	356	378	365.5	8.24
	Fiber 2	185	210	199.33	11.02
	Fiber 3	403	474	436.17	24.83
	Fiber 4	322	370	339.67	16.31
Dried	Fiber 1	217	280	240,83	27.24
	Fiber 2	465	499	476.67	12.63
	Fiber 3	265	284	273.67	7.00
	Fiber 4	306	322	315.67	6.86
	Fiber 5	309	342	326.00	12.23
	Fiber 6	193	252	228.83	22.55
Chemically treated	Fiber 1	208	244	220.83	14.97
	Fiber 2	214	280	249.67	23.89
	Fiber 3	114	148	127.50	12.44
	Fiber 4	155	271	207.83	50.46
	Fiber 5	268	368	309.17	42.95
	Fiber 6	349	375	364.67	9.52
Chemically treated and dried	Fiber 1	348	434	408.33	32.87
	Fiber 2	250	284	271.83	12.61
	Fiber 3	247	336	288.17	30.77
	Fiber 4	292	359	324.00	23.07
	Fiber 5	343	379	363.17	13.12
	Fiber 6	214	294	258.67	33.90

Source: author.

Figure 4.7. Statistical information on coconut fibers diameters: (a) standard deviation of diameters variation and (b) frequency of the measured values.

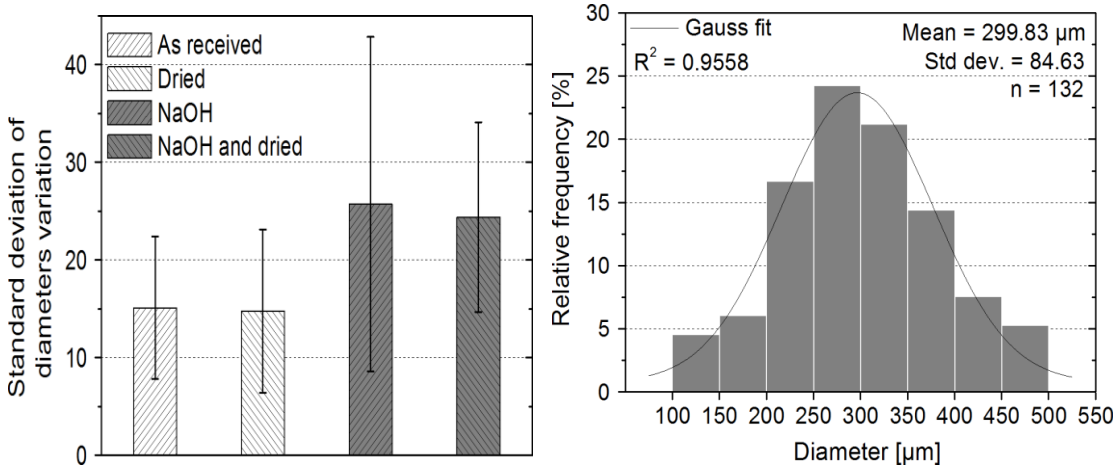

(a) (b)

Source: author.

4.1.2. X-ray tomography

Figure 4.8 (a) shows the coconut fiber cross section by X-ray tomography. It is possible to visualize the presence of several concentric walls and the presence of a representative cavity or void inside, called lumen. These regions represent voids therein, regions not effectively occupied by the main constituents of coconut fiber and multicells with approximate sizes (Tomczak, 2010). The coconut fiber outline is irregular and presents an elliptical form. These morphological characteristics found are in accordance with the images captured in the literature (Tomzcak, 2010; Brahmakumar et al., 2005; Satyanarayana et al., 1990). Figures 4.8 (b) and (e) were captured at the extremity and Figures 4.8 (c) and (d) were captured in the coconut fiber along the central longitudinal section, where the lumen is again displayed.

Figure 4.8. X-ray tomography observations of (a) transverse and (b-e) longitudinal sections along the inside of coconut fiber.

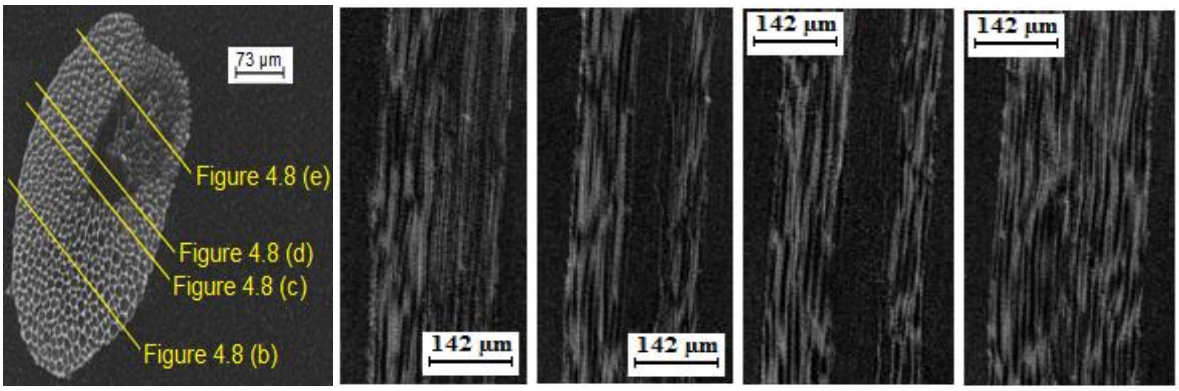

(a) (b) (c) (d) (e)

Source: author.

It is possible to observe in Figures 4.8 (b) crystalline microfibrils constituted of cellulose involved among amorphous layers of lignin and hemicellulose. This structure represents the variety of cells in accordance with the multicellular micrograph presented to the cross-section (Figure 4.8 (a)). These cells differ in chemical composition and helicoidal angle of the microfibrils. This set of parameters determines the mechanical properties of these natural fibers (Tomczak, 2010).

Figures 4.9 (a-c) present the tomography on the coconut fiber mat. Random distribution of the fibers due to their manual production is shown, some of which are involved by latex

and regions poor in fibers, influencing the mechanical properties of the mat. With this image it was possible to see a wide variation in thickness of the coconut fiber mat, 0.8 to 3.2 mm, due to the manual manufacturing.

Figure 4.9. X-ray tomography observations of coconut fiber mat: (a) lateral and (b) frontal views and (c) fiber involved by latex.

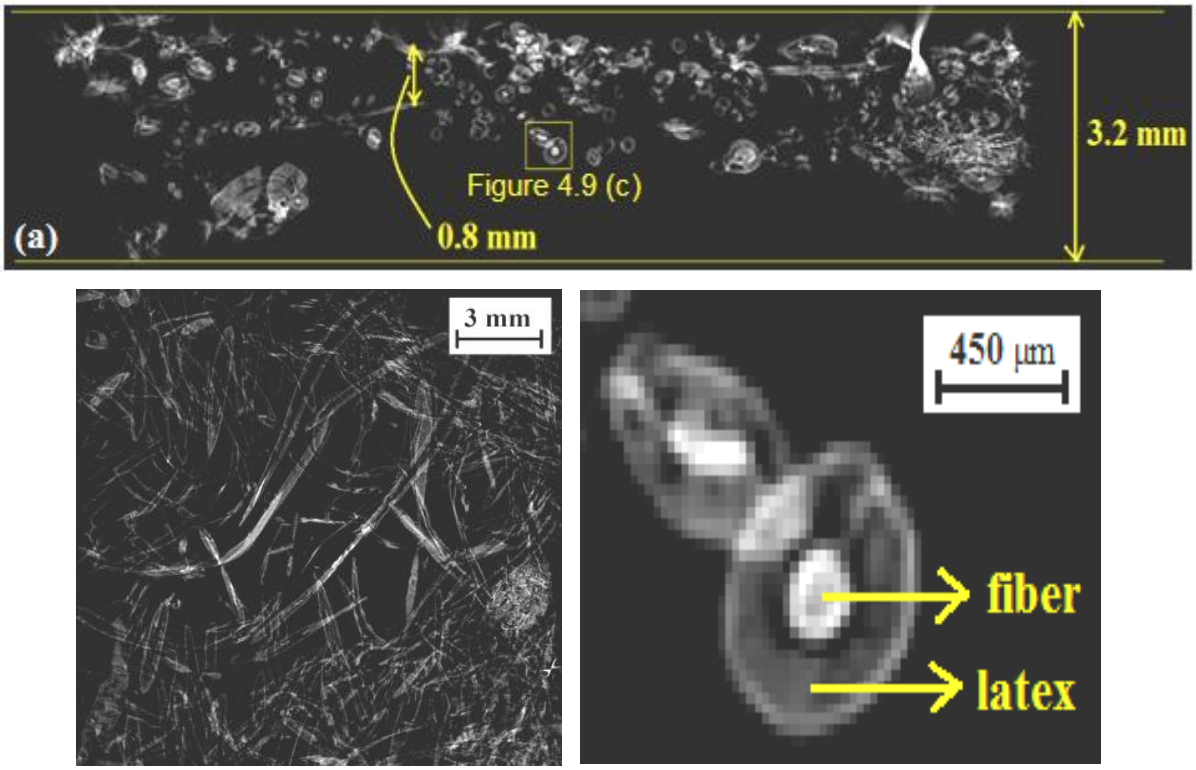

(b) (c)

Source: author.

Effective area of coconut fiber and coconut fiber mat

Figure 4.10 (a) shows the cross-section of coconut fiber captured by tomography. According to the difference of gray levels shown in Figure 4.10 (a), it is possible to visualize the regions occupied by fibers using the script created in MATLAB software and presented in last chapter.

Images with 81.75, 109, 136.25 and 163.5 gray levels related to the coconut fibers constituents of cross-section presented in Figure 4.10 (a) are shown in Figure 4.10 (b). Figure 4.10 (c) shows the corresponding quantity of each pixel's gray level presented in Figure 4.10 (a). According to Figure 4.10 (b), it is possible to report that coconut fiber constituents are

better represented by the range of gray levels from 81.75 to 109. However, the 136.25 and 163.5 levels also have significant points. Figure 4.10 (c) shows the image has gray level up to 200, with greater representation level up to 100.

The script implemented in MATLAB also determined the surface fraction of gray levels (Figure 4.10 (d)) and reported a significant area not occupied by the fiber. Around the fiber shown in Figure 4.10 (a), it is also possible to observe some pixels with similar gray levels to those inside the fiber and, therefore, the filters used in this script may have excluded pixels related to the fiber, resulting in an uncertain analysis. Thus, this analysis is qualitative and it make difficult to accurately quantify the area occupied by the fiber constituents or their empty area, because it represents the fiber constituents, voids and external region in the same filter.

Figure 4.10. (a) Cross-section of coconut fiber by tomography, (b) images in four gray levels, (c) quantity of pixels for each gray level and (d) surface fraction of the gray levels.

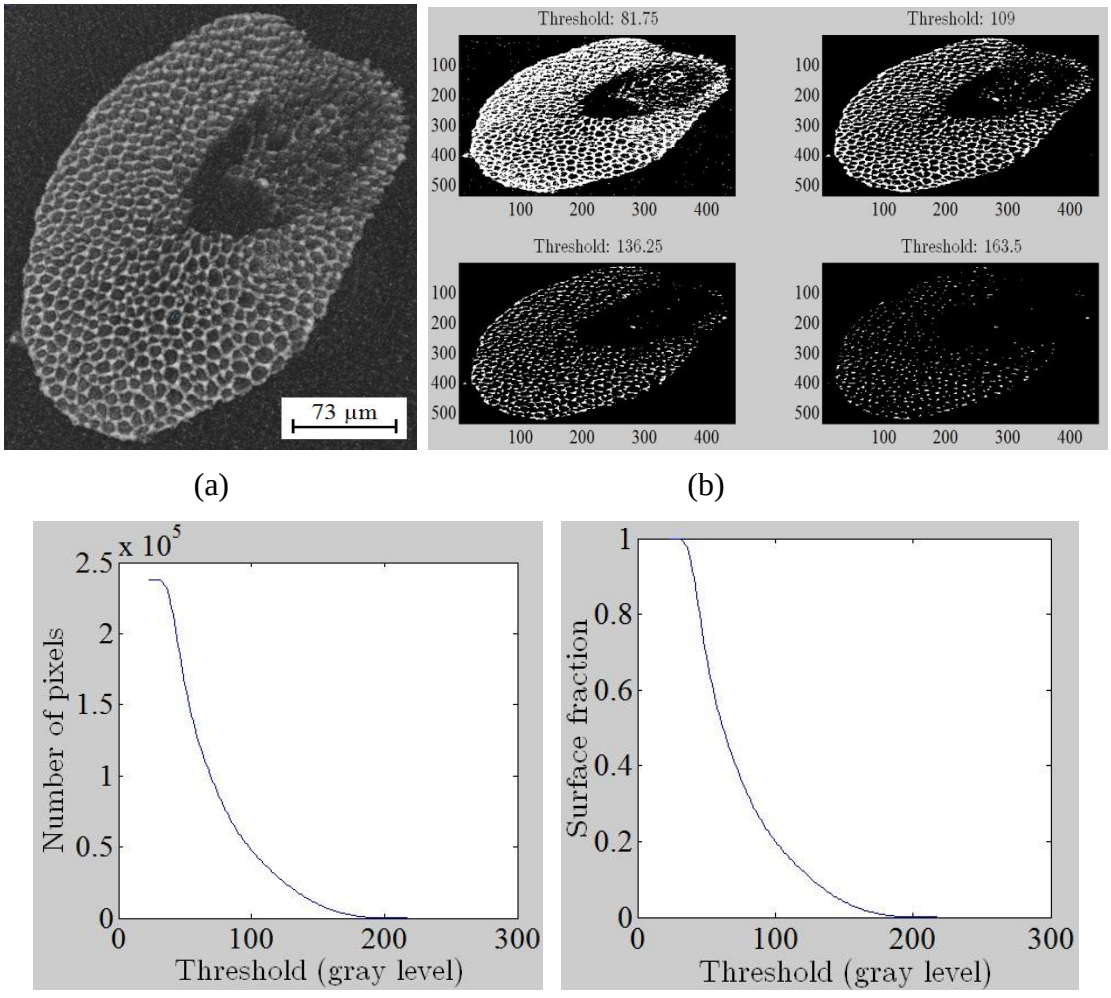

Source: author.

The same evaluation procedure to determine the representative pixels of cross-section of coconut fiber and the same script created in MATLAB software were also used in the longitudinal section (Figure 4.11 (a)). The longitudinal section shows the lumen along its length. Images with 95.625, 127.5, 191.25 and 159.375 gray levels of the Figure 4.11 (a) are shown in Figure 4.11 (b). Figure 4.11 (c) shows the corresponding quantity of each pixels gray level presented in Figure 4.11 (a).

Figure 4.11. (a) Longitudinal section of coconut fiber by tomography, (b) images in four gray levels, (c) quantity of pixels for each gray level and (d) surface fraction of the gray levels.

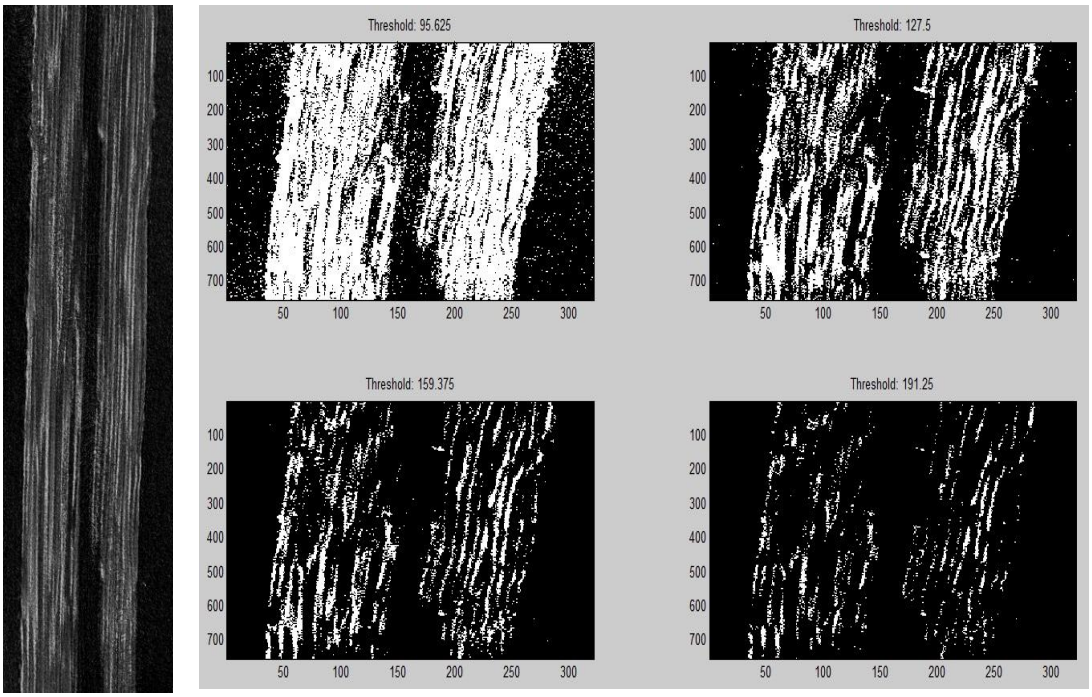

(a) (b)

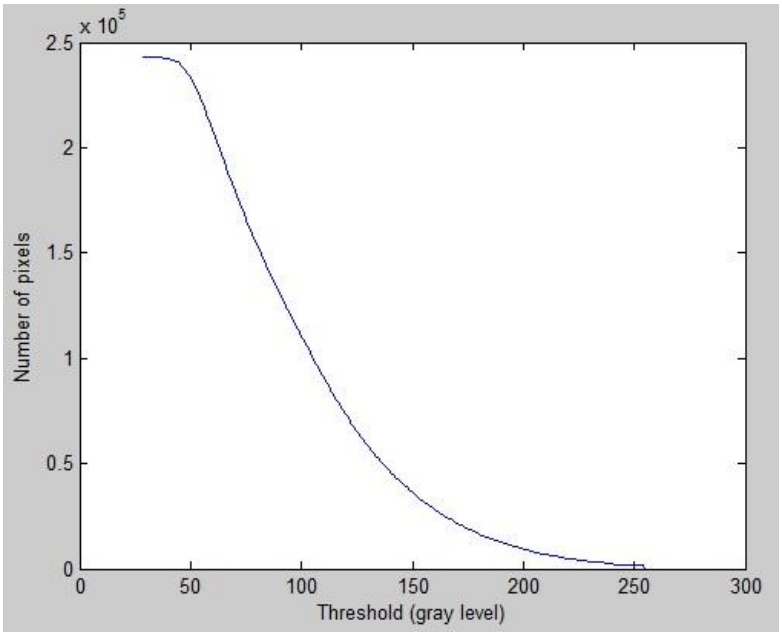

(c)

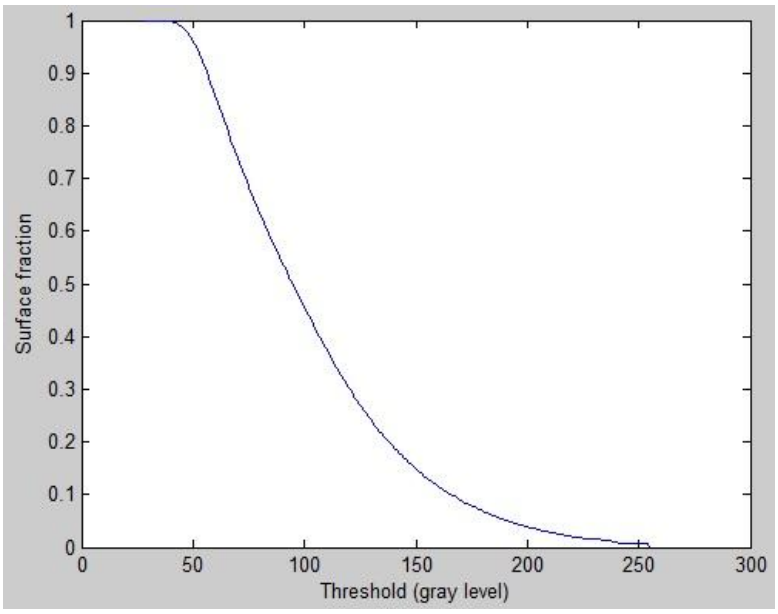

(d)

Source: author.

According to Figure 4.11 (b), it is possible to report that all levels presented above (95.625, 127.5, 159.375 and 191.25) have coconut fiber constituents, with a predominance of the first two. Figure 4.11 (c) shows the image's gray level up to 250, with greater representation up to level 100. This script determined a surface fraction of each gray level (Figure 4.11 (d)). Also, in similarity to the analysis of the cross-section, it was possible to visualize pixels with similar gray levels inside and outside the fiber longitudinal section shown in Figure 4.11 (a). In addition, the filters used in this study may have excluded some

coconut fiber constituents, suggesting that this analysis has uncertainties unable to be determined.

Therefore, similar to the analysis of the cross section, this analysis is qualitative and it is difficult to quantify accurately the area occupied by the fiber constituents or their empty areas, because it represented the fiber constituents, voids and outer region in the same filter.

Using the ImageJ software for image processing on the Figure 4.10 (a), adjusting it as binary image (only black and white elements) to better show the pixels containing the representative constituent fiber and making the manual contour line about it (red line in Figure 4.12 (a)) in order to determine the effective area only the components within the fiber, it has been found a minimum and maximum values of 39.6 and 43.3%, respectively, after five measurements at each 1 mm length. The presented error in this Figure is related to standard deviation found in the manual measurements during the outline path. In this case, the ImageJ software provided a mean value of 0.037 mm² to the total contour area and hence the cross section effective area was 0.016 mm². Fidelis et al. (2013) used a technique similar to the contour and it found a value of 0.052 mm² and standard deviation of 0.030 mm² for total contour area of coconut fiber.

Using this methodology on the cross-section of coconut fiber studied by Fidelis et al. (2013), it was found an effective area of 56.8%, a higher value due to the smaller size of its lumen. The effective areas of other vegetable fibers studied by Fidelis et al. (2013), such as curaua, jute and sisal, are higher than the coconut fiber: 95, 75 and 75%, respectively.

Figure 4.12. Determination of total and effective areas of transverse section of coconut fiber by ImageJ software: (a) contour line and (b) variation of effective area along the length.

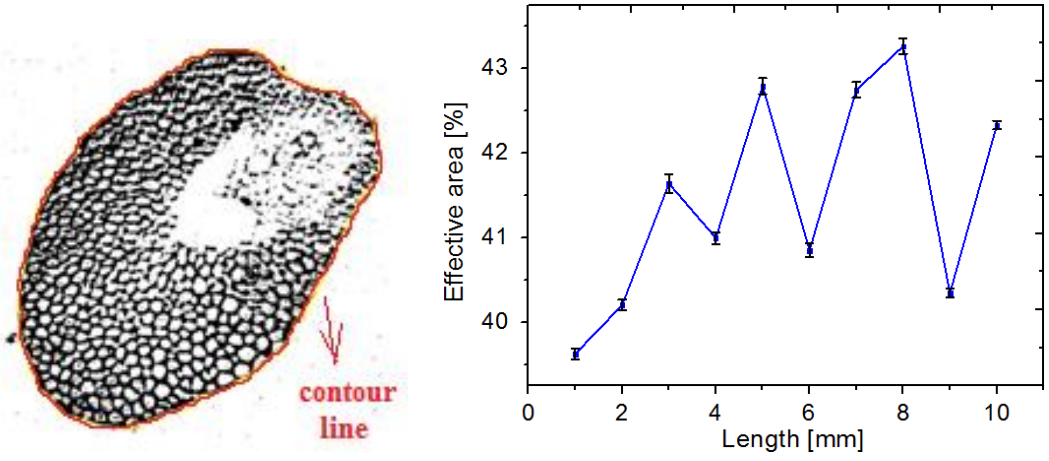

(a) (b)

Source: author.

Similarly, the effective area was also determined inside and outside the lumen along the longitudinal section of coconut fiber, because this region may influence the amount of its effective area. After five manual measurements in ImageJ software for each condition, the value of 42.72% (standard deviation of 0.07%) and 44.37% (standard deviation of 0.09%) were found for the effective area inside and outside the lumen, respectively. According to presented and expected results, there was a slight reduction in the effective area of the longitudinal section of coconut fiber with lumen. The effective areas of the transverse and longitudinal section with the lumen showed approximation, since that two areas contained lumen in their outlines.

Transforming the Figure 4.9 (a) in binary image to determine the effective area of the thickness of coconut fibers mat, a value of 8.4% was found. In this binary processing, pixels of latex were not included and this value represents just the area occupied by fibers. An effective area of approximately 93.8% occupancy of fibers was found after all front views or slices such the Figure 4.13 (a) were analyzed. The same value was found after measurement of the effective area occupied by the Figure 4.13 (b).

Figure 4.13. Effective area of coconut fiber mat: (a) slice from TXT and (b) digital image.

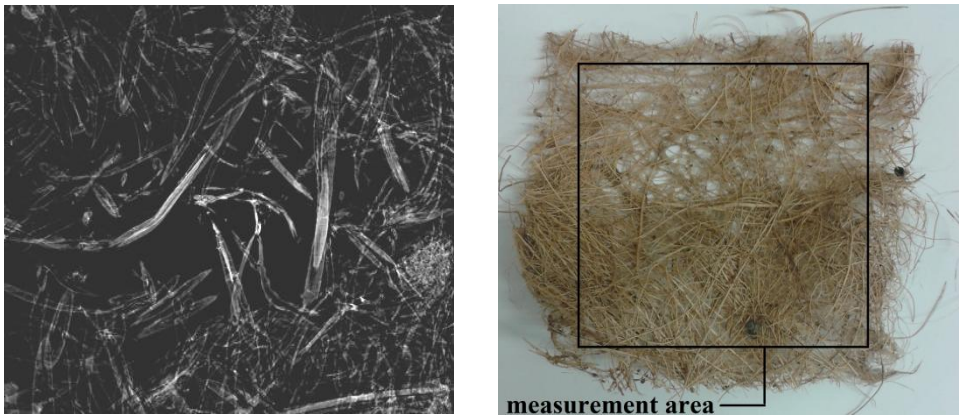

(a) (b)

Source: author.

4.2. In-situ tensile testing of coconut fibers

The stress values for the fibers were determined by $\sigma = F/A$, where F is the force resisted by the fiber, $A = \pi\phi^2/4$ and ϕ is the fiber diameter. The fiber diameter refers to the average of five measurements taken in diameter prior to the tensile test and measured along the length of each fiber. This procedure was performed on the SEM. Even though the

diameter of the coconut fiber may not be perfectly circular and presenting an elliptical shape, the measurement performed along its length have a strong correlation with the actual diameter or effective area of the fiber, as discussed in the previous chapter and referenced by Motta & Agopyan (2007). Furthermore, the morphology of coconut fibers presents various internal inhomogeneities.

Figure 4.14 presents four stress-strain curves for four different diameters in the untreated conditions, ranging from 254 to 393 µm.

Figure 4.14. (a) Stress-strain curves of untreated coconut fibers in different diameters and (b) onset of this curve.

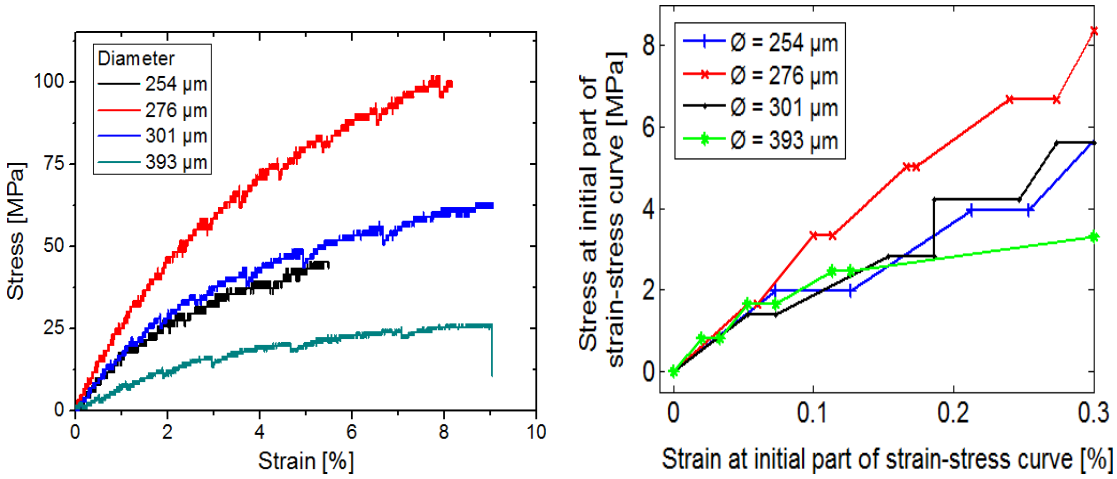

(a) (b)

Figure 6.15 (b) shows the start of the stress-strain curve and its tangent in which nonlinearities presented are related to the uncertainty of the measurement equipment conducting the test and the nature of lignocellulosic fibers' chemical bonds, and therefore, the modulus of elasticity will be called the initial modulus in this study. The uncertainty in this region is in agreement with other studies of Brazilian coconut fibers. Thus, the elastic modulus of elasticity shows dispersed values (Satyanarayana et al., 2007; Tomczak, 2010)

Through the stress-strain curve, it was determined the initial modulus of the fibers from the initial part of this curve. The tensile strength was determined as the maximum stress resisted by the fiber, and its strain associated was named failure strain. According to the curves above, the diameters of coconut fibers influenced significantly its mechanical behavior. This influence is better shown in Figure 4.15.

Figure 4.15. Diameter influence on the mechanical properties of coconut fibers under the conditions evaluated: as received, dried, treated by NaOH and treated by NaOH and dried.

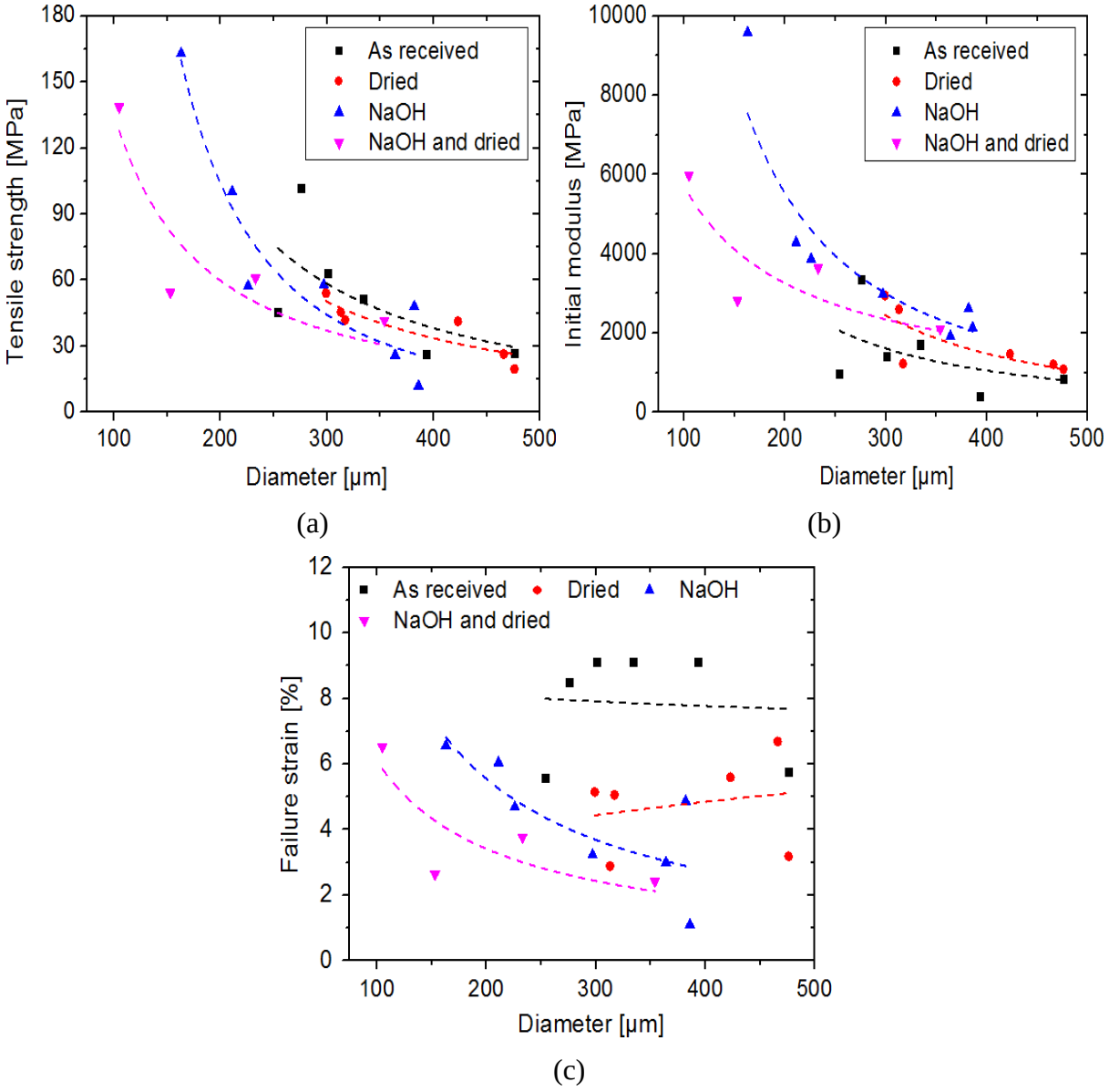

Source: author.

According to Figure 4.15, the initial modulus and tensile strength showed a decrease with increasing coconut fiber diameter, evaluating all four conditions. This behavior was observed in studies on coconut fibers of Tomczak (2010) and Fernandes et al. (2013), as well as others natural fibers such as pineapple (Kulkarni et al., 1983) and flax (Anderson et al. Baly 2005 and 2002). However, for the coconut fiber from India, the observed behavior is the opposite of this study (Kulkarni et al., 1983).

Despite this influence, it can be reported that from 300 mm in diameter the tensile strength and initial modulus converged to more stable values in the order of 20 to 60 MPa and

1 to 3 GPa, respectively. The values of failure strain showed slight variation with the diameter. The fiber diameter influence on the fiber mechanical behavior can be explained in terms of structural fiber properties. With the increased diameter, there are variations in the number of constituent cells, altering other structural parameters, such as helicoidal angle, volume and number of cells constituting defects. All of these factors decrease the mechanical properties of natural fibers (decreasing of modulus of elasticity and tensile strength) (Tomczak, 2010).

Figure 4.16 compares the tensile strength, initial modulus and failure strain on the four conditions of coconut fibers and also presents these three mechanical properties divided by its diameter, in order to evidence the fiber conditions.

Figure 4.16. Influence of fiber conditions on mechanical properties: tensile strength (TS), initial modulus (IM) and failure strain (FS); Ø = diameter.

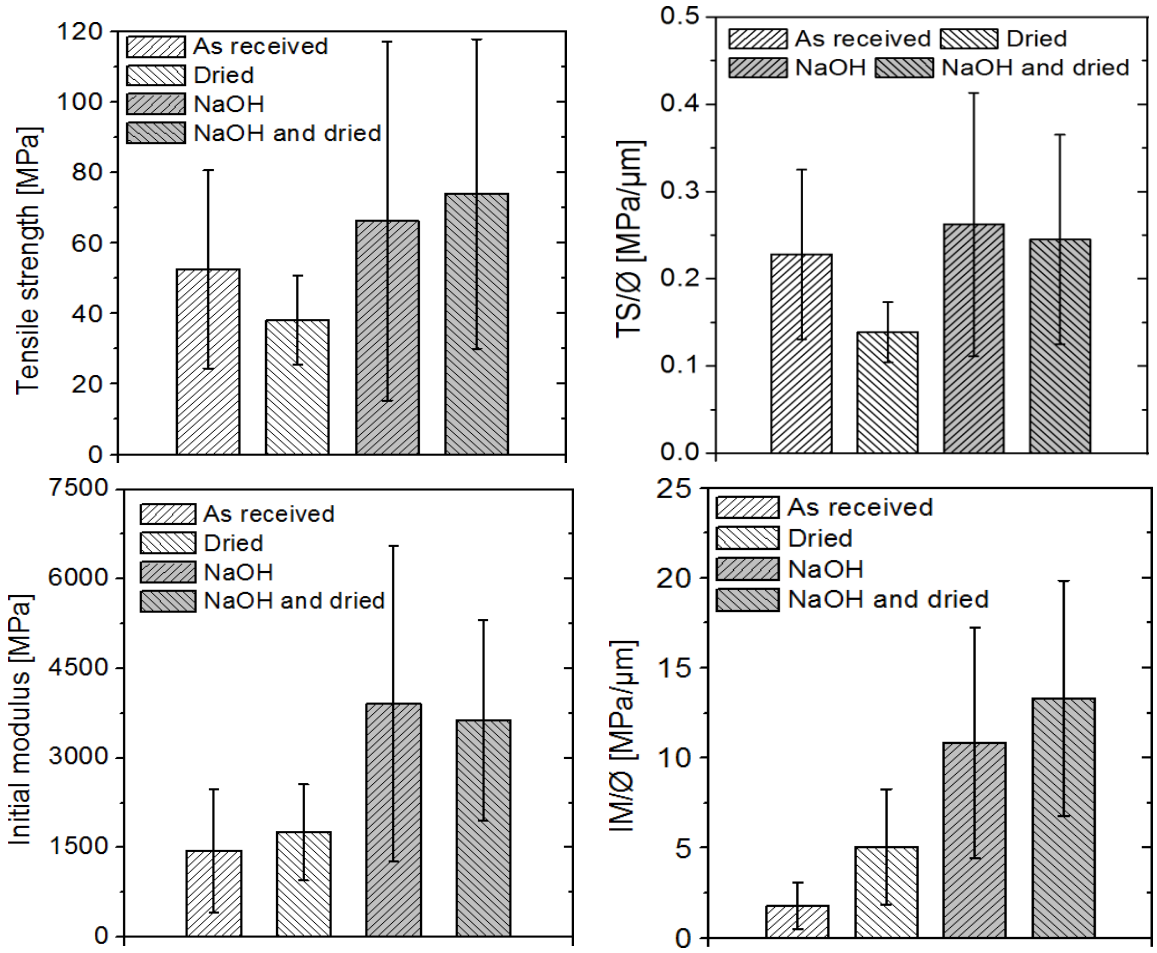

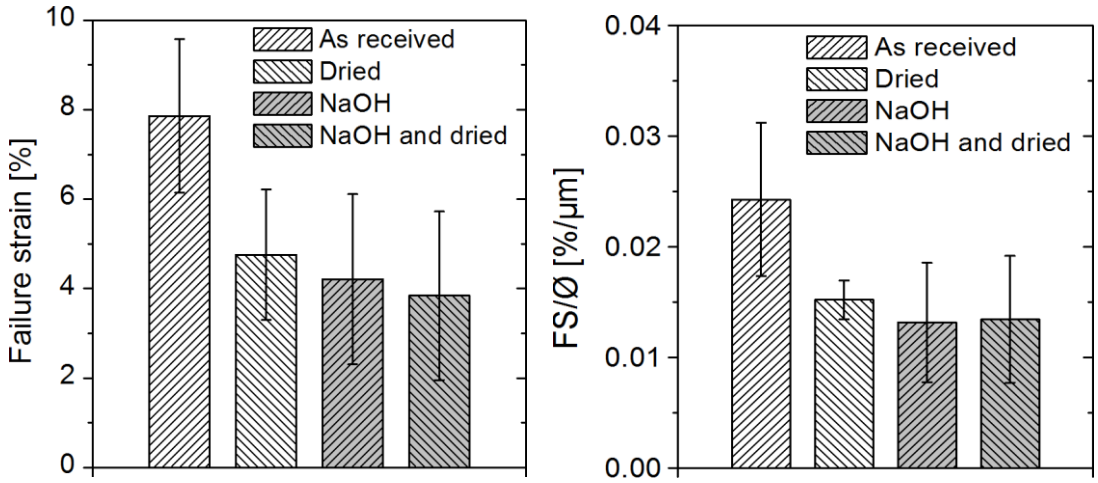

Source: author.

According to Figure 4.16, the chemical treatment by NaOH resulted in an increase in tensile strength and initial modulus, in terms of average values, although inversely influenced the deformation of rupture. This behavior suggests that the chemically treated surface used in this study increased the stiffness of the fibers. 'As received' and dried conditions presented similar mechanical properties. The high values of standard deviation were caused by morphological changes, chemical bonds strength and content variation in each coconut fiber of cellulose, hemicellulose and lignin.

The mechanical behavior of sisal fiber, another vegetable fiber, after being chemically treated with caustic soda was evaluated by some authors (Mwaikambo et al., 2006; Rong et al., 2001). The modulus of elasticity and tensile strength increased with concentration up to 0.16 wt% NaOH. After this value, there was a reduction in these properties, being associated with the degradation of crystalline cellulose.

Several authors have investigated the tensile behavior of natural fibers. There are large discrepancies among values reported for tensile strength and Young's modulus in the literature. As natural fibers generally present variable and irregular cross-sections, their measurement can lead to huge errors in the computation of stress. The gage length, strain rate, gripping, resolution of load cell and actuator precision can also play an important role in the final results. Finally, the methodology for measuring the modulus of elasticity is of great importance as the compliance of the machine should be taken into account (Fidelis et al., 2013).

Other tensile testing parameters, such as distance between the grips and displacement rate of testing, may influence on the natural fibers mechanical behavior (Tomczak et al. 2007). In a similar way to the influence of the diameter, the decrease in tensile strength and

failure strain with increasing length of the test fiber may be understood in terms of increase the number of defects in these fibers. On the other hand, the increase in modulus of elasticity with the increase of length between the grips may be associated to an increase in lignin content, obtaining, thereby, a fiber with higher initial resistance to applied stress or stiffness. This condition, however, results in lower failure strains (Kulkarni et al., 1981, 1983; Mukherjee & Satyanarayana, 1984, 1986; Satyanarayana et al., 1986).

Table 4.2 shows the influence of displacement rate on the tensile strength of fibers in the condition as received for a distance of 15 mm between the grips, the same adopted in this study. The increase in tensile strength and elongation at break with increasing displacement rate may be explained in terms of the viscoelastic behavior of lignocellulosic fibers, such as coconut fiber. They behave as an elastic material when are subjected to mechanical loading at higher displacement rates. In this case, the crystalline region is subjected to most of the applied stress (Mukherjee & Satyanarayana, 1984). This results in increasing of tensile strength and modulus of elasticity. However, the fiber behaves as a viscous fluid at low loading rates and, hence, the force application is distributed mainly by the amorphous region, resulting in lower stiffness. The initial modulus (particular denomination for modulus of elasticity) is less sensitive to loading rate variations when compared to the tensile strength and failure strain (Satyanarayana and Mukherjee, 1984).

Table 4.2. Influence of displacement rate on mechanical properties of untreated coconut fibers for a distance of 15 mm between the grips.

Reference	Displacement rate [mm/min]	Tensile strength [MPa]	Initial modulus [MPa]	Failure strain [%]
Present study	0.06	52.55 ± 28.10	1450.35 ± 1030.9	7.86 ± 1.72
Motta & Agopyan, 2007	2	105.97 ± 33.53	1900 ± 500	32 ± 11
Tomczak, 2010	5	152.70 ± 38.13	2199.3 ± 553.3	38.12 ± 12.01
Kulkarni et al., 1981	25	267.57 ± 50	not reported	11.5

Source: author.

Modifications in diameters of coconut fibers after tensile testing were observed by SEM micrographs. Regions close to fracture were analysed in order to provide the diametral variation measurements. In this case of Figure 4.17, the fiber began with 476 µm in diameter (Figure 4.17 (a)) and ended with 462 µm (Figure 4.17 (b)), representing a diametric

deformation of 2.94%. The diametric deformations were calculated by Equation 3.1, as presented previously.

Figure 4.17 (c) associates the diametric deformation with the initial diameter of 11 untreated coconut fibers chosen randomly. It can be observed a tendency of less diametric deformation on fibers with larger diameters. This result can be expected, since the same decrease in diameter would have a smaller impact for larger diameters, according to the equation used in this evaluation.

Figure 4.17. Diametric variation: (a) before and (b) after tensile test, (c) in function of the initial diameter.

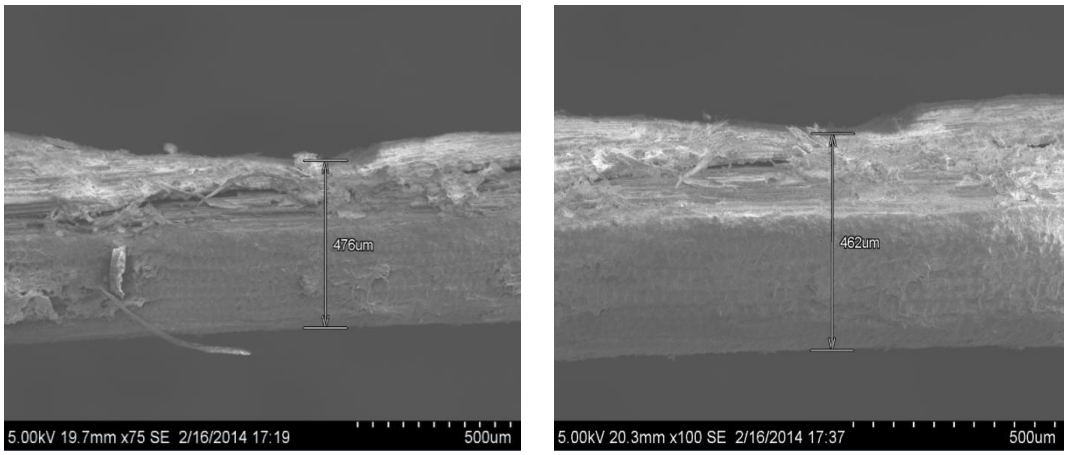

(a) (b)

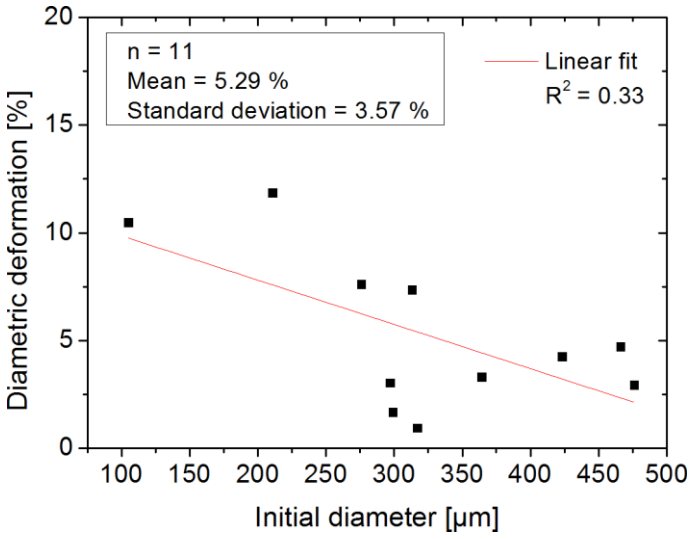

(c)

Source: author.

A micrograph rupture of coconut fiber is presented in Figure 4.18, which is presented in a ductile form and with microfibrils traces exposed. This behavior is usually observed in fibers with strain at break exceeding 4%. As is usual in lignocellulosic fibers, the rupture region is formed by numerous fibrils which must be individually broken until the final separation (Tomczak, 2007; Monteiro et al., 2006). The fracture occurred in the perpendicular direction to the tensile test direction.

Figure 4.18. Fiber rupture: (a) 150 x and (b) 420x.

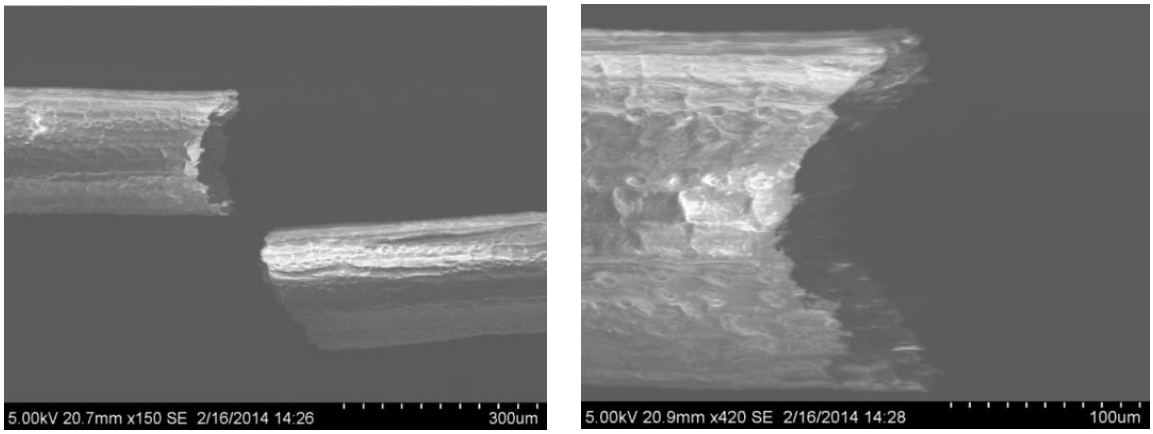

(a) (b)

Source: author.

The DIC technique monitored pixels relative to the material on its non-deformed condition and associated these pixels in the images of the deformed material to present the deformation fields into the region of interest during the tensile test. In Figure 4.19 it is possible to observe the displacement and strain fields obtained after processing the images in Correli[Q4] in *x* (test or longitudinal) direction and *y* (perpendicular to the test or transversal) direction. For all processes, the purple color represents the area with highest displacement of pixels and the red region of lower displacement. The procedure provided longitudinal (u_l) and transverse (u_t) displacements in pixels, as well as strains in both directions (ε_l and ε_t) in pixel/pixel.

A normal tensile stress is associated with an elongation in the test direction (positive strain) and contractions in the orthogonal directions (negative strain), which are proportional to elongation. Therefore, the deformed values are positive in x-axis and negative in y-axis. Through Figure 4.19 it can be observed that the line of highest pixels displacement is located orthogonal to the direction of the tensile test, in accordance to the actual fiber rupture previously presented. Therefore, the image correlation technique was able to present its

rupture mechanisms, predict the rupture process and provide its propagation before its occurrence (Dias et al., 2012). The longitudinal and transverse strains were random throughout the region analyzed.

Figure 4.19. Tensile testing on coconut fiber (280 µm in diameter) using the DIC technique. Instant A (30.86 MPa), instant B (37.35 MPa), instant C (40.60 MPa), instant D (50.34 MPa), instant E (64.96 MPa) and instant F (81.20 MPa).

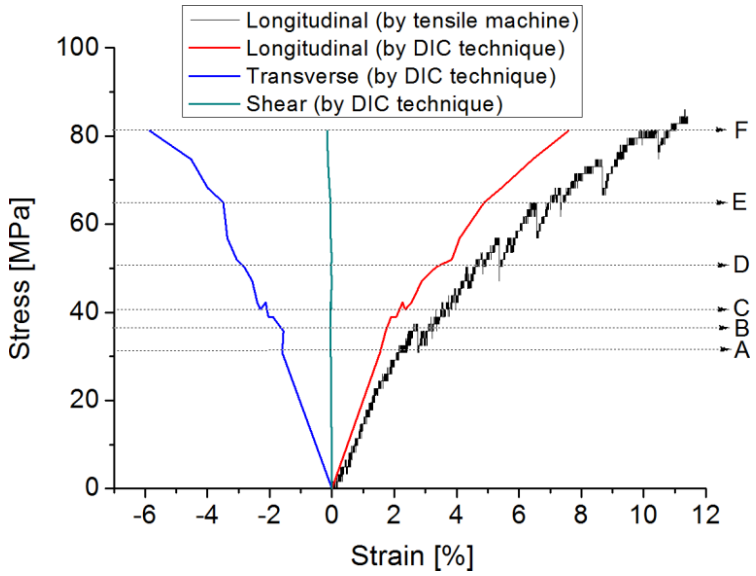

Instant	Strain [pixel/pixel]		Displacement [pixel]		Mesh displacement
	ε_l	ε_t	u_l	u_t	
A	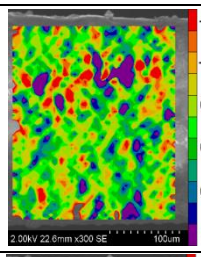	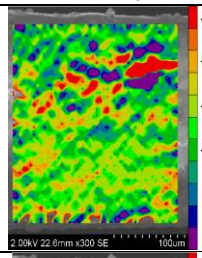	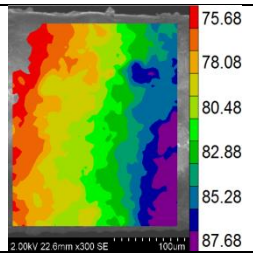	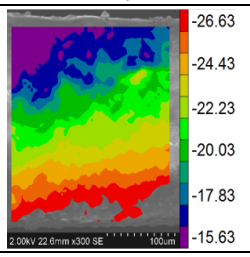	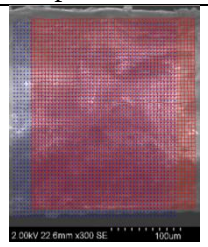
B	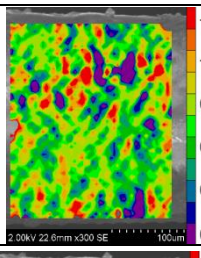	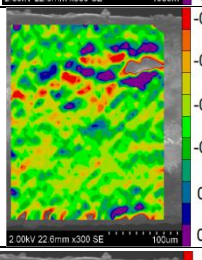	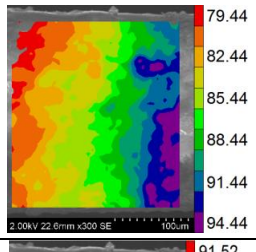	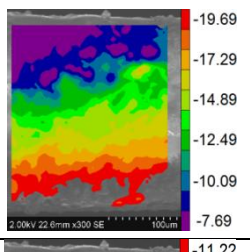	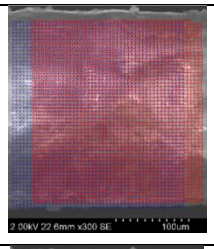
C	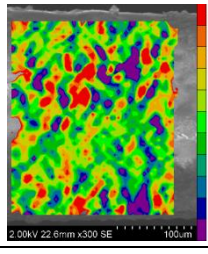	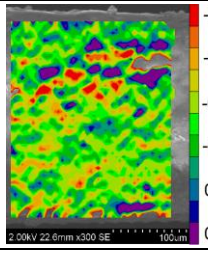	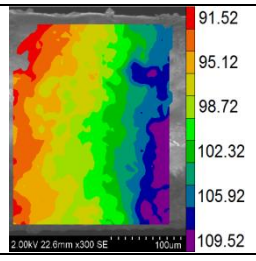	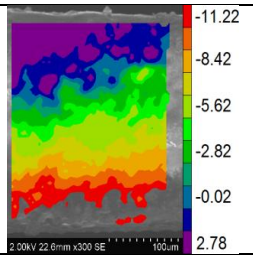	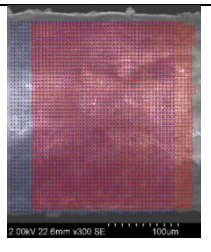

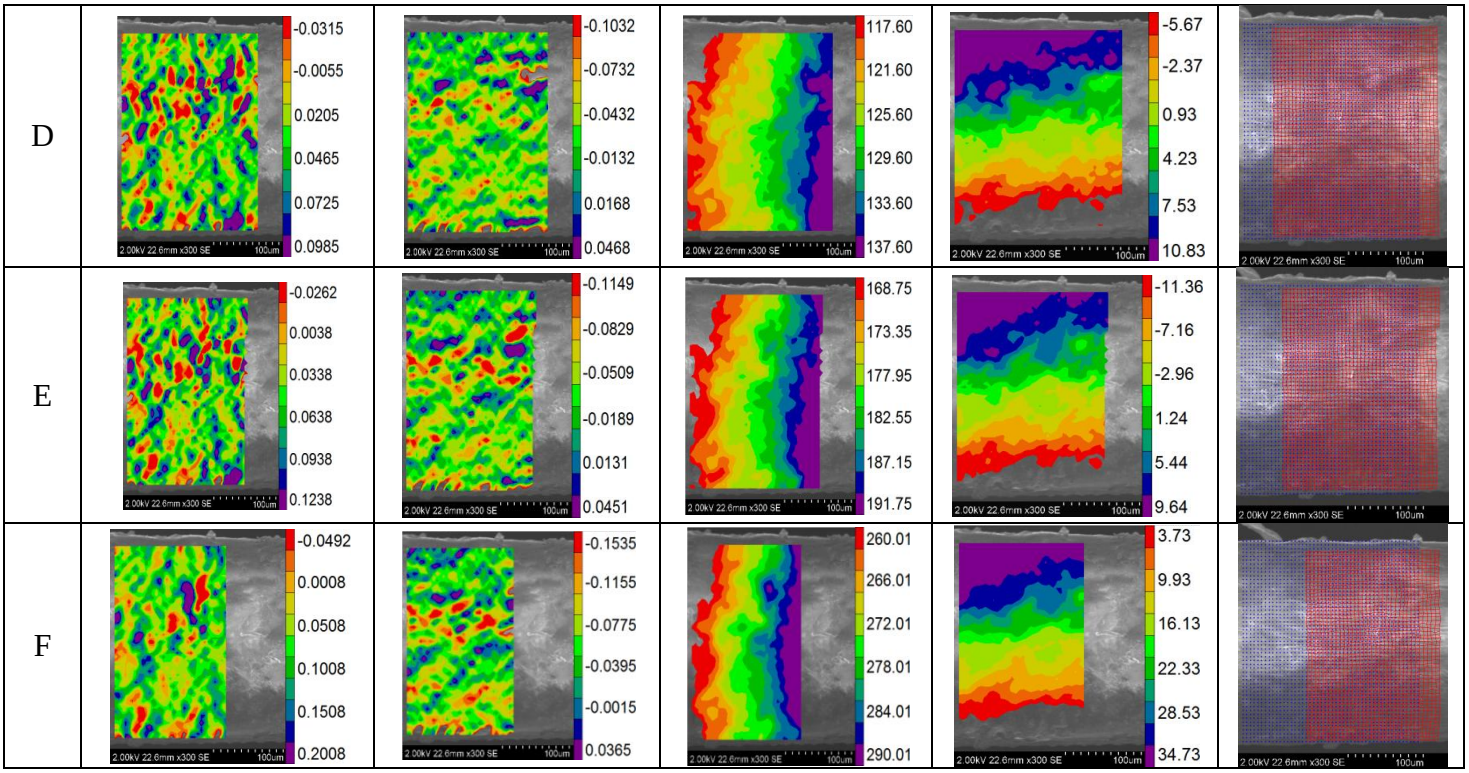

Source: author.

Correli[Q4] software developed in MATLAB provides also the images of mesh displacement within the region of interest during the course of the tensile test. The blue mesh represents the initial distribution of pixels (undeformed material) and red mesh is related to pixels displacement (deformed material). This method may inform the deformation mechanisms of the material in a global and quantitative manner.

Figure 4.20 shows mean strains in longitudinal and transverse directions as a function of the load in this test presented in images. Correli[Q4] software reported a measuring error of 0.03% for each mean strain.

According to Figure 4.20 (a), the longitudinal and transverse strains increase with the progress of the test. The longitudinal strain is higher in magnitude. The ratio of transverse and longitudinal strains in the elastic region at the same instant of time and the same region is denominated Poisson's ratio. Figure 4.20 (b) shows the values of this ratio along the tensile test on coconut fiber. However, as presented previously, the coconut fibers have not well-defined elastic regions and, therefore, it is not possible to report that this ratio is Poisson's ratio. The average of this ratio among the strains was 0.78 (standard deviation 0.08). Isotropic materials have Poisson's ratio between -1 and 0.5 (Furlani, 1995).

However, in accordance with morphological analysis of this study, coconut fibers have several voids in longitudinal direction and consequently have different properties in this

direction, suggesting that this fiber is not isotropic. The value of 0.78 is closer to the ratio of other vegetal material, such as the wood Guapuruvu, which has a Poisson's ratio of 0.62 (Macia & Nicolas, 2013). The voids in longitudinal direction found imply in decreasing of stiffness in this direction, resulting in larger contraction in this region and, consequently, increases the ratio between these strains when compared to an isotropic material. The Poisson's ratio is directly proportional to the transverse strain (Equation 2.28).

Figure 4.20. (a) Mean strain at longitudinal and transverse directions during the tensile test in coconut fiber and (b) ratio between the strains.

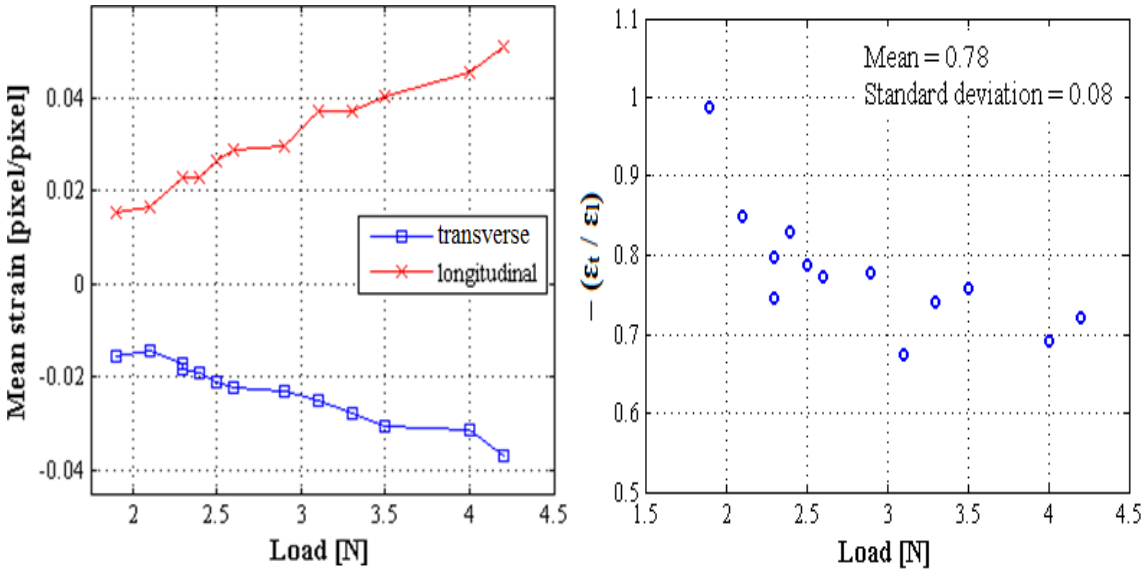

(a) (b)

Source: author.

4.3. Tensile testing on coconut fibers mat

The mechanical behavior of coconut fiber mat was characterized from its nominal stress (force per unit width) versus strain, according to EN ISO 10319:2008. The width was considered constant during the test hence the nominal stress of engineering was used; engineering strains were also used. Figure 4.21 shows a nominal stress-strain curve for the 20 x 10 mm² geometry specimen and another curve for the 40 x 20 mm² geometry. Ten specimens were tested for each dimension.

Even with significant dispersion inherent to the heterogeneous microstructure of mats, all curves showed a similar behavior as shown in Figure 4.21. The nominal stress increased linearly until the onset of breaking of several coconut fibers present in the specimen. In all

tests, a maximum value for this nominal stress was found, which corresponds to the onset of damage associated with a particular strain of each test and where the fibers, preferentially oriented in the test direction, starts to break. Other subsequent events of rupture or nominal stress peaks present are related to fibers that were not perfectly aligned in the test direction before it began, but were subjected to the test efforts in chain until the final rupture of the mat specimen. Figure 4.22 (a) presents the image before the test starts.

Figure 4.21. Nominal stress versus deformation for two geometries of coconut fiber mat.

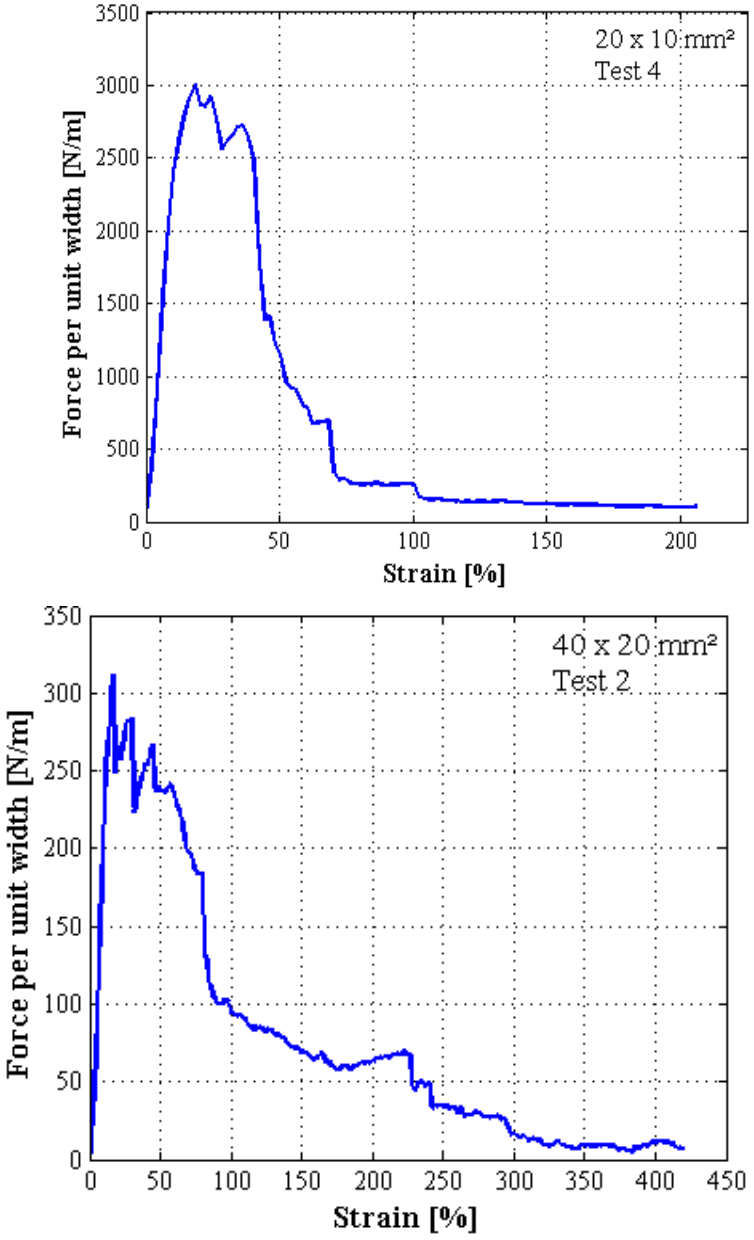

Source: author.

The mat macroscopic appearance at the moment of maximum nominal stress (27 seconds, 1083 N/m and 0.108%) showed some better aligned fibers in the test direction (Figures 4.22 (b-c)) and it was observed that the damage was due to sequenced fracture of the fibers (Figure 4.22 (d)). Figures 4.22 (c) (30 seconds, 655 N/m and 0.133%) and (d) (51 seconds, 82 N/m and 0.238%) detail the alignment and coconut fiber rupture, respectively, after the maximum nominal stress and the initial ruptures. After these initial ruptures, the stress transmission capacity of mat tension decreases abruptly, even though there are minor stress peaks during the test. The maximum nominal stress showed in Figure 4.22 (b) and the fiber rupture of Figure 4.22 (d) are possible to be displayed in the nominal stress-strain curve of the test mentioned, points 'a' and 'b' of Figure 4.23, respectively.

Figure 4.22. Coconut fiber mat images during tensile testing: (a) before tensile test, (b) maximum nominal stress (27 s, 1083 N/m and 0.108%), (c) aligned fiber (30 s, 655 N/m and 0.133%) and (d) ruptured fiber (51 s, 82 N/m and 0.238%).

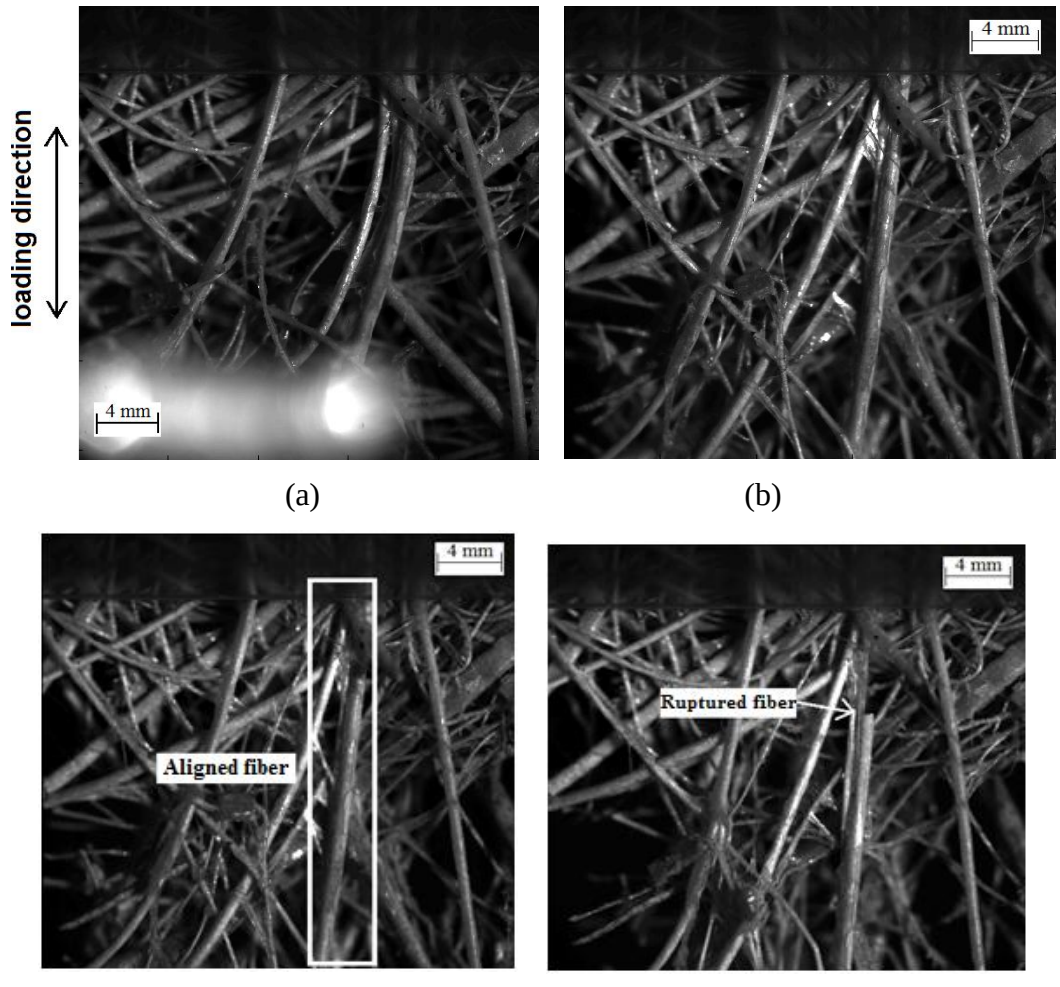

Source: author.

Figure 4.23. Nominal stress versus deformation curve for coconut fiber mat monitored by images.

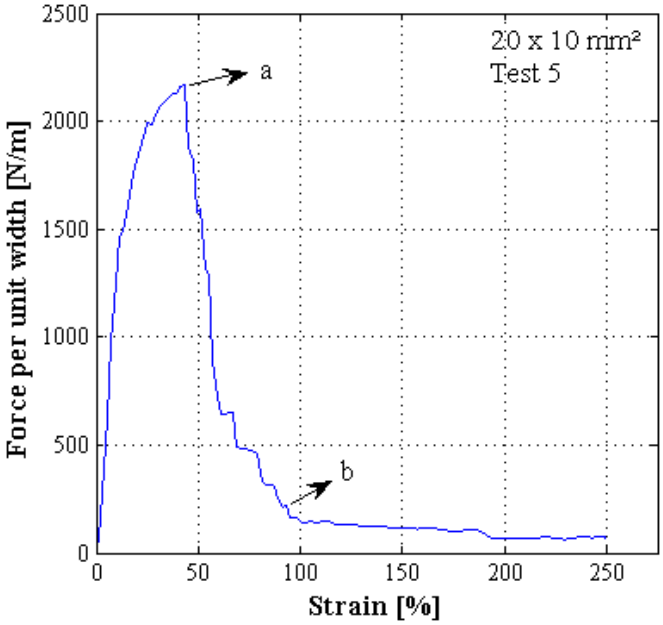

Source: author.

The extension of the nominal stress-strain curves, in terms of high values for strains, is the result arising from the damage onset occurs in different localizations and instants. This behavior increases the capacity of material energy absorption in comparison with the tensile tests on a single coconut fiber.

It was observed that the coconut fiber mats had weight changes in different areas, which led variations in their mechanical behavior. Figure 4.24 shows the nominal stress and strain as a function of the mass for 20 x 10 and 40 x 20 mm² geometry specimens. The average nominal stress and strain at break of the mats of smaller and larger geometries are 3315.9 N/m, 1593.7 N/m, 33.5% and 25.3%, respectively. The specimens with larger mass of fibers showed higher mechanical force for the two mat geometries and the random results for this property are shown in Figure 4.24. The mass did not influence the final strain at break results for the two geometries. The smaller geometry specimen showed higher nominal stress, since there are fewer discontinuities. This behavior corroborates the results of diameter influence on the mechanical properties of the coconut fibers.

Figure 4.24. Weight influence on the mechanical behavior for coconut fiber mat of 20 x 10 and 40 x 20 mm² geometries: (a) nominal stress and (b) final strain at break.

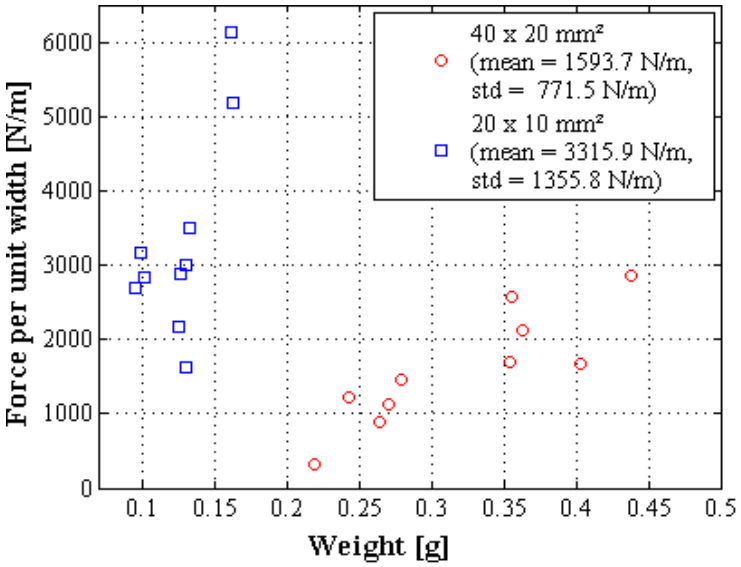

(a)

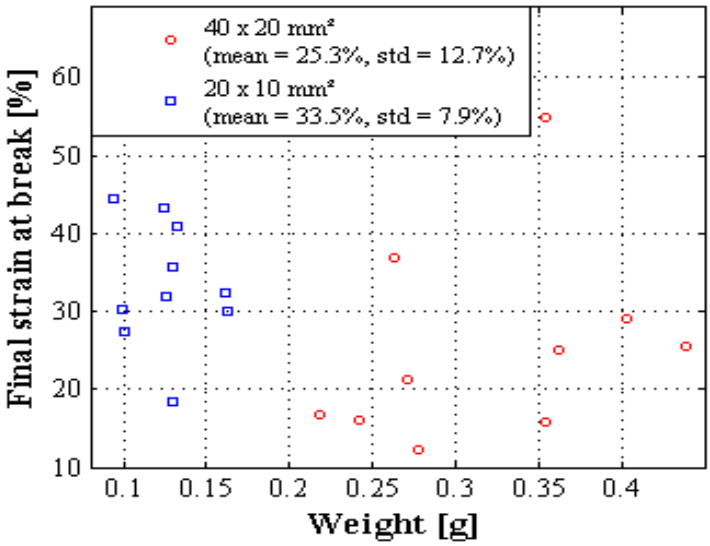

(b)

Source: author.

The DIC technique identified the displacements fields during the deformation process of the coconut fiber mat. In Figure 4.25, it was possible to observe the strain fields obtained after processing the images in Correli[Q4] in longitudinal (direction of the test, ε_l) and the transverse (perpendicular to the test, ε_t) directions for 20 x 10 mm² geometry. The purple color represents the area of greatest displacement of pixels and the red region of lower displacement inside of the region of interest.

Figure 4.25. Tensile testing on coconut fiber mat using DIC. Instant A (3 s; 5.55 %; 508.57 N/m), instant B (5 s; 9.70 %; 1018.07 N/m), instant C (18 s; 35.70 %; 1619.35 N/m), instant D (31 s; 61.64 %; 1162.85 N/m) and istant E (54 s; 107.66%; 281.51 N/m).

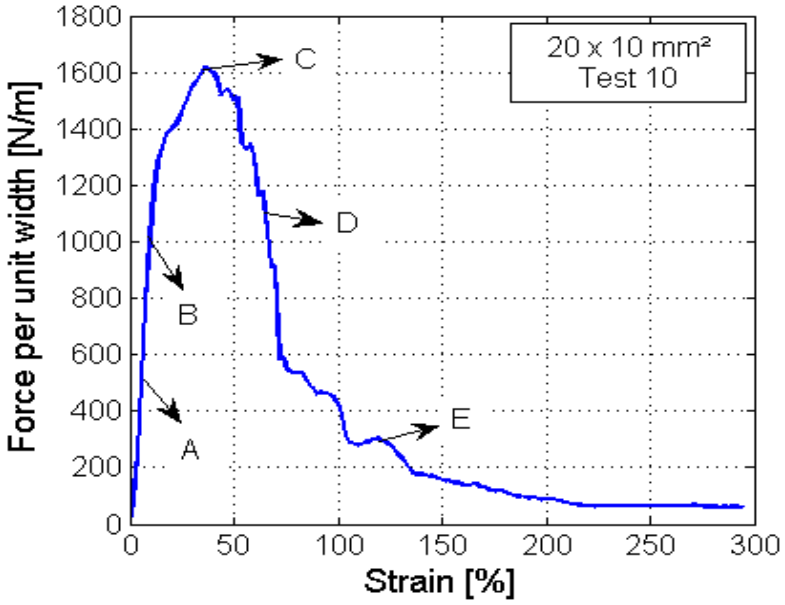

Instant	Strain [pixel/pixel]		Mesh displacement
	ε_l	ε_t	
A	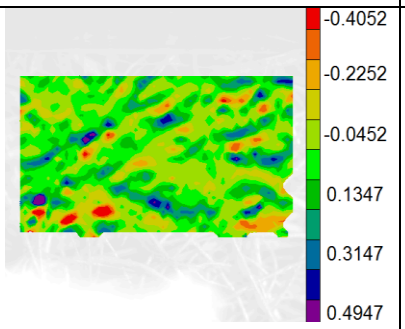	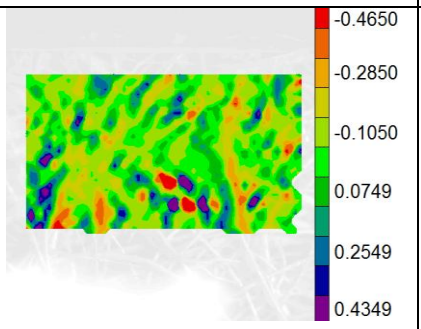	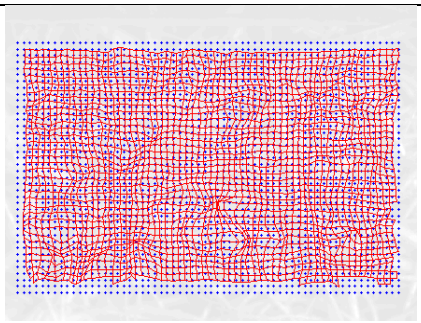
B	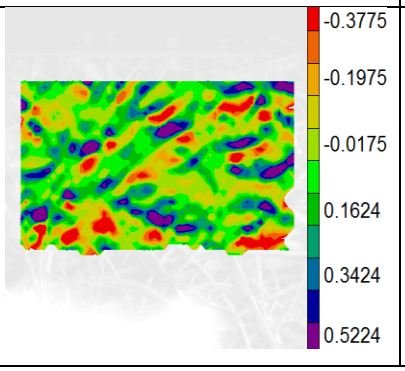	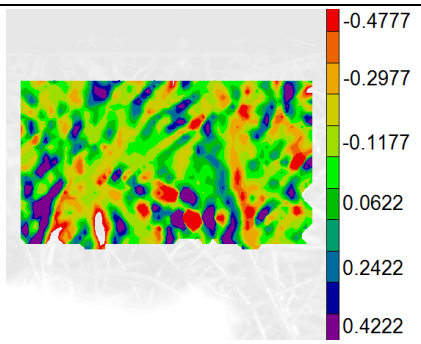	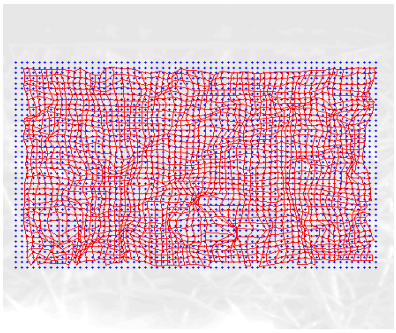

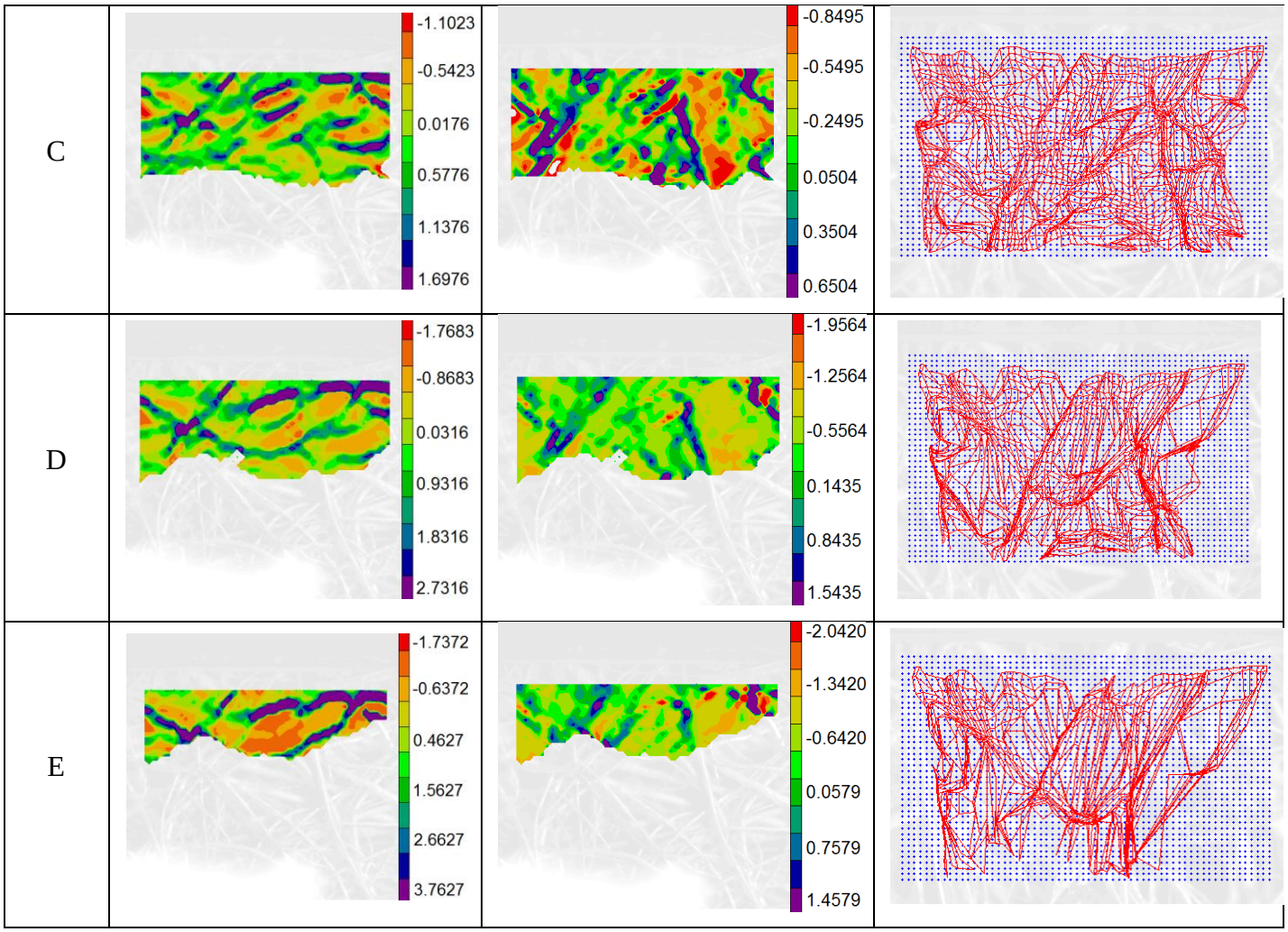

Source: author.

It can be possible to observe in Figure 4.25 that the strain regions and the mesh displacement are heterogeneously dispersed throughout the region of interest for the 20 x 10 mm² specimen geometry. A similar behavior was observed for the 40 x 20 mm² geometry. As reported previously, the longitudinal and transverse displacements values are positive and negative, respectively. The mean strains in the region of interest in the longitudinal and transverse directions in the elastic region of the tensile testing of mat were determined according to the procedure adopted in the coconut fibers. Figure 4.26 shows these strains during the loading on the mat in the two geometries. In this case, the software Correli[Q4] indicated a measuring error of 0.02% for each strain measurement.

According to Figure 4.26 (a), the longitudinal (ε_l) and transverse (ε_t) strains did not grow linearly as the test on mat. However, in accordance with this test, the longitudinal strain showed greater magnitude than the transverse strain. The ratios between the two strains in the elastic region were 0.35 (standard deviation of 0.02) and 0.37 (standard deviation of 0.13) for

the 20 x 10 mm² and 40 x 20 mm² geometries, respectively (Figure 4.26 (b)). The error of 0.02% presented by the Correli[Q4] software was more significant for the lower deformations of mat with higher geometry and thus the ratios between these strains were more dispersed. In loads lower than 40 N on the larger geometry of mat, the error values were higher than the mean values and therefore were not included in the measurements of this ratio calculation. However, the values found for this property are in the range of isotropic materials (-1 to 0.5), indicating from DIC, which the mat has multidirectional distribution of fibers and possess transverse isotropy in the plan presented.

A transversely isotropic material is one with physical properties which are symmetric about an axis that is normal to a plane of isotropy. This transverse plane has infinite planes of symmetry and thus, within this plane, the material properties are the same in all directions.

Figure 4.26. (a) Mean strains in the longitudinal and transverse directions during the tensile test on the mat in the elastic region and (b) ratio between the strains.

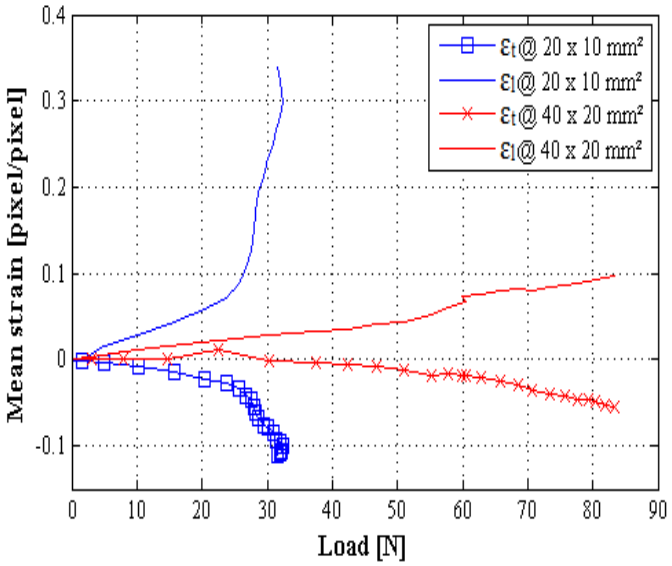

(a)

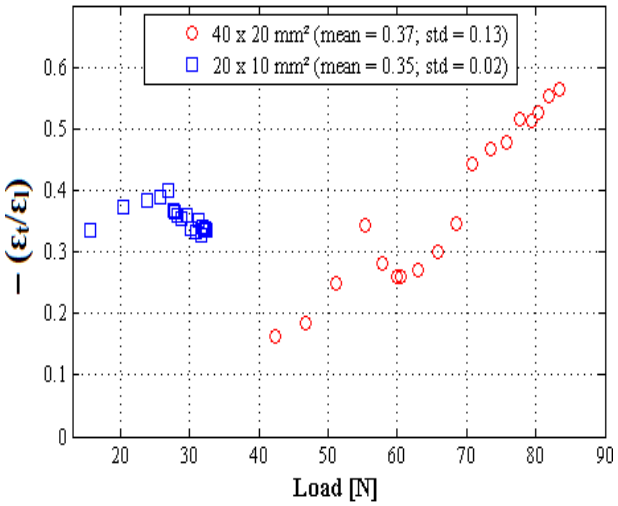

(b)

Source: author.

5. Morphological and mechanical behavior of the polypropylene

In this chapter, the results of morphological analysis on two conditions of polypropylene (virgin and recycled) are presented, in terms of impurities content, dimension of impurities, recycling and manufacturing influences on the morphological aspects.

Then this chapter shows the mechanical behavior of polymers through uniaxial mechanical tests followed by Digital Image Correlation techniques (DIC) and Digital Infrared Thermography (DIT). The DIC technique allowed analyzing the deformed and located regions on virgin polypropylene and thereby engineering stress-strain curves are plotted.

5.1. Morphological analysis of polypropylene

The morphologies of the virgin and recycled polypropylenes were characterized by X-rays tomography. Figure 5.1 presents a perspective view and a transverse section of virgin (Figure 5.1 (a)) and recycled (Figure 5.1 (b)) polypropylenes.

Some impurities identified by the gray levels were observed in both polymers. Aiming the calibration of the analysis of impurities quantities, some parameters were performed in the ImageJ software. The calibration parameters to identify and detect the impurities considered the presence of impurities in virgin polypropylene and the presence of discontinuities in recycled polypropylene as references. After six measurements in each direction (slices X, Y and Z), this software found 0.0419% and 2.1865% of impurities for PP and RPP, respectively. These results were extracted by the percentage of area occupied by red points presented in these Figures. 3D reconstructions show that the impurities (white points) are located along all directions of these polymers.

Discontinuities found in the RPP are located throughout the sample, as well as they present variable geometries and are independent of the injection direction. Impurities up to 1.93 mm (1930 μm) in length were found. However, impurities length between 50 and 350

µm were more present in the sample. The presence of these discontinuities may influence the mechanical behavior of this material.

Figure 5.1. Impurities on (a) PP and (b) RPP by X-ray tomography.

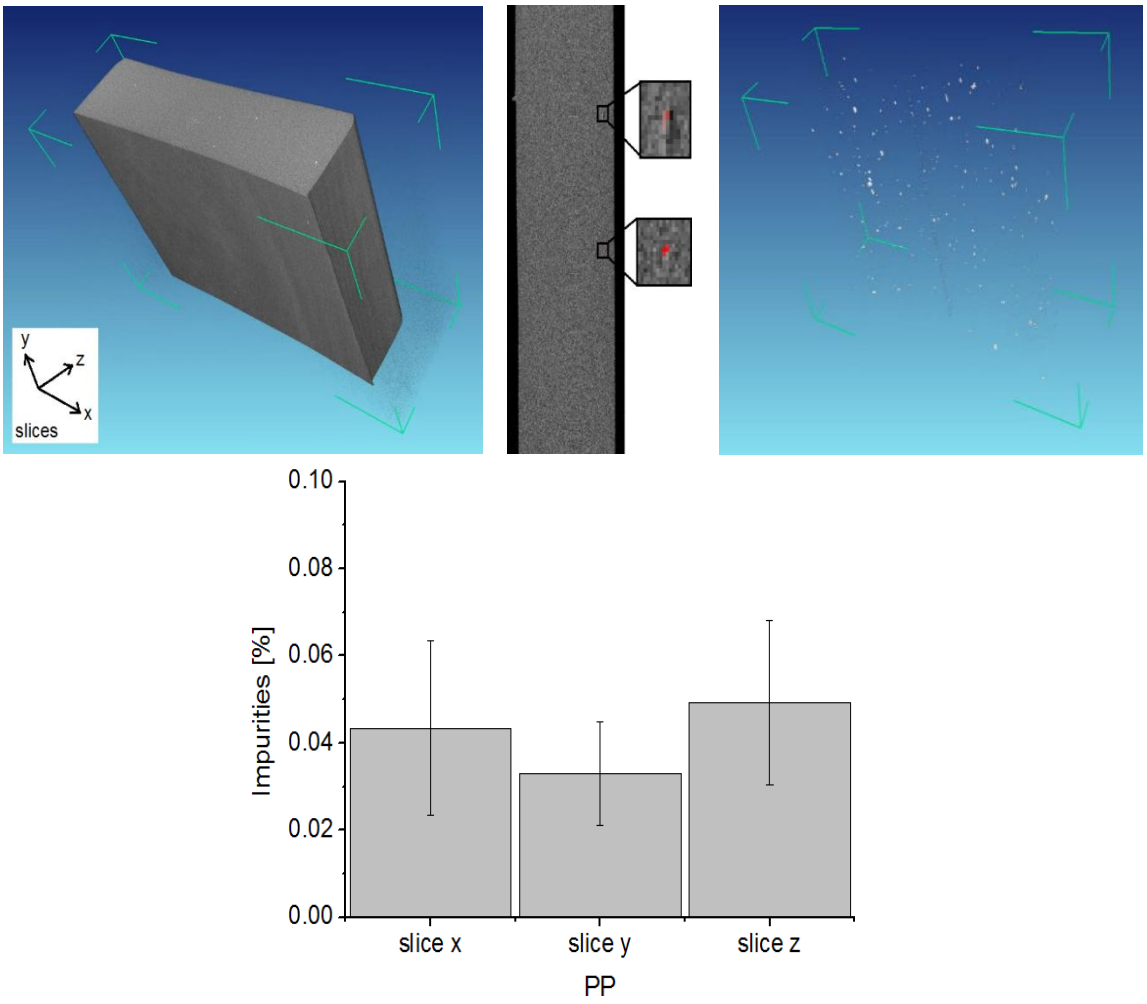

(a)

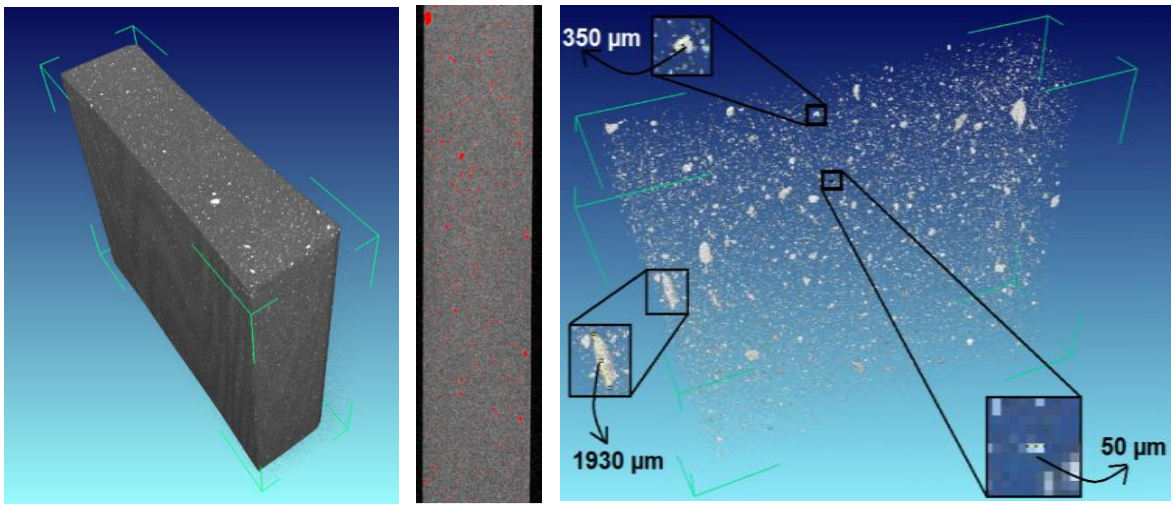

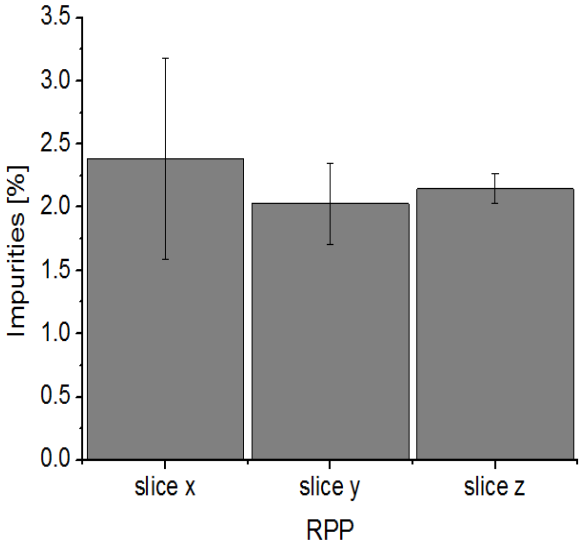

(b)

Source: author.

5.2. Tensile testing on polypropylene

Figures 5.2 (a-d) show the influence of the displacement rate (10, 15, 20, 25, 30 and 35 mm/min) on the mechanical behavior of virgin polypropylene according to the stress-strain curve, elastic modulus, tensile strength and strain at maximum stress. The tests were interrupted at approximately 100% strain.

Figure 5.2. The influence of the displacement rate (10, 15, 20, 25, 30 and 35 mm/min) on virgin polypropylene in the: (a) stress-strain curves, (b) modulus of elasticity, (c) tensile strength and (d) strain at maximum stress.

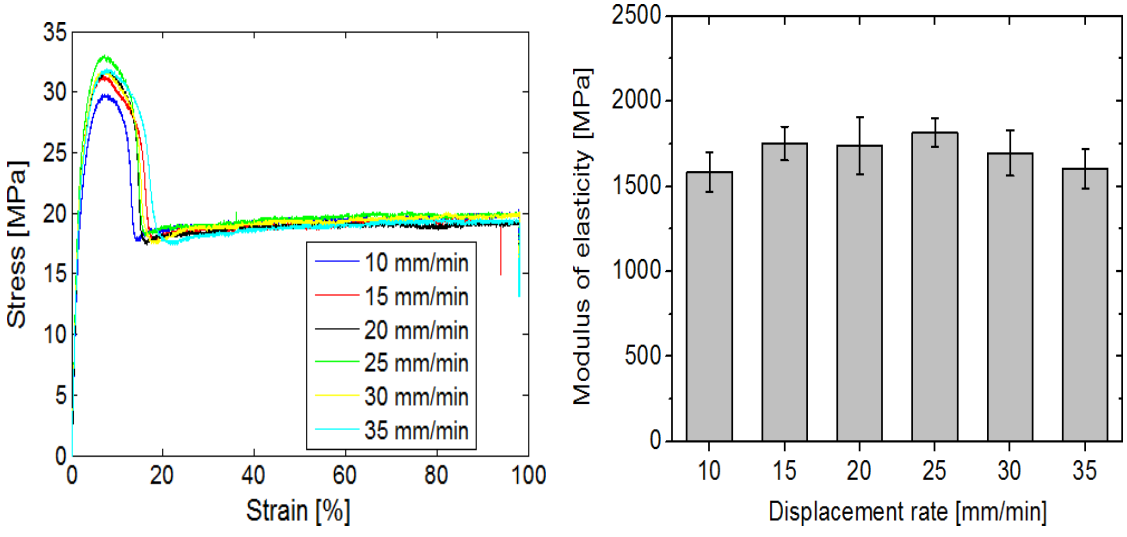

(a) (b)

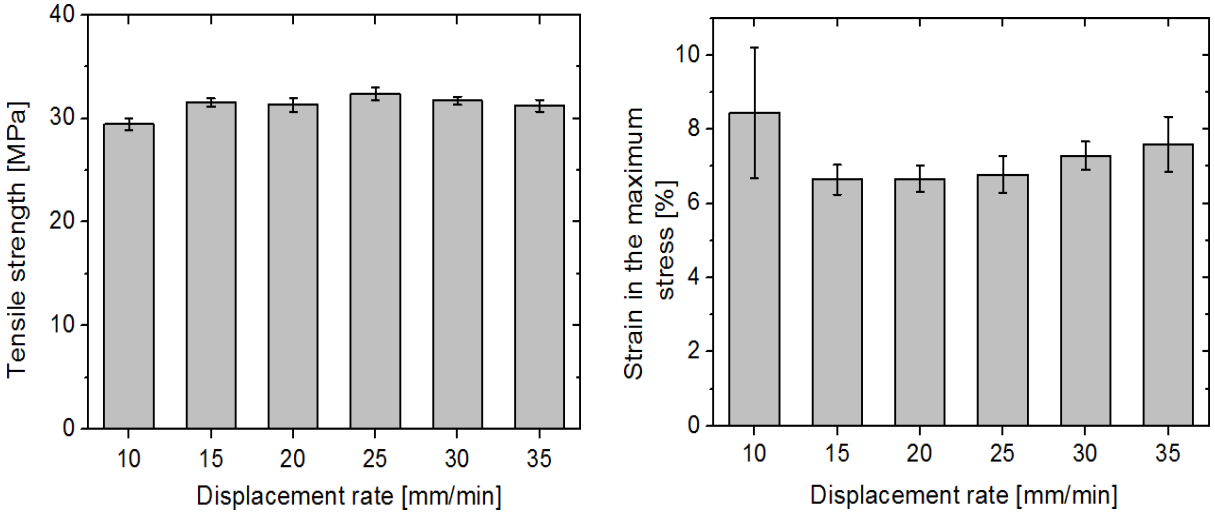

(c) (d)

Source: author.

Semicrystalline polymers, such as polypropylene, exhibit high ductility. This behavior was also found in this study. According to the Figure 5.2 (a), there was a stress peak, which formed a permanently necking that extended along the polypropylene specimen. During the displacement process, the morphology of this semi-crystalline polymer is transformed from a spherulitic structure to a fibrillar structure oriented in direction of the mechanical loading, reducing the mechanical strength and its cross-sectional area after maximum stress (Burke, 1999). Then, there was a slight increasing of strength after 20% strain due the alignment of the polymer chains during the plastic regime.

According to Figures 5.2 (a-d), the displacement rate showed no significant changes on the mechanical behavior of virgin polypropylene. The elastic region of the strain-stress curves was similar and therefore a slower strain rate, 10 mm/min, was assumed in the following tests because it allowed for a greater number of images to be captured along the mechanical loadings, facilitating the identification of elastic properties, strain observations and damage mechanisms by the DIC technique. Figures 5.3 (a-b) show a stress-strain curve at 10 mm/min and some images captured by Correli[Q4] software during the uniaxial tensile test, as well as the longitudinal and transverse strains.

The longitudinal and transverse strains distributed throughout the specimen in the elastic region were presented in Figure 5.3 (a) (instant A). The relationship between these mean deformations or Poisson's ratio at instant A is 0.375. In the region of maximum stress (instant B) there was a higher concentration of longitudinal strain in the upper region of the specimen. The mean longitudinal strain increased from 0.0032 (instant A) to 0.1010 (instant

B). On the other hand, the mean transverse strain is distributed throughout in the sample measurement region.

Figure 5.3. Stress-strain curve followed by DIC and DIT at: (a) instant A (5.09MPa; 0.37%; 2.3s), (b) instant B (29.94MPa; 8.58%; 8.7s), (c) instant C (17.43MPa; 17.43%; 20.4s), (d) instant D (17.93MPa; 24.66%; 25.15s), (e) instant E (18.43MPa; 38.68%; 236.8s) and (f) instant F (19.01MPa; 58.26%; 356.7s). For DIC, 1 pixel represents 52 µm.

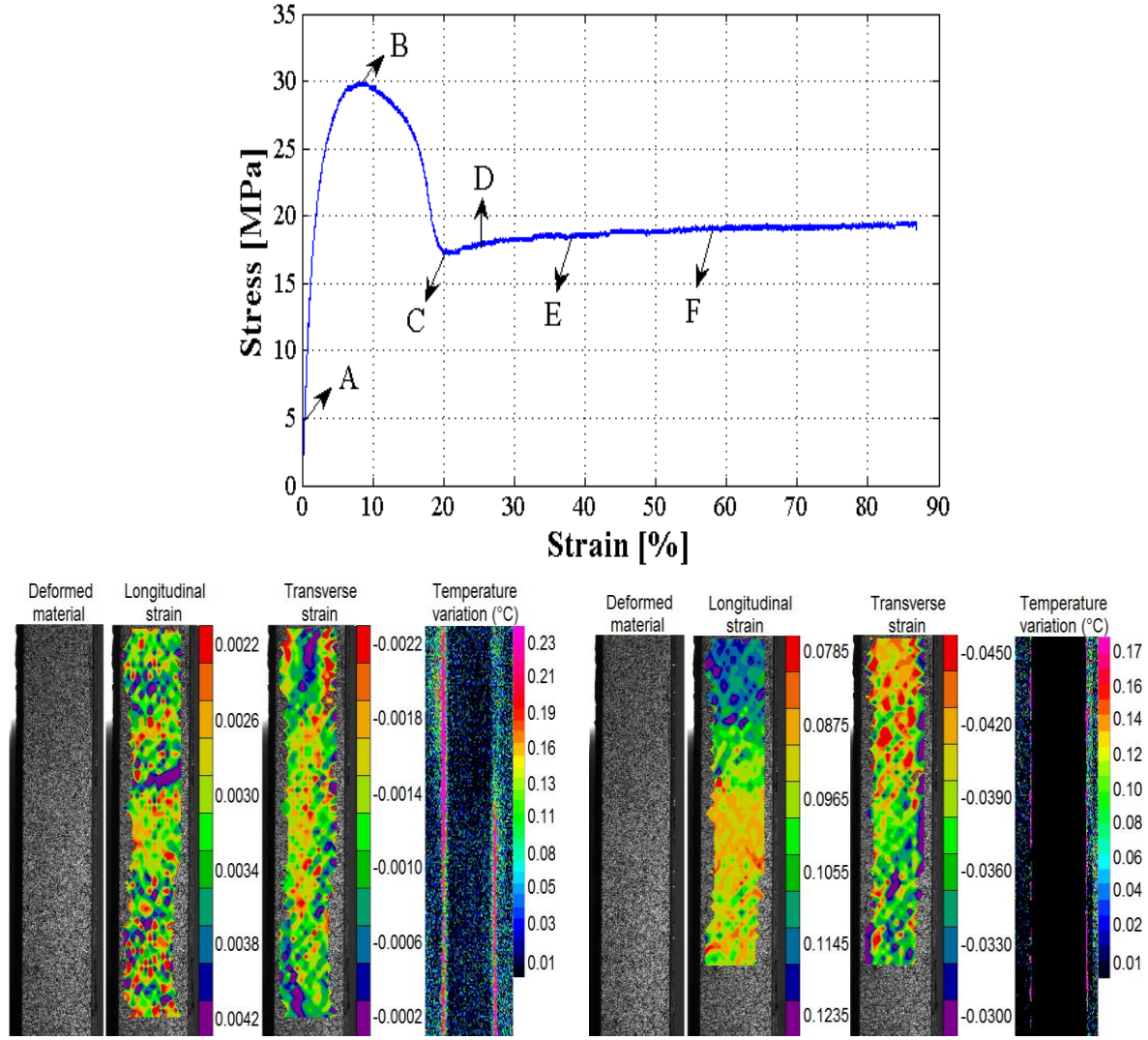

(a) (b)

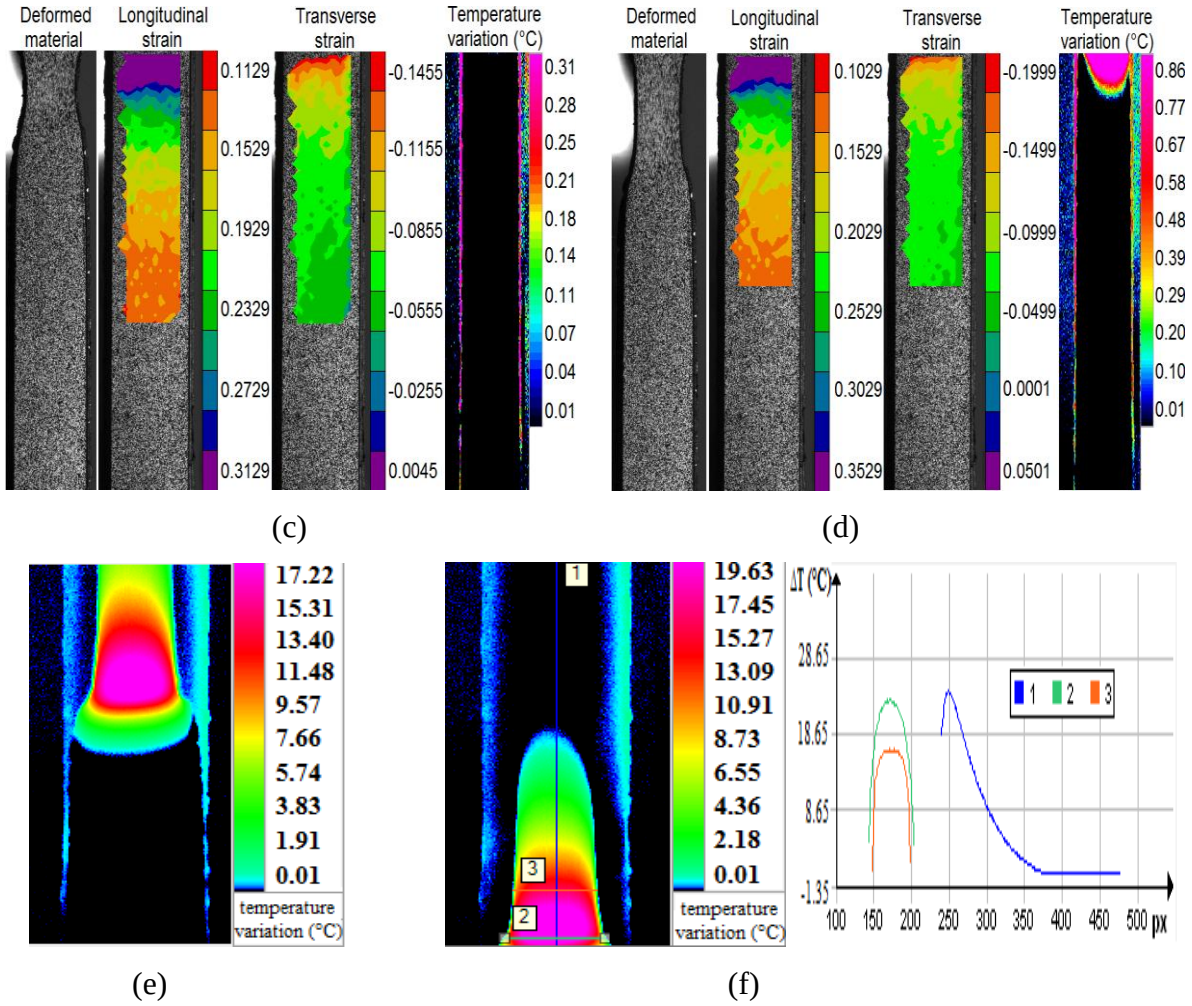

Source: author.

At the instants C and D, both located in the plastic region of the stress-strain curve, higher field strains are shown in the upper region of the same area with larger displacement in the yielding area (purple area). At these instants, it is possible to see that the yielding region progresses in this extremity. This extremity (purple area) deforms longitudinally around two times more than the central region of the sample (yellow area) (0.3 pix/pix against 0.15 pix/pix). The yielding region progress until large strains, but does not reach the partial or total rupture of the sample. The five stress-strain curves (Figure 5.2 (a)) demonstrate this event.

Up to the yield point, polypropylene deforms relatively homogeneously, however at large strains, in the yield and post-yield regimes, inhomogeneous deformations are observed in this polymer. The necking formation occurs due to alignment of the molecular chains which was imposed by the mechanical loading. This alignment causes the increase of resistance and yield strength.

The mean longitudinal strains measured in the elastic region and conducted by the tensile machine were compared with the mean longitudinal strains measured by Correli[Q4] software and the results showed strong proximity (Figure 5.4 (a)). The mean measurement error reported by the Correli[Q4] software was 0.01%. The mean longitudinal strain showed magnitude greater than the mean transverse strain, and the progression of both strains was regular (Figure 5.4 (b)), allowing the determination of the Poisson's ratio with low dispersion values (mean 0.377 and standard deviation 0.007) (Figure 5.4 (c)). These results demonstrate the isotropy of polypropylene (Poisson's ratio between -1 and 0.5). Values between 0.35 and 0.486 for this mechanical property were found by the literature using tensile equipment with strain gauges (Fouda & Seisa, 2013; Tscharnuter *et al*., 2011; Dean & Broughton, 2007). Therefore, good agreement between the results of mechanical extensometers and DIC technique were found.

Figure 5.4. Elastic region: (a) mean longitudinal strains measured by tensile machine and by Correli[Q4], (b) mean strains by Correli[Q4] and (c) Poisson's ratio.

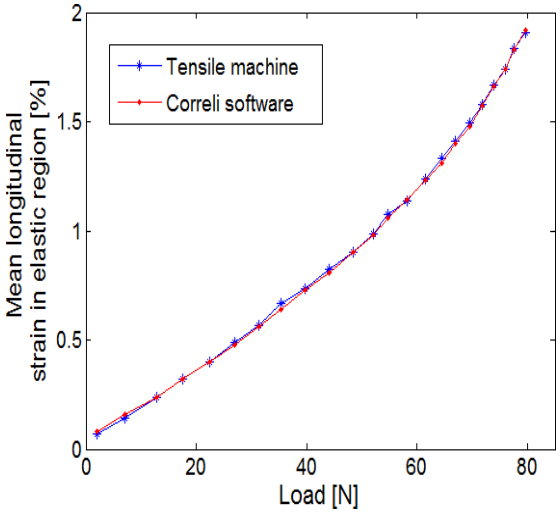

(a)

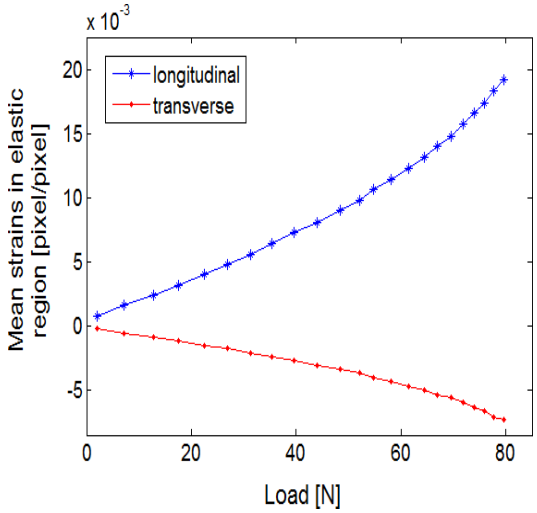

(b)

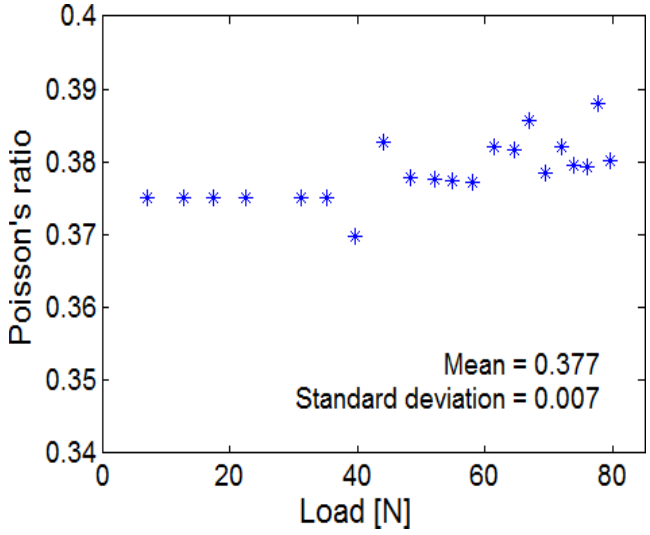

(c)

Source: author.

From the moment D, it was possible to visualize larger temperature variations through an adiabatic process. The alignment of polymer bonding in fibrillar form (tensile test direction) generated heat, while the deformation of the polymer chains in a spherulitic form (instants A and B) showed no temperature variations.

Polypropylene liberates energy in the form of heat during the tensile test in the moments in D, E and F, all located in the plastic region of the stress-strain curve. Instant C showed little temperature variation in tested specimen, although being located in the plastic region and presenting yielding zone, demonstrating that the heat released during the test depends on the time for a bad thermal conductor material, such as polypropylene, to present temperature gradients.

These gradients followed the polymer yielding during this test and evidenced localized deformed material zone, in agreement with the results obtained by DIC technique. The heating zones present inside-out direction for the polypropylene.

Instant F has the highest temperature variation found in this test, 19.63°C (after almost 6 minutes of test), and shows a graph with peak temperature variation and parabolic zones of heating (onset by necking formation).

The determination of instantaneous strains and stresses allowed the calculation and plotting of engineering stress-strains curves. Equations 3.2. to 3.9 were also used. Figures 5.5 (a-g) show the mechanical behavior of engineering and true stress-strain curves on three regions of polypropylene: global (all specimen), inside the region suffering greater yielding and instability (necked) and outside the necking (unecked). In approximately 0.15 pix/pix

(15%) of longitudinal strain in the outside of necking region of engineering and true stress-strain curves there was a small reduction and decrease in longitudinal strain, indicating polymer relaxation in this region. On the other hand, there was continuity and advance of longitudinal strain in the region inside the necked region from yielding point.

Figure 5.5. Monitoring the mechanical behavior of polypropylene in different regions: (a) deformed material, (b) all specimen analyzed, (c) necked region, (d) unecked region, (e) engineering stress-strain, (f) true stress-strain, (g) longitudinal and (h) transverse strains during the test.

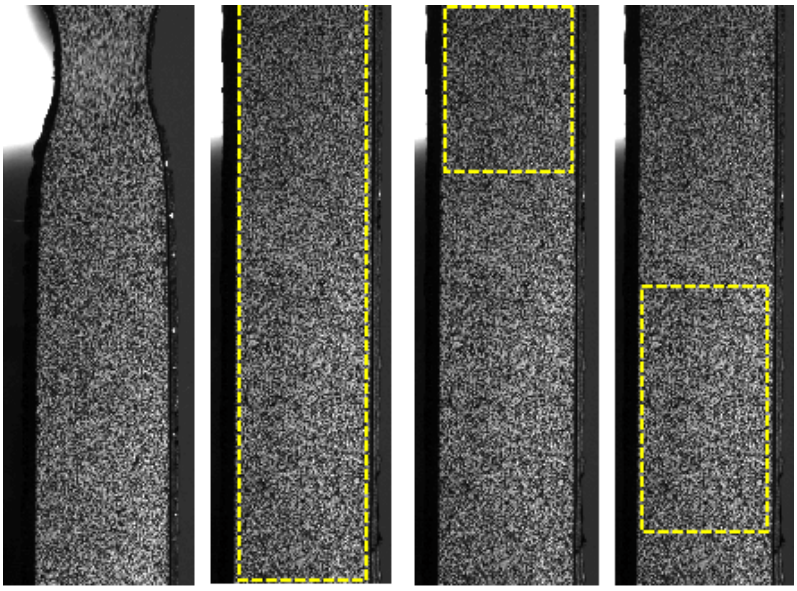

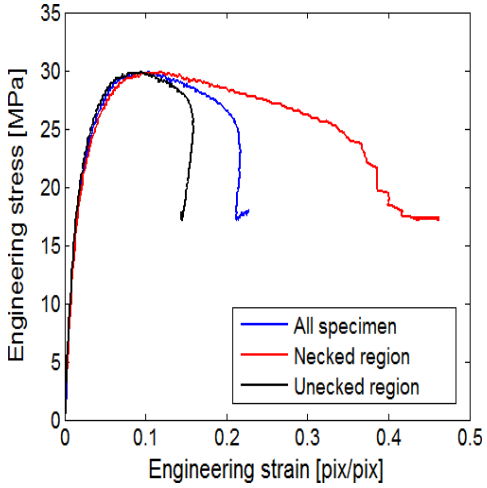

(e)

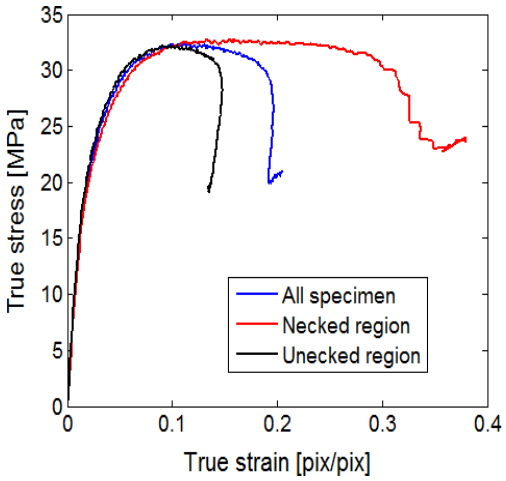

(f)

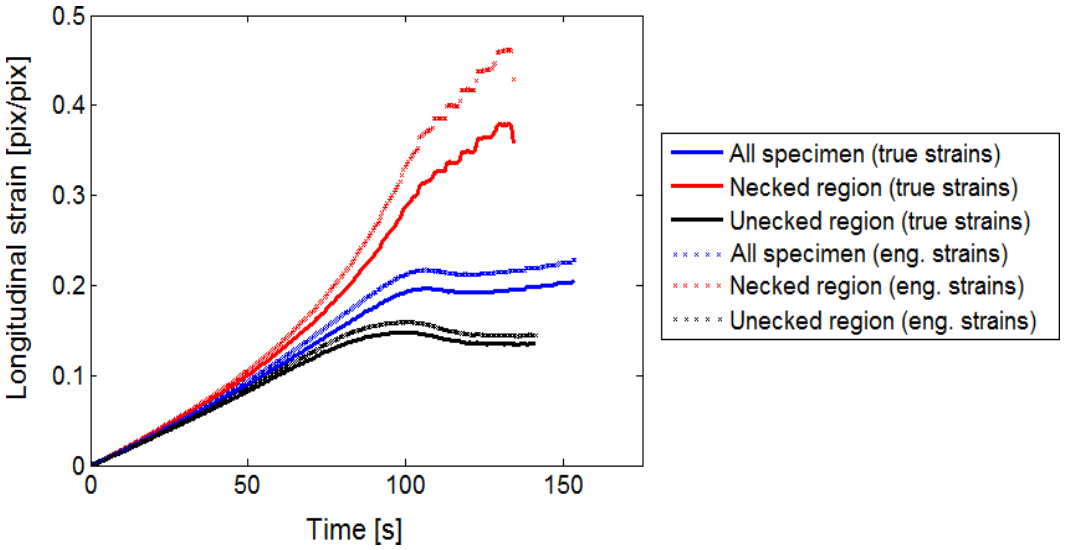

(g)

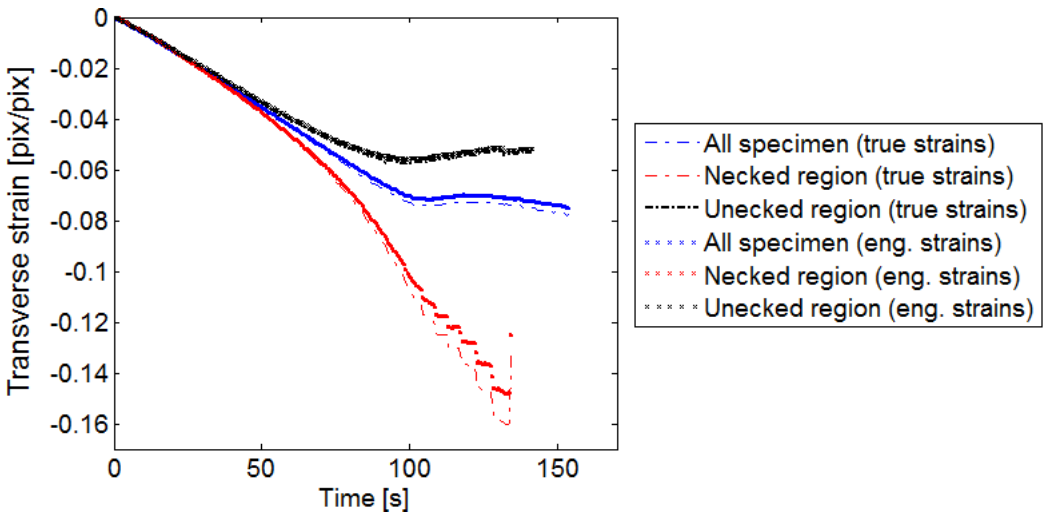

(h)

Source: author.

It was observed in Figure 5.5 that up to 0.1 to pix/pix (10%) the stress-strain curves are similar in the three regions analyzed: global, within the region and out of necking. The true stress is higher than the engineering stress in plastic regime and similar for smaller strains or elastic regime due to correction of instantaneous areas during the test. In engineering and true stress-strain curves the longitudinal strains are governed by the necking formation. Figures 5.5 (g-h) also associate this initiation and propagation to the location of longitudinal and transverse strains.

Transverse strains indicating significantly transverse contractions even in the pre-yield regime for three regions analyzed are shown in Figure 5.5 (g). In post-yield regime there was difference in this strain during the tensile testing. In the necking region the transverse strains

in post-yield regime were relatively higher and increasingly progressed. However, unstable points at the end of the time x transverse strain curve related to instability in necking formation were found (Jerabek et al., 2010). The transverse strain or contraction of the material in the region out of the necking had no large modifications after the post-yield regime. The region analyzed throughout the specimen (global) shows intermediate behavior between regions inside and outside of the necking.

As the neck stabilizes at a certain constant local strain, it then propagates along the specimen so that the crosshead displacement determines the neck propagation velocity. In this state, the undrawn material outside the necking area remains essentially unaffected.

6. Morphological and mechanical behavior of the composites

This chapter presents the morphological behavior of internal regions of composites manufactured by virgin and recycled polypropylene and reinforced by coconut fibers. The volume fraction of fibers and the compatibility aspects on fiber-matrix are here discussed.

Thus, through the results on tensile testing is possible to evaluate the coconut fibers effects as reinforcement in PP and RPP, as well as provide the fields of the failure mechanisms and damage onset in these materials.

6.1. Morphological aspects of composites

The morphology of composites was visualized by X-rays tomography. Through the analysis of five images in each direction (slice), the volume fraction of fibers within the composites manufactured with virgin polypropylene was determined (Figures 6.1 (a-c)). Impurities found in composites fabricated by recycled polypropylene had similar gray levels to the fibers in its interior, and therefore, these materials did not have this physical property determined (Figure 6.1 (d)). The average volumetric fractions of coconut fiber for PP-1L and PP-2L were 9.44 and 11.54%, respectively. RPP-1L and RPP-2L have the same quantities of layers of mats than PP-1L and PP-2L, respectively, but not necessarily the same volume of fibers. However, the volume fractions for the composites fabricated by recycled polypropylene may be close to these respective values.

It was possible to visualize that the fibers are located in injection direction. The coconut fibers mats were inserted manually into the mold. The injection flow also contributed to the fibers remain in the end of the mold. However, tomography micrographs showed that the mats maintained their bidirectional arrangement and transverse isotropy of fibers after the injection of polypropylene.

Figure 6.1. X-ray tomography and 3D-reconstruction on (a) PP-1L, (b) PP-2L, (c) RPP-1L and (d) RPP-2L.

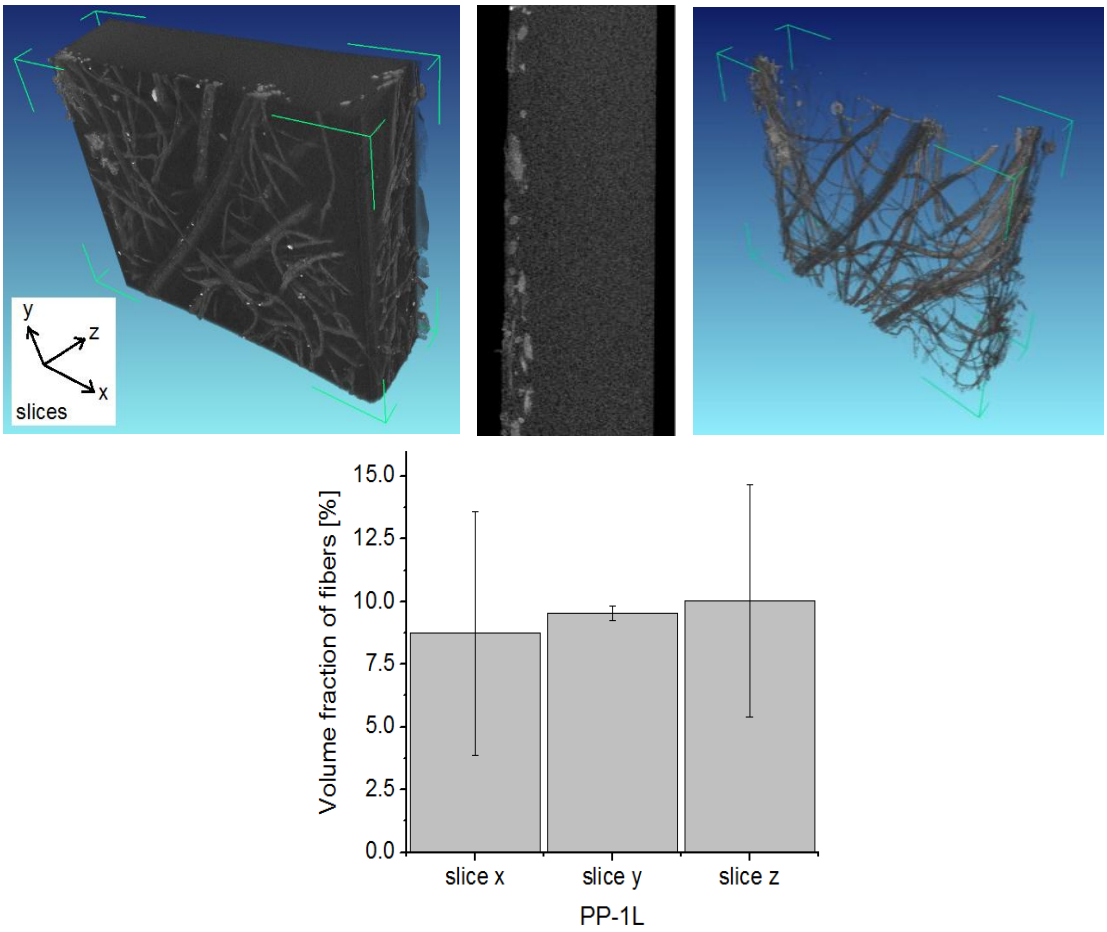

(a)

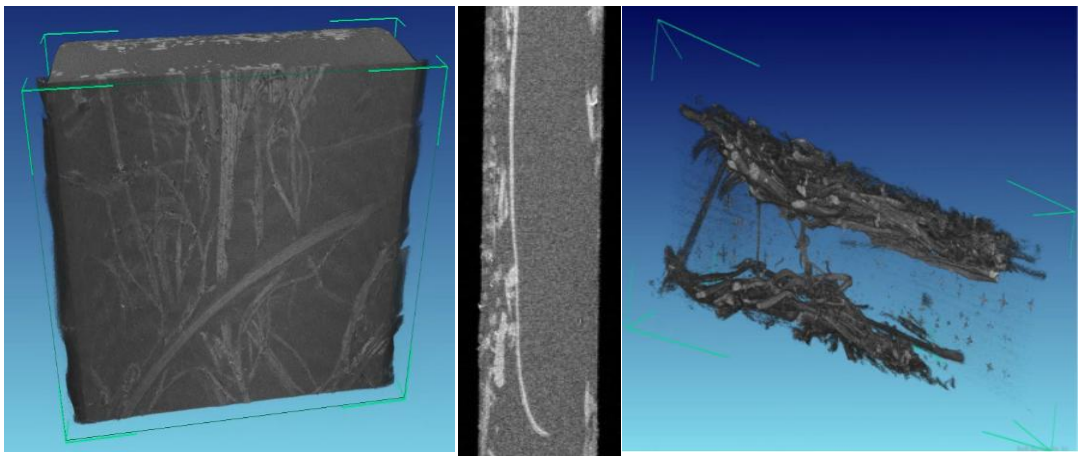

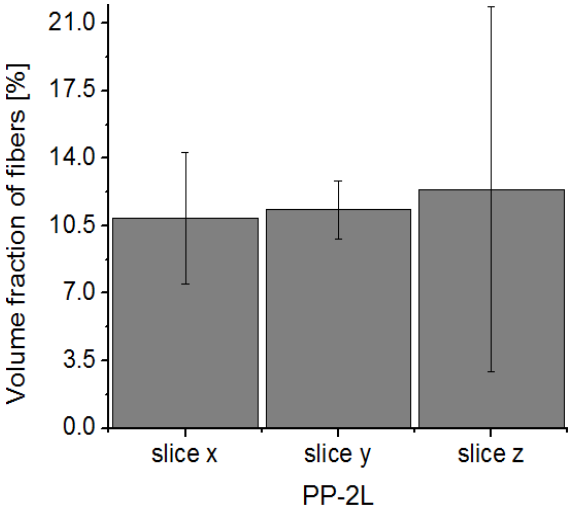

(b)

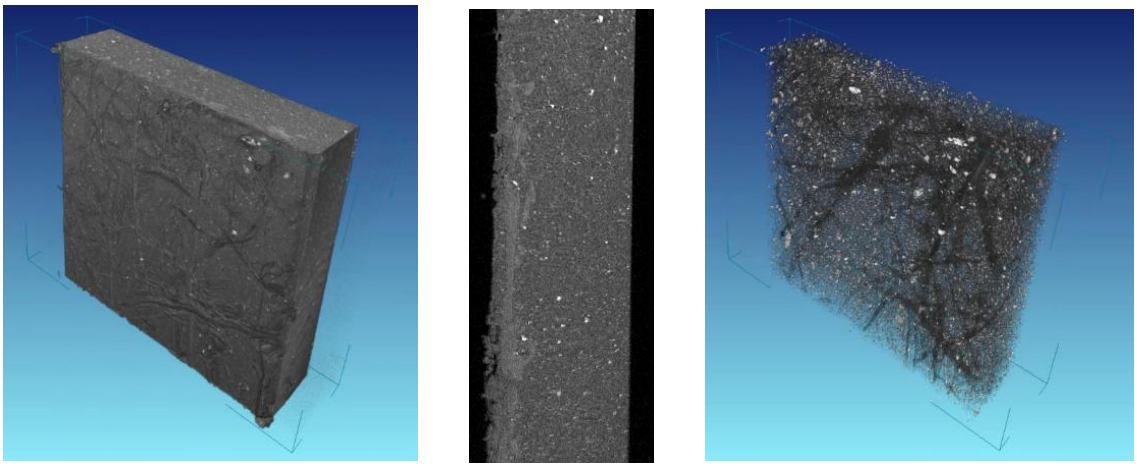

(c)

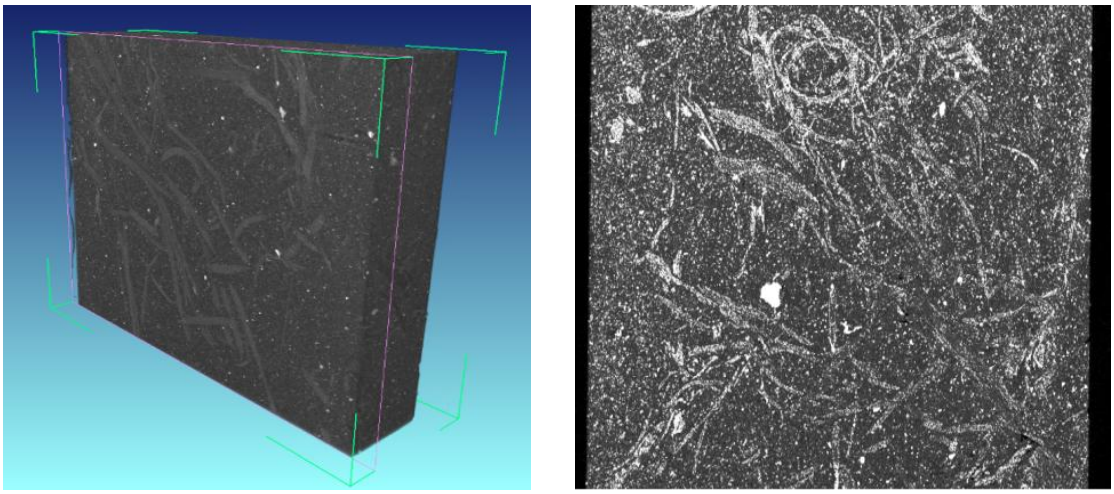

(d)

Source: author.

Figure 6.2 shows some magnifications of a sample of PP-1L. Some coconut fibers are found not completely involved by the polymer, indicating incompatibility between fiber and matrix. The pressure provided by the injection equipment (3 bar) may have been insufficient to full impregnation and wettability of the fiber. Poor adhesion, possibly associated with the low pressure during the manufacturing, generated voids outside the sample, acting as stress concentrator and crack propagation initiator.

Figure 6.2. Coconut fibers partially involved by polymer.

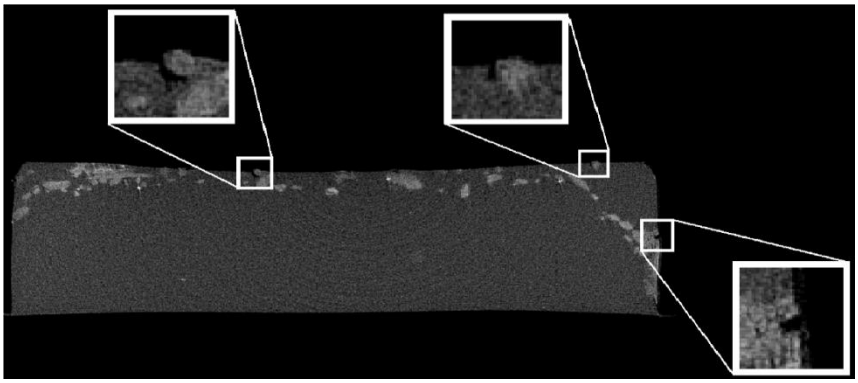

Source: author.

6.2. Tensile testing on composites

Figures 6.3 (a-h) present a tensile test used as a reference for the following approaches in relation to the strain and damage evolutions of manufactured composites. The test shows a specimen of recycled polypropylene composite with a layer of coconut fiber mat (RPP-1L). The region of Figure 6.3 (c) was analyzed in relation to longitudinal, transverse and shear strains, as well as the temperature variation during the test was measured by DIT technique.

Points A and B are located in the elastic region of the stress-strain curve and presented ratios between the average transverse and longitudinal strains, or Poisson's ratio, amounting to 0.20 and 0.25, respectively. From the instant A, the DIC technique showed greater strain in the center of the specimen, the material failure region, including the shear strains (Figure 6.3 (c)).

Figure 6.4 (a) presents the average values of these two strains by DIC technique during the tensile test. The ratio between them during the elastic region is shown in Figure 6.4 (b). The recycled polypropylene composite with a layer of coconut fiber presented an average Poisson's ratio of 0.22 (standard deviation 0.03). However, after measurements on all samples

of coconut fiber, coconut fiber mat, PP, PP-1L, PP-2L, RPP, RPP-1L and RPP-2L, the average values for the Poisson's ratio are 0.78, 0.32, 0.377, 0.292, 0.319, 0.3317, 0.3333 and 0.3213, respectively.

Figure 6.3. Tensile test followed by DIC and DIT on a RPP-1L: (a) stress x longitudinal strain curve, (b) stress x shear strain curve, (c) material rupture, (d) instant A (5.09 MPa; 0.38 %; 2.3 s), (e) instant B (10.09 MPa; 0.72 %; 4.4 s), (f) instant C (17.51 MPa; 1.60 %; 9.7 s), (g) instant D (22.35 MPa; 4.09 %; 25.0 s) e (h) instant E (19.76 MPa; 6.75 %; 41.1 s).

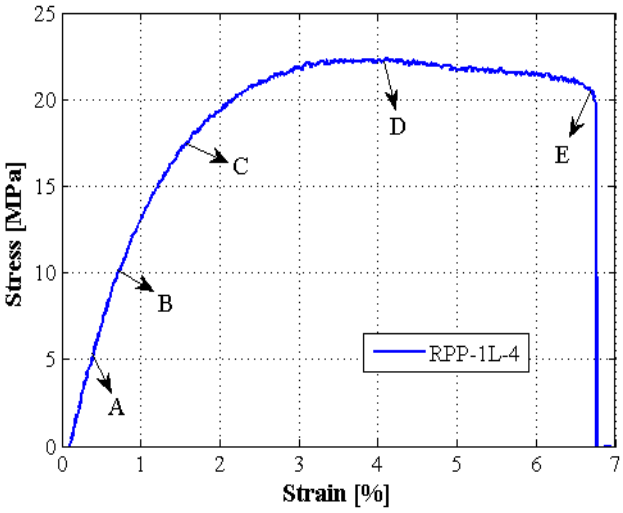

(a)

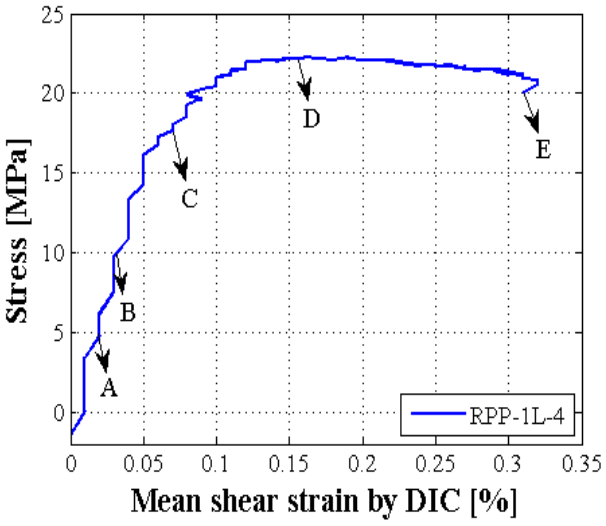

(b)

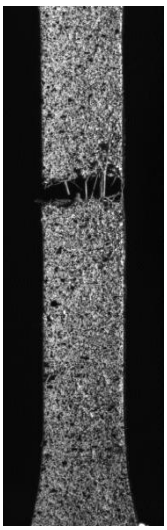

(c)

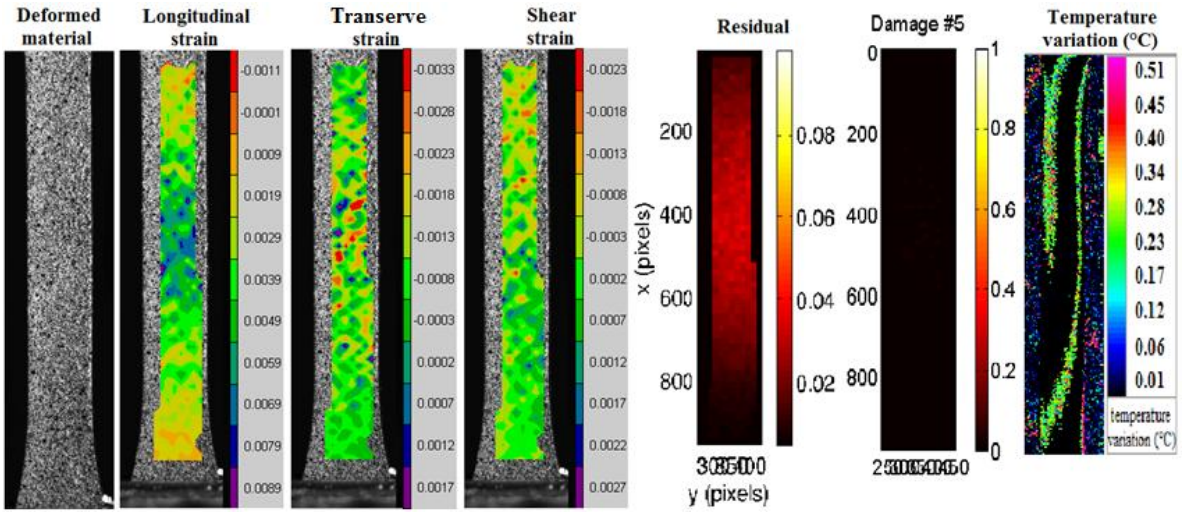

(d) Instant A

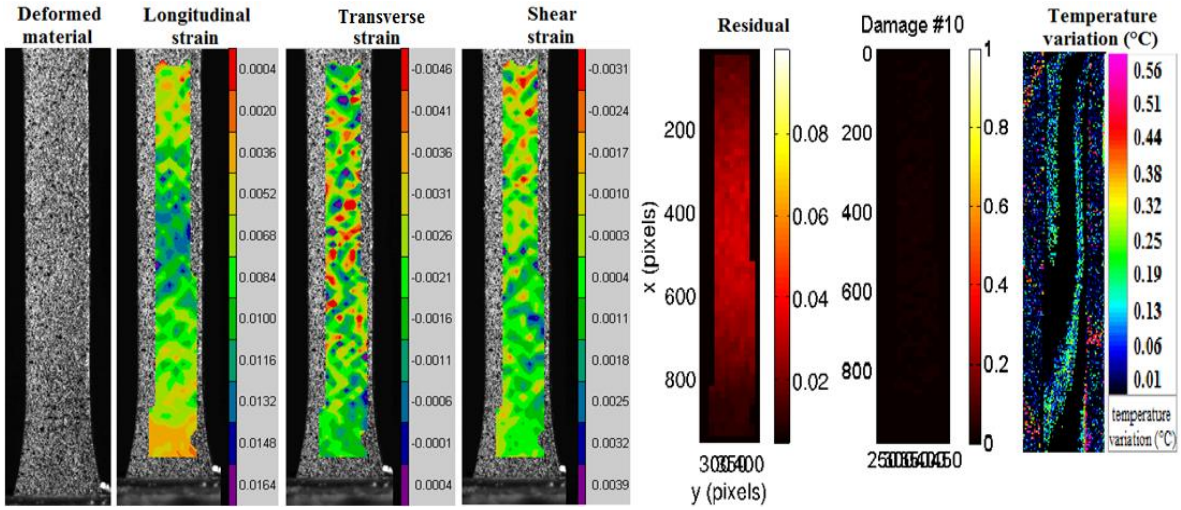

(e) Instant B

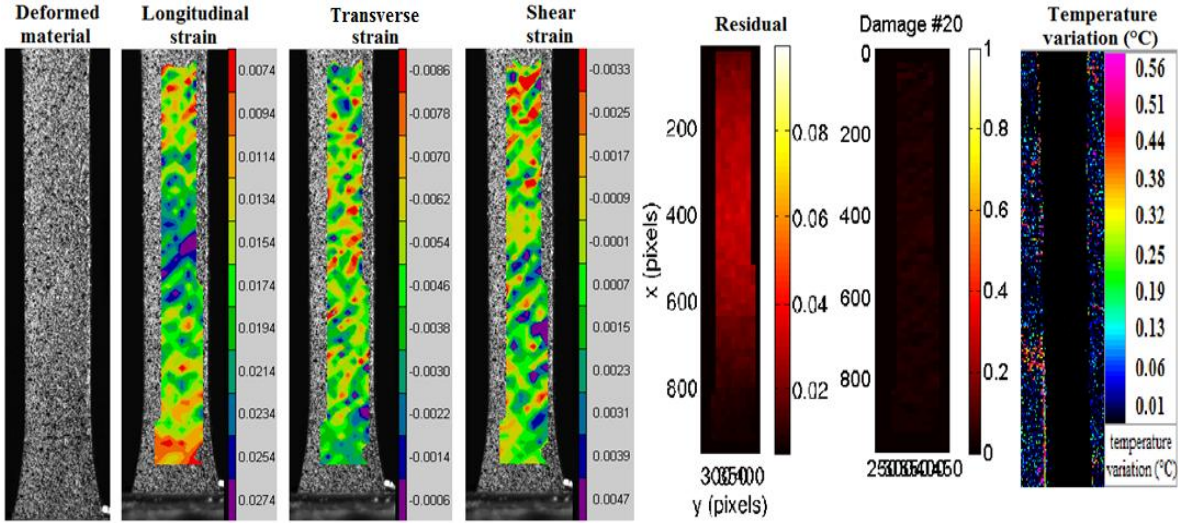

(f) Instant C

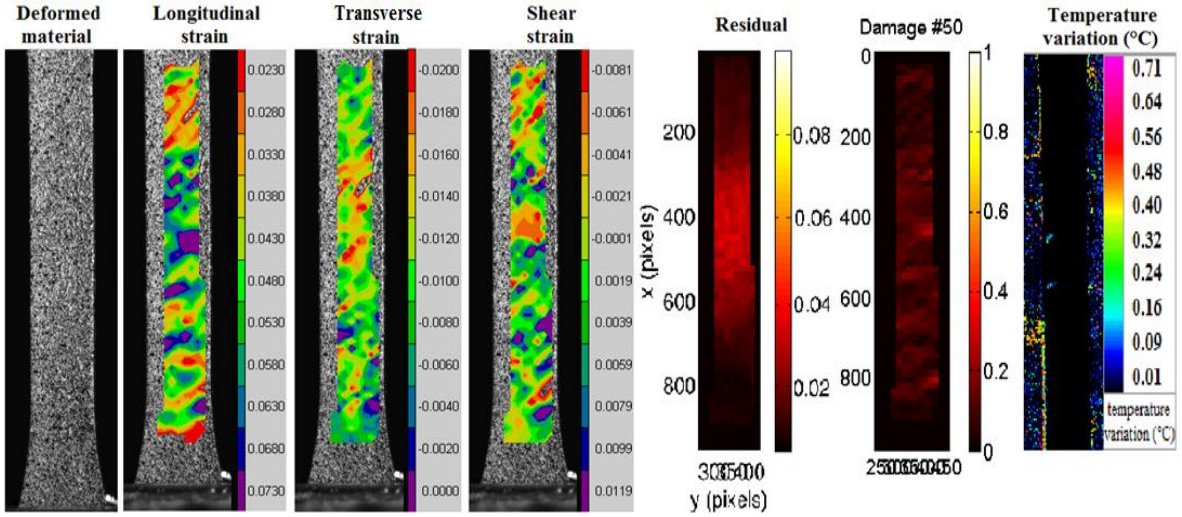

(g) Instant D

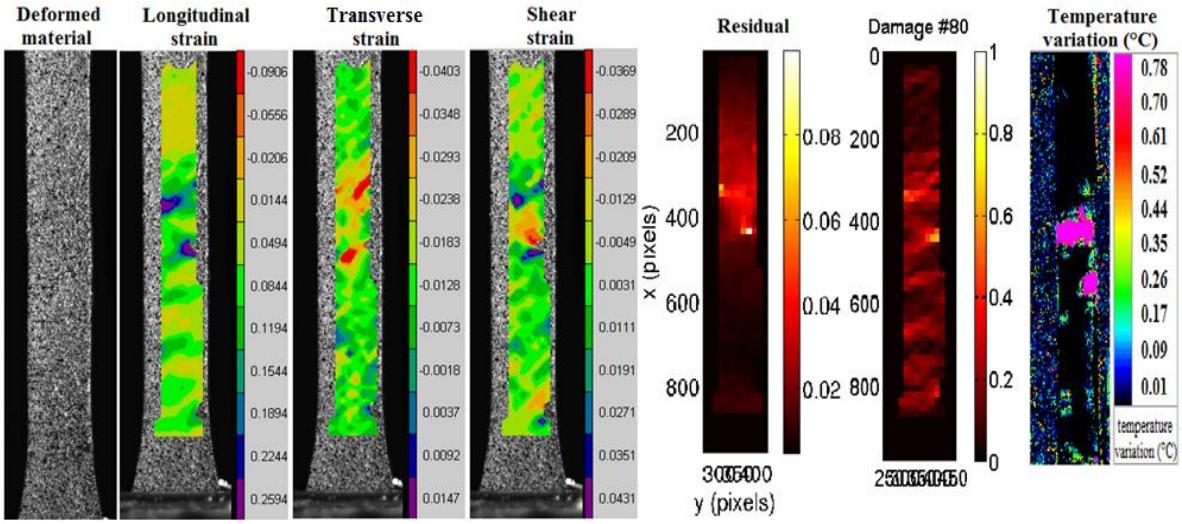

(h) Instant E

Source: author.

The damage variable, D, was determined throughout the region of interest of the specimen, presenting a final value of approximately 0.63 (Figure 6.5), mainly located in the region of the higher longitudinal strain and higher pixel residual displacement. It was possible to observe several damaged regions with increasing normal stress during the test, in which its appearance began in the plastic region of the material (point C). This damage onset is in agreement with the damage's theory.

In this case, the largest relative error, ρ, was reached in the last image with value 5.2%. The characteristic deformation ε_p was 0.4 x [1, 2, 4, 8, 16] with corresponding amplitude C_p = [-1.000, 305.1249, 478.0118, 570.1922, 617.8091]. Therefore, an acceptable error was found (lower than 7%).

Figure 6.4. (a) Longitudinal and transverse strains measured by DIC and (b) Poisson's ratio on RPP-1L.

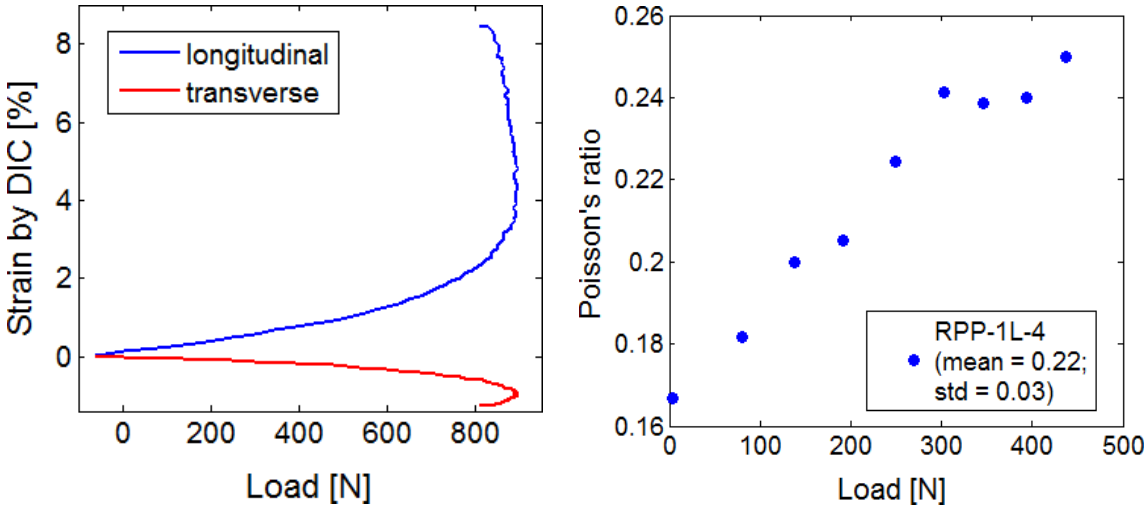

(a) (b)

Source: author.

Figure 6.5. Damage evolution x equivalent strain curve on RPP-1L.

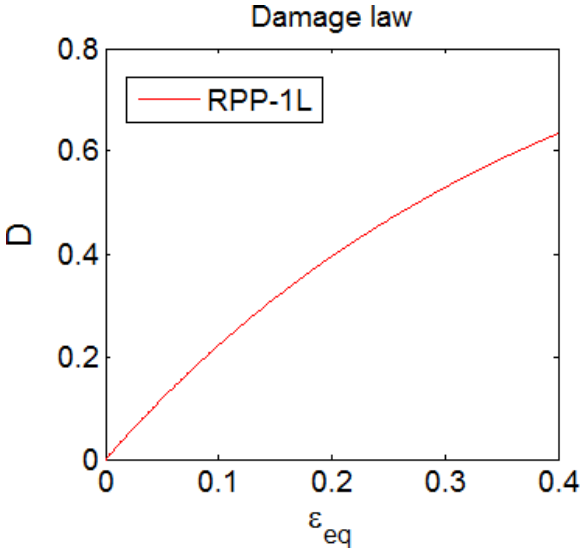

Source: author.

At the beginning of the tensile test, the displacement of residual pixel was presented throughout the region analyzed on the specimen. However, this displacement was more pronounced in the fracture region, from the onset of the plastic regime of the stress-strain curve (point C). Through DIC analysis it can be concluded that the rupture of the material occurred mainly due to longitudinal strains imposed by the normal stresses. Transverse and shear strains were also present and contributed to the damage and fracture of the material. In

this test, maximum longitudinal strains (before rupture), transverse and shear (identified by DIC) were 8.44%, -1.28% and 0.31%, respectively.

The temperature of the material showed variation from the instant D. The first temperature gradients in the center of the specimen and located in the region of greatest deformation of the material were visualized. In the last instant captured prior to the rupture, instant E, there was an temperature increase of approximately 0.78°C in this region, showing that the mechanical loading inserted an adiabatic process on this material.

Coconut fibers addition effects on virgin and recycled polypropylene

Figure 6.6 shows the stress-strain curves for PP-1L, PP-2L, RPP, RPP-1L and RPP-2L. All materials studied showed good ductility. Regarding the addition of coconut fibers in PP, it can be reported that the second layer of coconut fiber mat increased the ductility and elongation at break. Recycled polypropylene (RPP) had resistance loss after the maximum stress, similar to the mechanical behavior of virgin polypropylene, but ruptured around 8%. In addition, the RPP lost ductility and presented non-repeatable stress-strain curves with the addition of coconut fiber mats.

The incorporation of fibers into the polymer matrix reduced the elongation at break of the composites. This is a common observation with almost all filled composites where elongation decreases monotonically with addition of more fiber into the polymer (Rozman, 1999, 2000; Klason et al., 1984). The ductility of PP has been suppressed by the presence of fibers. The reduction may be attributed to the decreased deformability of a rigid interface between fiber and matrix material.

Figure 6.6. Stress-strain curves on PP-1L, PP-2L, RPP, RPP-1L and RPP-2L.

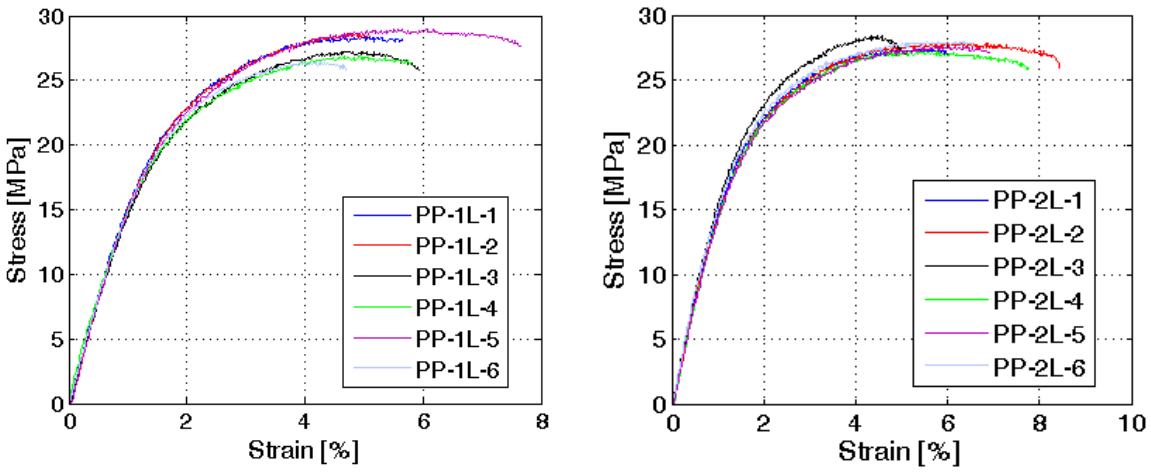

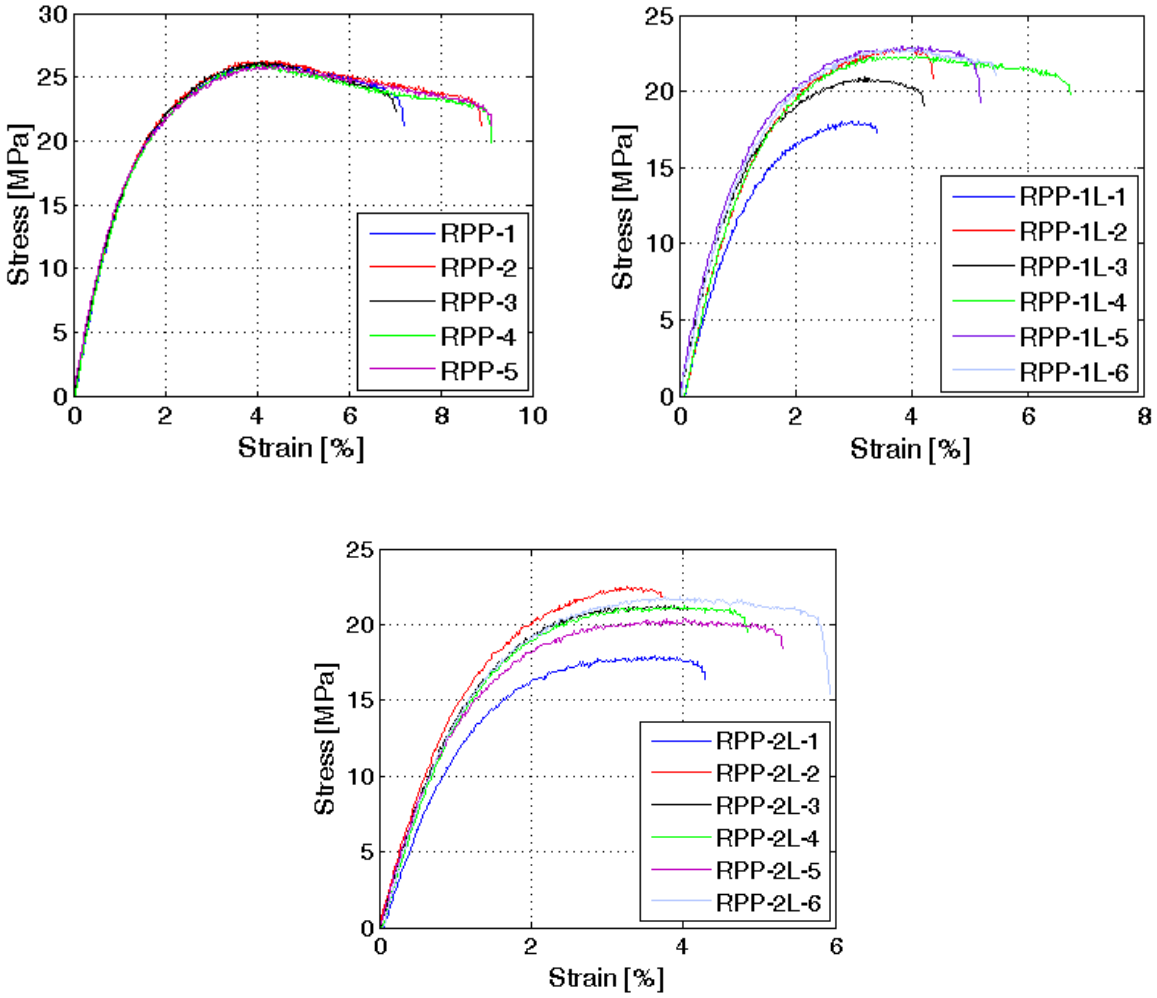

Source: author.

Figure 6.7 shows the influence of coconut fiber in virgin and recycled polypropylene. Recycled polypropylene showed lower tensile strength than virgin polypropylene, but higher modulus of elasticity. This behavior is in agreement with the works of Aurrekoetxea et al. (2001). PP reprocessing induces some mechanical and thermal degradations, besides that possible impurities within this recycled material may generate discontinuities or non-formed chemical bonds (Strapasson, 2004). Virgin polypropylene not broken, unlike the recycled polypropylene, which showed an average strain at break of 8.3%.

It is verified that the tensile strength decreases relatively to coconut fiber addition in virgin and recycled polypropylene (Figure 6.7). However, this vegetable fiber improved the modulus of elasticity for virgin polypropylene, but deteriorated this property in the recycled polypropylene, suggesting that the impurities presented in X-ray tomography of this recycled polymer had less interaction with the fiber in comparison to this polymer in virgin condition.

Figure 6.7. Influence of PP recycling and coconut fiber addition on: (a) tensile strength, (b) modulus of elasticity and (c) strain at break.

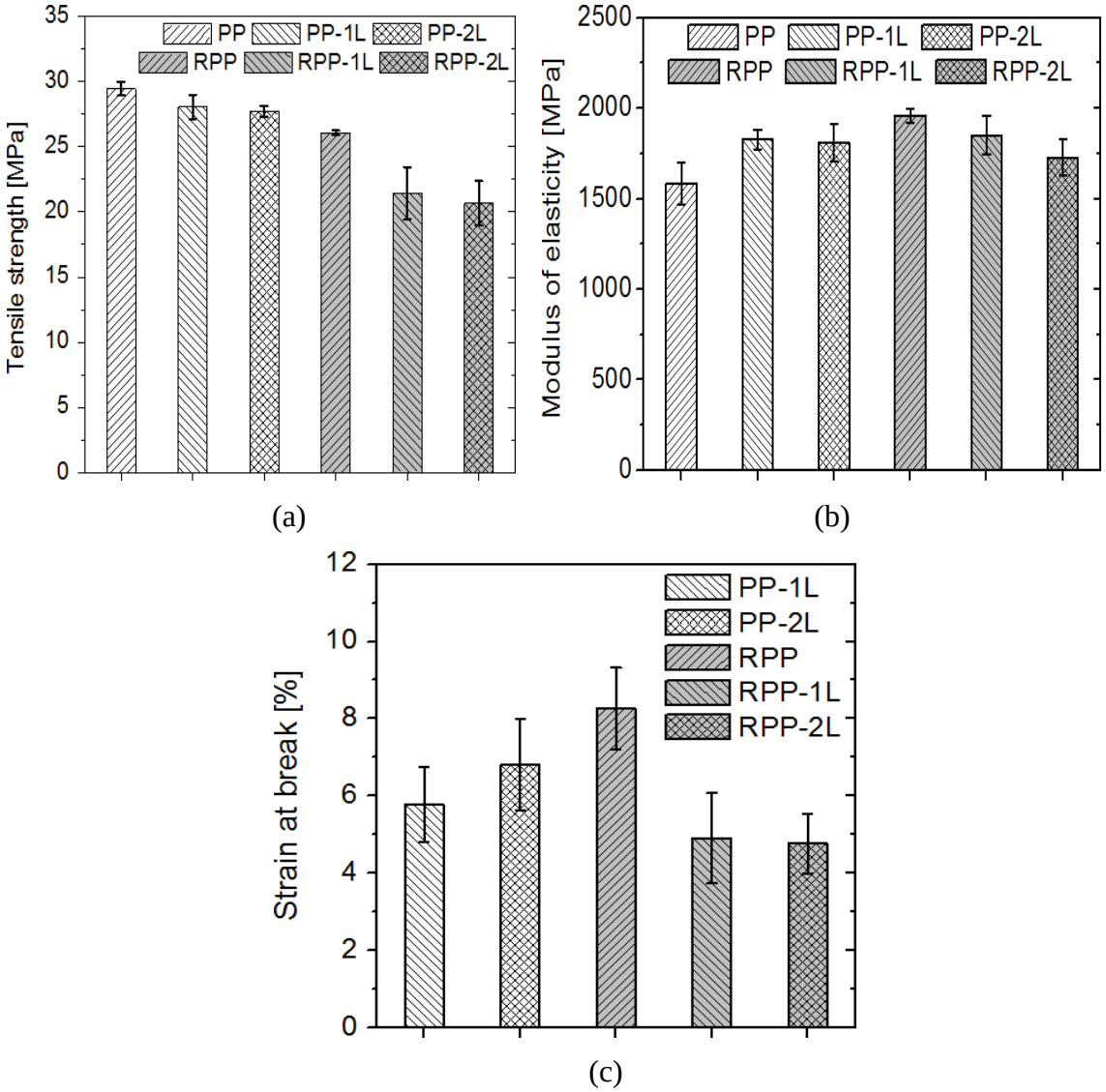

Source: author.

As previously mentioned, the average tensile strength of this fiber is 50 MPa. This value is higher than the resistance for the virgin and recycled polypropylene, which have average tensile strengths of 29 and 26 MPa, respectively. However, the orientation of coconut fiber was dispersed in the composite, with fibers in the transverse direction to the direction of uniaxial loading performed in the composites. Only coconut fibers in the longitudinal direction can reinforce the material when requested in this direction. Fibers oriented in the transverse direction imply to concentrate the longitudinal loading in fiber-matrix interface, which in turn demonstrates to be lower than the longitudinal strength of the coconut fiber. Thereby, the inferior mechanical behavior presented after the addition of coconut fibers

suggests that there was poor compatibility of the coconut fibers with the virgin and recycled polypropylene. Some studies corroborate the poor iteration between the coconut fibers with polymer matrices.

Gelfuso et al. (2011) manufactured composites of polypropylene reinforced by coconut fiber mats and used two methods of surface treatment on the mats: chemical treatment with 2% of NaOH and mechanical treatment based on ultrasonic shockwave. Gelfuso et al. (2011) reported that as the fiber load increased, the weak interfacial area between the fiber and matrix increased, consequently, the tensile strength decreased. This behavior was observed for all the samples, treated and untreated. On the other hand, tensile strength values of composites fabricated with coconut fibers mechanically treated were higher than those of the composites fabricated with coconut fibers chemically treated, independent of fiber content. This effect may be associated to the friction occurring between the fibers during the mechanical treatment by ultrasonic shockwave. This friction promotes the wear of fiber surface and develops a rough surface topography increasing the mechanical interlocking with matrix thus enhancing fiber–matrix interface adhesion and improving mechanical properties. However, the tensile strength decreases as the interactions fiber-fiber increase instead of fiber-matrix. The highest tensile strength value was observed for composites fabricated with mechanically treated coconut fibers containing 10 vol. (%) fibers.

Indicula et al. (2004) found similar results and suggested that the high content of coconut fiber leads to agglomeration and stress transfer becoming blocked and, as a result, mechanical strength decreases. It is well known that the alkali treatment by NaOH is able to remove the natural and artificial impurities from the fiber surface as well as change the crystal structure of the cellulose. Moreover, depending on the concentration of the alkali treatment, it can reduce fiber diameter and thereby composite tensile strength decreases.

Rozman et al. (2000) reported that the tensile strength of composites with polypropylene gradually decrease as the coconut fiber loading is increased. Other studies have also indicated that the incorporation of filler into thermoplastic matrix may not necessarily increase the tensile strength of a composite (Rozman, 1998; Ahmad, 1994; Bigg, 1987). Unlike fibers which possess uniform cross section and relatively high length to diameter ratio (aspect ratio), for irregular-shaped coconut fibers, their capability to support stress transfer from the matrix is rather poor.

Ishizaki et al. (2006) analyzed the effect of fiber content on flexural modulus of the polypropylene composites using 10, 20 and 30% coconut fiber volume. The results showed

that after adding the fiber there was a decrease in flexural modulus of the composite compared to pure polypropylene, followed by a slight increase with increasing fiber concentration.

6.3. Rupture observations of composites

Figure 6.8 shows the rupture micrographs of the composites of this work. Figures 6.8 (a-b) show some fibers involved by latex, indicating that the fiber had this elastomer as the main contact. Figures 6.8 (c-d) show the presence of pull-out on some coconut fibers; other coconut fibers remained inside the composite, but with its extremity fractured. Figures 6.8 (e-f) show the contact between the coconut fiber with the PP and the RPP, respectively, in which it is possible to visualize the poor adhesion between the fibers and polymer matrices.

Figure 6.8 (g) presents a coconut fiber transversely located in a PPR-2L composite. Only the fibers located longitudinally may reinforce the material when the material is mechanically submitted in this direction. The longitudinal mechanical stresses concentrate the loadings on the fiber-matrix interface in fiber located in the transverse direction.

Figures 6.8 (h-i) show that the distribution of coconut fibers is related to the direction of injection during the manufacturing process of the composite. The coconut fibers are pressed until the mold cavity by the polymer in the liquid state, remaining in that region until its solidification. Figure 6.8 (i) shows a fiber with large diameter and located transversely, demonstrating, once more, that this fiber orientation compromises the mechanical behavior of composite and in this case, it acted as a rupture initiator of the material.

The fiber-fiber friction and high fiber concentration in a given region hinder the wettability with polymeric matrices, creating the voids between the fibers (Figures 6.8 (h-i)) (Gelfuso et al., 2011). However, some fibers have good adhesion to polypropylene, suggesting that the manual processing of latex distribution on mat was dispersed, because regions rich and poor of this elastomer were found (Figure 6.8 (j)).

Ishizaki et al. (2006) studied the morphological and mechanical behavior of polypropylene/coconut fiber composite and it was reported that the fibers were uncoupled with the polymeric matrix, suggesting poor affinity between the phases. This morphology explained the decrease in flexural modulus on the compositions containing fibers when compared to pure PP.

Rozman et al. (2000) indicate that one of the modes of composite failure is through fiber pull-out. SEM micrographs show that the fiber is being scraped off, which leaves quite a smooth surface on the matrix. This may indicate the occurrence of debonding through the

weak interfacial between fiber and PP matrix. Rozman et al. (2000) also presented irregularities in size of the fibers in the composites. There were two sizes shown, i.e., about 280 mm and 100 mm. The irregularity in size may affect the efficiency of stress transfer.

Figures 6.8 (k-l-m) show rupture micrographs of virgin and recycled polypropylene, suggesting that the virgin polymer exhibits homogeneous and ductile fracture regions due to its crystallinity and purity of constituents. On the other hand, recycled polypropylene, with different crystallinity and containing impurities due to its reprocessing (Strapasson, 2004) presents regions of brittle and ductile fracture, demonstrating distinct morphologies.

Figure 6.8. Rupture micrographs in composites.

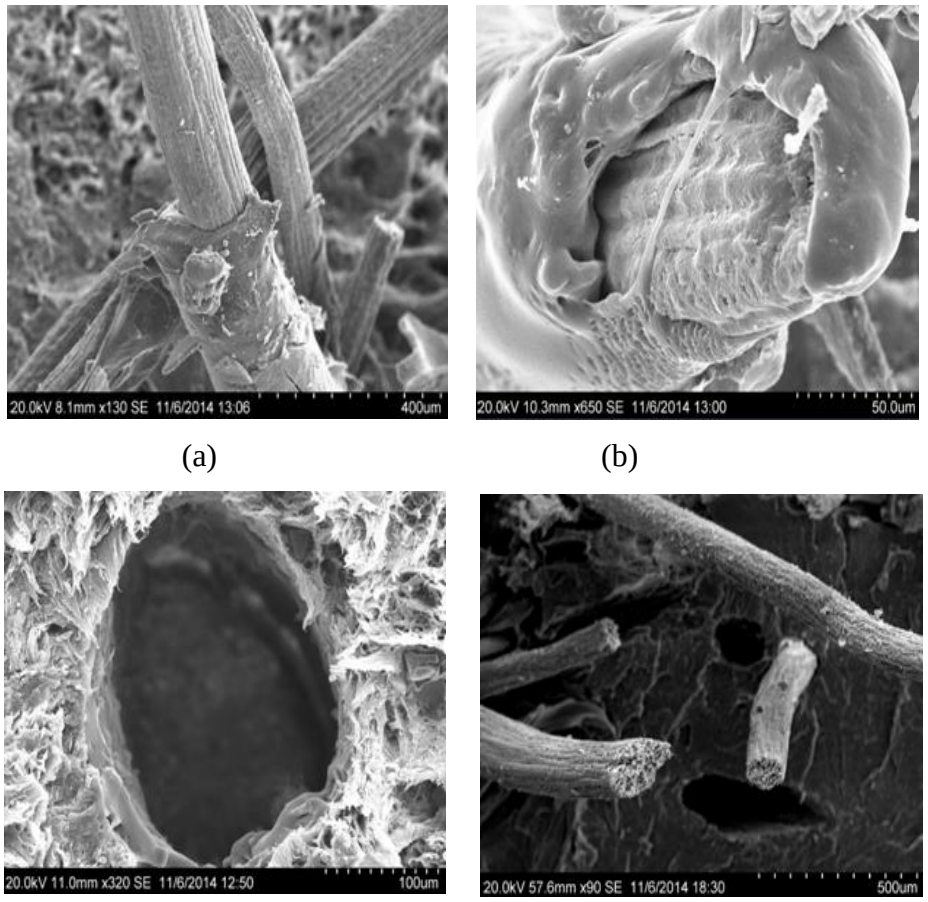

(a) (b)

(c) (d)

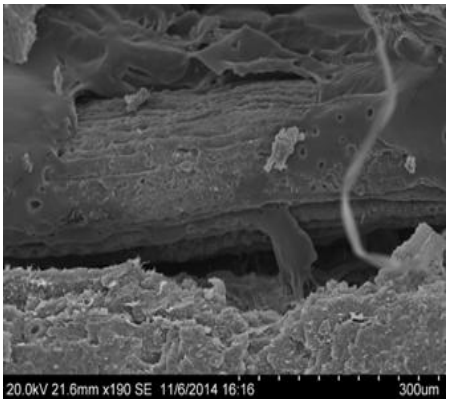
20.0kV 21.6mm x190 SE 11/6/2014 16:16
300um

(e)

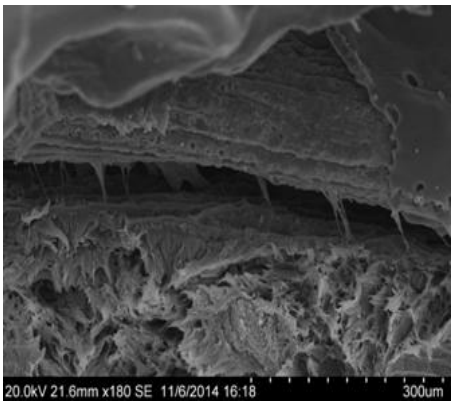
20.0kV 21.6mm x180 SE 11/6/2014 16:18
300um

(f)

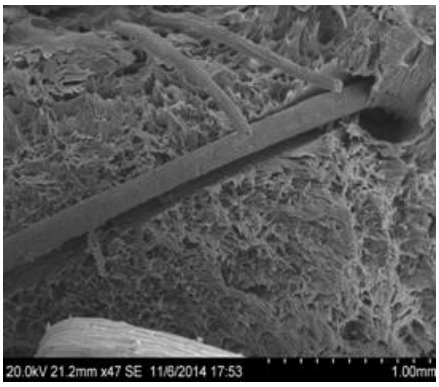
20.0kV 21.2mm x47 SE 11/6/2014 17:53
1.00mm

(g)


20.0kV 18.8mm x120 SE 11/6/2014 16:32
400um

(h)

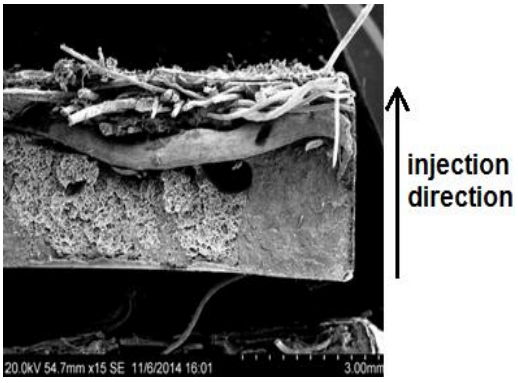
20.0kV 54.7mm x15 SE 11/6/2014 16:01
3.00mm
injection
direction

(i)


20.0kV 36.8mm x180 SE 11/6/2014 16:07
300um

(j)

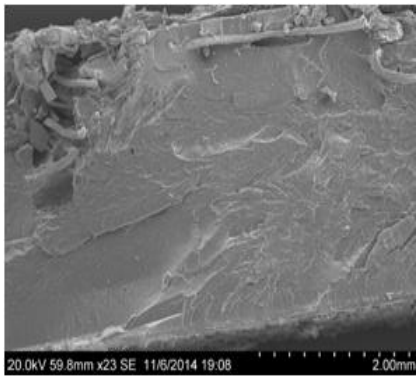
20.0kV 59.8mm x23 SE 11/6/2014 19:08
2.00mm

(k)

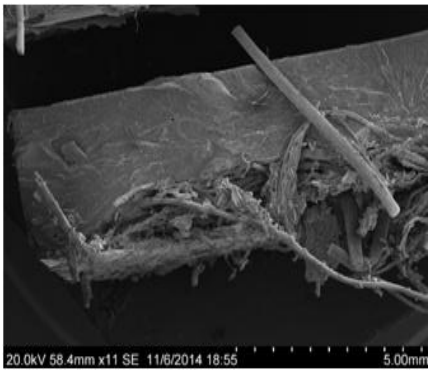
20.0kV 58.4mm x11 SE 11/6/2014 18:55
5.00mm

(l)

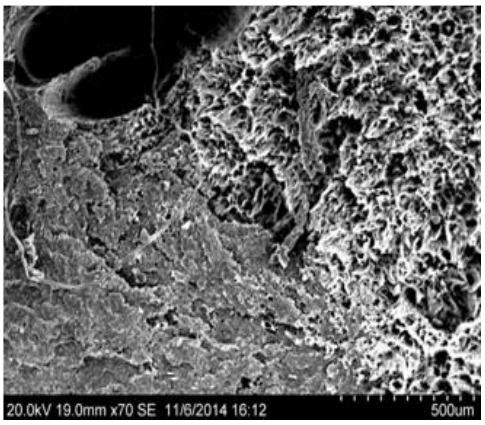

(m)

Source: author.

Figure 6.9 shows the rupture micrograph of a fiber that was broken during tensile test in a composite. Microcracks close to its rupture area are shown. During the tensile test on individual coconut fiber, the DIC analysis presented heterogeneous strains around these fibers. Two images of tensile test on individual coconut fiber are again presented at the right side of this micrograph. The morphology of failure mechanisms in individual coconut fiber and when they are inside of composite are similar.

Figure 6.9. Microcracks on coconut fiber.

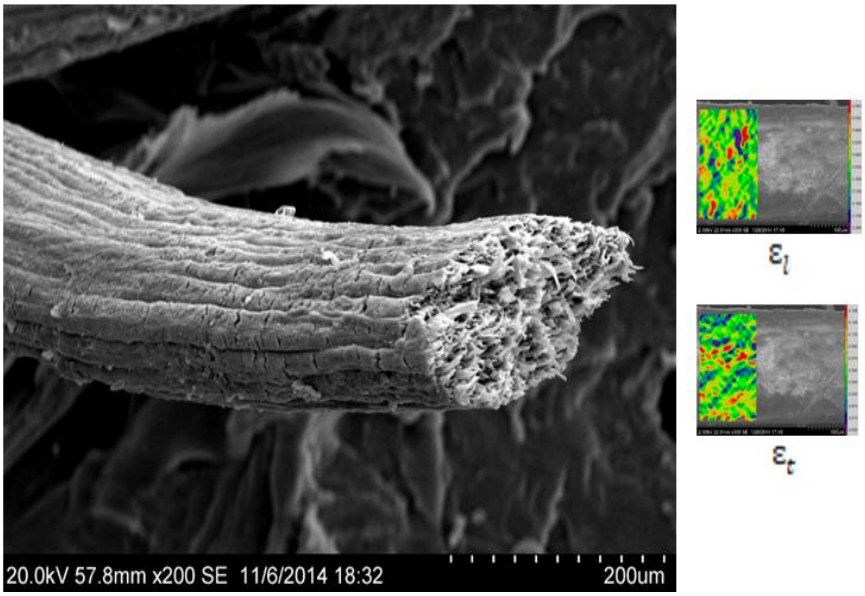

Source: author.

7. Numerical modeling

The experimental measurements were compared with the measurements provided by the numerical model shown in Equation 3.10. Figure 7.1 shows the differences between the two mechanical behaviors of five different fiber diameters. The higher differences were found during image acquisition, in which a relaxation of tensile stress is shown, typically found in ductile and viscoelastic materials. In the others points, the numerical model showed good agreement with the experimental results. It is recommended that the model should have between 70 and 95% proximity with the experimental results. This recommendation was based after analyzing hundreds of stress-strain curves corresponding to a large number of materials (Gerscovich, 2009).

Figure 7.1. Experimental and modeling measurements in stress-strain curves on coconut fiber.

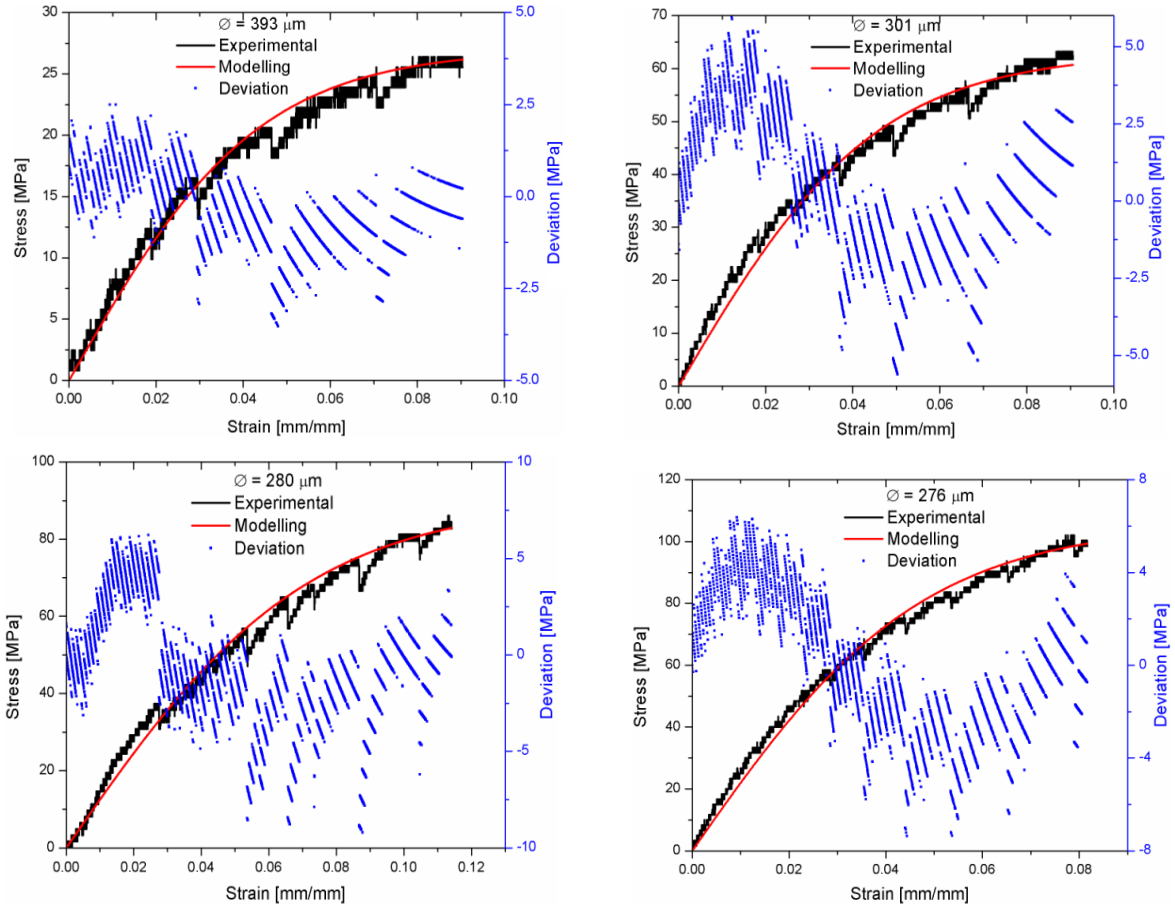

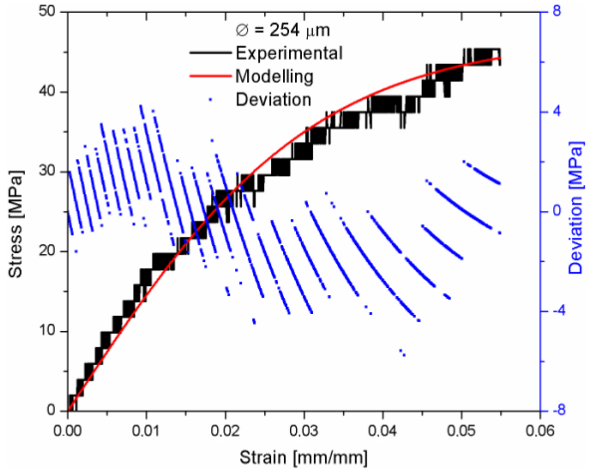

Source: author.

Even though using a numerical model well correlated with experimental measurements, the random mechanical behavior of coconut fibers relative to their diameters, as presented previously, made it difficult to obtain more precise values for the parameters 'a' and 'b'. Figure 7.2 shows that the values of these parameters decreased with increasing diameter. Therefore, the parameters determination for the coconut fibers by the numerical model adopted in this study also showed a decrease in mechanical properties of coconut fibers as a function of its diameter.

Figure 7.2. Relation of parameters obtained by the numerical model and the diameter of coconut fiber.

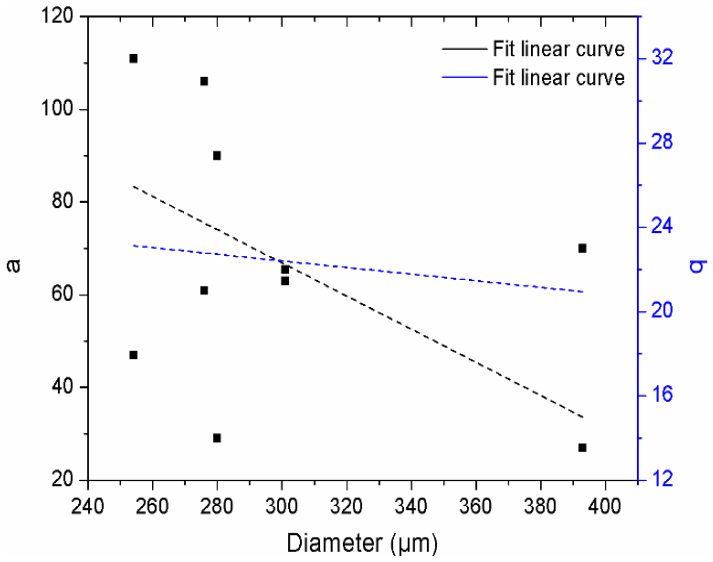

Source: author.

Figures 7.3 to 7.8 present the experimental measurements and the measurements obtained by the numerical model through tensile tests on PP, PP-1L, PP-2L, RPP, RPP-1L and RPP-2L.

Figure 7.3. Experimental and modeling measurements in stress-strain curves on PP.

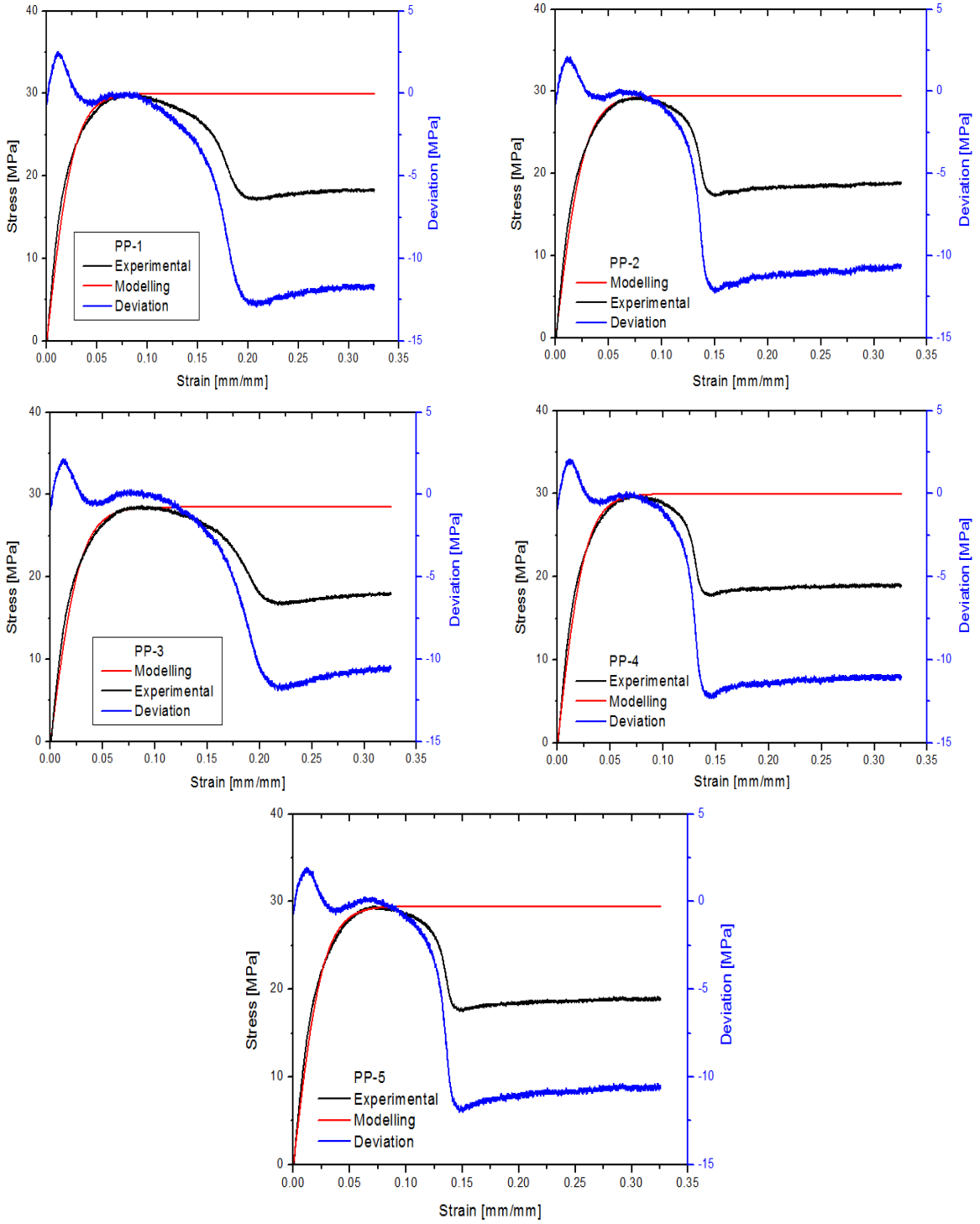

Source: author.

Figure 7.4. Experimental and modeling measurements in stress-strain curves on PP-1L.

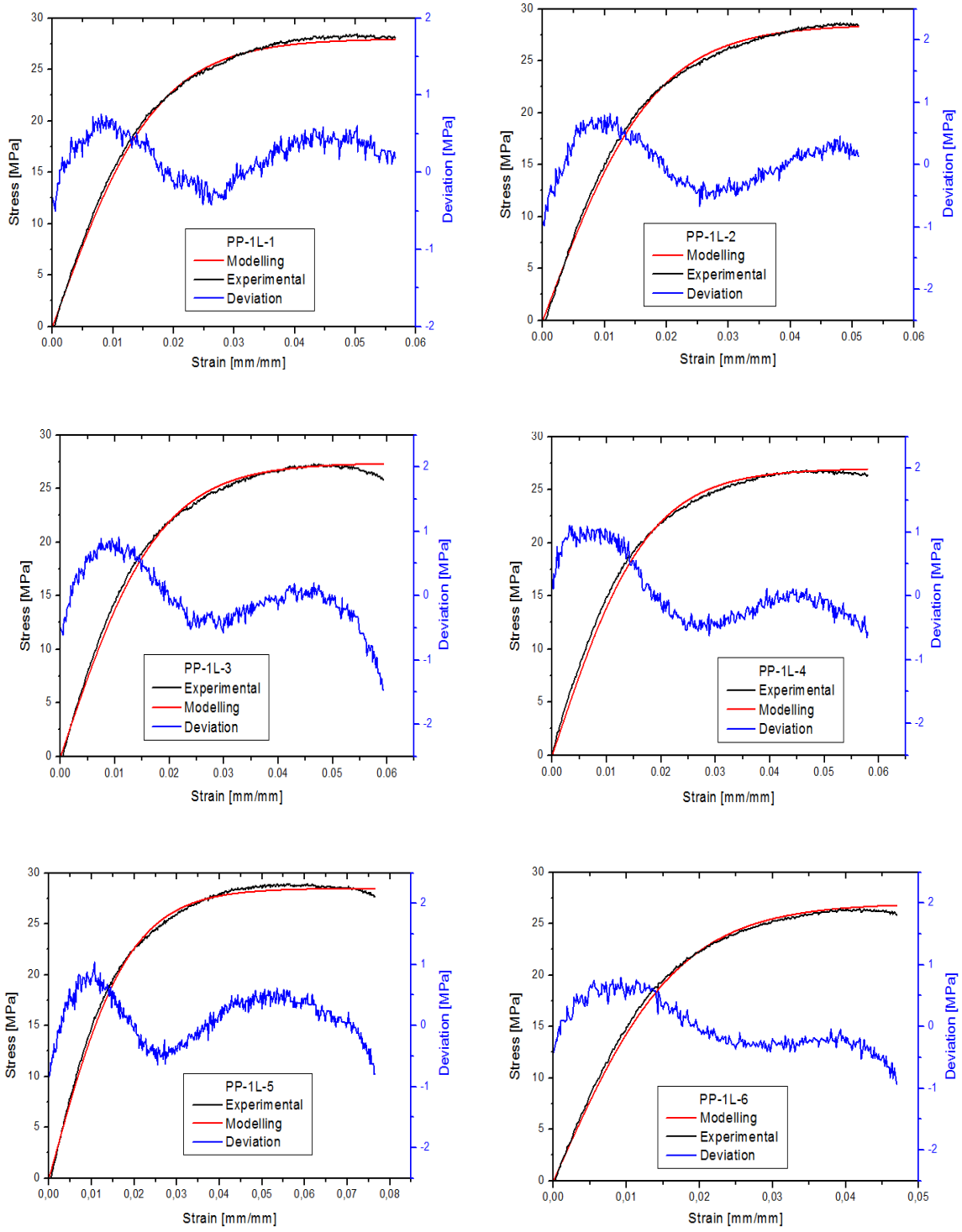

Source: author.

Figure 7.5. Experimental and modeling measurements in stress-strain curves on PP-2L.

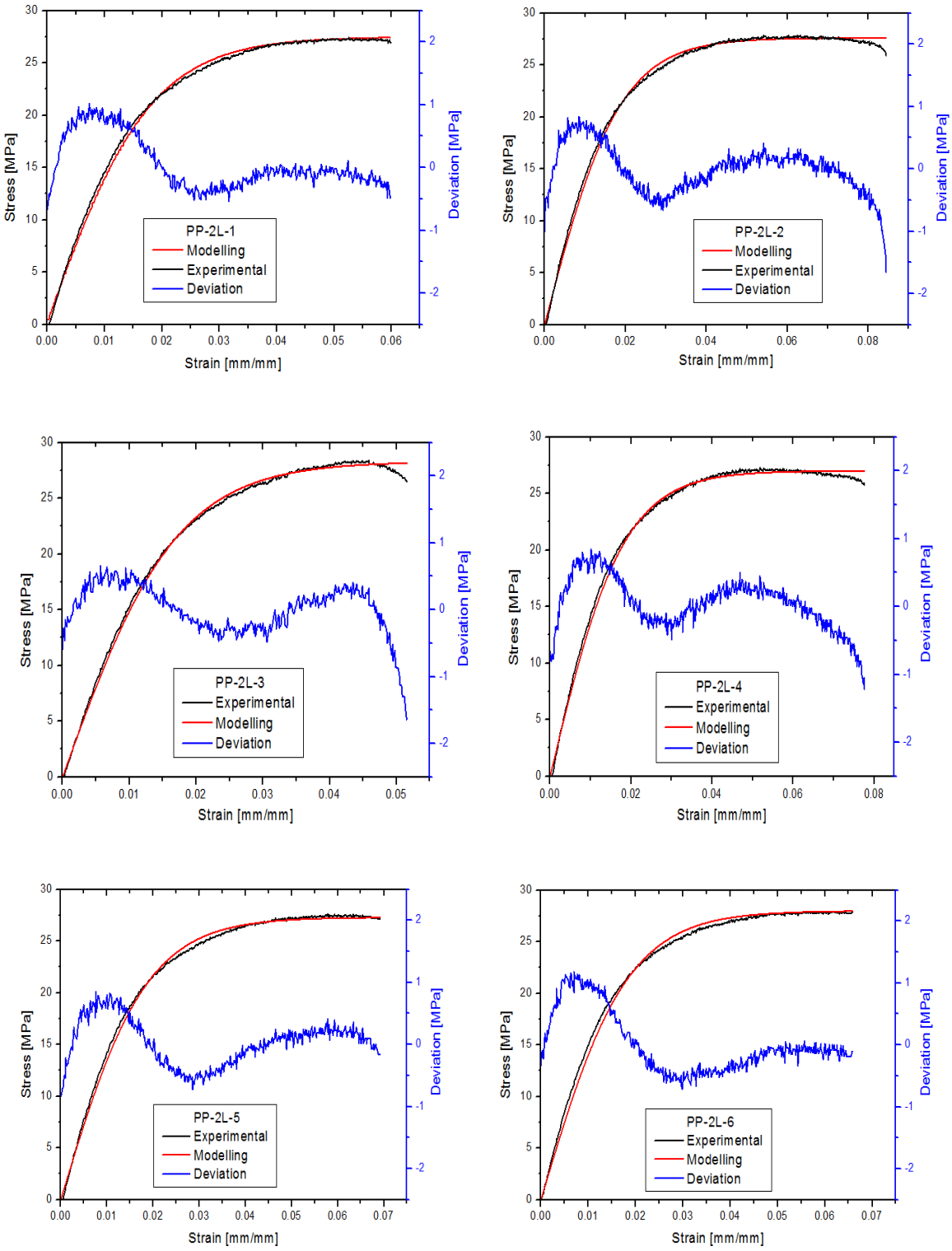

Source: author.

Figure 7.6. Experimental and modeling measurements in stress-strain curves on RPP.

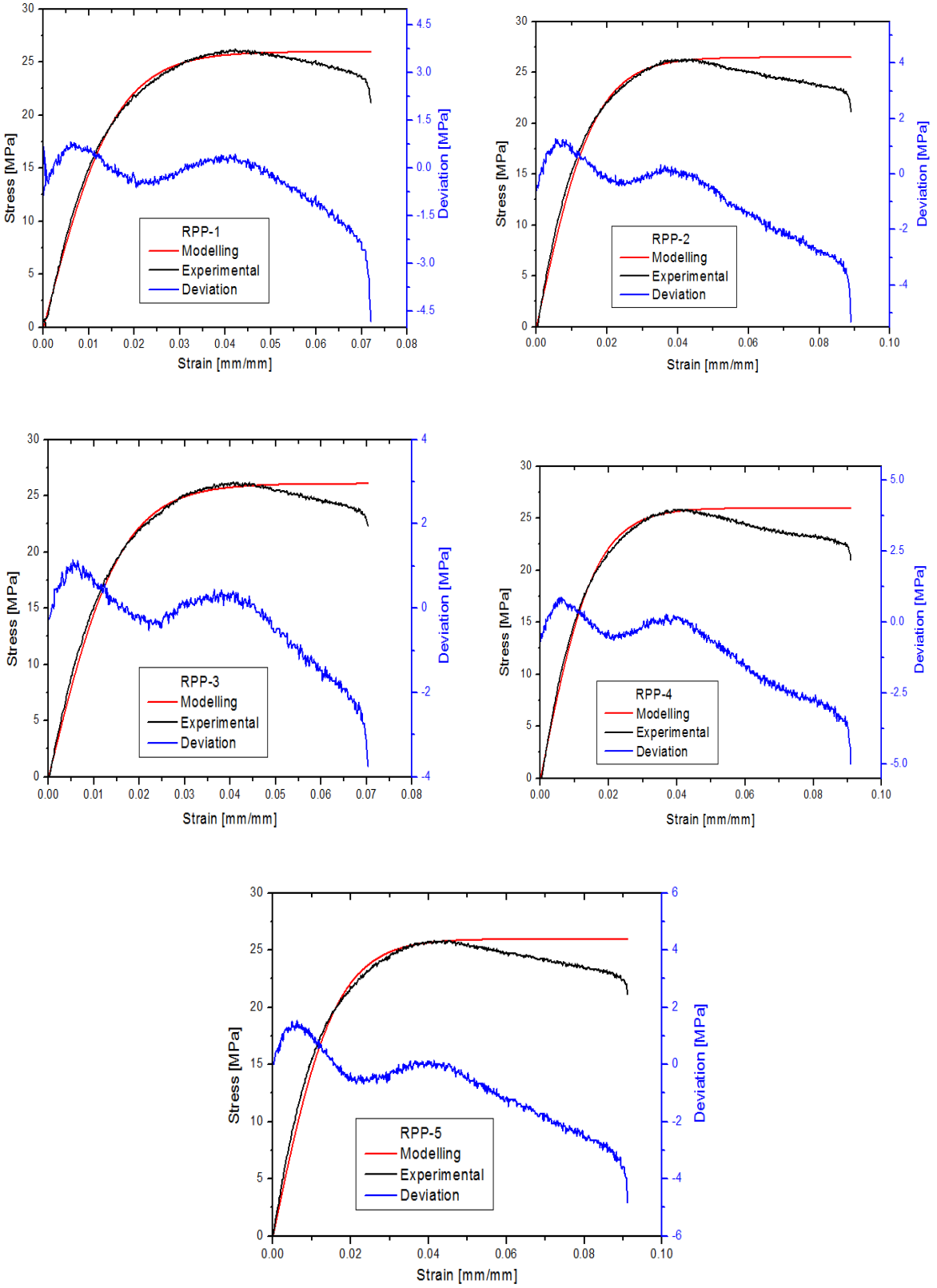

Source: author.

Figure 7.7. Experimental and modeling measurements in stress-strain curves on RPP-1L.

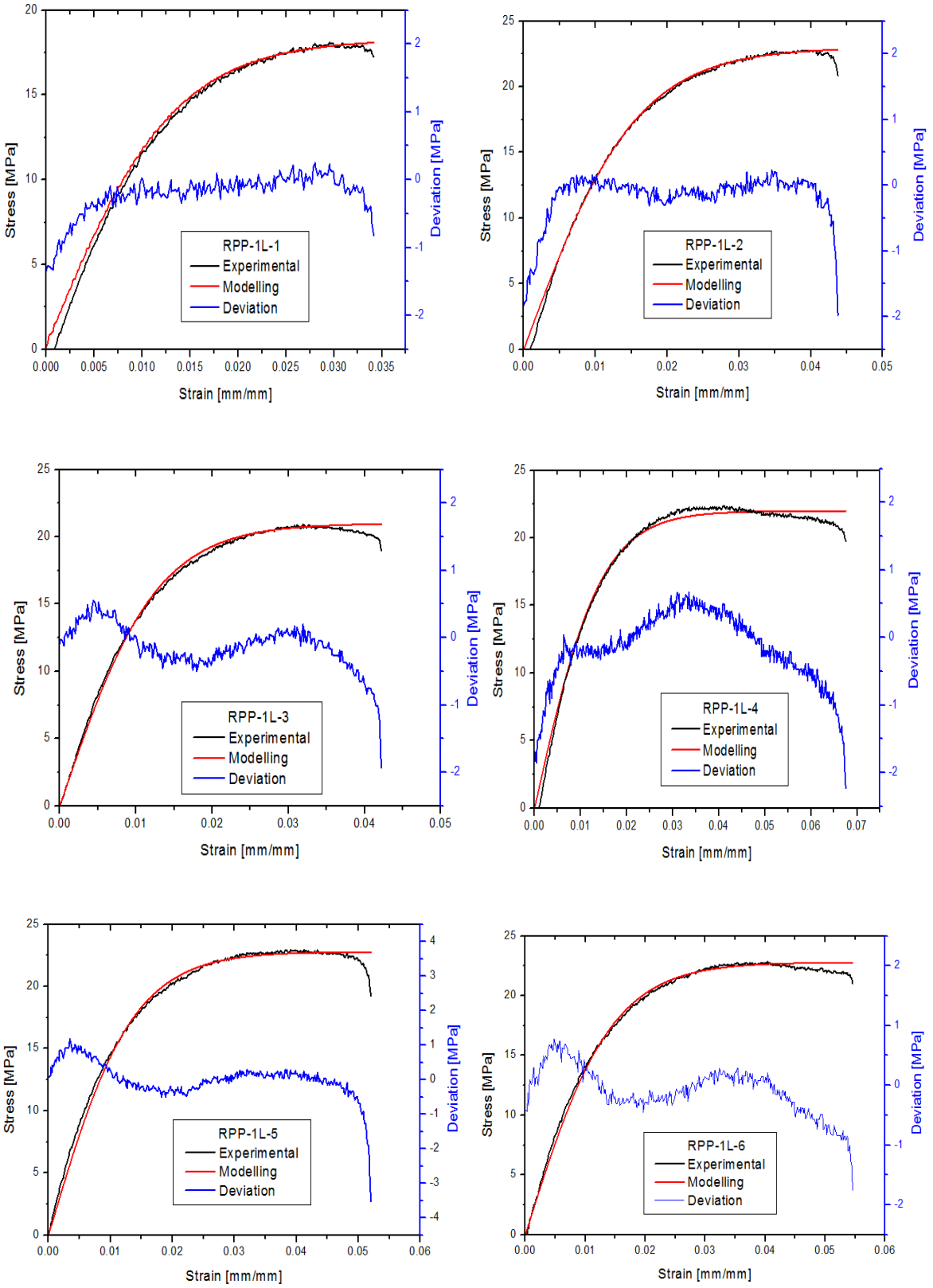

Source: author.

Figure 7.8. Experimental and modeling measurements in stress-strain curves on RPP-2L.

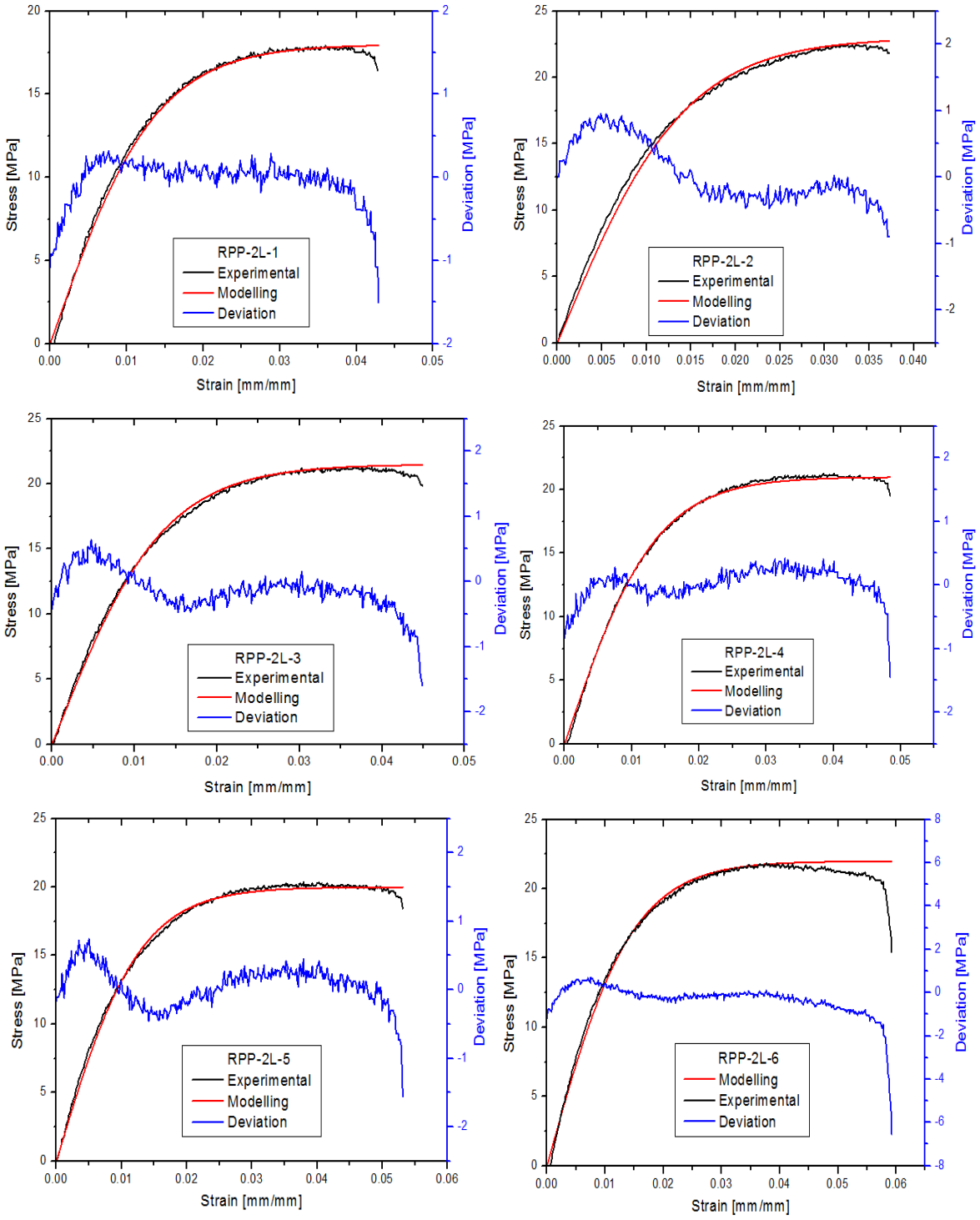

Source: author.

It was observed that the mechanical behavior provided by numerical and experimental model are similar. During most part of the two stress-strain curves, the deviations in the stress values are close to zero in the elastic and plastic regimes, except for the plastic regime of PP and RPP. The largest deviations are found when the stress of each material approached the

rupture, since the materials studied showed necking formation and decrease of the strength in the plastic regime.

After the necking onset, the numerical model adopted linear values until the rupture, not including the reduction of strength before the rupture, disregarding the necking formation. The model may predict the maximum stress, but it was not able to predict the ultimate stress. Therefore, PP and RPP, which had higher necking regions showed the higher differences between the experimental and calculated behaviors. Before the rupture onset, deviations did not exceed 1.5 MPa, representing, on average, 6% of the rupture strength of the PP, PP-1L, PP-2L, RPP, RPP-1L and RPP-2L.

Thus, the experimental mechanical behavior and the one obtained by numerical modeling presented proximity of 94%, allowing this model to be adopted as a valid tool to estimate the real mechanical behavior of materials used in this work. The characteristic parameters 'a' and 'b' of each material obtained by the model used are shown in Table 7.1.

Table 7.1. Material parameters using numerical modeling.

Material	Parameters															
	a								b							
	1	2	3	4	5	6	mean	std	1	2	3	4	5	6	mean	std
Coconut fiber	27	63	90	106	47		66.6	31.88	23	22	14	21	32		22.4	6.43
PP	30	29.5	28.5	30	29.5		29.5	0.61	37	37	35	38	38		37.0	1.22
PP-1L	28	28.5	27.4	27	28.5	27	27.7	0.70	58	55.5	55	57	54	59	56.4	1.91
PP-2L	27.5	26.5	28.3	27	27.3	28	27.4	0.66	55	54	58.3	55	54	55	55.2	1.59
RPP	26	26.5	26.1	26	26		26.1	0.22	63	61	63	63	63		62.6	0.89
RPP-1L	18.3	23	21	22	22.8	22.8	21.7	1.80	75	64	79	70	74	70	72.0	5.18
RPP-2L	18	23	21.5	21	20	22	20.9	1.74	73	70	74.4	74	79	69	73.3	3.59

Source: author.

According to the results in Table 7.1 and during the calibration of the model to the real behavior of material, it was observed that the parameter 'a' is more related to the maximum stress during the tensile test and the parameter 'b' is related mainly with the concavity of the stress-strain curve and, consequently, its ductility. Thus, it can be reported that the addition of coconut fibers reduced the parameter 'a' and the increased parameter 'b', ie, the addition of

coconut fibers reduced the maximum stress and increased the ductility. The experimental stress-strain curves are in agreement with this analysis.

Coconut fiber has the higher values for the parameters of the numerical model adopted and therefore this simulation also suggests that there was poor iteration between fiber and matrix, because PP decreased by 6.1 and 7.1% in the parameter 'a' after adding the first and second layers of coconut fiber mat, respectively. RPP decreased by 16.9 and 19.9%, respectively. However, PP had the parameter 'b' increased by 52.43 and 49.2% after adding the first and second coconut fiber layer, respectively. RPP had this last parameter increased by 15.0 and 17.1%, respectively.

The stress-strain relation obtained from test data of the coconut fibers, polymers and composite materials is known to be nonlinear, and it appears to follow a hyperbolic tangent curve. All nonlinear effects of the constitutive behavior are attributed to damage. This mechanical behavior is in agreement with high-density polyethylene (HDPE) wood-plastic composite materials studied by Lu (2002) and fiberglass composite materials studied by Marcelo (2004).

After the determination of the parameters that constitute the mechanical behavior, it was possible to determine the characteristic stress-strain curve of the materials studied by means of average values of the parameters ‘a’ and ‘b’ (Figure 7.9). The stress-strain curves for PP and RPP were plotted until the region where the model had good approximation with empirical results, ie, until the strain 0.075 to 0.05 mm/mm, respectively.

Figure 7.9. Stress-strain curves obtained by the numerical model.

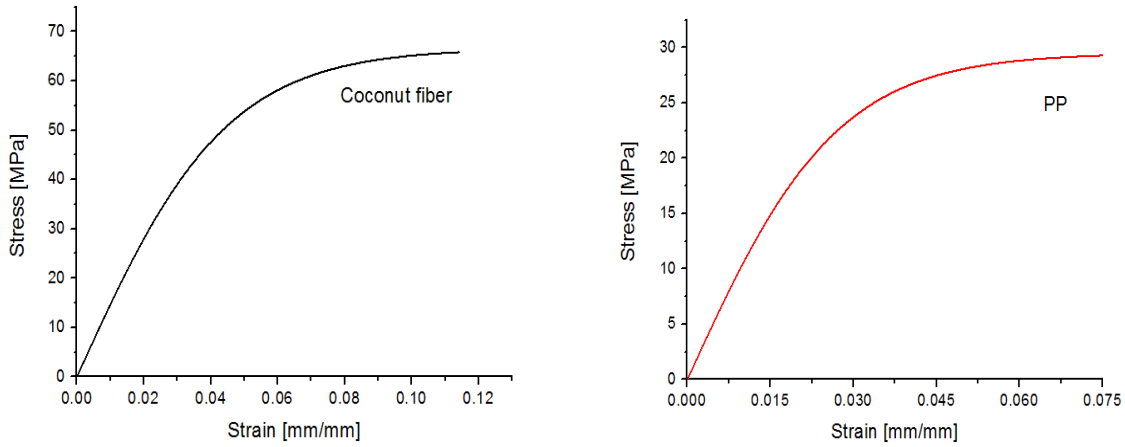

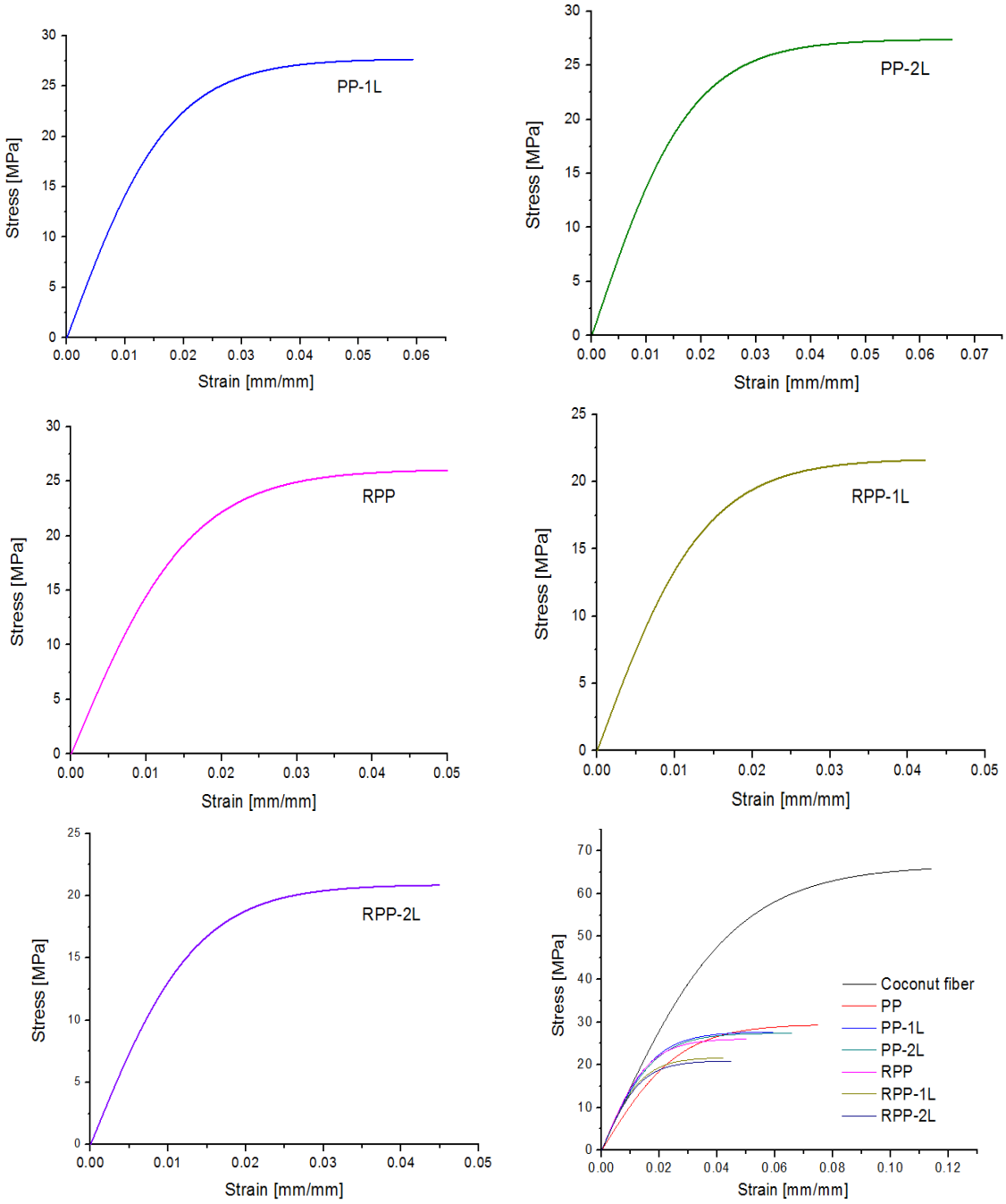

Source: author.

It can be seen that the adopted numerical model presented three material classes in terms of mechanical behavior. The first, with more strength and strain at break belongs to the coconut fiber; the second class belongs to the PP, PP-1L, PP-2L and RPP and the third belongs to the inferior mechanical performance: RPP-1L and RPP-2L. RPP was the material that suffered greatest reduction of mechanical properties with the addition of coconut fiber layers.

Lockyear (1999) modeled the stress-strain curve on high density polyethylene (HDPE) through a hyperbolic tangent and obtained a similar mechanical behavior from the elastic region until its rupture at 1.5% strain. Lu (2002) also found similarity between the experimental and mechanical behavior obtained by hyperbolic tangent on HDPE. However, the anisotropic characteristics found through of ductile and brittle observations found in some directions of this material could not be properly simulated by a single-element model. The same numerical modeling was used by Marcelo (2004) to predict the mechanical behavior of polymeric composite materials reinforced by glass fiber and, it was reported that the model predicted the maximum stress, but it was not able to predict the ultimate stress.

8. Damage mechanics

In this chapter, three approaches of evolution curves displaying damage measurements are presented. These curves are determined from numerical simulation parameters (chapter 7), from stiffness modifications during loading/unloading tensile test and from strain fields measured by DIC technique. The first two relate to the damage values using longitudinal strain and the third relates the damage fields and damage laws with longitudinal and transverse strains (equivalent strain).

8.1. Damage evolution from numerical simulation parameters

Mean values of parameters 'a' and 'b' shown in Table 7.1 (chapter 7) were substituted in the Equation 3.14 to determine the damage curves as a function of strain of each material. The evolution of the damage through numerical simulation parameters are presented in Figure 8.1. According to this simulation, the materials added by coconut fibers and RPP showed damage near the unit (completely damaged), starting this value in approximately 0.04 mm/mm (4%) of strain. Coconut fiber and PP, more ductile materials, showed damage close to the unit at higher deformations.

Figure 8.1. Damage evolution and stress-strain curves from numerical simulation parameters.

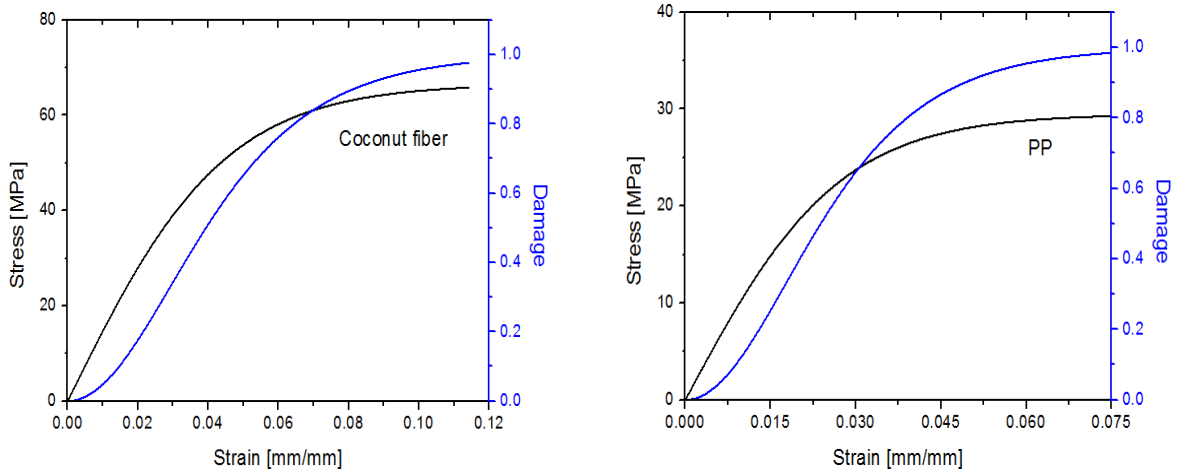

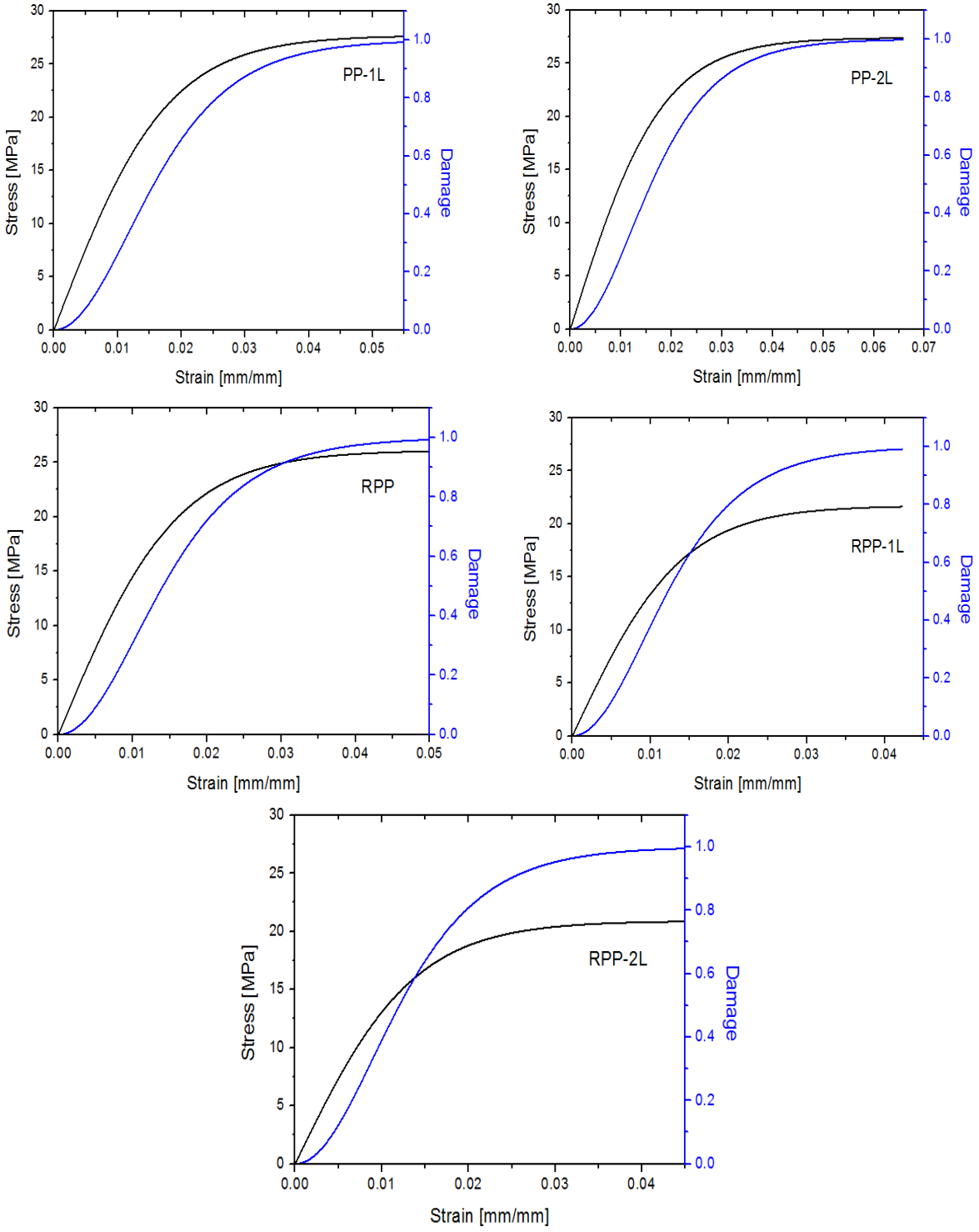

Source: author.

According to Lemaitre's theory (1984), the crack propagation of a material subjected to mechanical stress may occur during maximum loading and loading at break. The property related to the maximum and break stress is called critical damage.

The critical damage found on coconut fiber, PP-1L and PP-2L was close to zero (Table 8.1), because these materials showed proximity between both stresses, suggesting that the

initiation and crack propagation occur sequentially and immediately after the maximum stress (Marcelo, 2004). The stress-strain curves of these materials showed a close relationship between maximum stresses and rupture.

Composites manufactured with recycled polypropylene had more distinct stresses and therefore they presented higher values for the critical damage and more time to crack propagation and rupture. Marcelo (2004) found a critical damage 0.792 and 0.933, in addition to a large discrepancy between these two stresses in polymeric materials reinforced by glass fibers, demonstrating higher ductility than the materials of this work.

Table 8.1. Critical damage from experimental stress-strain curves.

Material	Critical damage							
	1	2	3	4	5	6	mean	std
Coconut fiber	0.03125	0.02222	0.03774	0.03279	0.04348		0.0335	0.0079
PP-1L	0.01173	0.00872	0.05199	001863	0.04323	0.02208	0.0261	0.0176
PP-2L	0.01824	0.06886	0.06471	0.05505	0.01813	0.00299	0.0380	0.0282
RPP	0.19108	0.19365	0.1465	0.1871	0.18065		0.1798	0.0192
RPP-1L	0.04608	0.08425	0.09163	0.11567	0.16	0.08029	0.0963	0.0384
RPP-2L	0.08372	0.02963	0.06667	0.08235	0.09426	0.29389	0.1084	0.0936

Source: author.

Figure 8.2 shows the deformation of PP-1L and RPP-1L by DIC analysis. The time between maximum and rupture stresses and the consequent rupture of these materials is more prolonged in recycled polypropylene composites (3.5 s for PP-1L and 16.12 s for RPP-1L).

Figure 8.2. Crack propagation in composite manufactured with PP and RPP during tensile testing: (a) composite PP-1L in maximum stress (30.63 s) and (b) during the rupture stress (34.13 s), resulting in 3.5 s crack propagation. (c) Composite RPP-1L during maximum stress (25.02 s) and (d) during the rupture stress (41.14 s), resulting in 16.12 s crack propagation.

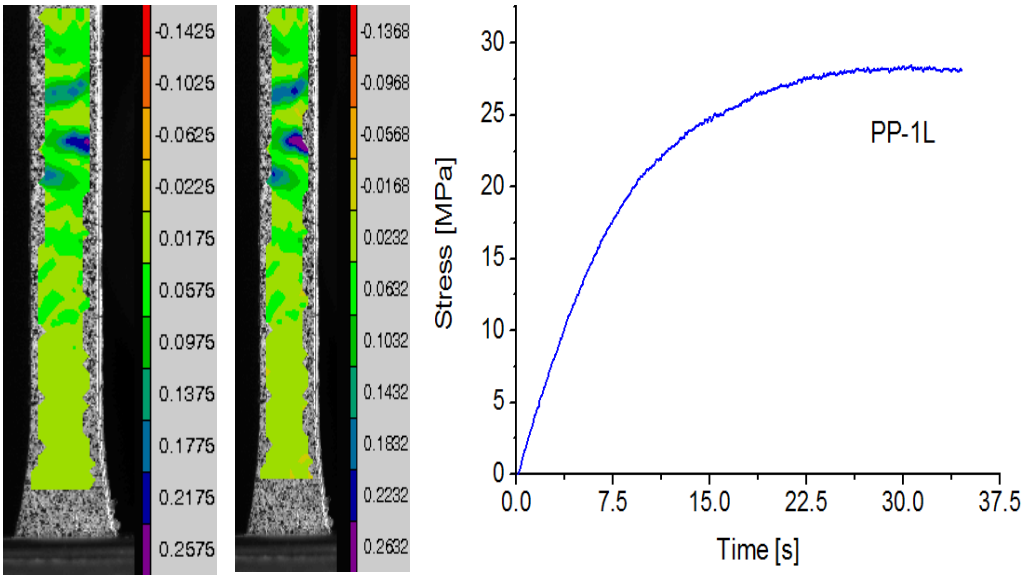

(a) (b)

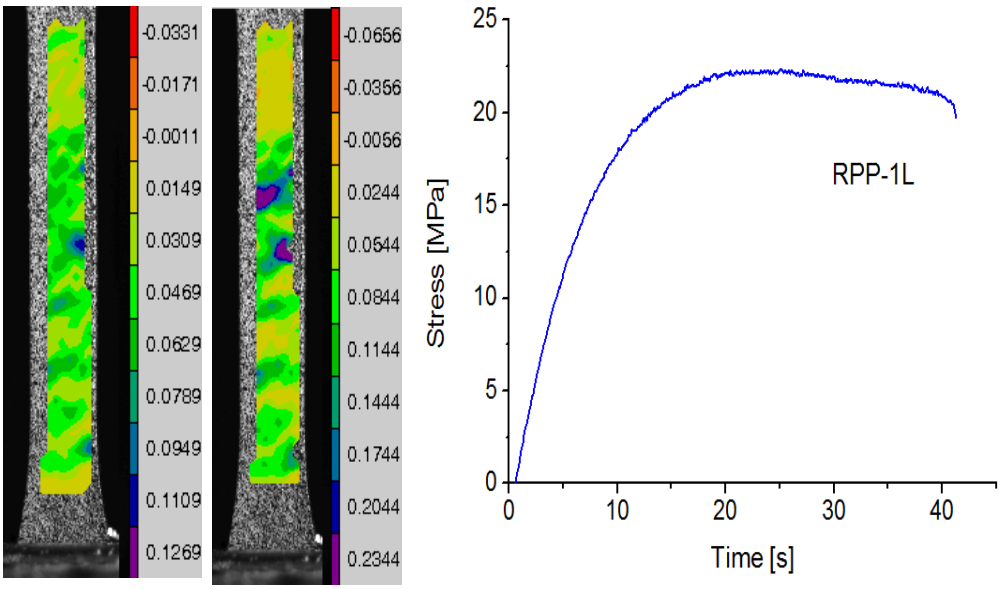

(c) (d)

Source: author.

8.2. Damage evolution using strain fields from DIC

The damage fields of each material were determined by the comparison between the image of undeformed material and images of deformed material. Figures 8.3 to 8.9 show the damage evolution on untreated coconut fiber with 280 μm in diameter, PP, PP-1L, RPP, RPP-1L and RPP-2L. These tests are chosen as representatives to show the behavior of each material. This present approach allows one to identify a damage law through longitudinal and transverse strains during uniaxial tensile test. Other damage laws used in this study just analyze longitudinal strains. The final damage on materials loaded in uniaxial direction is typically less than 0.5, but the coconut fiber, PP, PP-1L, PP-2L, RPP, RPP-1L, RPP-2L presented around of 0.63 (Périé et al., 2002).

Périe et al. (2009) found between 0.7 and 0.8 of final damage on a carbon/carbon composite subjected to 11 biaxial loading and unloading. Hild & Roux (2008) found a final damage close to the unit on vinyl ester/glass fibers composite under biaxial loadings, suggesting that the composites submitted to biaxial loadings have a higher final damage. Furthermore, these materials researched in the literature present a brittle behavior and possess different values for the final damages.

According to damage fields shown in the Figures 8.3 to 8.9, it was possible to visualize that the most affected regions after the onset of the plastic region on each material increased in intensity and extension, becoming the fracture region or rupture indication. The damage fields are practically nonexistent in the elastic region, demonstrating that the longitudinal strains are prevalent relative to the transverse strains in the process of damaging the material.

Even if this approach of damage evolution associate the longitudinal and transverse strain (resulting in equivalent strain), any damaged regions in the elastic region of stress x strain curve were not found, suggesting that the transverse strains did not have sufficient magnitude to represent damaged regions. Damage points on coconut fibers, PP, PP-1L, PP-2L, RPP, RPP-1L and RPP-2L were started at 2.17%, 2.495%, 1.501%, 1.599%, 1.6456%, 1.4876% and 1.4086% respectively.

Figure 8.10 shows a comparison between the measured and computed (reconstructed) displacement fields (in pixels) in the instant F for coconut fiber. The corresponding residual here is estimated to be $\rho = 0.259078$ and the difference between measured and computed measurements estimated in 20%, the same value found in biaxial testing on carbon/carbon composites (Périé et al., 2009). A good agreement is also observed between the prescribed and identified laws for PP, PP-1L, PP-2L, RPP, RPP-1L and RPP-2L. The corresponding

residual was estimated to be 0.061971, 0.051668, 0.046721, 0.050685, 0.056788 and 0.072723, respectively, and the difference of displacement field measurements are estimated in 0.95%, 3.33%, 3.17%, 5.00%, 5.00% and 4.00%, respectively. Thus, the reconstructed displacement fields coincide with the measurements.

Figure 8.3. Damage evolution on untreated coconut fiber (Ø = 280µm) using strain fields from DIC (ε_p = 0.4 x [1, 2, 4, 8, 16]; C_p = [-10, 12936, 20376, 24373, 26446]; ν = 0.780).

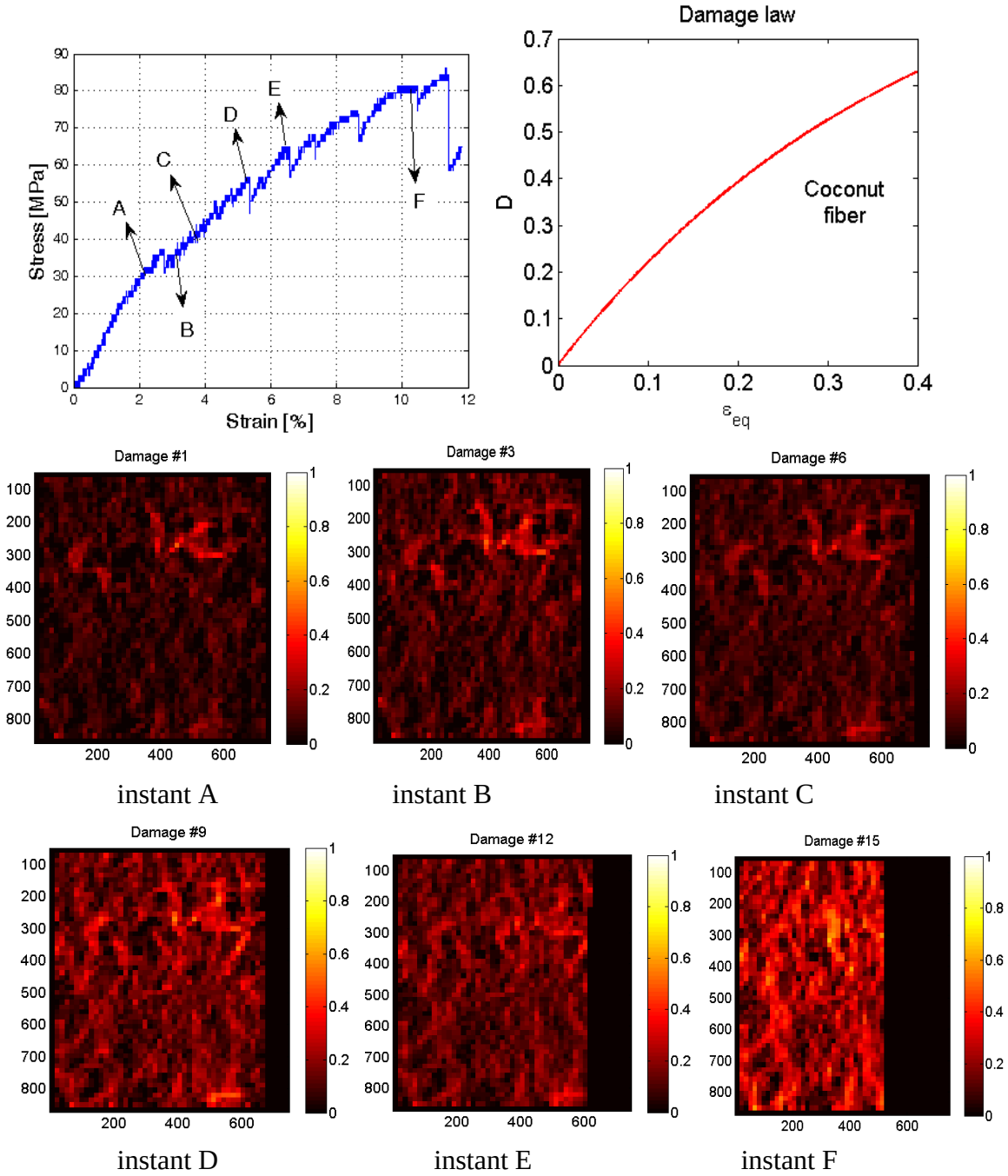

Source: author.

Figure 8.4. Damage evolution on PP using strain fields from DIC (ε_p = 0.4 x [1, 2, 4, 8, 16]; C_p = [-1, 902.5, 1513.4, 1868.7, 2060.2]; ν = 0.377).

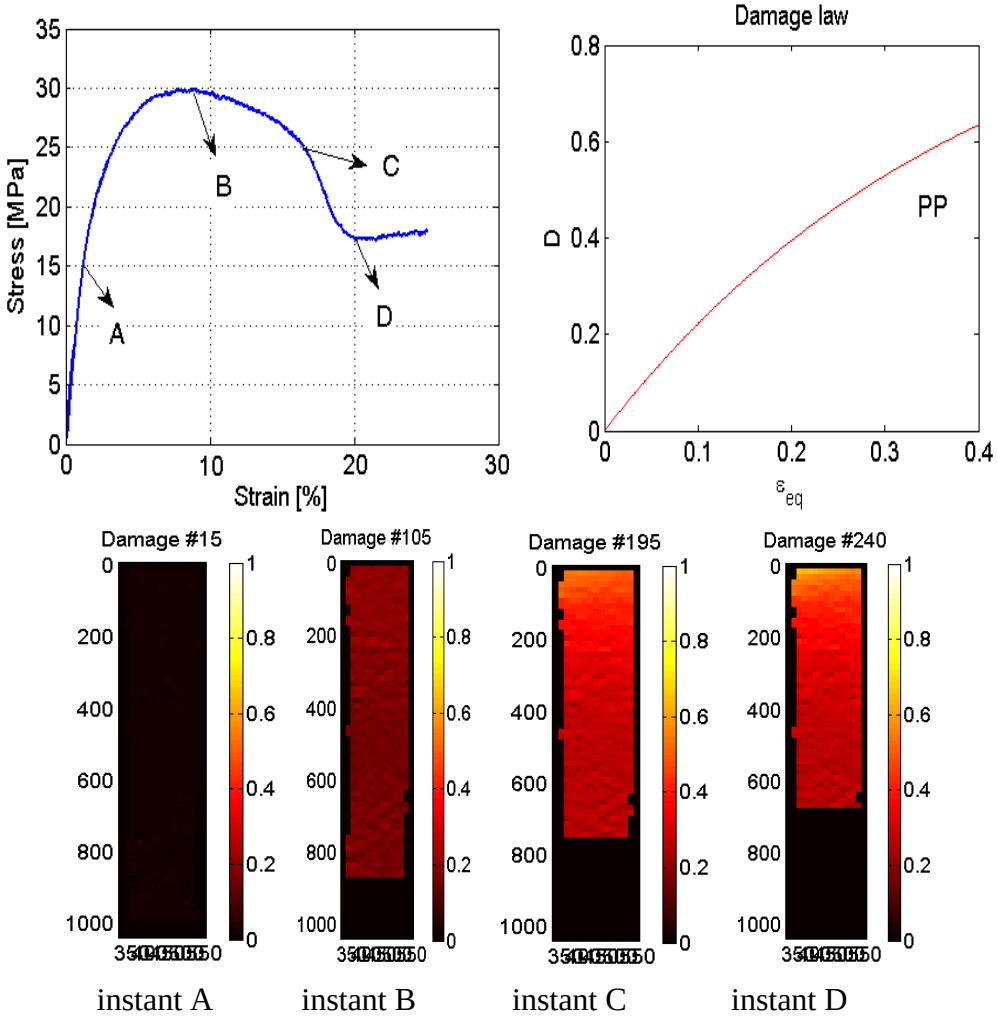

instant A instant B instant C instant D

Source: author.

Figure 8.5. Damage evolution on PP-1L using strain fields from DIC (ε_p = 0.4 x [1, 2, 4, 8, 16]; C_p = [-1, 556.8, 875.7, 1046.6, 1135.1]; ν = 0.292).

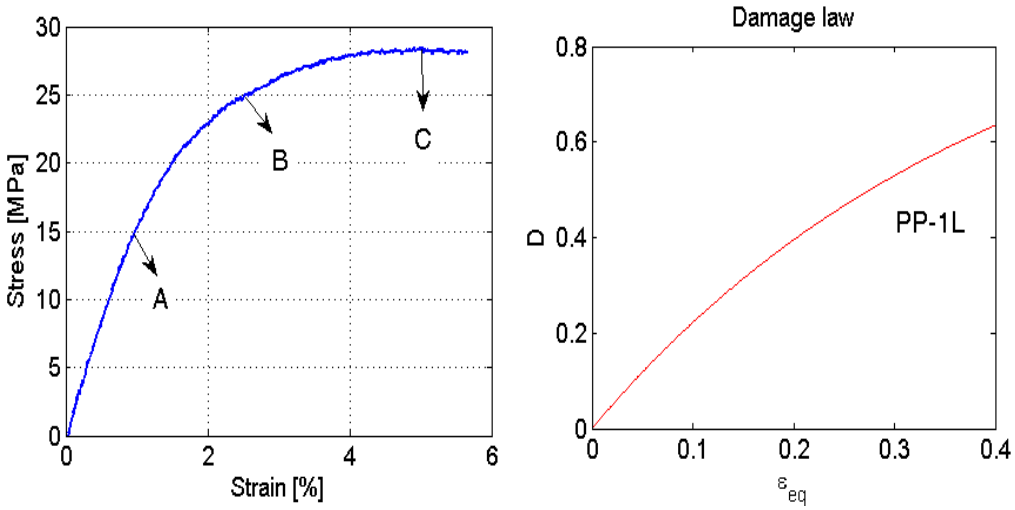

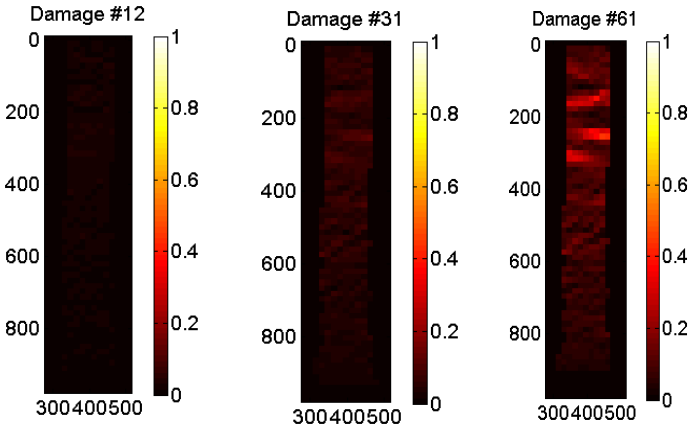

Source: author.

Figure 8.6. Damage evolution on PP-2L using strain fields from DIC (ε_p = 0.4 x [1, 2, 4, 8, 16]; C_p = [-1, 240.1, 372.1, 441.4, 476.9]; ν = 0.319).

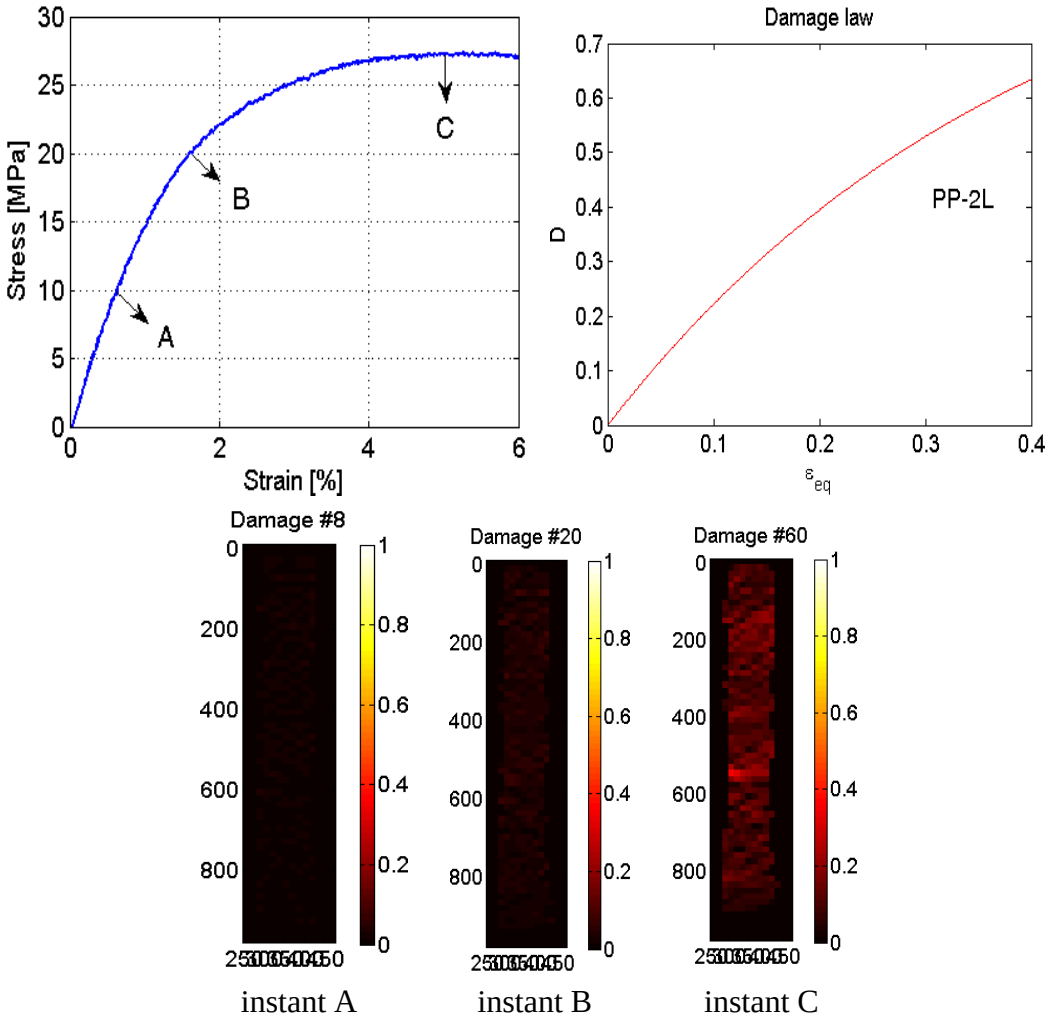

Source: author.

Figure 8.7. Damage evolution on RPP using strain fields from DIC (ε_p = 0.4 x [1, 2, 4, 8, 16]; C_p = [-1, 503.2, 791.9, 946.8, 1027.1]; ν = 0.3317).

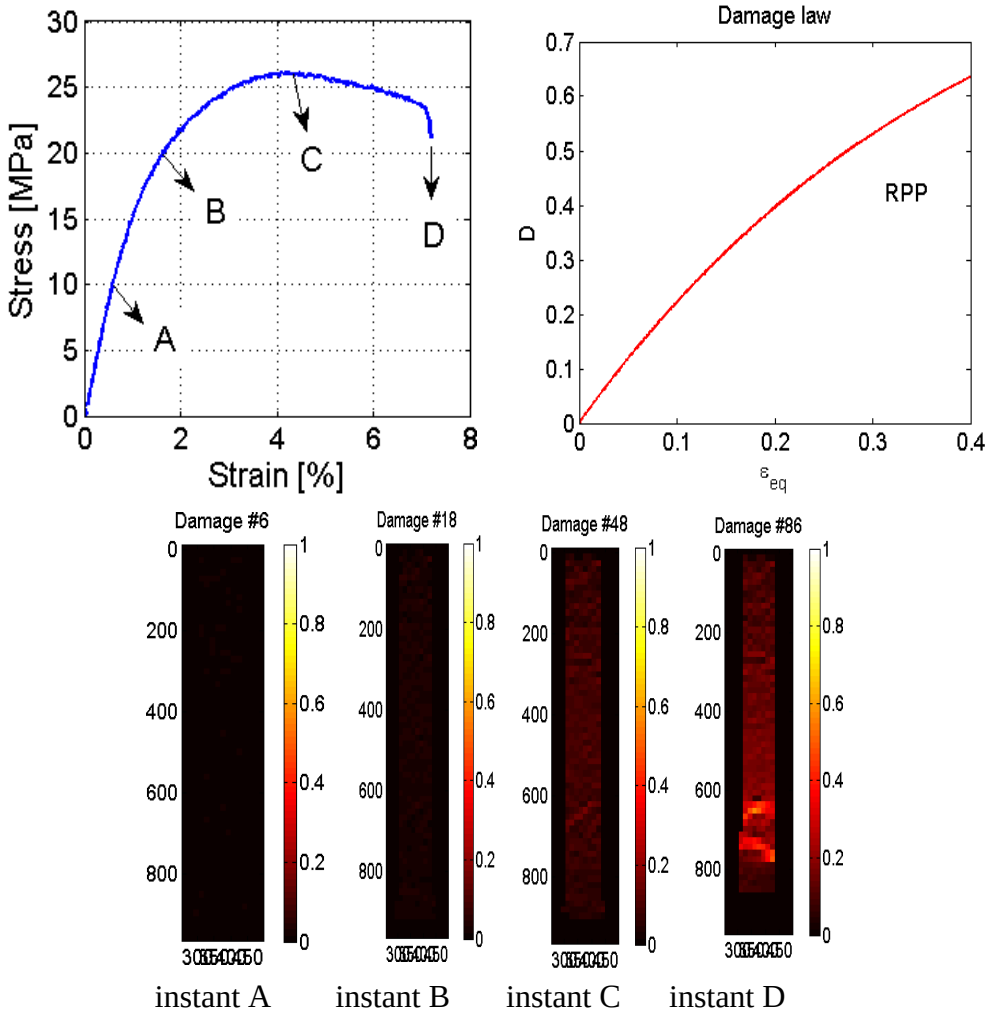

Source: author.

Figure 8.8. Damage evolution on RPP-1L using strain fields from DIC (ε_p = 0.4 x [1, 2, 4, 8, 16]; C_p = [-1, 82.0, 127.6, 151.7, 164.1]; ν = 0.3333).

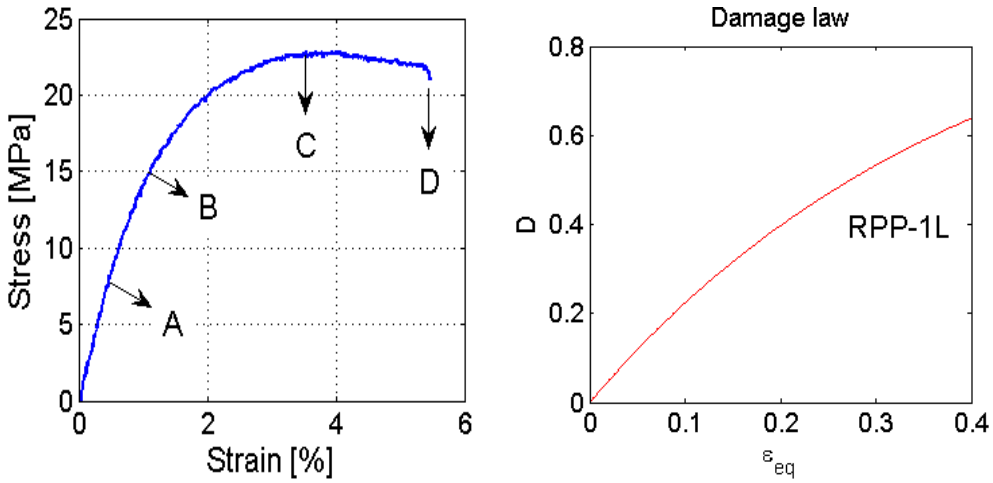

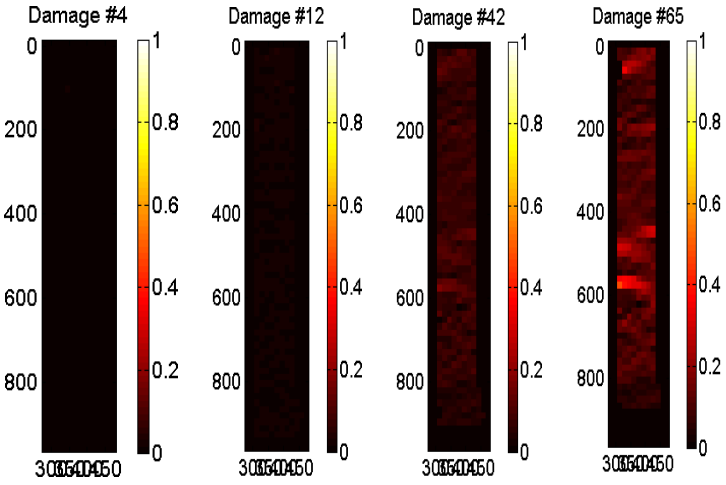

Source: author.

Figure 8.9. Damage evolution on RPP-2L using strain fields from DIC (ε_p = 0.4 x [1, 2, 4, 8, 16]; ν = 0.3213).

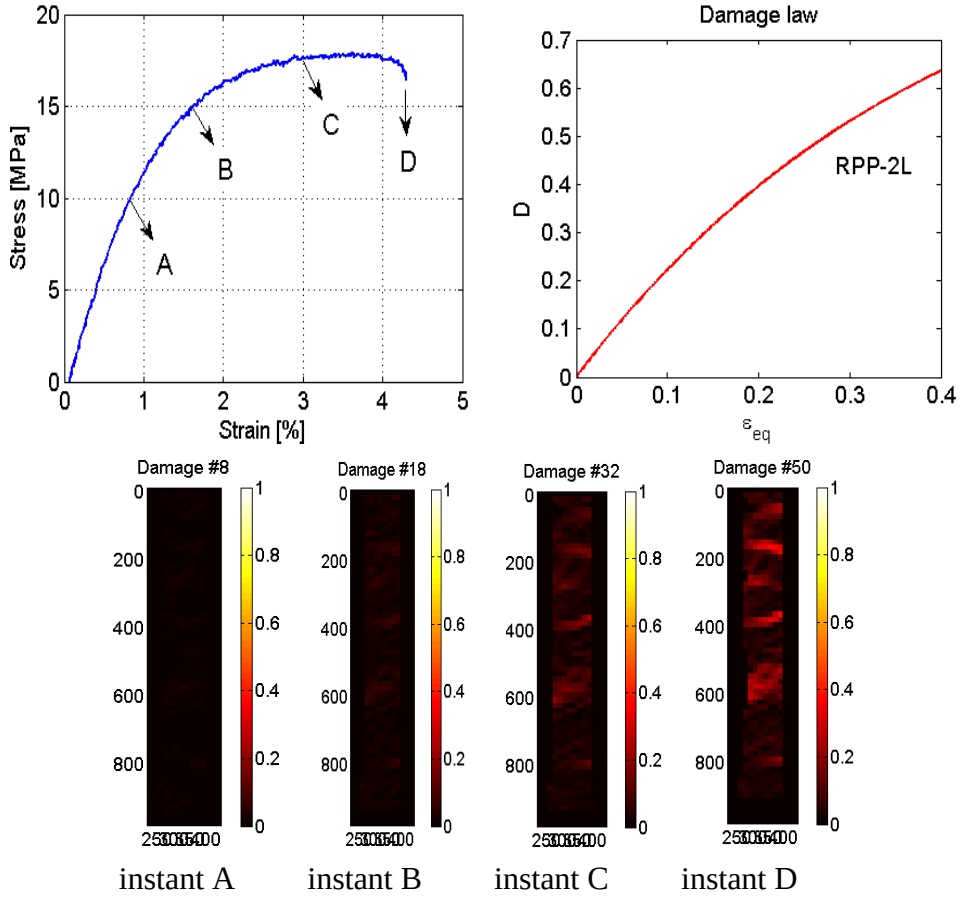

Source: author.

Figure 8.10. Comparison between measured and reconstructed displacements (expressed in pixels), and corresponding differences for the last instant on (a) coconut fiber, (b) PP, (c) PP-1L, (d) PP-2L, (e) RPP, (f) RPP-1L and (g) RPP-2L.

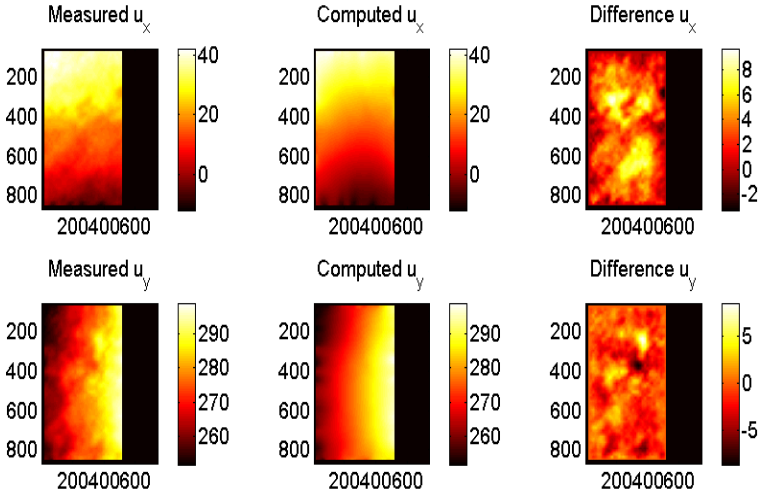

(a)

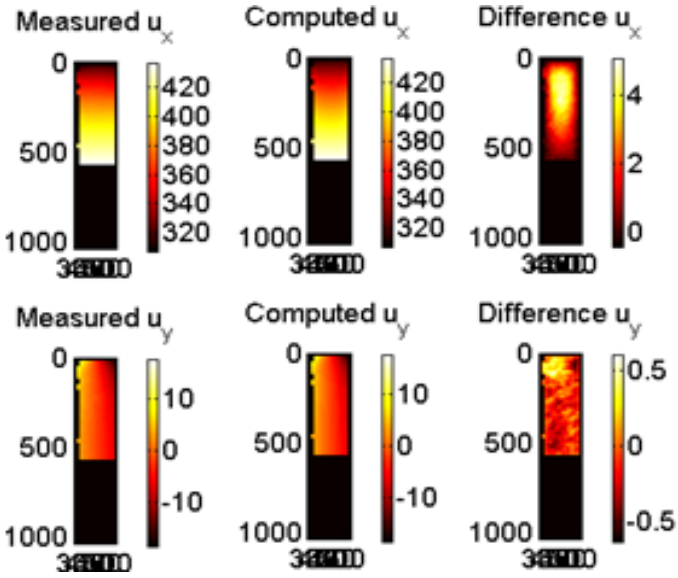

(b)

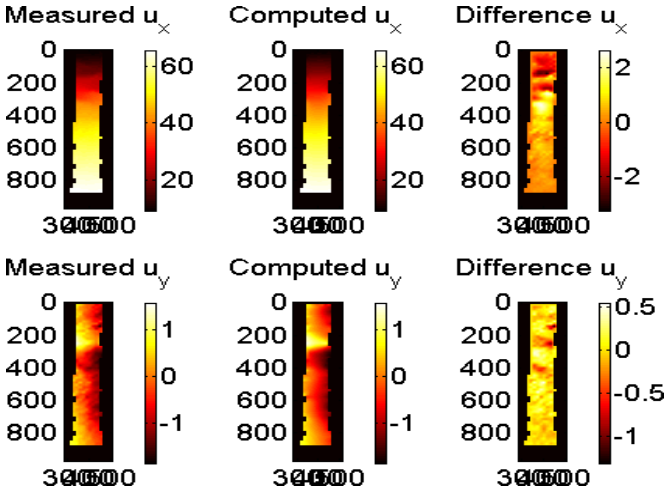
Measured u_x
Computed u_x
Difference u_x
Measured u_y
Computed u_y
Difference u_y

(c)

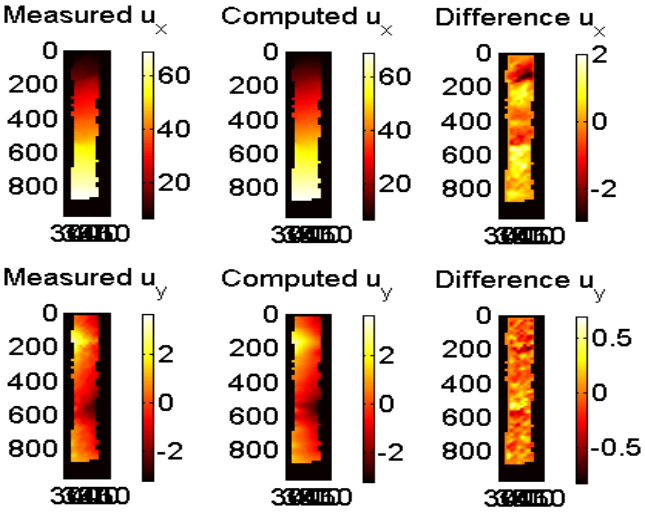
Measured u_x
Computed u_x
Difference u_x
Measured u_y
Computed u_y
Difference u_y

(d)

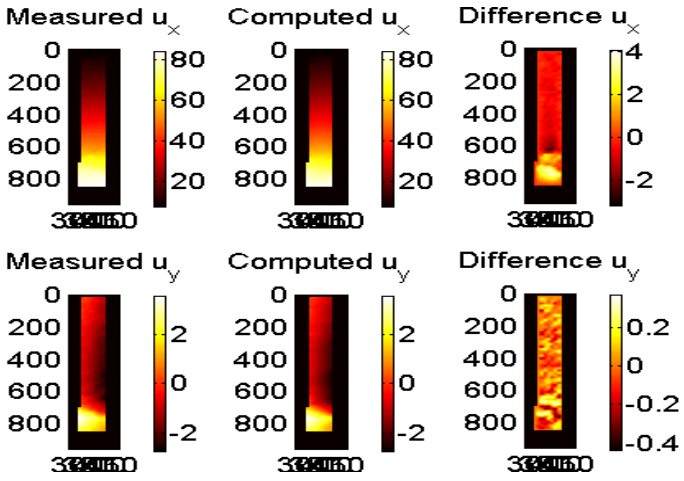
Measured u_x
Computed u_x
Difference u_x
Measured u_y
Computed u_y
Difference u_y

(e)

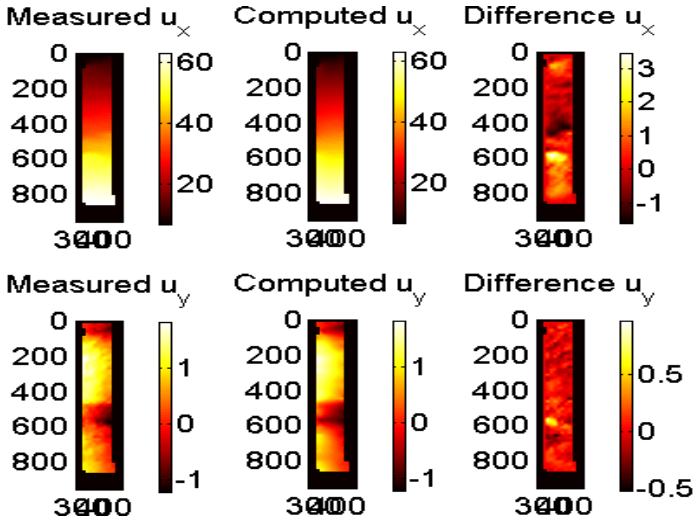

(f)

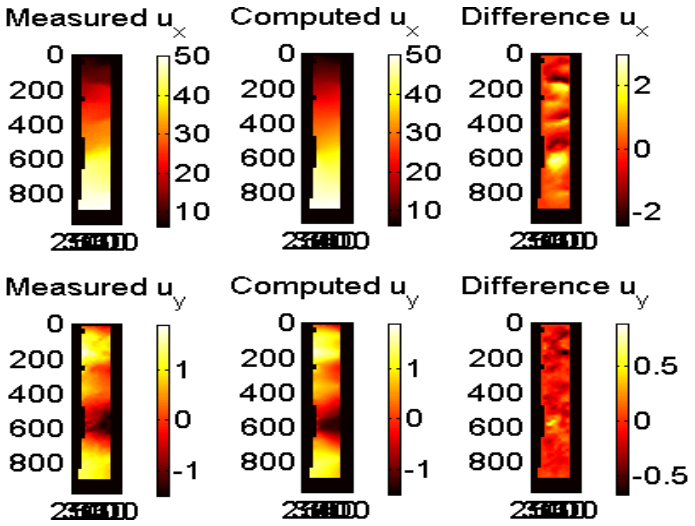

(g)

Source: author.

8.3. Damage evolution from load/unload tensile testing

Figure 8.11 shows the rupture observations on PP-2L during load/unload tensile testing with four cycles of loading. At the beginning of the second cycle of loading it was possible to determine the fracture region (Figure 8.11 (a)). The rupture propagation (Figure 8.11 (b)) began in last cycle and some coconut fibers were visualized in the final rupture (Figure 8.11 (c)).

Figure 8.11. Rupture observations on PP-2L by DIC during load/unload tensile testing: (a) 33.12 s; 5.17 MPa; 0.004 pix/pix (second cycle of loading; average engineering longitudinal strain) (b) 140.49 s; 26.19 MPa; 0.05246 pix/pix (engineering longitudinal strain) and (c) 140.99 s.

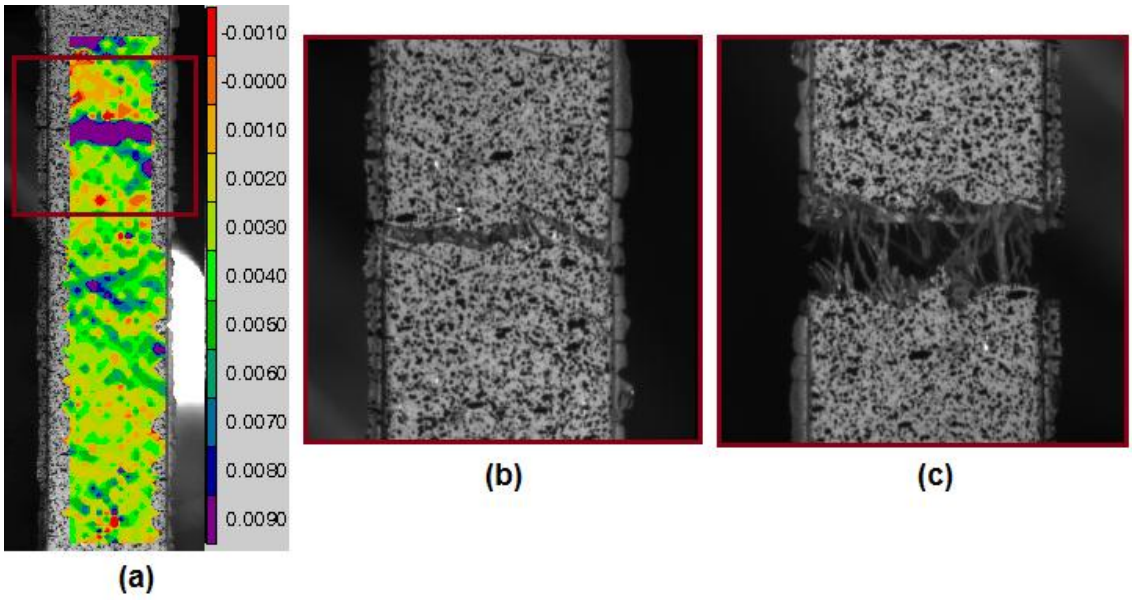

Source: author.

According to Equation 2.15, it is necessary to plot the true stress-strain curve to determine the damage evolution through stiffness modifications of the material submitted to the load/unload tensile testing. The modulus of elasticity will be used to determine the modifications in the stiffness.

Figure 8.12 presents the engineering and true stress-strain curves on the same PP-2L discussed. It is possible to report that the two curves are similar (Figure 8.12 (a)) and the values found for the damage evolution are also similar (Figure 8.12 (b)). Due to this proximity, and in order to simplify the determination of the damage evolution on the materials of this work, the engineering stress-strain curve will be used to determine changes in their stiffnesses and the progress of their damage during load/unload tensile testing.

Figures 8.13 show the tensile test after loading/unloading cycles on PP, PP-1L, PP-2L, RPP, RPP-1L and RPP-2L, in order to determine the damage through the evolution of the stiffness modifications during longitudinal strains.

Figure 8.12. (a) Engineering and true stress-strain curves on PP-2L and (b) engineering and true damage measurements during load/unload tensile testing.

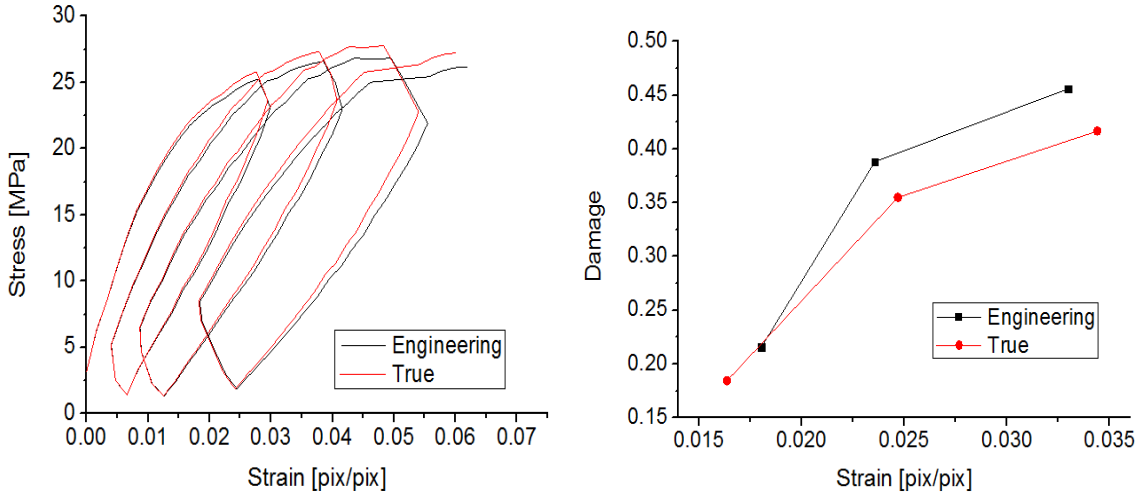

Source: author.

Figure 8.13. Loading/unloading cycles and damage evolution on PP, PP-1L, PP-2L, RPP, RPP-1L and RPP-2L through engineering stress-strain curves.

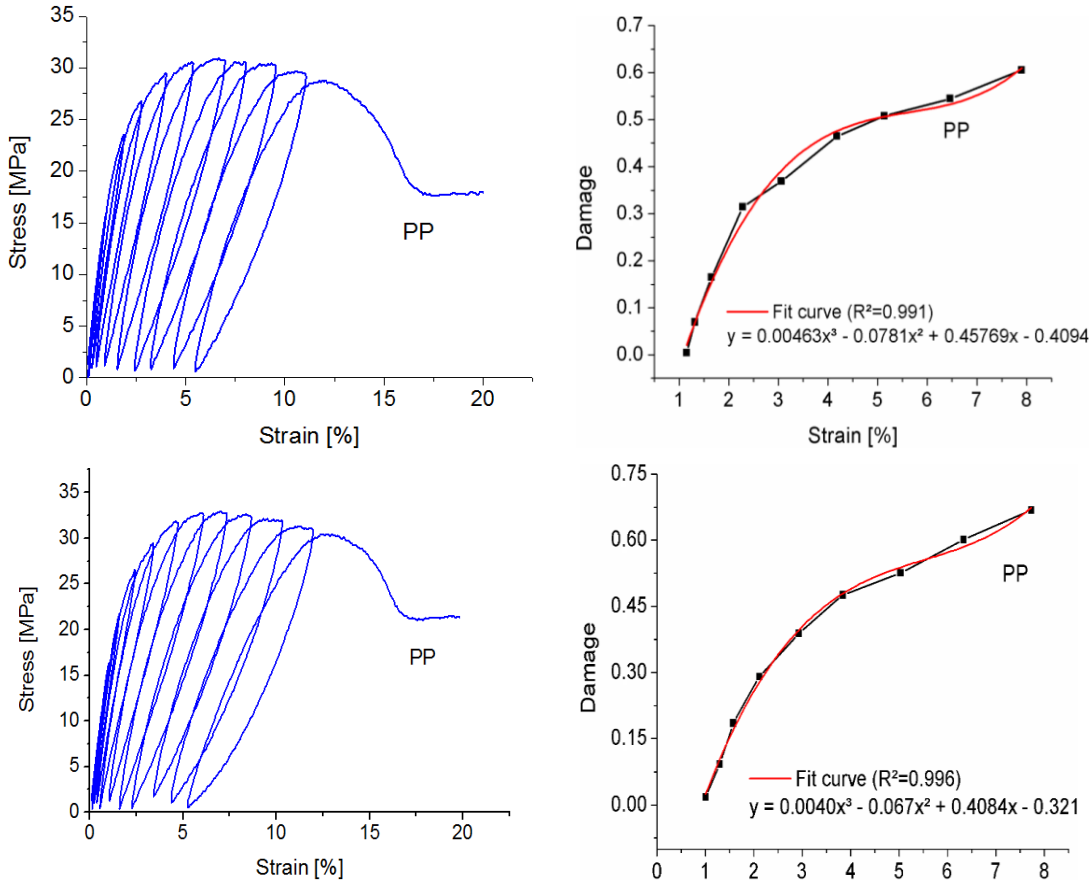

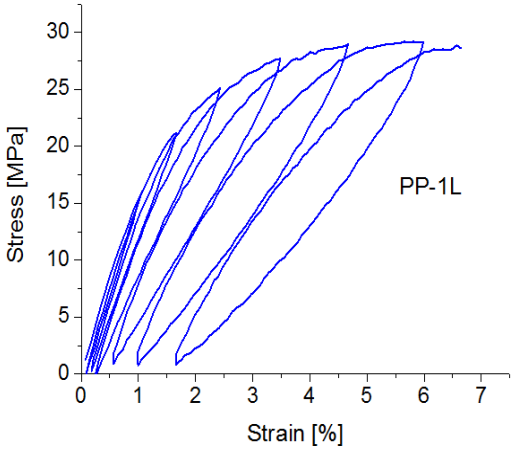
Stress [MPa]
Strain [%]
PP-1L

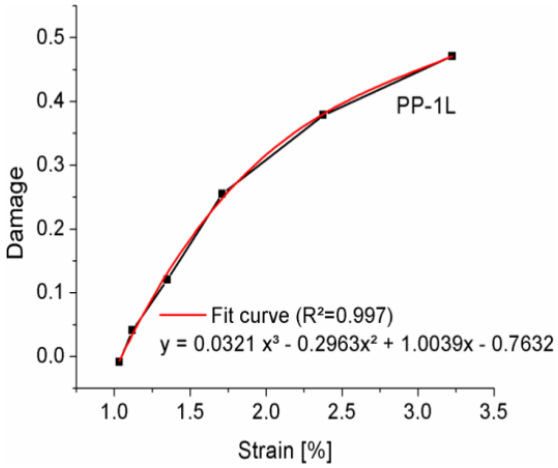
Damage
Strain [%]
PP-1L
Fit curve (R²=0.997)
y = 0.0321 x³ - 0.2963x² + 1.0039x - 0.7632

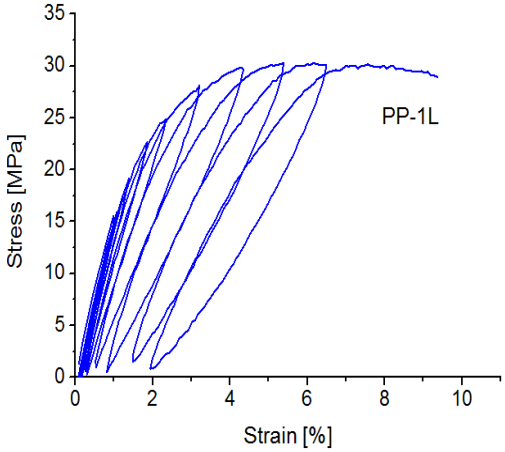
Stress [MPa]
Strain [%]
PP-1L

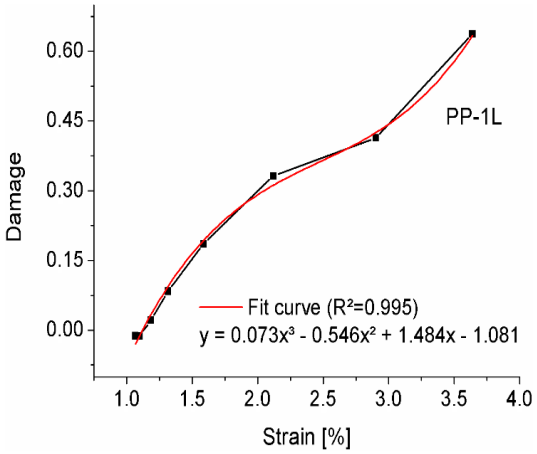
Damage
Strain [%]
PP-1L
Fit curve (R²=0.995)
y = 0.073x³ - 0.546x² + 1.484x - 1.081

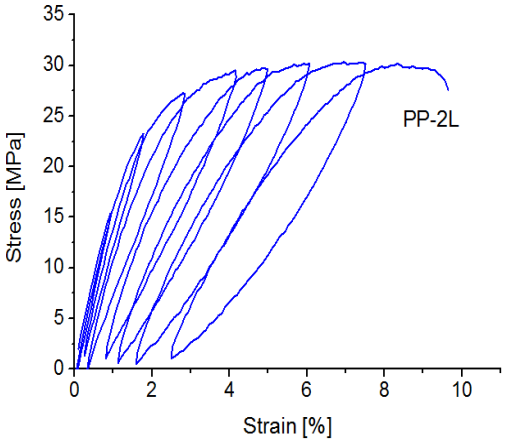
Stress [MPa]
Strain [%]
PP-2L

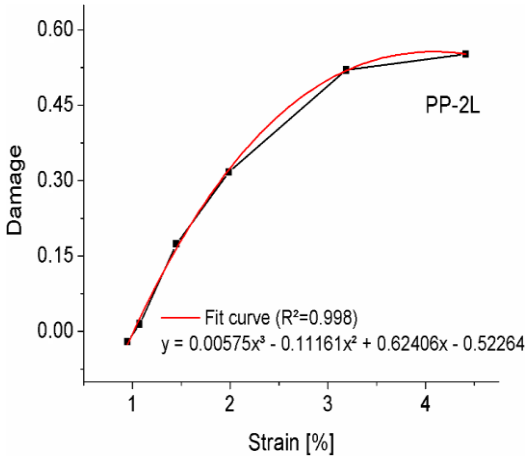
Damage
Strain [%]
PP-2L
Fit curve (R²=0.998)
y = 0.00575x³ - 0.11161x² + 0.62406x - 0.52264

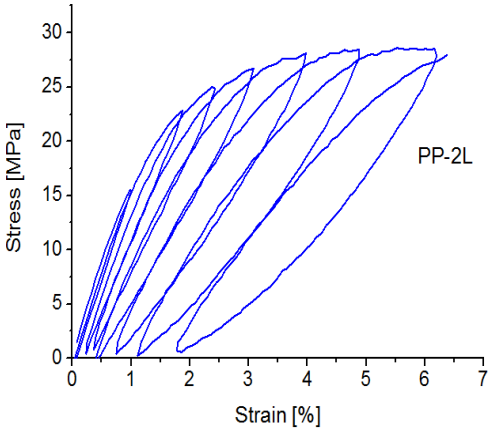
Stress [MPa]
Strain [%]
PP-2L

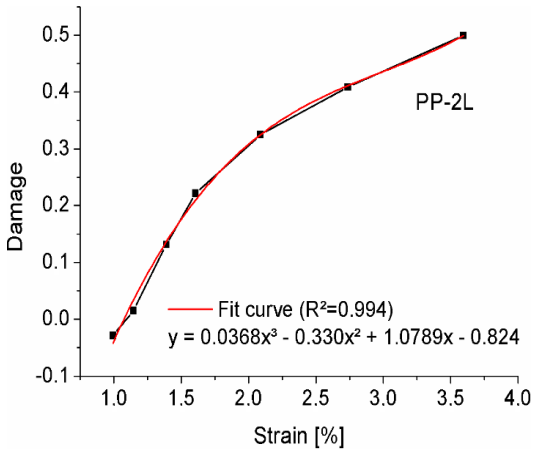
Damage
Strain [%]
PP-2L
Fit curve (R²=0.994)
y = 0.0368x³ - 0.330x² + 1.0789x - 0.824

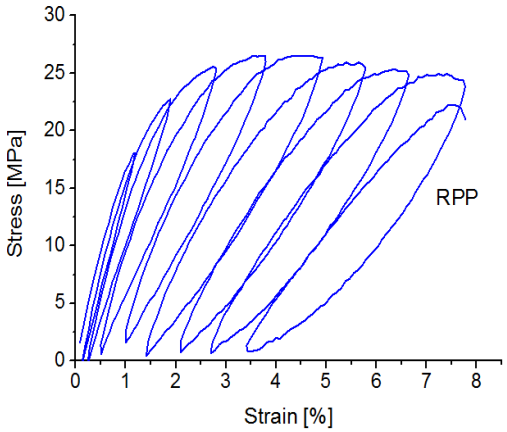
Stress [MPa]
Strain [%]
RPP

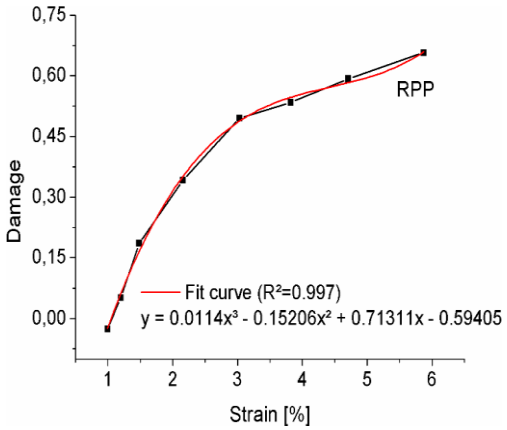
Damage
Strain [%]
RPP
Fit curve (R²=0.997)
y = 0.0114x³ - 0.15206x² + 0.71311x - 0.59405

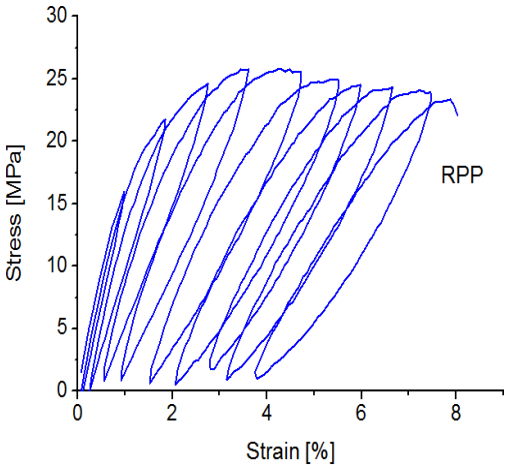
Stress [MPa]
Strain [%]
RPP

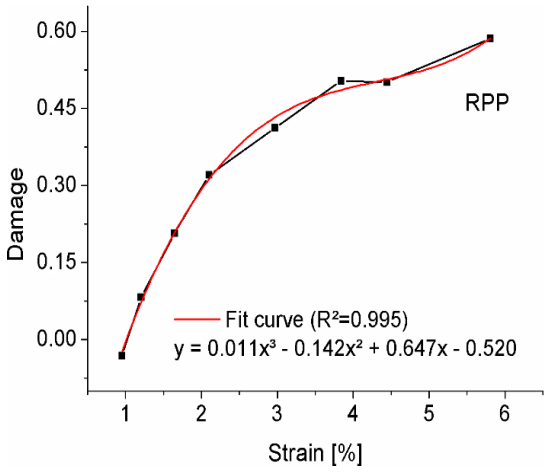
Damage
Strain [%]
RPP
Fit curve (R²=0.995)
y = 0.011x³ - 0.142x² + 0.647x - 0.520

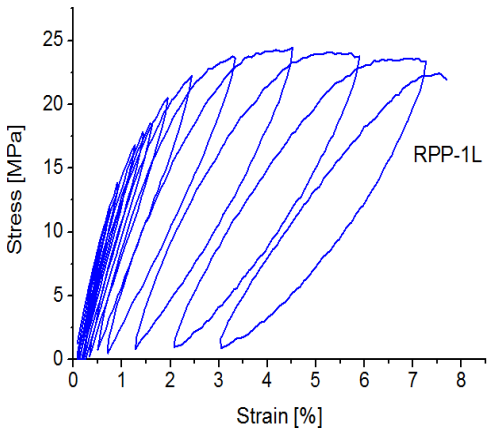
Stress [MPa]
Strain [%]
RPP-1L

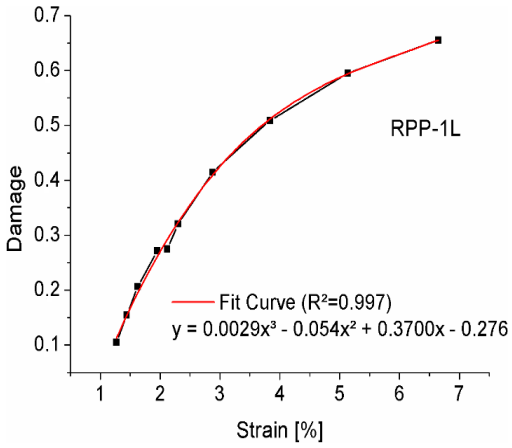
Damage
Strain [%]
RPP-1L
Fit Curve (R²=0.997)
y = 0.0029x³ - 0.054x² + 0.3700x - 0.276

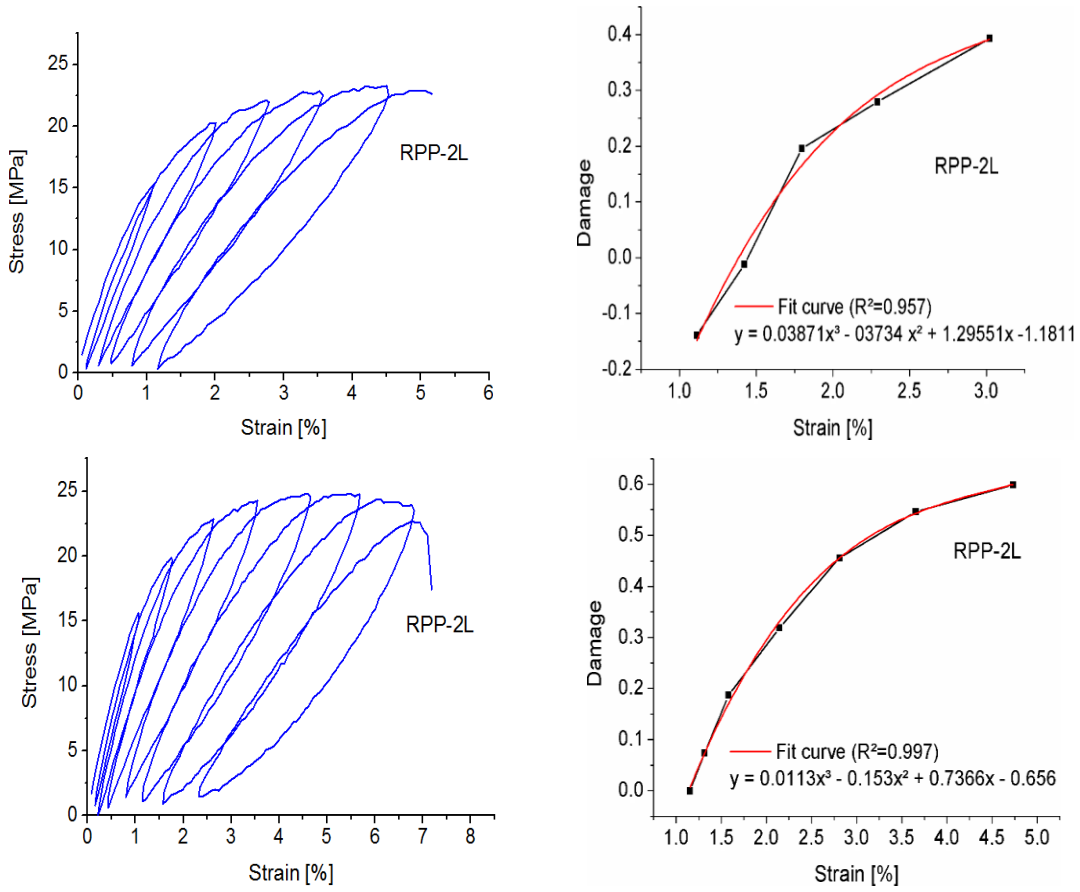

Source: author.

Stiffness modifications were found after the first loading for all materials of this study. An inelastic behavior was observed in these materials, since only part of the strains is recovered during unloading. Hysteresis in each loading during the plastic strains were found, suggesting that this material showed a nonlinear and elastoplastic behavior and was also subjected to the relaxation effect of their polymer bonds (Gerscovich, 2009).

Semicrystalline polymers, such as polypropylene, are viscoelastics (Gonçalez, 2013). Brusselle-Dupend et al. (2001) observed that after stress unloading, the PP does not instantaneously recover the initial strain during tensile testing. This strain is completely restored as a function of time, suggesting that the material presents a viscoelastic behavior (Brusselle-Dupend et al., 2001).

It can be seen in the curves of Figure 8.13 that in approximately 0.3 of damage and 2% of longitudinal strain there were regions where the degradation rate increased. This event is related to an intrinsic property of the material called critical damage (Dc) and presented a value of 0.3. This damage value was also found as an intrinsic property of reinforced polymer by glass fibers, after damage study using numerical model performed by Marcelo (2004).

Figure 8.13 also has plotted polynomial third order fitting curves with much agreement (R^2 minimum of 0.9957), indicating that the constitutive equations presented show good relationship between the longitudinal strain in the elastic and plastic regions (ε_{ep}) with the damage values.

Table 8.2 presents the longitudinal strains associated to the onset of the damages. The values shown are similar to those shown by Marigo's theory (1981). Marcelo (2004) found initial damage 1.4% (ε_{pD}) in polymers reinforced with glass fibers. After the start of each damage stage, the rupture happened by interatomic separation. The strain during the final damage (ε_{pR}) was also inserted in this Table and it is related to the final elongation at break previously mentioned, in which the fiber addition decreased these values. Some ε_{pR} values are also in agreement with the values found by Marigo's theory (1981), since both approaches used the same final elongation at break for its determination.

Table 8.2. Damage measurements in load/unload testings.

Material	**Strain at damage initiation (ε_{pD})**	**Strain at final damage (ε_{pR})**	**Damage at final rupture**
PP (sample 1)	1.652%	7.900%	0.6049
PP (sample 2)	1.573%	7.728%	0.6683
PP-1L (sample 1)	1.586%	3.640%	0.6367
PP-1L (sample 1)	1.349%	3.225%	0.4709
PP-2L (sample 1)	1.448%	4.410%	0.5519
PP-2L (sample 2)	1.389%	3.594%	0.4996
RPP (sample 1)	1.481%	5.871%	0.6572
RPP (sample 2)	1.266%	5.806%	0.5862
RPP-1L (sample 1)	1.270%	6.648%	0.6550
RPP-2L (sample 1)	1.797%	3.021%	0.3930
RPP-2L (sample 2)	1.580%	4.733%	0.5988

Source: author.

According to damage evolution equation and the data reported in Table 8.2, the addition of coconut fiber led to the rupture of the composites with lower modulus of elasticity, because there was a decrease of the final damages due to the fiber insertion. Some samples presented similar final damages to those found in the Marigo's theory (1981). Values between 0.5 and

0.9 final damage are generally found for quasi-brittle materials, as well as 0.2 to 0.3 and 0.2 to 0.5 for isotropic and anisotropic materials, respectively (Lemaitre et al., 2009).

Conclusions and perspectives

This study investigated the morphological and mechanical behaviors of coconut fiber, virgin and recycled polypropylene and composites fabricated by these materials. It was approached on deformation mechanisms, failure aspects, damage onset, as well as understand the micro-structural effects of coconut fiber addition in these polypropylenes.

From the viewpoint of morphological behavior, various parameters were determined, such as the average diameter of coconut fibers, empty areas inside this fiber, and impurities in polymers and fiber volume fraction in composites. Chemical treatment by an aqueous solution of 5% NaOH removed impurities around the external surface of the coconut fiber. Heating at 60°C did not change this morphology. XRT showed that about 57 to 60% of the inside of the coconut fibers are voids and that the coconut fiber mat has random distribution of fibers. XRT presented 0.0419% and 2.1865% of volume of impurities for PP and RPP, respectively. Impurities up to 1930 µm of length in RPP were observed, however, sizes of 50 to 350 µm were more present. The average volumetric fractions of coconut fiber for PP-1L and PP-2L were 9.44 and 11.54%, respectively. Some coconut fibers within composites were not fully involved by the matrix, suggesting incompatibility between fiber and matrix. By SEM, the fibers have different interfaces within the composite (fiber-matrix, fiber-latex and fiber-fiber); RPP showed heterogeneous regions of rupture due to impurities. The rupture micrographs of the composite manufactured by PP suggest that the fracture was ductile and that there were homogeneous regions due to the purity of their components. RPP presented fragile and ductile fractures areas. Rupture micrographs of ruptured fibers inside the composite shows microcracks around the rupture, similar to tensile testing on individual fibers.

From the viewpoint of mechanical behavior on the materials, several aspects were determined, such as deformation fields, numeric modeling and damage fields. DIC technique monitored the longitudinal and transverse deformations and informed the fracture mechanisms during the tensile tests. The diameter and surface treatments of coconut fibers influenced the mechanical behavior. The geometry and mass of mats were significant in terms of nominal stress. The fiber content and recycling modified the mechanical behavior of polypropylene and some properties were reduced with the coconut fibers addition. It was possible to determine the 2D displacements and temperature variation during a tensile test on the polypropylene. The yielding and necking formation mechanisms were followed by an

analysis of longitudinal and transverse strains by digital image correlation. During plastic deformation process the polypropylene presented an adiabatic process with an increase of approximately 20°C during the alignment of polymer chains in a fibrillar shape and there was no change in temperature captured by DIT technique before the alignment. The heating zones were originated by the necking formation and presented parabolic shapes and peak temperature in the center of this polymer.

The experimental measurements of tensile tests were compared to the measurements provided by the model of hyperbolic tangent curve. The numeric model could was consistent with the experiments up to the maximum stress, but it was not able to predict the ultimate stress. Prior to the rupture, the deviations between experimental and modeled measurements were inferior to 6% of the rupture stress. Through numerical parameters obtained by this model it was possible to determine damage curves. Critical damages from experimental stress-strain curves were determined and it was reported that the composites fabricated by RPP take more time to rupture propagation. Damage evolution using strain fields demonstrated that the longitudinal strains are predominant in relation to the transverse deformation in the damage process. Damage evolution from loading/unloading tensile testing presented stiffness modifications, as well as a non-linear and elastoplastic behavior. A critical damage value in accordance with the literature of the composite was found (Dc = 0.3). The damage evolution was well represented by polynomial fits of third order curve, suggesting that constitutive relationships between the longitudinal deformation and damage values were found. The values of longitudinal deformation related to the initiation of damage using strain fields and using loading/unloading are similar.

Another reason and motivation for this work was to show that higher use of coconut fiber and recyclable plastics can reduce or provide utility to waste in cities where these materials are abundant. For this, the continuity of research in this area is important, and therefore, some issues for further work are suggested.

Suggestions for future works

- Manufacturing composites with virgin and recycled polypropylene and coconut fibers using surface treatments adopted in this work;
- Using a more compatible binder with polypropylene for manufacturing coconut fiber mats;

- Manufacturing composites using other compatibilizers or additives in polypropylene and coconut fiber;
- Manufacturing composites with unidirectional coconut fibers and evaluating the mechanical behavior in this direction;
- Evaluating the thermal and chemical behavior of the materials used in this work;
- Evaluating the acoustic behavior of coconut fiber mats and composites made with coconut fiber;
- Modeling the mechanical behavior through numerical parameters on materials which have different maximum and rupture stress;
- Modeling the mechanical properties of composites according to the coconut fibers content;
- Simulating the process of crack formation and propagation in materials used in this study;
- Associating the mechanical model adopted with other modeling approaches;
- Performing pull-out tests on the fibers and evaluating specific properties of the fiber-matrix interface.

Appendix A: Principle and calibration of Digital Image Correlation (DIC)

A.1. Principle of Digital Image Correlation (DIC)

Optical techniques such as digital image correlation (DIC) are particularly suitable for soft polymeric materials, as local stress concentrations arising from the indentation of the specimen and the weight of an attached mechanical extensometer are entirely avoided (Hild & Roux, 2006).

In general, DIC is based on the principle of comparing speckle patterns on the surface or volume of the deformed and the undeformed sample or between any two deformation states. For this purpose, a virtual grid of subsets of a selected size and shape (2D or 3D), consisting of certain pixel gray value distributions, is superimposed on the preexisting or artificially sprayed on surface pattern and followed during deformation by an optical camera system. In this manner, information on the in-plane local strain distribution is gained without assuming the constitutive behavior of the material a priori. Furthermore, this method can also be applied to complex parts and geometries to gain information on the deformation behavior of components in real service (Sun et al., 2007; Hemelrijck et al., 2008; Verhulp et al., 2004; Sutton et al., 2008; Bruck et al., 2004).

Moreover, out-of-plane movements of the specimen affect the apparent size of the specimen and, thus, may also alter the strain result in 2D measurements. Finally, the range of the depth of sharpness is limited and determines the operating distance to the measured object if significant out-of-plane movements occur. Knowledge of the intrinsic material behavior of polymeric materials from the small strain range up to ultimate failure is of crucial importance for developing adequate material laws for numerical modeling and for a deeper understanding of the microscopic deformation mechanisms (Jerabek et al., 2010).

In two-dimensional digital image correlation, displacements are directly detected from digital images of the surface of an object (specimen). Figure A.1 (a) shows a typical example of an experimental setup for two-dimensional digital image correlation. The plane surface of

an object is observed usually by a charge-coupled device (CCD) camera with an imaging lens. Then, the images on the surface of the object, one before and another after deformation, are recorded, digitized and stored in a computer as digital images. These images are compared to detect displacements by searching a matched point from one image to another. Here, because it is almost impossible to find the matched point using a single pixel, an area with multiple pixel points (such as 20 × 20 pixels) is used to perform the matching process. This area, usually called subset, has a unique light intensity (gray level) distribution inside the subset itself. It is assumed that this light intensity distribution does not change during deformation (Yoneyama & Murasawa, 2008).

Figure A.1 (b) shows the part of the digital images before and after deformation. The displacement of the subset on the image before deformation is found in the image after deformation by searching the area of same light intensity distribution with the subset. Once the location of this subset in the deformed image is found, the displacement of this subset can be determined. In order to perform this process, the surface of the object must have a feature that allows matching the subset. If no feature is observed on the surface of the object, an artificial random pattern must be applied. Figure A.1 (c) shows a typical example of the random pattern on the surface of an object produced by spraying paint. The above concept is common among other techniques in digital image correlation (Yoneyama & Murasawa, 2008).

Figure A.1. (a) Setup for displacement measurement using digital image correlation. (b) Matching the subset before and after deformation. (c) Typical example of random pattern on specimen surface.

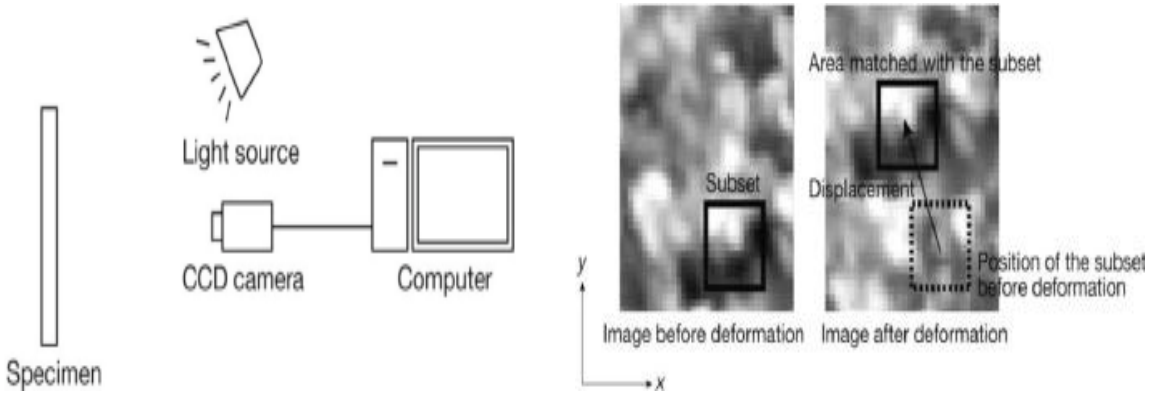

(a) (b)

(c)

Source: Yoneyama & Murasawa (2008).

Based on the above basic concept, several functions exist to match the subset from one image to another. One is the magnitude of gray intensity value difference as:

$$R(x, y, x^*, y^*) = \sum |F(x, y) - G(x^*, y^*)| \quad \text{(A.1)}$$

and another is the normalized cross-correlation as:

$$C(x, y, x^*, y^*) = \frac{\sum F(x,y) G(x^*,y^*)}{\sqrt{\sum F(x,y)^2 \sum G(x^*,y^*)^2}} \quad \text{(A.2)}$$

where F(x,y) and G(x*,y*) represent the gray levels within the subset of the undeformed and deformed images, and (x,y) and (x*,y*) are the coordinates of a point on the subset before and after deformation, respectively. The symbol of the summation represents the sum of the values within the subset. The coordinate (x*,y*) after deformation relates to the coordinate (x,y) before deformation. Therefore, displacement components are obtained by searching the best set of the coordinates after deformation (x*,y*) which minimize R(x,y,x*,y*) or maximize C(x,y,x*,y*). Functions except for Equations A.1 or A.2 can be used, however, the normalized cross-correlation (Equation A.1) is widely used for matching the subset in digital image correlation (Yoneyama & Murasawa, 2008).

The determination of a suitable method of observation, associated with the need to prepare a suitable surface, is essential to use natural contrast in digital image correlation. When images haves not natural contrast, the solution consists obtain satisfactory images is to insert an artificial texture on the surface of the samples (Grédiac & Hild, 2011). The usual

way to create such patterns is to apply a paint spray over the surface to be analyzed in order to generate a texture or a field where there will be a kind of mesh (Queiroz, 2013).

The utilization of DIC technique was performed by Correli[Q4] program, a software implemented in MATLAB and developed by researchers from LMT-Cachan. The image analysis program developed is responsible for providing the field of apparent displacements in 2-D mapping called the "reference image" to a "displaced image" from a discrete set of positions, detecting homologous points from measures of similarity between potential homologous areas between images (Queiroz, 2013).

To use this software in the tensile test was necessary to evaluate the image quality through the texture of the images in question. It was also necessary to analyze if the reference images or not deformed (before the tensile test) had stability when captured several times, because the existence of deformity between two or more undeformed images the program could evaluate them as mechanical deformation without this having happened. This procedure was performed with *TestMain4* software, developed by researchers at LMT-Cachan.

A.2. Calibration of Digital Image Correlation (DIC)

Initially, it was verified if the same region of interest of two images captured before the test had stability. The *TestMain4* software, developed by researchers of LMT-Cachan, is able to evaluate the deformities in pixels between two images. Thereby, two images taken prior to the tensile were evaluated. The images stability becomes important to inform real results about deformation mechanisms adopted in this study. The pixels deformation between two images mechanically unloaded compromises the accuracy and may invalidates the results.

Figure A.2 (a) shows an image of coconut fiber prior to the mechanical loading. This image was used as the reference image, where the region to be analyzed (region of interest) is within the red rectangle. Figure A.2 (b) presents other image of the same fiber for the stability analysis and to be compared with the first one. Both images were taken under the same conditions, in different periods and before the tensile test. Figures A.2 (c) and (a) show, respectively, the resulting displacement field in pixels at x and y axis, Ux and Uy, and Figure A.2 (e) represents the residual difference in pixels between images.

As the two images had no apparent deformation (Figures A.2 (a-b)), the *TestMain4* software showed no displacement fields in pixels before the iterative measurements (Ux = Uy = 0) and reported initial residual difference in pixels between images of 7.13%. After 20 iterative measurements, the software provided Ux = -0.0037 pixel (represents -0.918 nm or

9.18 x 10^{-4} µm) and Uy = -0.0609 pixel (represents -15.102 nm or -1.51 10^{-2} µm) as the maximum displacement in *x* and *y* axis, respectively. The y-axis (horizontal) has a longer length of the fiber to the pixels representative of the x-axis (vertical) and thus the displacement field in *y*, Uy, was more susceptible to distortion. As shown in Figures A.2 (c-e), the displacement fields and the residues in the two axes are distributed in dispersed forms throughout the analyzed region of interest.

Figure A.2. Stability analysis: (a) reference image with the region of interest, (b) comparison image, (c) displacement field in pixels in *x* (Ux) and (d) *y* (Uy) axis and (e) residual difference in pixels between images. The size of each pixel is 248 nm.

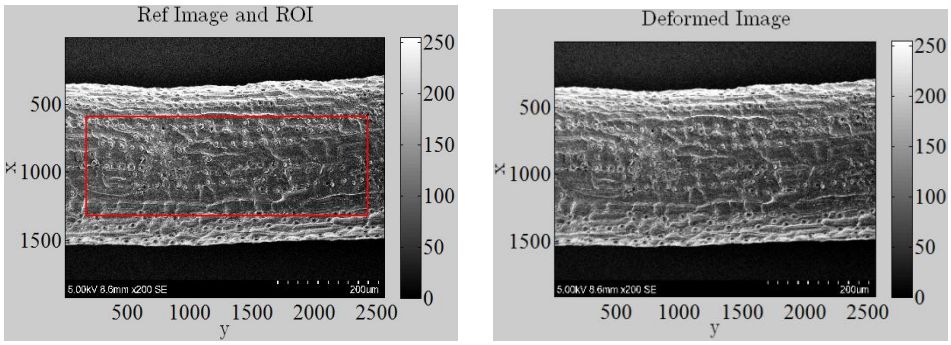

(a) (b)

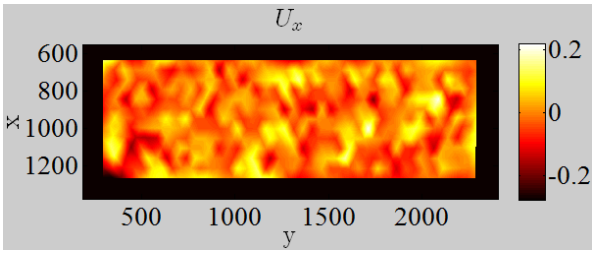

(c)

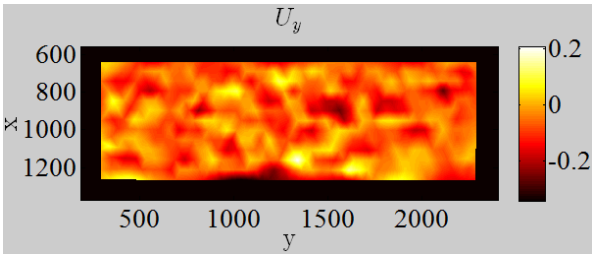

(d)

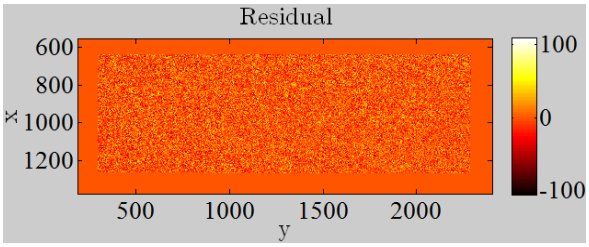

(e)

Source: author.

In all iterative measurements, the residual value between the two images was equal to 7.13% and in this case, therefore, it has 92.87% of stability (100% - 7.13%) in the region of interest. Guery et al. (2014) performed a procedure for stability analysis of images and found a value of 4.3% in the residual value for images acquired in 316L stainless steel with gold-metalized surface.

In order to obtain a lower level of deformation between two images, the brightness and contrast levels in SEM equipment were modified. At first, brightness and contrast were reduced in this new stability analysis for gray levels had fewer white pixels. Figures A.3 (a-b) show the reference image and the comparison image, respectively. Figures A.3 (c-d) show, respectively, the resulting displacement field in pixels at *x* and *y* axis, Ux and Uy, respectively. Figure A.3 (e) represents the residual difference in pixels between both images.

Figure A.3. Stability analysis: (a) reference image and the region of interest, (b) comparison image, (c) displacement field in pixels in *x* (Ux) and (d) *y* (Uy) axis and (e) residual difference in pixels between images. The size of each pixel is 248 nm.

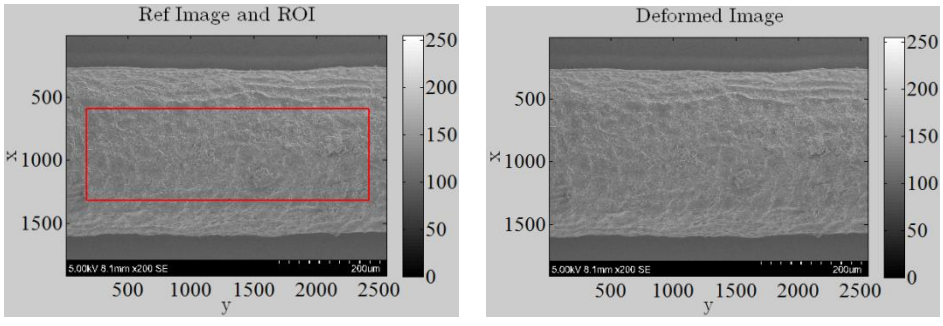

(a) (b)

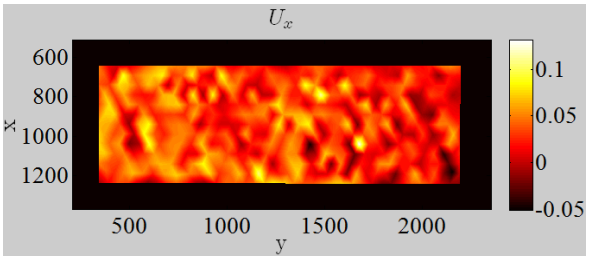

(c)

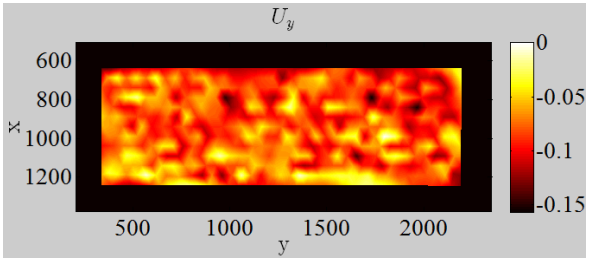

(d)

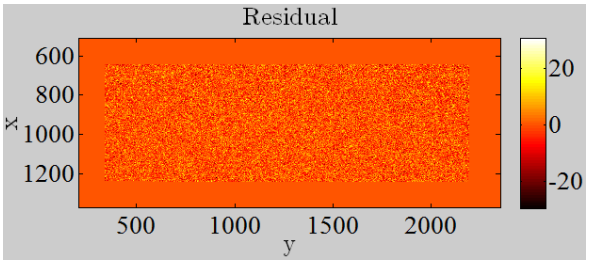

(e)

Source: author.

As the two images had no apparent deformations (Figures A.3 (a-b)), the *TestMain4* software showed no displacement fields in pixels before the iterative measurements (Ux = Uy = 0) and reported initial residual difference in pixels between images of 2.9%. In this example, the displacement fields converged to values of Ux = 0.0313 pixel (represents 7.760 nm or 7.760 x 10^{-3} µm) and Uy = -0.0787 pixel (represents -19.506 nm or -1.9506 x 10^{-2} µm) and the program ended in sixth iteration without reaching the twentieth iteration, indicating, in addition to lower residual level, greater stability between these last two images when compared to the first example. As shown in Figures A.3 (c-e), the displacement fields and the residues were dispersed throughout the analyzed region of interest and Uy was more susceptible to distortion, similar to the previous example.

Therefore, the captured image obtained from coconut fiber also meets the requirements of images repeatability without great displacements and last capture procedure adopted through lower brightness and contrast, and the surface preparation enabled it to be used in the traction tests.

The low distortion image was then evaluated in terms of its texture, since this property is one of the main parameters for a good quality analysis and measurement of the displacement field by DIC technique. The Correli[Q4] software examines some parameters before to calculate the pixel displacements. Good analyses are obtained when the numbers of gray levels are high and distinct from each other.

Therefore, before applying the DIC technique for the tensile tests, an analysis of the texture characteristics was also carried out. Figure A.4 shows the image that will be used as example and its region of interest. The gray levels histogram of this region of interest is presented in the Figure A.5.

Figure A.4. Coconut fiber texture analysis: (a) external surface and (b) and region of interest. The size of each pixel is 248 nm.

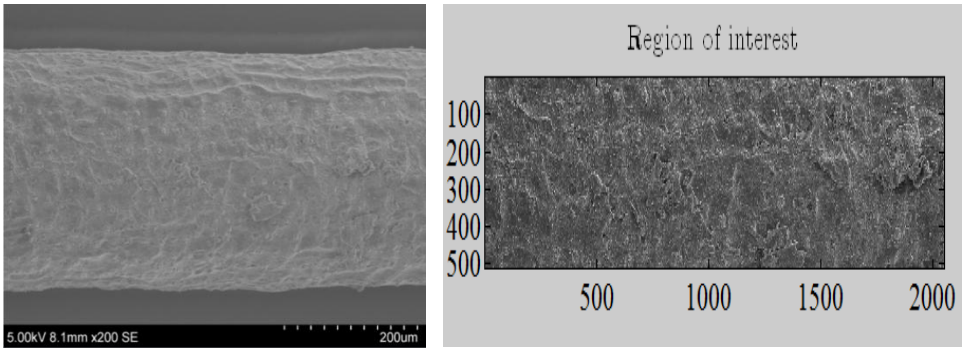

(a) (b)

Source: author.

Figure A.5. Gray levels histogram of the coconut fiber surface texture.

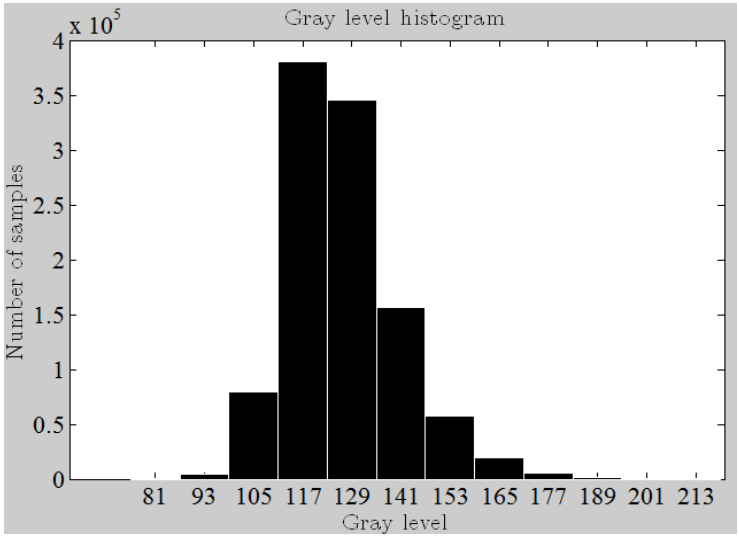

Source: author.

The histogram shown in Figure A.5 indicates that there are gray levels to deformation calculations in tensile test ranging up to 189, but the levels of gray predominate between 117 and 141. There are more than 8.8 x 10^5 samples of gray levels in this range. Due to the high amount of gray levels and an high representative number it can be reported that preparations by metallization on the surface of coconut fiber provides images to be used by the DIC technique.

To select the element size, a practical limit of the camera's dynamic range to the variation value (fluctuation) less than 1% was adopted, i.e., to lower values of this limit, there are not enough gradients to get displacement during the test. Figure A.6 shows the percentage of elements (for each size) with respect to this limit. In accordance to this criterion, it is observed that the even with inclusion of elements with size of 8 pixels (that provides results in lower quality) the image will present all its elements.

Figure A.6. Criterion fluctuation: (a) fraction of elements that reached the limit of 1% minimum fluctuation in different sizes of elements and (b) fluctuations in relative sizes of different elements.

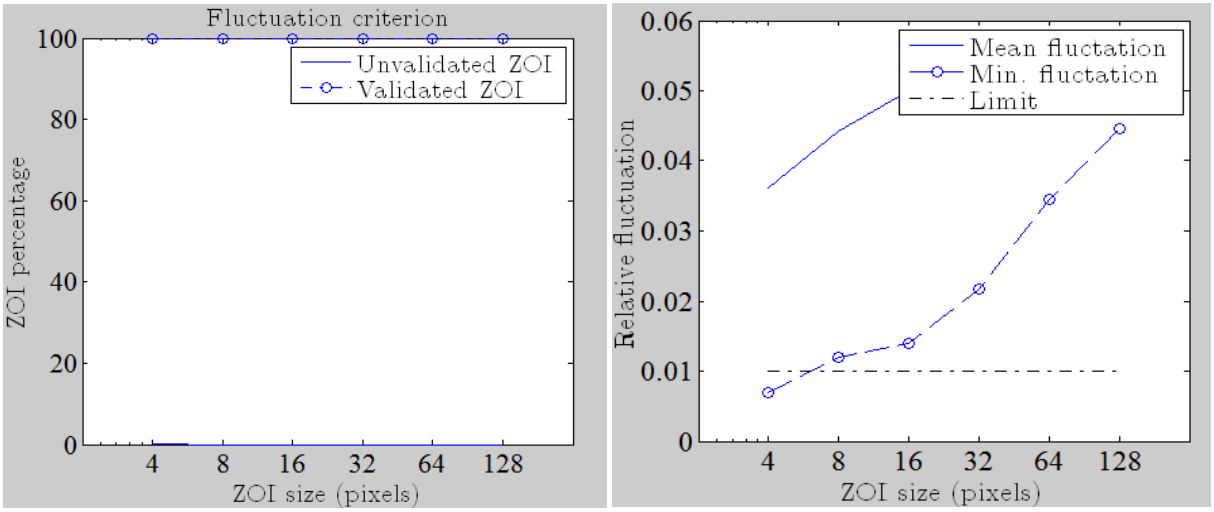

(a) (b)

Source: author.

The correlation radius of image texture is also important criterion which is calculated from a parabolic interpolation of the autocorrelation function at the origin. The inverse of two eigenvalues of the curvature provides an estimation of the two radius correlation (Figure A.7), when the mean of all elements of a given size is used.

In this criterion, a practical limit to the correlation radius value in choosing the size of the element is at most 25% of the element size. Above this value, measurements are unreliable. It is observed in Figure A.7 that almost all elements in the region of interest in this example are less than 25%, respecting therefore this criterion.

The quantitative analysis of texture and how they determine the error and deviation in measurements of displacement fields with respect to the element size were also evaluated as calibration. At the same Correli^{Q4} software, a virtually displaced image was generated from the predetermined displacement in the vertical direction, similar to the displacement of a rigid body. In practice, increments of 0.5 pixels are sufficient, since the mean error and corresponding standard deviation are linear functions of the prescribed displacement (Hild & Roux, 2008).

Figure A.7. Criterion of primary and secondary correlation radius.

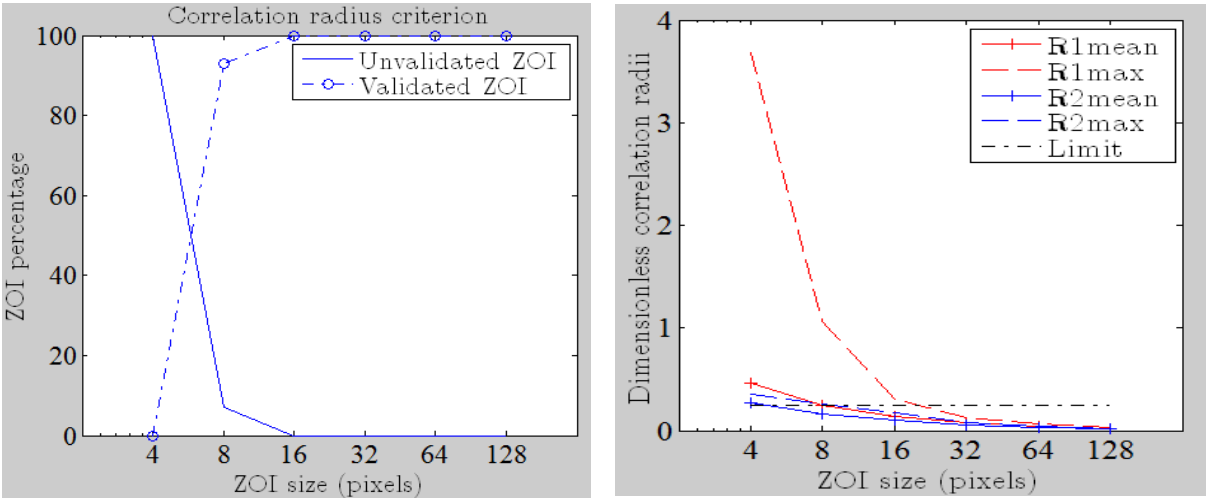

Source: author.

The algorithm then correlates two images and measures the estimated displacements (u_{est}) in the horizontal direction. These directions are chosen to maximize interpolation sensitivity, which is the main errors source. After this uncertainty analysis, four different results were presented (Figures A.8 and A.9). In this case, there is a significant decrease when the element size is equal or greater than 16 pixels and the sizes of 4 and 8 pixels provide greater average errors for the increment of 0.5 pixels.

The quality of the estimation is determined by two indicators, the systematic error (δ_u) and the standard deviation (σ_{sd}). The first determines the difference between the measured displacement (u_{pre}) and deformation truly occurred (u_{est}) as follows: $\delta_u = \| << u_{est} >> - u_{pre} \|$.

The standard deviation σ_u determines the difference of measured displacement (u_{est}) in relation to its average as follows: $\sigma_{sd} = [(u_{est} - << u_{est} >>)^2]^{1/2}$.

Figure A.8. Measurement uncertainties related to virtual displacements imposed by the test for different sizes of elements (4, 6, 8, 16, 32, 64 and 128 pixels): (a) error and (b) standard deviation.

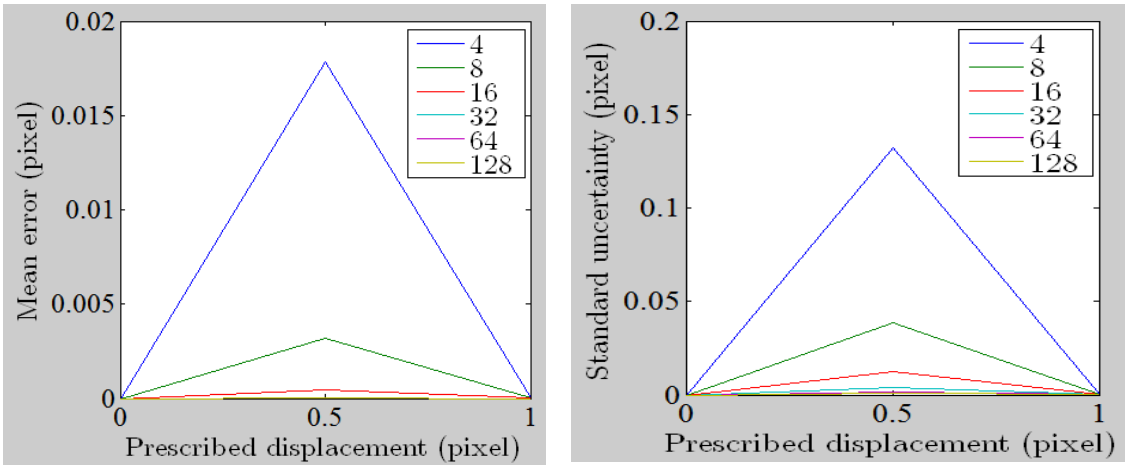

(a) (b)

Source: author.

Figure A.9. Average (a) and standard deviation (b) of the displacements errors due to the element size.

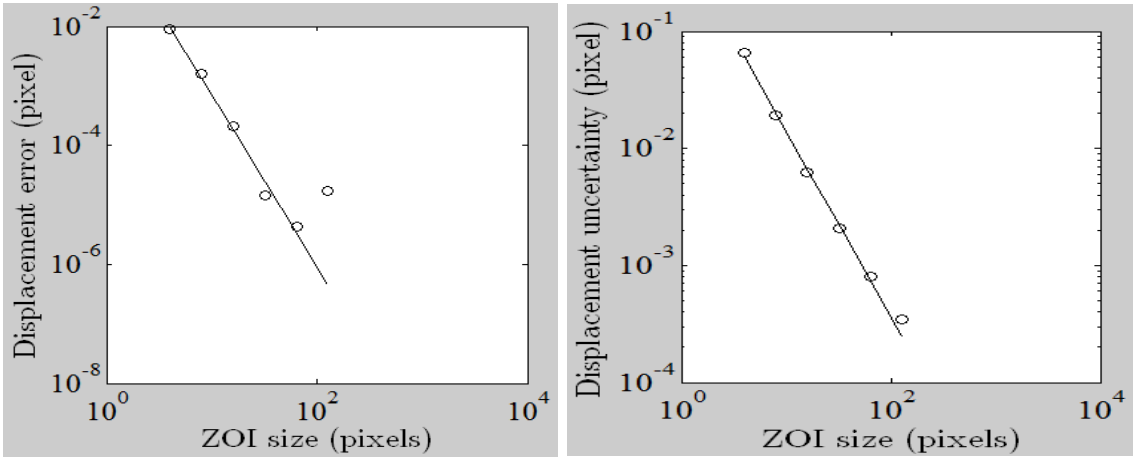

(a) (b)

Source: author.

Figure A.9 shows that the measured average errors are at the same order of magnitude as the standard deviation. This result shows that these measurements are basically impartial and slightly dispersed in relation to the true value. Another point that can be reported is that the standard deviation decreases as the element size increases, according to previous information. With this second analysis, it can be concluded that elements of 16 pixels can be chosen and the displacement uncertainty for this size is approximately 8 x 10^{-3} pixel, respecting the mentioned criterias.

The same procedure of stability analysis between two images used in coconut fiber applied for DIC technique prior to the tensile test was applied to the coconut fiber mat. Figure A.10 shows the image that was used as an example and its region of interest.

Figure A.10. Stability analysis in the coconut fiber mat: (a) reference image with the region of interest, (b) comparison image, (c) displacement field in pixels in *x* (Ux) and (d) *y* (Uy) axis and (e) residual difference in pixels between images. The size of each pixel is 12 µm.

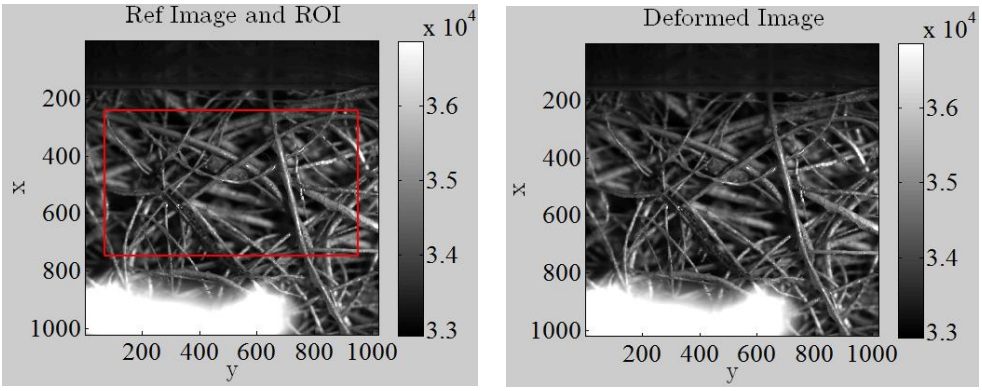

(a)

(b)

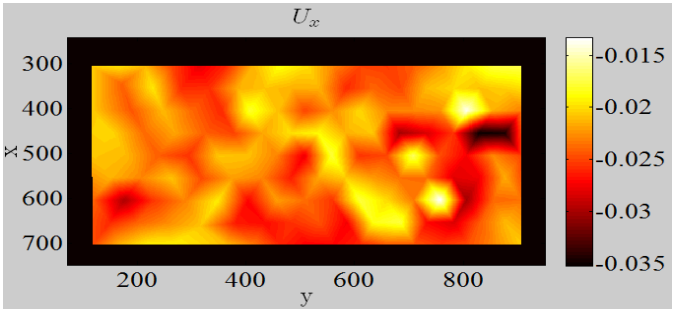

(c)

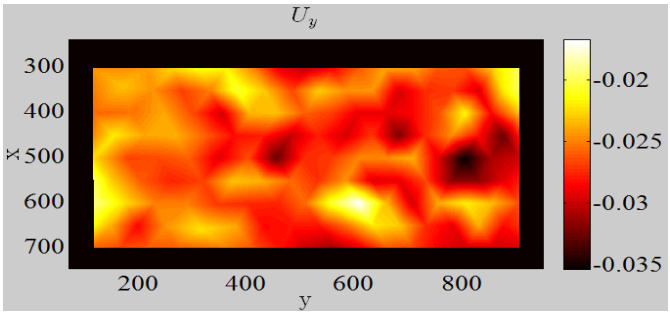

(d)

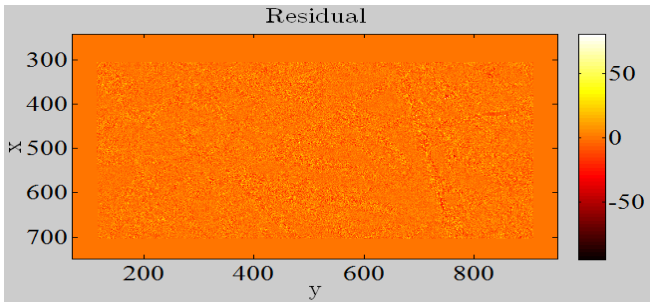

(e)

Source: author.

As the two images had no apparent deformations (Figures A.10 (a-b)), the *TestMain4* software showed no displacement fields in pixels before the iterative measurements (Ux = Uy = 0) and reported initial residual difference in pixels between images of 0.2%. In this example, the fields displacement converged to values of Ux = -0.0231 pixel (represents -0.277 µm or -277 nm) and Uy = -0.0260 pixel (represents -0.312 µm or -312 nm), indicating more stable images with lower residual levels than those of coconut fiber. Captured images of coconut fiber mats also presented displacement fields dispersed along this analysis.

Therefore, the images of coconut fibers mat also reached the requirements for repeatability images with low distortion. The region of interest of Figure A.10 (a) was then evaluated for its texture quality, according to the procedure already used. Figure A.11 shows the histogram of gray levels of the region.

The high values of the gray levels and the highly representative number of these levels shown in Figure A.11 provided good images for DIC technique. Other parameters of variation value (float) of at least 1%, practical limit of 25% for the radius of correlation of the texture image and the measurement uncertainties with respect to virtual displacements imposed by the test for various sizes of elements (4, 6, 8, 16, 32, 64 and 128 pixels), as used previously for the coconut fiber, were also satisfactory for the coconut fiber mat.

Figure A.11. Gray levels histogram of the coconut fiber mat surface texture.

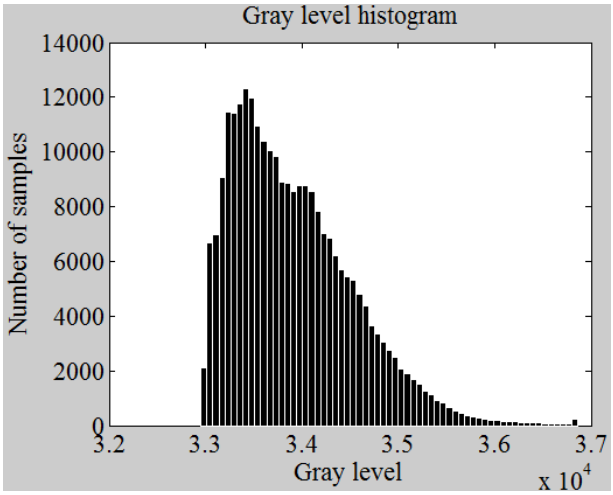

Source: author.

Appendix B: Principle and calibration of Digital Infrared Thermography (DIT)

B.1. Principle of Digital Infrared Thermography (DIT)

Several non-destructive evaluation (NDE) techniques such as radiography, eddy-current testing, ultrasonic testing, acoustic emission and vibration analysis are outinely used for condition monitoring. It is well known that temperature is one of the most useful parameter that indicates the structural health of an object (Epperly et al., 1997). Therefore, monitoring the temperature of machineries or a process is undoubtedly one of the best predictive maintenance methodologies. Various temperature measurement systems like thermocouples and resistance temperature detectors are in general contact type and not provide a visual image of the object under investigation. Infrared thermography is a novel NDE method that measures the temperature of a body remotely and provides the thermal image of the entire component or machinery. In general, faults associated with abnormal temperature distribution can be easily detected by infrared thermography (IRT) in advance that allows preventive maintenance before failure (Bagavathiappan et al., 2013).

The origin and theory of infrared thermography (IRT) has been described in detail elsewhere (Meola, 2012). For completeness, the basic theory and the fundamental equations are described here. All objects with temperature above 0K (i.e. 273 °C) emits electromagnetic radiation in the infrared region of electromagnetic spectrum. Infrared radiation (wavelength in the range of 0.75–1000 μm) is positioned in-between microwave and visible part of the electromagnetic spectrum. This vast range can be further subdivided into near infrared (0.76–1.5 μm), medium infrared (1.5–5.6 μm) and far infrared (5.6–1000 μm). In 1800, Sir William Herschel discovered infrared radiation and the recording of the first thermal image was done

by his son John Herschel which added new dimension to the temperature measurement. It took almost two centuries to adopt IRT in civilian domain mainly because of non-availability of quality equipment and technical knowhow (Bagavathiappan et al., 2013).

In thermal radiation theory, blackbody is considered as a hypothetical object which absorbs all incident radiations and radiates a continuous spectrum according to Planck's law as follows.

$$L_\lambda = \frac{c_1}{\lambda^5\left[exp\left(\frac{c_2}{\lambda T}\right)-1\right]} \tag{B.1}$$

where λ is the wavelength of the radiation (μm), L_λ is the power radiated by the blackbody per unit surface and per unit solid angle for a particular wavelength (W m^{-2} μm^{-1} sr^{-1}), T is the temperature in absolute scale (K), c_1 and c_2 are the first and second radiations constants, respectively (Bagavathiappan et al., 2013). On integrating Planck's law over all frequencies, Stefan–Boltzmann's law is derived which is expressed as follows.

$$\frac{q}{A} = \varepsilon\sigma T^4 \tag{B.2}$$

where q is the rate of energy emission (W), A is the area of the emitting surface (m^2), T is the absolute temperature (K) and σ is the Stefan–Boltzmann's constant (σ = 5.676 x 10^{-8} Wm^{-2} K^{-4}) and ε is the emissivity of the emitting surface for a fixed wavelength and absolute temperature T. For a perfect blackbody emissivity is unity, but for real surfaces it is always less than unity (Bagavathiappan et al., 2013). The wavelength of the peak of the emission spectrum is also related to the absolute temperature of the emitting surface by Wien's displacement law, which is expressed as follows.

$$\lambda_{max}T = 2897.7\ \mu m\ K \tag{B.3}$$

In IRT, infrared radiation emitted by a body is detected in a noncontact way by an infrared detector and using Stefan–Boltzmann's law (Equation (B.2)), the temperature of the body is obtained. Infrared detectors are the heart of IRT systems. Several types of detectors are available and they can be classified into two main categories, thermal (like pyrometers, bolometers, etc.) and semiconductors (like photoconductive, photovoltaic detectors). Infrared detectors are in general placed inside a protective housing, consisting of the optical

arrangements (lens, mirrors, etc.), detector elements, cooling system and associated electronics. Hence, they are also called infrared cameras. Infrared cameras have undergone several modifications during the last few decades (Bagavathiappan et al., 2013).

Figure B.1 shows the schematic of a typical IRT experimental setup, where the infrared camera, display unit and a typical infrared image of a mechanical component (compressor motor) along with its original photograph are shown. The infrared (IR) camera is placed suitably in front of the object under investigation in such a way that unrestricted optical access is available. Environmental conditions must be favorable for accurate temperature measurement. The acquired thermal images are displayed in the personal computer (PC) and real time temperature of the object can be measured in a non-contact way. The images can also be stored digitally for further post-processing. Here a typical infrared thermal image of a mechanical component along with its original photograph is shown (Bagavathiappan et al., 2013).

Figure B.1. Schematic of a typical experimental setup for IRT based condition monitoring experiments.

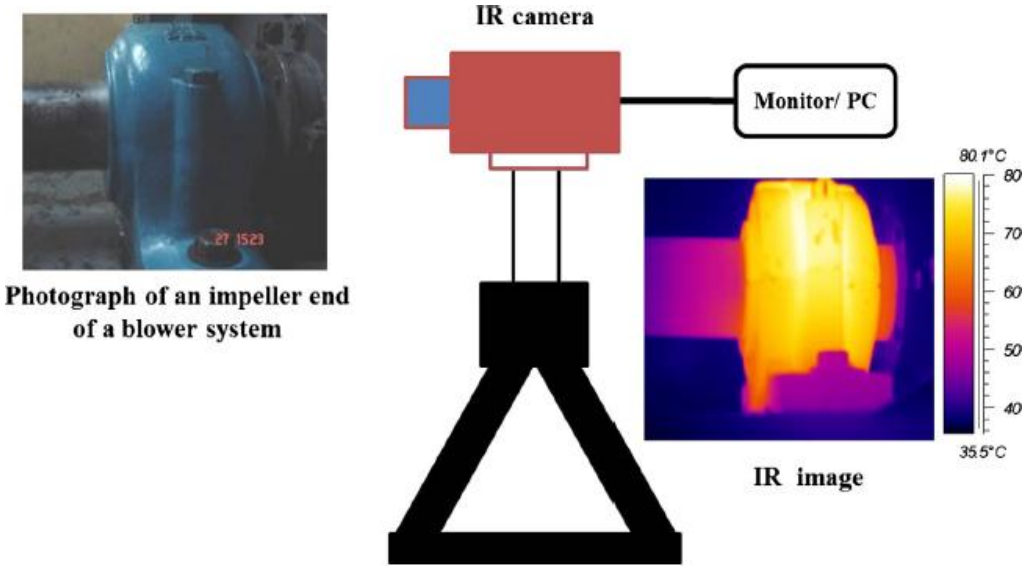

Source: Bagavathiappan et al., 2013.

The use of infrared thermography for in situ detection of fatigue damage in materials has been established as a valid NDE technique (Steinberger et al, 2006; Toubal, 2006). The application of this method has also shown to be useful for the determination of the high cycle fatigue strength (HCFS) of some composite materials (Quaresimin, 2002; Colombo et al., 2011, 2012).

As indicated, DIT is a well established non-contact NDE technique for monitoring fatigue damage in structural components. Thermography is a measurement technique that relies on the use of an infrared camera to provide a time-dependent contour map of an objects surface temperature. This technique involves decoding temperature information which results from the IR radiation emitted by an object. The passive approach is ideal for cyclic loading because the resulting hysteretic heating allows for a time-dependent temperature variation which can be monitored with the IR camera. The recorded images can then be analyzed to determine the material fatigue strength or to understand damage initiation and development.

Slip bands along primary slip planes (i.e., local plasticity) and microscopic cracking at the grain boundaries (i.e., microscopic damage) can be present during loadings. In polymeric composites materials subjected to macroscopically applied elastic stresses, similar local microscopic stress fluctuations can cause intrinsic energy dissipation. The main mechanisms causing energy dissipation may be attributed to the viscoelastic nature of the matrix material, matrix cracking, fiber fracture, and interface cracking/friction among others (Steinberger et al., 2006). Specifically for a textile composite, additional dissipative mechanisms may include matrix deformation and fiber reorientation for off-axis loading conditions (Selezneva, 2011).

B.2. Calibration of Digital Infrared Thermography (DIT)

Infrared cameras from Flir (manufacturer of the infrared camera used in this work) are designed and factory calibrated for accurate temperature measurements and thermal imaging. When maintained with Flir's annual calibration services, they will be highly reliable in spotting thermal anomalies and other temperature phenomena. Without proper maintenance and calibration, accurate measurements cannot be assured.

The manufacturer of infrared camera provides the software modules for camera calibration. These systems use temperature references and are calibrated and tracked annually by manufacturer (Flir). Thereby, prior to the tests followed by Digital Infrared Thermography (DIT), the systems of calibration software developed by manufacturer were used in order to identify the uncertain measurements. According to these systems and the manufacturer's manual, the measurements accuracy was approximately 2% of reading.

References

Amafibra, 2007. Available on the website www.amafibra.com.br, accessed on 31/10/2007.

Amundsen, A. H. (2014). Behaviour and Modeling of Fibre-Reinforced Polymers. Master's thesis at Norwegian University of Science and Technology.

Anderson, J., Sparnis, E., Jofe, R., Wallström, L. Strength distribution of elementary flax fibres. Composites Science and Technology, 65, p. 693–702, 2005.

Anderson, T. L. Fracture Mechanics - Fundamentals and Applications. Third Edition. CRC Press. Taylor & Francis Group. 2005

Baly, c. Analysis of the flax fibres tensile behaviour and analysis of the tensile stiffness increase. Composites – Part A, 33, p. 939–48, 2002.

ASTM C1557 - 03(2013). Standard Test Method for Tensile Strength and Young's Modulus of Fibers.

ASTM D638-10 (2041). Standard Test Method for Tensile Properties of Plastics.

Aurrekoetxea, J. et al. 2001. Effects of recycling on the micro-structure and the mechanical properties of isotactic polypropylene. Journal of Materials Science 36: 2607-2613.

Bagavathiappan, S., Lahiri, B.B., Saravanan, T., Philip, J, Jayakumar, T. Infrared thermography for condition monitoring – A review. Infrared Physics & Technology 60 (2013) 35–55.

Bartczak, Z., Galeski, A., Argon, A., Cohen, R. One the plastic deformation of the amorphous component in semicrystalline polymers. Polymer 1996;37(11):2113–23.

Bismarck A., Mohanty, A. K., Aranberri-askargorta I., Czapla S., Misra, M., Hinrichsen G. Surface characterization of natural fibers; surface properties and the water up-take behavior of modified sisal and coir fibers. Green Chem 2001;3(2):100–7.

Bledzki, A. K., Gassan, J. Composites reinforced with cellulose based fibres. Progress in Polymer Science. 24 (1999) 221–274.

Bledzki, A. K., Mamun, A. A., Volk, J. Barley husk and coconut shell reinforced polypropylene composites: The effect of fibre physical, chemical and surface properties. Composites Science and Technology 70 (2010) 840–846.

Bonnet, M., Constantinescu, A. (2005). Inverse problems in elasticity. Inverse Problems, 21, R1–R50.

Brahmakumar, M., Pavithran C., Pillai, R. M. Coconut fibre reinforced polyethylene composites: effect of natural waxy surface layer of the fibre on fibre/matrix interfacial bonding and strength of composites. Composites Science and Technology 65 (2005) 563–569.

Brígida, A. I. S., Calado, V. M. A., Gonçalves, L. R. B., Coelho, M. A. Z. Effect of chemical treatments on properties of green coconut fiber. Carbohydrate Polymers 79 (2010) 832–838

Bruck, H. A., Fowler, G., Gupta, S. K., Valentine, T. M. (2004). Using geometric complexity to enhance the interfacial strength of heterogeneous structures fabricated in a multi-stage, multi-piece molding process. Experimental Mechanics 44 (2004) 261.

Brusselle-dupend, N., Lai, D., Feaugas, X., Guigon, M., Clavel, M. "Mechanical Behavior of a Semicrystalline Polymer Before Necking. Part I: Characterization of Uniaxial Behavior", Polymer Engineering and Science, v. 41, n. 1, pp. 66-76, 2001.

Bucknall, C.B., Toughened Plastics. Applied Science Publishers, London, 1977.

Bueno, M. R. P. Materiais nanoestruturados sintéticos tipo esmectitas: sua síntese, caracterização e aplicação em nanocompósitos de polietileno. Master's thesis. Federal University of Rio Grande do Sul, 2008.

Burke, P. E. H. (1999). The tensile deformation process of polypropylene at high pressure. Doctoral's thesis. University of Toronto. 1999.

Cassales, A. R., Morais, J. P. S., Rosa, M. F., Alexandre, L. C., Norões, A. K. M., Mota, M. C. G. Caracterização morfológica por MEV de fibras de línter de algodão. 8º Brazilian Congress of Cotton. São Paulo, SP, Brazil, 2011.

Cayard, M. Fracture toughness testing of polymeric materials. Doctoral's thesis. Texas A&M University, College Station, TX, 1990.

Chalal, H., Avril, S., Pierron, F., Meraghni, F. Experimental identification of a nonlinear model for composites using the grid technique coupled to the virtual fields method. Composites Part A, 37, 315–325, 2006.

Chalal, H., Meraghni, F., Pierron, F., Grédiac, M. Direct identification of the damage behaviour of composite materials using the virtual fields method. Composites Part A, 35, 841–848, 2004.

Claire, D., Hild, F., Roux, S. Identification of damage fields using kinematic measurements. C R Mecanique, 330, 729–734, 2002.

Claire, D., Hild, F., Roux, S. A finite element formulation to identify damage fields: The equilibrium gap method. Int J Num Meth Eng, 61, 189–208, 2004.

Claire, D., Hild, F., Roux, S. Identification of a damage law by using full-field displacement measurements. Int J Damage Mech, 16, 179–197, 2007.

Cofer, W. F., Mclean, D. I., Paynter, M. E., Wanh, H. The Development and Verification of Element Models to Optimize the design of Wale/Chock Structural Sections. Prepared for

Office of Naval research under Contact N00014-97-C-0395. University of State of Washington, Pulman, WA, 1998.

Colombo, C., Libonati, F., Pezzani, F., Salerno, A., Vergani, L. Fatigue behaviour of a GFRP laminate by thermographic measurements. Eng Procedia 2011; 10:3518–27, 2011.

Colombo, C., Vergani, L., Burman, M. Static and fatigue characterization of new basalt fibre reinforced composites. Compos Struct 2012; 94:1165–74, 2012.

Davis, H. E.; Troxell, G. E.; Hauck, G. F. W. The testing of engineering materials, ed. 4, p. 371, McGraw-Hill, USA, 1982.

Dean, G. D., Broughton, W. A model for non-linear creep in polypropylene. Polymer Testing 26 (2007) 1068–1081.

Defoirdt, N., Biswas, S., Vriese, L., Tran, L. Q. N., Acker, J. V., Ahsan, Q. Assessment of the tensile properties of coir, bamboo and jute fiber. Compos A – Appl Sci Manuf 2010; 41: 588–95.

Dias, R. P., Sousa J. L. A. O., Almeida, L. C. Aplicação da técnica de correlação de imagens digitais à análise experimental de estruturas de concreto armado. XX Congress of undergraduate research of University of Campinas, 2012.

Duncan & Chang (1970). Nonlinear analysis of stress and strain in soils. Journal of Soil Mechanics and Foundation Division, ASCE, vol 96, No. SM5, September. Eichhorn & Baillie, 2001

Elmajdoubi, M., Vu-khanh, T. Effect of cooling rate on fracture behaviour of polypropylene, Elsevier Science, Canada, 2003.

Embrapa, Tropical Agroindustry of Fortaleza (Brasil). Website: www.cnpat.embrapa.br .

EN ISO 10319:2008 – Geosynthetics – Wide-width tensile test.

Epperly, R. A., Heberlein, G. E., Eads, L. G. A tool for reliability and safety: predict and prevent equipment failures with thermography, in: IEEE Petroleum and Chemical Industry Conference, Banff, Alta, 1997, pp. 59–68.

Fernandes, E. M., Correlo, V. M., Mano, J. F., Reis, R. L. Novel cork–polymer composites reinforced with short natural coconut fibres: Effect of fibre loading and coupling agent addition. Composites Science and Technology 78 (2013) 56–62.

Fidelis, M. E. A., Pereira, T. V. C., Gomes, O. F. M., Silva, F. A., Filho, R. D. T. The effect of fiber morphology on the tensile strength of natural fibers. Journal of Materials Research and Technology. 2013;2(2):149–157.

Fiebig, J.; Gahleitner, M.; Wolfschwenger, J. Ageing of polypropylene: processes and consequences. Polymer Testing, p. 257-266, 1999.

Fouda, I. M., Seisa, E. A. Study of some opto-mechanical parameters characterizing polypropylene suture fibers. Optik 124 (2013) 2691–2695.

Friedrich, K. Crazes and shear bands in semi-crystalline thermoplastics. Adv Polym Sci 1983; 52–53:225–74, 1983.

Frank R. R., Bast and other fibers, Woodhead Publishing, 2005.

Furlani J. E. Um estudo sobre a variação numérica do coeficiente de poisson na madeira, considerando a anisotropia do material. Master thesis. Campinas State University, 1995.

Galeski A. Strength and toughness of crystalline polymer systems. Prog Polym Sci 2003; 28:1643–99.

Gelfuso, M. V., Silva, P. V. G., Thomazini, D. Polypropylene matrix composites reinforced with coconut fibers. Mat. Res. vol.14, no.3, São Carlos, 2011.

George, J., Sreekala, M. S., Thomas S. A review on interface modification and characterization of natural fiber reinforced plastic composites. Polymer Enginnering and Science, v. 41, n. 9, p. 1471-1485, 2001.

Gerscovich, D. M. S. Modelos Constitutivos - Modelo Hiperbólico. Report from University of State of Rio de Janeiro, 2009.

Godara, A., Raabe, D., Bergmann, I., Putz, R., Müller, U. Influence of additives on the global mechanical behavior and the microscopic strain localization in wood reinforced polypropylene composites during tensile deformation investigated using digital image correlation. Composites Science and Technology 69 (2009) 139–146.

Gonçalez V. Estudo do comportamento viscoplástico de polímero semicritalino aplicado na indústria do petróleo. Doctoral thesis. COPPE/UFRJ. Rio de Janeiro. 2013.

Grédiac, M., Hild, F. Mesures de champs et identification en mécanique des solides. Lavoisier, 2011.

Guery, A., Latourte, F., Hild, F., Roux, S. Characterization of SEM speckle pattern marking and imaging distortion by Digital Image Correlation. Meas Sci Tecnhol 25:12, 2014.

Hamada, H.; Fujihara, K.; Harada, A. The influence of sizing conditions on bending properties of contínuos glass fiber reinforced polypropylene composites. Elsevier Science, Japan, 2000.

Hemelrijck, D. V., Makris, A., Ramault, C., Lamkanfi, E., Paepegem, W. V., Lecompte, D. Biaxial testing of fibre-reinforced composite laminates. Proc. I Mech. E, Part L 222 (2008) 1464.

Hild F., Roux S. CORRELI[Q4]: A Software for “Finite-element” Displacement Field Measurements by Digital Image Correlation. Internal Report N° 269. LMT-Cachan. April, 2008.

Hild, F., Roux, S. Digital Image Mechanical Identification (DIMI). Experimental Mechanics (2008) 48:495–508.

Hild, F., Roux, S. Digital image correlation: from displacement measurement to identification of elastic properties – a review. Strain 42 (2006) 69.

Holbery, J., Houston, D. Natural-fiber-reinforced polymer composites in automotive applications. JOM. November 2006, Volume 58, Issue 11, pp 80-86.

Incarnato, L., Scarfato, P., Acierno, D., Milana, M. R., Feliciani, R. Influence of recycling and contamination on structure and transport properties of polypropylene. Journal of Applied Polymer Science, 89 (7): 1768-1778, 2003.

Indicula, M., Malhotrab, S.K., Joseph, K. & Thomas, S. Dynamic mechanical analysis of randomly oriented intimately mixed short banana/sisal hybrid fiber reinforced polyester composites. Composites Science & Technology. 2005; 65:1077-1087.

Ishizaki, M. H., Furtado, C. R. G., Leite, M. C. A. M., Leblanc, J. L. Caracterização Mecânica e Morfológica de Compósitos de Polipropileno e Fibras de Coco Verde: Influência do Teor de Fibra e das Condições de Mistura. Polímeros: Ciência e Tecnologia, vol. 16, n° 3, p. 182-186, 2006.

Jansson A, Moller K, Gevert T. Degradation of post-consumer polypropylene materials exposed to simulated recycling-mechanical properties. Polymer Degradation and Stability, 82: 37-46, 2003.

Jerabek, M., Major, Z., Lang R. W. Strain determination of polymeric materials using digital image correlation. Polymer Testing 29 (2010) 407–416.

John, M. J., Thomas, S. Carbohydrate Polymers 2007, doi:10.1016/j.carbopol.2007.05.040.

Joshia, S. V., Drzalb, L. T., Mohantyb, A. K., Arorac, S. Are natural fiber composites environmentally superior to glass fiber reinforced composites? Compos A – Appl Sci Manuf 2004;35:371–6.

Kachanov, L. M. Time of rupture process under creep conditions. Izvestia Akademii Nauk, n. 8, 1958, p. 26-31.

Karian, G. H., Handbook of Polypropylene and Polypropylene Composites, Marcel Dekker Inc.:New York, 2003.

Kasliwal, S. G., Jones, J. W. Misturadores contínuos realizam boa formulação de termoplásticos com fibras naturais. Revista Plástico Industrial, São Paulo, n.83, p. 110-121, jul. 2005.

Klason, C., Kubát, J., Strömvall, H.–E. The efficiency of cellulosic fillers in common thermoplastics. Part I. Filling without processing aids or coupling agents. Intern. J. Polymeric Mater. 10: 159-187, 1984.

Kulkarni, A. G., Satyanarayana, K. G., Sukumaran, K. Mechanical behaviour of coir fibres under tensile load. Journal of materials science, 16, p. 905-914, 1981.

Kulkarni, A. G., Satyanarayana, K. G., Rohatgi, P. K., Vijayan, K. Mechanical properties of banana fibres (Musa sepientum). Journal of materials science 18, p. 2290-2296, 1983.

La Mantia, F. P., Dintcheva, N. T. Thermomechanical degradation of filled polypropylene. Macromolecular Symposia, 194: 277-286, 2003.

Lemaitre, J. How to use damage mechanics. Nuclear Engineering and Design, Amsterdam, v. 80. p. 233-245.

Lemaitre, J. Handbook of Materials Behavior Models, Academic Press, 2001.

Lemaitre, J., Chaboche, J-.L., Benallal A., Desmorat R. *Mécanique des matériaux solides*. 3e édition. 2009. LMT-Cachan.

Li, X., Tabil, L. G., Panigrahi S. J. Polym. Environ. 2007; 15:25-33.

Lockyear, S. A. Mechanical Analysis of Transversely Loaded Wood/Plastic sections. Master's thesis. Washington State University, 1999.

Lu, G. HDPE wood-plastic composite material model subject to damage. Master's thesis. Washington State University. May 2002.

Mascia, N. T., Nicolas, E. A. Determination of Poisson's ratios in relation to fiber angle of a tropical wood species. Construction and Building Materials 41 (2013) 691–696.

Marcelo, A. O. J. Application of damage mechanism in polymeric composite materials reinforced by fiberglass. Master's thesis. Federal University of Ceara, 2004.

Marigo, J-J. Formulation d'une loi d'endommagement d'un matériau élastique. C R Acad Sci Paris t, 292, 1309–1312, 1981.

Marsh, G. Next step for automotive materials, Materials Today, v.6, n.4, p. 36-43, abr. 2003.

Matthews, F. L.; Rawlings, R. D. Composite materials: engineering and science. Great Britain, Chapman & Hall, 1994. 470 p.

McCormick N., Lord J. Digital Image Correlation. Methods & Materials. Volume 13, Issue 12, December 2010, Pages 52–54.

Meola, C., Boccardi, S., Carlomagno, G. M., Boffa, N. D., Monaco, E., Ricci, F. Nondestructive evaluation of carbon fibre reinforced composites with infrared thermography and ultrasonics. Composite Structures. Volume 134, 15 December 2015, Pages 845–853.

Meola, C. Origin and theory of infrared thermography, in: C. Meola (Ed.). Infrared Thermography Recent Advances and Future Trends, Bentham eBooks, 2012, pp. 3–28.

McCormick N., Lord J. Digital Image Correlation. Methods & Materials. Volume 13, Issue 12, December 2010, Pages 52–54.

Monteiro, S. N., Terrones, L. A. H., Carvalho, E. A., D'Almeida, J. R. M.. Effect of the fiber/matrix interface on the strength of polymeric composites reinforced with coir fibers. Revista Matéria, v. 11, n. 4, pp. 395 – 402, 2006.

Motta, L. A. C., Agopyan, V. Caracterização de fibras curtas empregadas na construção civil. Technical report of the Polytechnic School of University of São Paulo. Department of Civil Construction Engineering, 2007.

Mukherjee, P. S. and Satyanarayana, K. G. (1984) Structure and properties of some vegetable fibers. Part I: Sisal fiber. J. Mater. Sci. 19, 3925-3934.

Mulinari, D. R., Baptista, C. A. R. P., Souza, J. V. C., Voowall, H. J. C.Mechanical Properties of Coconut Fibers Reinforced Polyester Composites. Procedia Engineering 10 (2011) 2074–2079.

Mwaikambo, L.Y., Ansell, M. P. Mechanical properties of alkali trated plant fibres and their potential as reinforced materials II. Sisal fibres. Journal of materials science, 41, p. 2497-2508, 2006.

Narisawa. I., Ishikawa, M. Crazing in semi-crystalline thermoplastics. Adv Polym Sci 1990;91–92:353–91.

Nitta, K-H., Yamana, M. Poisson's Ratio and Mechanical Nonlinearity Under Tensile Deformation in Crystalline Polymers. Division of Material Sciences, Graduate School of Natural Science and Technology, Japan. Available on website: http://cdn.intechopen.com/pdfs-wm/30970.pdf, captured in 13.11.2014.

Pannirselvam, P. V., Lima, F. A. M., Dantas, B. S., Santiago, B. H. S., Ladchumananadasivam, Fernandes M. R. P. Desenvolvimento de projeto para produção de fibra de coco com inovação de tecnologia limpa e geração de energia. Journal Analytica. Federal University of Rio Grande - Center of Technology. Natal (Brazil), 2005.

Pawlak, A., Galeski, A. Plastic deformation of crystalline polymers, the role of cavitation and crystal plasticity. Macromolecules 2005;38(23):9688–97.

Pawlak, A., Galeski, A. Cavitation during tensile deformation of polypropylene. Macromolecules 2008;41(8):2839–51.

Périé, J. N., Leclerc, H., Roux, S. & Hild F. Digital image correlation and biaxial test on composite material for anisotropic damage law identification. International Journal of Solids and Structures 46 (2009) 2388–2396.

Périé, J.-N., Calloch, S., Cluzel, C.. Hild, F. Analysis of a multiaxial test on a C/C composite by using digital image correlation and a damage model. Experimental Mechanics 42 (3), 318–328, 2002.

Pickering, K. L., Beckermann, G. W., Alan, S. N., Foreman, N. J. Compos. Part A: Appl. Sci. Manufact. 2007; 38: 461-468.

PlasticsTechnology (2014): Available on website: www.ptonline.com, accessed on 04.02.2014.

Poematec, 2007 Available on website: www.poematec.com.br, accessed on 31/10/2007.

Prasad, S. V., Pavithran, C., Rohatgi, P. K. Alkali treatment of coir fibres for coir–polyester composites. J Mater Sci, 18 (1983), pp. 1443–1454.

Quaresimin, M. Fatigue of woven composite laminates under tensile and compressive loading. ECCM-10, Brugge, Belgium, 3–7 June 2002.

Queiroz W. R. L. Projeto de um equipamento de fadiga para caracterização do dano em telhas de aço devido à ação do vento aplicando correlação digital de imagens e modelagem computacional. Doctoral thesis. Federal University of Ceará. 2013.

Rabello M., Aditivação de polímeros, ArtLiber: São Paulo, 2000.

Razera, I. A. T. Fibras lignocelulósicas como agente de reforço de compósitos de matriz fenólica e lignofenólica. Doctoral thesis. University of São Paulo, 2006.

Ridruejo, A., González, C., Llorca, J. Damage micromechanisms and notch sensitivity of glass-fiber non-woven felts: An experimental and numerical study. Journal of the Mechanics and Physics of Solids 58(2010)1628–1645.

Rong, M. Z.; Zhang, M. Q.; Liu, Y.; Yang, G. C.; Zeng, H. M. The effect of fiber treatment on the mechanical properties of unidirectional sisal-reinforced epoxy composites. Composites Science and Technology, 61, p. 1437-1447, 2001.

Rozman, H. D., Ismail, H., Jari, R.M., Aminullah, A., Ishak Z.A. Int J Polym Mater 1998;39:161-72.

Rozman, H. D., Tan, K. W., Kumar, R. N., Abubakar, A., Ishak, Z. A. M., Ismail, H. The effect of lignin as a compatibilizer on the physical properties of coconut fiber/polypropylene composites. European Polymer Journal 36 (2000) 1483-1494.

Saeed, M.-U., Chen, Z., Li, B. Manufacturing strategies for microvascular polymeric composites: A review. Composites: Part A 78 (2015) 327–340.

Sain, M., Panthapulakkal, S. In Green Fibre Thermoplastic Composites, Baillie C (Edt.) Cambridge, 2004.

Sanadi, A. R., Caulfield D. F., Jacobson R. E., Rowell R. M. Ind. Eng. Chem. Res. 1995; 34(5): 1889-1896.

Santos, A. M. Estudo de compósitos híbridos polipropileno / fibras de vidro e coco para aplicações em Engenharia. Master thesis. Federal University of Paraná. Curitiba, 2006.

Satyanarayana, K. G., Guimarães, J. L., Wypych, F. Studies on lignocellulosic fibers of Brazil. Part I – Source, production, morphology, properties and applications. Composites: Part A, 38, 1694–1709, 2007.

Satyanarayana, K. G., Mukherjee, P. S., Ravikumar, K. K., Sukumaran, K., Pillai, S. G. K., Kulkarni, A. G. Structure and properties of some vegetable fibres – Talipot and Plamyrah fibres. J Mater Sci 1986;21:57–63.

Satyanarayana, K. G., Sukumaran K., Mukherjee, P. S., Pavithran, C., Piuai, S. G. K. Natural Fibre-Polymer Composites. Cement & Concrete Composites 12 (1990) 117-136.

Satyanarayana, K. G., Guimarães J. L., Amico S. C., Sydenstricker T. H. D., Ramos L. D., Metals Materials Processes 2005; 17:183-194

Selezneva, M., Montesano, J., Fawaz, Z., Behdinan, K., Poon, C. Microscale experimental investigation of failure mechanisms in off-axis woven laminate*s at elevated temperatures*. Composites Part A 2011;42:1756–63.

Silva, G. C., Souza, D. A., Macahado, J. C., Hourston, D. J. Mechanical and thermal characterization of native Brazilian coir fiber. Journal of Applied Polymer Science, 76, 1197–1206, 2000.

Sreenivasan S., Bahama Iyer, P., Krishna Iyer, K. R. J Mater Sci, 31 (1996), p. 721.

Steinberger, R., Valadas-Leitao, T. I., Ladstatter, E., Pinter, G., Billinger, W., Lang, R. W. Infrared thermographic techniques for non-destructive damage characterization of carbon fibre reinforced polymers during tensile fatigue testing. Int J Fatigue 2006;28:1340–7.

Strapasson R. Valorização do polipropileno através de sua mistura e reciclagem. Master thesis. Federal University of Paraná (Brazil). 2004.

Struik, L C E, Physical aging in amorphous polymers and other materials, Elsevier Scientific Pub. Co.; New York, 1978, ISBN 0444416552 : 9780444416551.

Sun, W., Dong, E. L., Xu, Luo, B., He, X. Tensile test of membrane materials using digital image correlation method. Proc. SPIE (2007) 6423.

Sutton, M. A., Yan, J. H., Avril, S., Pierron, F., Adeeb, S. M. Identification of heterogeneous constitutive parameters in a welded specimen: uniform stress and virtual fields methods for material property estimation. Exp. Mech. 48 (2008) 451.

The National Non-Food Crops Centre. Renewable raw materials in car production. Available on website: www.nnfcc.co.uk/nnfcclibrary/productreport/download.cfm?id=78#search=%22bmw%20%22renewable%20raw%20materials%22%22, accessed on 09 set. 2006.

Tomczak, F. Estudos sobre a estrutura e propriedades de fibras de coco e curauá do Brasil. Federal University of Paraná. Doctoral thesis. Curitiba (Brazil), 2010.

Tomczak, F., Sydenstricker, T. H. D, Satyanarayana, K. G. Studies on lignocellulosic fibers of Brazil. Part II: Morphology and properties of Brazilian coconut fibers. Composites: Part A 38 (2007) 1710–1721.

Toubal, L., Karama, M., Lorrain, B. Damage evolution and infrared thermography in woven composite laminates under fatigue loading. Int J Fatigue 2006;28:1867–72.

Tscharnuter, D., Jerabek, M., Major, Z., Pinter, G. Irreversible deformation of isotactic polypropylene in the pre-yield regime. European Polymer Journal 47 (2011) 989–996.

Varma, D. S., Varma, M., Varma, I.K. Textile Res Inst, 54 (1984), p. 349.

Verhulp, E., Rietbergen, E. V., Huiskes, R. (2004). A three-dimensional digital image correlation technique for strain measurements in microstructures. J. Biomech. 37 (2004) 1313.

Wambua, P., Ivens, J., Verpoest, I. Compos. Sci. Tech. 2003; 64: 1259-1264.

Watase, A., Birgul, R., Hiasa, S., Matsumoto, M., Mitani, K., Catbas, F. N. Practical identification of favorable time windows for infrared thermography for concrete bridge evaluation. Construction and Building Materials. Volume 101, Part 1, 30 December 2015, Pages 1016–1030.

Yoneyama, S.; Murasawa, G. Digital Image Correlation. Experimental Mechanics. Unesco - Eolss. Sample Chapters, 2008.

Yuan, X., Jayaraman, K., Rhattachanyya, D. Compos. Part A: Appl. Sci. Manufact. 2004; 35: 1363-1374.

Zárate, C. N.; Aranguren, M. I.; Reboredo, M. M. Influence of fibers volume fraction and aspect ratio in resol-sisal composites. Journal of Applied Polymer Science, v. 89, p. 2714-2722, 2003.

Zulkifli N. I., Samat N., Anuar H., Zainuddin N. Mechanical properties and failure modes of recycled polypropylene/microcrystalline cellulose composites. Materials & Design. Volume 69, 15 March 2015, Pages 114–123.